Transverse Momentum of Charged Particles in low-Q^2 DIS at HERA

Dissertation

zur Erlangung des Doktorgrades
des Department Physik
der Universität Hamburg

vorgelegt von

Anastasia Grebenyuk

aus Saint Petersburg

Hamburg
2012

Gutachter der Dissertation:	Dr. Hannes Jung Dr. Thomas Schörner-Sadenius
Gutachter der Disputation:	Dr. Hannes Jung Prof. Dr. Johannes Haller
Datum der Disputation:	26.03.2012
Vorsitzender des Prüfungsausschusses:	Dr. Georg Steinbrück
Vorsitzender des Promotionsausschusses:	Prof. Dr. Peter Hauschildt
Dekan der MIN Fakultät:	Prof. Dr. Heinrich Graener
Leiterin des Fachbereichs Physik:	Prof. Dr. Daniela Pfannkuche

Abstract

In this thesis, measurement of the transverse momentum and pseudorapidity distributions of charged particles in deep-inelastic ep scattering at a centre of mass energy of $\sqrt{s} = 319$ GeV are presented. The analysis is based on data collected by the H1 detector in 2006, corresponding to an integrated luminosity of 88.64 pb^{-1}. The phase space of the measurement is defined by $5 < Q^2 < 100$ GeV^2 and $0.05 < y < 0.6$. The transverse momentum and pseudorapidity distributions of charged particles are measured in the virtual photon-proton centre of mass frame (hadronic centre of mass frame) in different regions of x and Q^2. The measured distributions are compared to predictions from different Monte Carlo generators using different approaches to simulate the parton cascade.

The measurement shows the importance of parton emissions unordered in transverse momentum. A QCD model, exhibiting this feature, such as the BFKL-like colour dipole model is best in the description of the data, whereas a model generating emissions according to the DGLAP approach undershoots the data at low Bjorken-x. It is shown that the region of small transverse momenta is primarily affected by the hadronisation process, whereas the region of large transverse momenta is mainly driven by perturbative parton radiation.

Kurzfassung

In der vorliegenden Arbeit wird eine Messung der Transversalimpuls- und Pseudorapiditätsverteilungen von geladenen Teilchen in tiefunelastischer ep-Streuung vorgestellt. Der dazu verwendete Datensatz hat eine integrierte Luminosität von 88.64 pb^{-1} und wurde bei einer Schwerpunktsenergie von $\sqrt{s} = 319$ GeV mit dem H1 Detektor im Jahr 2006 aufgezeichnet. Die Analyse wird in dem Bereich $5 < Q^2 < 100$ GeV^2 und $0.05 < y < 0.6$ vorgenommen. Die Transversalimpuls- und Pseudorapiditätsverteilungen von geladenen Teilchen werden im virtuellen Photon-Proton Schwerpunktsystem (hadronisches Schwerpunktsystem) in verschiedenen Regionen von x und Q^2 gemessen. Die Messungen werden mit Vorhersagen von verschiedenen Monte Carlo Generatoren verglichen, die unterschiedliche Ansätze bei der Simulation der Parton-Kaskade verwenden. Die Messung zeigt die Bedeutung der Parton-Emissionen bezüglich ungeordneter Transversalimpulse. Ein Modell der QCD, wie beispielsweise das BFKL-ähnliche Farbdipol-Modell (CDM), ist am besten geeignet um die Daten zu beschreiben, während ein Modell, das Emissionen mit Hilfe des DGLAP Ansatzes erzeugt, die Daten bei niedrigen Bjorken-x unterschätzt. Es wird gezeigt, dass der Bereich kleiner Transversalimpulse hauptsächlich durch die Hadronisierungsmodelle beeinflusst wird, während der Bereich der großen Transversalimpulse im Wesentlichen durch perturbative Parton Strahlung geprägt ist.

To my family

Contents

List of Figures

Chapter 1

Introduction

A series of important experiments performed during the past decades has established the new layer in the structure of matter - the protons and neutrons are no longer regarded as elementary particles but are found to be made of quarks. The dynamics of quarks can be described by quantum field theory, Quantum Chromodynamic (QCD), possessing local gauge symmetry - like the theories that proved already successful in describing the electromagnetic interactions of charged particles, QED, and electromagnetic and weak interactions of leptons and quarks, electroweak standard theory.

A main research tool in particle physics consists of accelerating elementary particles to high energy (beam) and letting them impact other particles (target). The analysis of the products of these collisions gives evidence of the structure of the colliding particles. It was scattering at large angles in the experiment the alpha particles hitting gold atom which resulted in the picture of Bohr atom with nucleus as the centre and electronic shells around it.

In case of nucleon there is one serious complication - isolated quarks and gluons are experimentally unavailable due to colour confinement and therefore the conclusions about the behavior of the latter inside nucleon are deduced from experiments rather indirectly. The most clean and effective way is inelastic scattering of leptons off nucleons. The momentum q, transferred by scattered lepton to nucleon, characterises in such processes how small distances can be probed inside the nucleon. The second important variable, Bjorken-x, defined by the equation $(xP + q)^2 = x^2P^2$, gives the plausible measure of the part of the nucleon momentum P with which the lepton was interacting elastically: $xP + p_l = xP' + p_{l'}$, where $P^2 = P'^2 = m_p^2$ and $p_l^2 = p_{l'}^2 = m_l^2$. From the early models of constituent quarks, according to which the nucleon consists of three valence quarks, i.e. the quarks defining its quantum numbers, each of mass $m_q \simeq m_p/3$, one would expect $x \simeq 0.3$, but the pioneering Deep Inelastic Scattering (DIS) experiments [1–3] showed significant contribution from very small x in contradiction with this model. It is now firmly established, that quark-antiquark pairs ("sea" quarks) and gluons carry a major part of proton momentum and hence the region of small $x \simeq 10^{-4}$ continues to be the region of intense experimental and theoretical studies.

At the Large Hadron Collider (LHC), the world's largest and highest-energy particle accelerator, the main goal is to answer the question if the Higgs mechanism for generating elementary particle masses via electroweak symmetry breaking actually

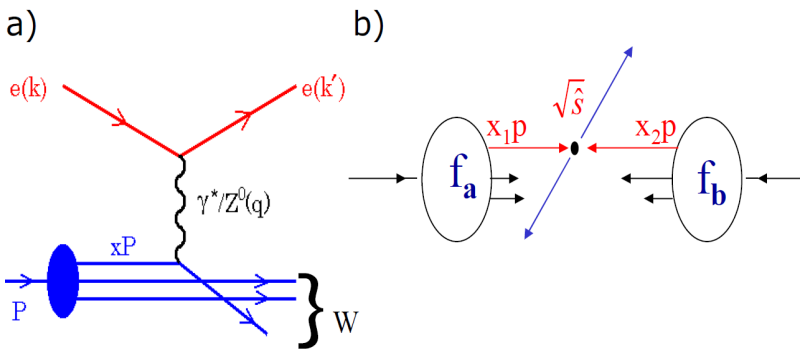

Figure 1.1: Manifestation of partons in the proton in a) ep and b) pp scattering.

realised in nature and is to demonstrate or rule out the existence of the Higgs boson. The LHC at present successfully operates at 3.5 TeV per beam. The current status of this fundamental search is reported recently by CMS and ATLAS collaborations: an excess of events is observed around $m_H \sim 124-126$ GeV with a local significance of $3.1-3.5$ standard deviations (σ) [4,5]. The LHC is designed to collide in the nearest future protons at up to 7 TeV. The pairs of interacting partons have invariant mass equal to $\sqrt{\hat{s}} = \sqrt{x_1 x_2}\sqrt{s}$ (see figure 1.1) and thus production of objects with mass 100 GeV is possible at $\sqrt{x_1 x_2} \simeq 10^{-2}$. It means that the parton distributions at small x gained from DIS experiments play crucial role for the interpretation of LHC results.

Small values of the fractional proton momentum carried by the interacting parton at moderate four-momentum transfer squared $Q^2 \equiv -q^2$ can be accessed at HERA. This is a region of high parton densities in the proton, dominated by gluons and "sea" quarks. At small Bjorken-$x \simeq 10^{-4}$, further referred to as x, partons in the proton can subsequently emit many partons before interacting with a virtual photon (figure 1.2).

In perturbative QCD multi-parton emissions are described only with certain approximations, in a restricted phase space. At large Q^2 and not too small x values the Dokshitzer-Gribov-Lipatov-Altarelli-Parisi (DGLAP) [6–9] evolution equation is expected to be a good approximation. The DGLAP equation corresponds to a strong ordering of the virtualities of the propagator partons, k_{Ti}, with increasing x, which implies strong ordering of the transverses momentum of the emitted partons, $p_{Ti} \ll p_{Ti+1}$, in the parton cascade from the proton side towards the virtual photon. The DGLAP approximation leads to resummation of leading logarithms of transverse momenta $\alpha_s \log(Q^2)$. This approximation, however, may become inadequate for small x, where $\log(1/x)$ terms become important. In this region the Balitsky-Fadin-Kuraev- Lipatov (BFKL) [10–12] scheme is expected to be appropriate, where a resummation terms of $\alpha_s \log(1/x)$ is performed.

Measurements of $F_2(x, Q^2)$ are well described by the NLO or NNLO DGLAP evolution and might be too inclusive to exhibit signals for BFKL.

However, significant deviation from the DGLAP approach are observed in the fractional rate of di-jet events [13–16], in inclusive jet production [17,18], in measurement of the transverse energy flow [19–24] and in transverse momentum spectra [25]. Measurement of charged particle transverse momentum were proposed in [26] as a

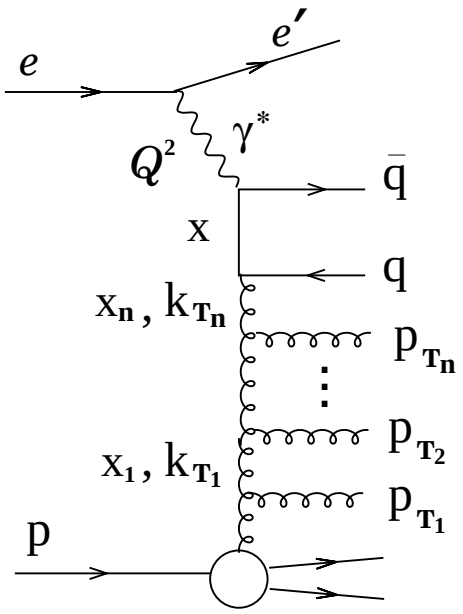

Figure 1.2: Generic diagram for deep-inelastic ep scattering at small x. The longitudinal momentum of emitted gluons i are labeled as $p_{T,i}$. The fractional momentum of the proton carried by the propagating gluon i and its transverse momentum are denoted with x_i and $k_{T,i}$, respectively.

more direct probe of the underlying parton dynamics. It has been shown with the aid of QCD models that the hard p_T spectrum is sensitive to parton radiation, while the contribution from hadronisation is small.

Measurements of the transverse momentum of charged particles have been performed earlier by the H1 collaboration [25], but the low statistics available at that time did not allow systematic differential investigations.

This thesis presents the study of the inclusive, event normalised, charged particle transverse momentum and pseudorapidity distribution at low Q^2, using data collected with the H1 detector in 2006 when positrons and protons collided with energies of 27.6 GeV and 920 GeV, respectively, corresponding to a centre of mass energy of $\sqrt{s} = 319$ GeV. The integrated luminosity of the data set is 88.6 pb^{-1}, which is about seven times larger than used in the previous publication [25].

One of the challenging task of this analysis was to reach the forward (towards the proton remnant) direction to the maximum limit allowed by the detector tracking system. Compared to the DGLAP scheme more gluons with sizable transverse momentum are emitted near the proton direction. For this reason charged particles with high transverse momentum produced close to the proton direction, are considered to be especially sensitive to QCD dynamics at low x. This was a first attempt to include forward tracks in to a H1 analysis after HERA upgrade.

Chapter 2

Theoretical Framework

2.1 Lepton-Proton Scattering and Kinematics

In high energy ep-collisions, when the exchanged photons have large virtualities, defined as $Q^2 \equiv -q^2$, where q^2 is the squared four-momentum transferred from the electron[1] to the photon, the wavelength of the virtual photons can be much smaller than the size of a proton, $\lambda \approx \frac{1}{Q} \ll 1$ fm. Hence the virtual photon can probe distances, that are small compared with the proton size, where, as it was discovered, point-like particles, partons, manifest themselves. In deep inelastic scattering (DIS) photons interact with partons, which carry a part x of a proton momentum, and scatter off them destroying thereby the proton. In cases, when very high momenta are transferred, the process can also occur via the exchange of an electroweak vector bosons, Z^0 or $W^{\pm}$. The processes where photon/Z^0 bosons are exchanged are called neutral current (NC) processes, whereas the exchange of a $W^{\pm}$ is called a charged current (CC) process. Example diagrams of NC and CC DIS scattering are shown in figure 2.1. This analysis is restricted to a kinematic region of low momentum transfer so that only photon exchange has to be considered.

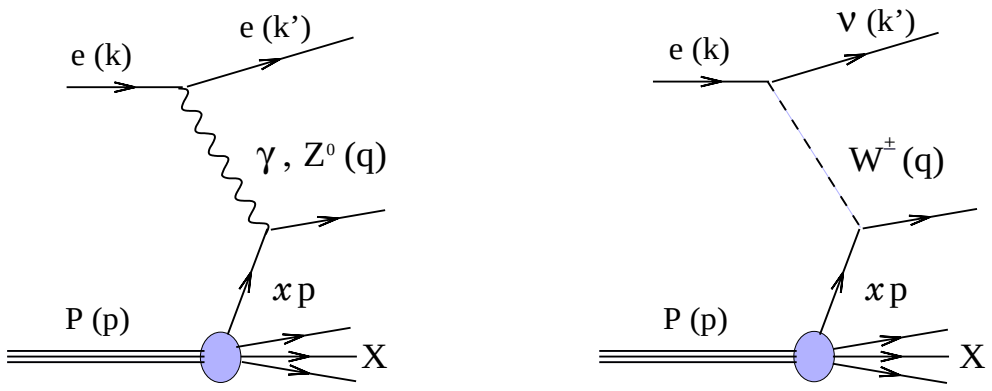

Figure 2.1: Illustration of $ep \to lX$ reaction in the lowest order. The exchanged boson may be photon or Z^0 in NC or $W^{\pm}$ in CC events. The four-momenta of the particles are indicated in brackets.

Let p, k and k' be the four-momenta of the incoming proton, the incoming electron and the outgoing electron, respectively. The main kinematic variables used

[1] The term electron refers to both the electron and the positron.

to describe inclusive DIS are:

- the centre of mass energy
$$s \equiv (k+p)^2 \; ; \tag{2.1}$$
- the virtuality of the exchanged boson
$$Q^2 \equiv -q^2 = -(k-k')^2 \; ; \tag{2.2}$$
- the Bjorken scaling variable x
$$x = \frac{Q^2}{2p \cdot q} \tag{2.3}$$
in the quark-parton model can be interpreted as the momentum fraction of the proton carried by the struck quark, see section 2.3;
- the inelasticity variable y
$$y = \frac{p \cdot q}{p \cdot k} \tag{2.4}$$
defined as the fractional energy loss of the electron in the proton rest frame.

These variables are related to the square of the centre of mass ep energy by $Q^2 = sxy$. Thus at fixed s DIS interaction can be fully characterised by only two variables, Q^2 and x.

2.2 The NC DIS Cross Section

The differential NC cross section is proportional to the convolution of the leptonic, $L^{\mu\nu}$, and hadronic, $W^{\mu\nu}$, tensors:

$$d\sigma_{NC} \propto L^{\mu\nu} W_{\mu\nu} \; . \tag{2.5}$$

The convolution $L^{\mu\nu}W_{\mu\nu}$ is shown graphically in figure 2.2. The electron tensor $L^{\mu\nu}$

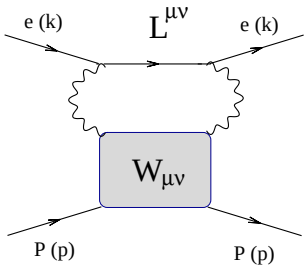

Figure 2.2: Graphical representation of the convolution $L^{\mu\nu}W_{\mu\nu}$.

is fully defined by the electron momenta k and k' and is equal to

$$L^{\mu\nu} = 2\left[k'^{\mu}k^{\nu} + k'^{\nu}k^{\mu} - g^{\mu\nu}(k',k)\right] . \tag{2.6}$$

Equation (2.6) can be rewritten in the explicit gauge-invariant ($q_\mu L^{\mu\nu} = 0$) form

$$-\frac{L^{\mu\nu}}{2Q^2} = -\left(g^{\mu\nu} + \frac{q^\mu q^\nu}{Q^2}\right) F_{e1} + \left(k^\mu + \frac{q^\mu (k,q)}{Q^2}\right)\left(k^\nu + \frac{q^\nu (k,q)}{Q^2}\right)\frac{F_{e2}}{(k,q)}\,, \tag{2.7}$$

where the "structure functions" of the electron are constants:

$$F_{e1} = \frac{1}{2}\,, \qquad F_{e2} = 1\,, \qquad F_{e2} = 2F_{e1}\,.$$

The hadronic tensor is more complicated than the leptonic one and so far cannot be calculated theoretically. In its most general form, $W_{\mu\nu}$ can be written as an expression analogous to (2.7) in terms of the proton structure functions:

$$W_{\mu\nu} = -\left(g_{\mu\nu} + \frac{q_\mu q_\nu}{Q^2}\right) F_1(x,Q^2) + \left(p_\mu + \frac{q_\mu (p,q)}{Q^2}\right)\left(p_\nu + \frac{q_\nu (p,q)}{Q^2}\right)\frac{F_2(x,Q^2)}{(p,q)}\,. \tag{2.8}$$

In contrast to the structure functions of the point-like electron the structure functions F_1 and F_2 of the proton are not constants and have to be determined experimentally.

The double-differential cross section for unpolarised ep scattering can be written in terms of these structure functions:

$$\frac{d^2\sigma}{dx dQ^2} = \frac{4\pi\alpha^2}{xQ^4}\left[(1-y)F_2(x,Q^2) - y^2 x F_1(x,Q^2)\right]\,, \tag{2.9}$$

where α is the electromagnetic coupling constant. F_1 and F_2 are related via the longitudinal structure function $F_L = F_2 - 2xF_1$. The magnitude of F_L is proportional to the cross section for protons colliding with longitudinally polarised virtual photons, $F_L \propto \sigma_L$.

2.3 The Quark-Parton Model

In the simple Bjorken-Feynman Quark-Parton Model (QPM) the proton is made of point-like spin-$\frac{1}{2}$ constituents, called partons [27]. In this model the DIS cross section can be approximated by an sum of elastic lepton-quark cross sections over all relevant types (flavors) of quarks, see figure 2.3. The wave function of this quark in the vertex $p \to k_i X$ is equal to $\sqrt{f_i(x)}$. The square of $\sqrt{f_i(x)}$ gives the quark distribution, or quark density, $f_i(x)$, of flavor i in the proton. The parton tensor $W_{i\mu\nu}$ in the approximation shown in figure 2.3 is calculable in the same manner as the electron tensor $L^{\mu\nu}$, see eq. (2.6):

$$W_{i\mu\nu} = 2e_i^2 Q^2\left[-\left(g^{\mu\nu} + \frac{q^\mu q^\nu}{Q^2}\right)\frac{1}{2} + \left(p^\mu + \frac{q^\mu (p,q)}{Q^2}\right)\left(p^\nu + \frac{q^\nu (p,q)}{Q^2}\right)\frac{x}{(p,q)}\right]\,,$$

where the relation $k_i = xp$ was used and the squared electric charge e_i^2 of the quark is introduced. Due to relation $W_{\mu\nu} = \sum_i f_i(x) W_{i\mu\nu}$ (followed from figure 2.3) one

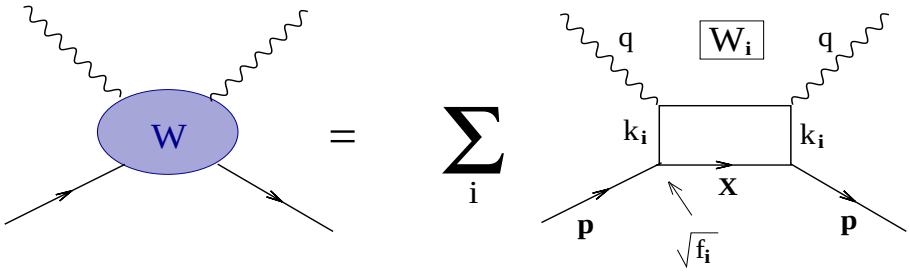

Figure 2.3: Graphical representation of the $W_{\mu\nu}$ in simple partonic model.

obtains:

$$W_{\mu\nu} = 2Q^2 \left[-\left(g^{\mu\nu} + \frac{q^\mu q^\nu}{Q^2}\right) \frac{\sum_i e_i^2 f_i(x)}{2} + \left(p^\mu + \frac{q^\mu (p,q)}{Q^2}\right)\left(p^\nu + \frac{q^\nu (p,q)}{Q^2}\right) \frac{x \sum_i e_i^2 f_i(x)}{(p,q)} \right] .$$

Comparing this expression with equation (2.8) one derives

$$F_1(x) = \frac{\sum_i e_i^2 f_i(x)}{2}, \qquad F_2(x) = x \sum_i e_i^2 f_i(x), \qquad F_2(x) = 2x F_1(x) \; , \tag{2.10}$$

where the sum runs over all quarks and antiquarks in the proton. That is, the structure functions $F_{1,2}$ in this approximation depend only on x and are independent on Q^2. This was observed in early DIS experiments [1–3] and is known as Bjorken scaling. The last relation in eq. (2.10) is known as the Callan-Gross relation. Thus, the QPM predicts $F_L(x) = F_2(x) - 2xF_1(x) = 0$ illustrating the fact that particles with spin $\frac{1}{2}$ cannot absorb longitudinally polarised photons elastically.

Let us summarize that in this model the proton structure functions are calculated as a sum of the constant structure functions of the charged point-like partons, averaged with their momentum distributions depending on only x.

2.4 Quantum Chromodynamics

The QPM assumes only essentially free quarks in the proton. This approximation contradicts the fact that no free partons were observed in experiment, but only mesons and baryons, - strong indication on the existence of some additional particle bounding ('gluing') quarks together. This problem and many others were solved by the theory of the strong interactions, Quantum Chromodynamics (QCD). According to QCD all hadrons consist of a fermions - the quarks - which are exchanged by vector bosons - the gluons. QCD is a gauge theory of the $SU(3)_c$ gauge group and the gluons play the similar role as the photons in QED. Quarks are spin-1/2 fermions which carry colour charge and represent the fundamental representation **3** of the gauge group $SU(3)_c$. That is the quarks fields are vectors in the complex 3-dimensional space of colours: q^c, $c = 1, 2, 3$ (antiquarks - $\bar{q}^{\bar{c}}$). Gluons are spin-1 bosons which also carry colour charges since they correspond to the adjoint representation **8** of $SU(3)_c$, which means that gluon fields are traceless Hermitian tensors, $g^{a\bar{b}}$. The

basis of these tensors consists of the eight Gell-Mann matrices, $\lambda_i^{a\bar{b}}$, $i = 1, 2, ..., 8$. The $q \to gq$ vertex is described by λ_i^b, the $g \to q\bar{q}$ - $\lambda_i^{a\bar{b}}$ etc. The vertex $g \to gg$ is given by the structure constants f_i^{jk} which are completely antisymmetric in the three indices and originate from the commutation relation

$$[\lambda^j, \lambda^k] = i f_i^{jk} \lambda^i \ .$$

Colourless mesons and baryons are described by two $SU(3)_c$ -invariant tensors: $E^{a\bar{b}} = \mathrm{diag}(1,1,1)$ and ϵ^{abc} - completely antisymmetric tensor with $\epsilon^{123} = 1$ so that the meson vertex $M \to q\bar{q}$ is given by $E^{a\bar{b}}$ and the baryon vertex to valence quarks $B \to qqq$ - by ϵ^{abc}.

The important property of QCD is the asymptotic freedom, which means that at short distance, or high-energy, coloured partons interact very weakly and become almost free particles. At long distance the force between them does not diminish but becomes even stronger. This is believed to be the reason of the confinement of coloured partons inside the hadrons. Asymptotic freedom follows from the analysis of the the strong coupling constant by methods of the renormalisation group. According to this analysis, the strong coupling constant depends on renormalisation scale μ_r and in the one loop approximation (leading order) looks as follows

$$\alpha_s(\mu_r) \approx \frac{12\pi}{(33 - 2N_f) \ln \frac{\mu_r^2}{\Lambda^2}} \ , \tag{2.11}$$

where $\Lambda \sim 200$ MeV is the QCD scale and N_f is the number of quark flavours. For $N_f < 17$ α_s decreases with increasing μ_r, which allows perturbation theory to be used accurately in describing of experiments performed at very high energies.

QCD was confirmed experimentally in 1979 at PETRA by the analysis and discussion of three-jet events initiated by the gluons [28].

2.4.1 Divergences and Factorisation Theorem

A better description of the proton is achieved by allowing interactions between partons in the frame of QCD. Some of the diagrams, additional to Born level diagram, are shown in figure 2.4. They are gluon radiation from quark line (QCD Compton, QCDC) and $g \to q\bar{q}$ (boson gluon fusion, BGF). Though the expansion parameter α_s of such perturbative series is assumed to be small, still many diagrams contribute to the cross section and have to be summed up, making the task to compute QCD corrections to the QPM difficult. An essential point in these calculations is the concept of factorisation. When carrying out the calculation of *ep* cross sections one has the diagrams for real gluon emission, the second and the third diagrams in figure 2.4, and for virtual corrections (see figure 2.5 as an illustration of virtual gluon loops in the quark propagators and vertices), and all these diagrams are divergent. The real emissions contain infra-red divergences, arising due to the radiation of soft quanta with small momenta $k \to 0$, and collinear divergences, corresponding to emission parallel to the initial quark ($k_T^2 \to 0$), while virtual corrections are both infra-red and ultra-violet (UV) divergent (large loop momenta). The method of the dimensional regularisation applied to the UV divergences in the virtual diagrams shows

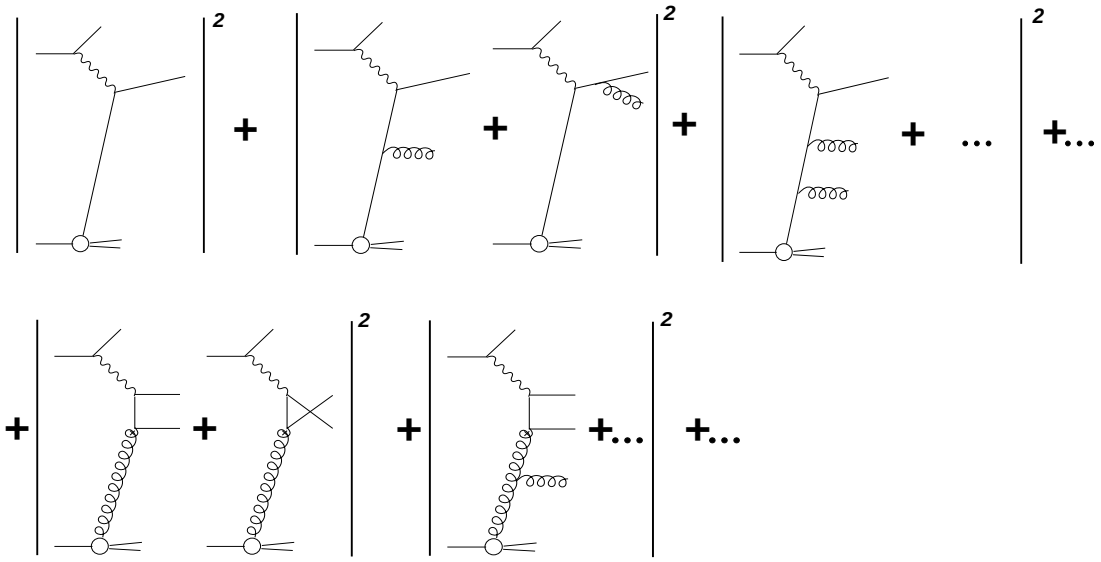

Figure 2.4: Diagrams contributing to the ep cross section in QCD. The QPM is supplemented by QCDC and BGF.

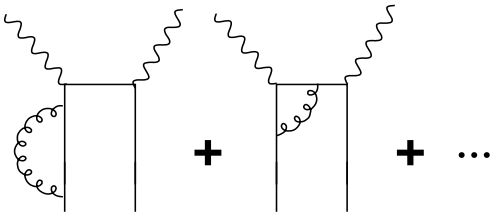

Figure 2.5: Virtual gluon loops in the quark propagators and vertices.

that they cancel between propagator and vertex corrections[2] .

As to the soft, infra-red, divergences, the Kinoshita-Lee-Nauenberg (KLN) theorem [31,32] guarantees that they are exactly canceled when one adds virtual corrections to real emission diagrams.

We are then left with the collinear divergences in the real gluon emissions, appearing as terms $\ln \frac{Q^2}{\mu^2}$, where μ is the infra-red cut-off of small k_T ($k_T^2 > \mu^2$). Since this cut-off is connected with some effective quark masses, the collinear divergences are also called mass singularities. How to deal with collinear divergences is mainly the content of the factorisation theorem [33–35]. The general idea of factorisation is a rearrangement of the perturbative expansion so that it is factorized into a part free from mass singularities and another one containing all (and only) mass singularities. The last part can be absorbed into the "bare" parton distribution function (PDF), $f_i^0(x)$, introduced in the QPM (see figure 2.3), which makes it dependent on the infra-red cut-off μ. Removing this infra-red cut-off is done by going from the bare to the dressed parton density. Actually, the computed correction has to be convoluted by the bare quark density and at this stage a factorisation scale μ_f is introduced and define a dressed density at that point. This procedure allows us to replace the diver-

[2]General statement is that the Ward identity insures a cancellation between the UV divergences arising from virtual quark wave function and vertex corrections [29,30].

gent bare density by the finite dressed one, introducing a scale dependence. Since a physical quantity, such as $f(x, Q^2)$, must not depend on the factorisation scale μ_f, the derivative of it with respect to $\ln \mu_f^2$ has to vanish. This gives the well-known DGLAP (Dokshitzer-Gribov-Lipatov-Altarelli-Parisi) evolution equation. Thus, the factorisation scale determines which of the radiated gluons are considered to belong to the hadronic structure (the PDF). Finally, the electron-proton structure function F_2 with the singularities removed is the convolution of redefined, or dressed, parton distribution function (further on referred to as just parton distribution function) with the partonic hard-scattering function C:

$$F_2(x, Q^2) = x \sum_{i=q,\bar{q},g} \int_x^1 \frac{d\xi}{\xi} C_i \left(\frac{x}{\xi}, Q^2, \mu_f^2 \right) f_i(\xi, \mu_f^2) = x \sum_{i=q,\bar{q},g} (C_i(Q^2, \mu_f^2) \otimes f_i(\mu_f^2))(x) \, , \tag{2.12}$$

where the sum runs over all partons in the proton. The choice of μ_f is arbitrary and, qualitatively, the factorisation scale corresponds to the resolution with which the proton is being probed. The partonic hard-scattering functions C_i can be calculated perturbatively for any scale. For $\mu_f = Q$ it reduces to the Born graph and parton distribution function is such as it is seen by a photon with virtuality Q^2. The changes of parton density with the scale is governed by so-called evolution equations so that once the PDF is given at one scale it can be calculated for any other scale.

2.4.2 DGLAP Evolution Equations

As was mentioned above, there are two steps in the derivation of the DGLAP evolution equation. The first is to deal with collinear divergences when calculating the corrections due to gluon emissions, and the second - to resum the perturbative expansion (factorisation theorem). The derivation of the DGLAP evolution equation in leading order (LO) is presented in this subsection. To distinguish the partonic distribution function, f_i, for quarks and gluons, let us denote q_i as a quark density for flavour i and g as the gluon density in the proton. The partonic distribution function introduced in the QPM we denote as q_i^0. Then the expression of $F_2(x)$ in the QPM, given in (2.10), can be also written as:

$$F_2(x) = x \sum_i e_i^2 q_i^0(x) = x \sum_i e_i^2 \int_x^1 \frac{d\xi}{\xi} q_i^0(\xi) \delta(1 - \frac{x}{\xi}) \equiv x \sum_i e_i^2 (E \otimes q_i^0)(x) \, , \tag{2.13}$$

where $E(x) = \delta(1 - x)$ is the unit function w.r.t. the convolution: $E \otimes f = f$.

Let us consider first the $q \to qg$ splitting and the corresponding QCDC diagram (see second term in figure 2.4). The calculation of this diagram requires the knowledge of the squared vertices illustrated in figure 2.6 - they are called the splitting functions - and the integration over the internal momenta of the exchanged quarks. This leads to the following modification of the function E (eqs.(10.32) and (10.34) of [36]):

$$E \to E + \frac{\alpha_s}{2\pi} \ln \frac{Q^2}{\mu^2} P_{qq}^{(0)} \, , \tag{2.14}$$

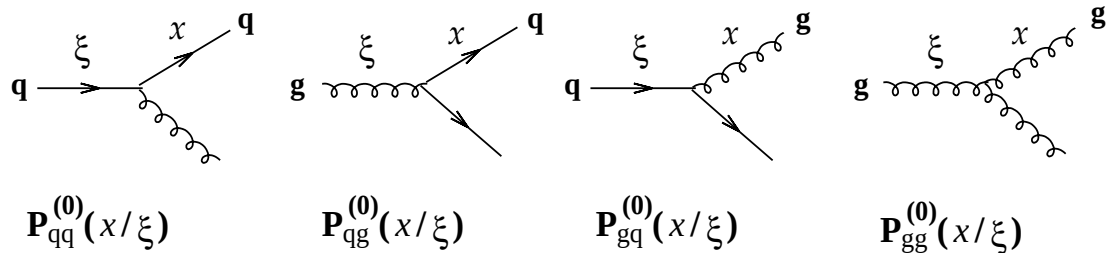

Figure 2.6: Splitting functions

where

$$P_{qq}^{(0)}(z) = \frac{4}{3} \cdot \frac{1+z^2}{1-z} , \qquad z \equiv \frac{x}{\xi} \tag{2.15}$$

is the $q \to qg$ splitting function shown first in figure 2.6. Here μ^2 is just the infra-red cut-off of small k_T, discussed above, which regulates the collinear singularities. Equation (2.14) is valid when Q^2 is large but x is not too small.

The infra-red cut-off should be removed, and this is done by the introducing a factorisation scale μ_f^2 and then, by factorizing the eq. (2.14) as follows

$$E + \frac{\alpha_s}{2\pi} \ln \frac{Q^2}{\mu^2} P_{qq}^{(0)} \simeq (E + \frac{\alpha_s}{2\pi} \ln \frac{Q^2}{\mu_f^2} P_{qq}^{(0)}) \otimes (E + \frac{\alpha_s}{2\pi} \ln \frac{\mu_f^2}{\mu^2} P_{qq}^{(0)})) . \tag{2.16}$$

This factorisation is valid up to the first order in α_s. Then the LO F_2, given by eq. (2.17), transforms into

$$\begin{aligned} F_2(x,Q^2) = x \sum_i e_i^2 ((E + \frac{\alpha_s}{2\pi} \ln \frac{Q^2}{\mu^2} P_{qq}^{(0)}) \otimes q_i^0)(x) = \\ x \sum_i e_i^2 ((E + \frac{\alpha_s}{2\pi} \ln \frac{Q^2}{\mu_f^2} P_{qq}^{(0)}) \otimes q_i(\mu_f^2))(x) , \end{aligned} \tag{2.17}$$

where $q_i(\mu_f^2)$, E and $P^{(0)}$ etc. are functions of x and where a dressed parton density at the factorisation scale μ_f^2 is introduced:

$$q_i(\mu_f^2) \equiv (E + \frac{\alpha_s}{2\pi} \ln \frac{\mu_f^2}{\mu^2} P_{qq}^{(0)}) \otimes q_i^0 = q_i^0 + \frac{\alpha_s}{2\pi} \ln \frac{\mu_f^2}{\mu^2} (P_{qq}^{(0)} \otimes q_i^0) . \tag{2.18}$$

Comparing eq.(2.17) with the general factorisation equation (2.12), one obtains that at α_s order the partonic hard-scattering function C_i is equal to:

$$C_i(x, Q^2, \mu_f^2) = e_i^2 (E + \frac{\alpha_s}{2\pi} \ln \frac{Q^2}{\mu_f^2} P_{qq}^{(0)})(x) . \tag{2.19}$$

$F_2(x, Q^2)$ should not depend on the scale μ_f^2, and the derivation of equation (2.17) with respect to $\ln \mu_f^2$ must be equal to zero. At α_s order this leads to the LO DGLAP equations:

$$\frac{dq_i(\mu_f^2)}{d \ln \mu_f^2} = \frac{\alpha_s}{2\pi} (P_{qq}^{(0)} \otimes q_i(\mu_f^2)) \quad \Leftrightarrow \quad \frac{dq_i(x,\mu_f^2)}{d \ln \mu_f^2} = \frac{\alpha_s}{2\pi} \int_x^1 \frac{d\xi}{\xi} q_i(\xi, \mu_f^2) P_{qq}^{(0)}(\frac{x}{\xi}) . \tag{2.20}$$

In (2.20) we have limited ourselves to the case of gluon emission by a quark coming out the proton. In that case, $P_{qq}^{(0)}(\frac{x}{\xi})$ describes the probability to find a quark of momentum fraction x emerging from an incident quark of momentum ξ. This can be generalised to the probability to find a parton a (quark or gluon) emerging from parton b by emission of a third parton[3]. The four cases are summarised in figure 2.6. Equation (2.20) for the quark density then becomes:

$$\frac{dq_i(x,Q^2)}{d\ln Q^2} = \frac{\alpha_s}{2\pi}\int_x^1 \frac{d\xi}{\xi}\left(q_i(\xi,Q^2)P_{qq}^{(0)}(\frac{x}{\xi}) + g(\xi,Q^2)P_{qg}^{(0)}(\frac{x}{\xi})\right) , \tag{2.21}$$

where the probability to find a quark in a gluon (second vertex in figure 2.6) is given by

$$P_{qg}^{(0)}(z) = \frac{1}{2}[z^2 + (1-z)^2] . \tag{2.22}$$

Similar for the quark density, the gluon density evolves as:

$$\frac{dg(x,Q^2)}{d\ln Q^2} = \frac{\alpha_s}{2\pi}\int_x^1 \frac{d\xi}{\xi}\left(\sum_i q_i(\xi,Q^2)P_{gq}^{(0)}(\frac{x}{\xi}) + g(\xi,Q^2)P_{gg}^{(0)}(\frac{x}{\xi})\right) , \tag{2.23}$$

where

$$P_{gq}^{(0)}(z) = \frac{4}{3}\cdot\frac{1+(1-z)^2}{z}$$

and

$$P_{gg}^{(0)}(z) = 2N_c\left[\frac{1}{z} + \frac{1}{1-z} - 2 + z(1-z)\right] , \tag{2.24}$$

where $N_c = 3$.

In perturbative QCD the splitting functions can be expanded as power series in α_s:

$$P(z,\alpha_s) = \frac{\alpha_s}{2\pi}P^{(0)}(z) + \left(\frac{\alpha_s}{2\pi}\right)^2 P^{(1)}(z) + \left(\frac{\alpha_s}{2\pi}\right)^3 P^{(2)}(z) + \cdots \tag{2.25}$$

Keeping only the first term in this expansion leads to the LO splitting functions, taking into account the second term results in next-to-leading (NLO) splitting functions, and so on. The splitting functions are known up to NNLO, i.e. $O(\alpha_s^2)$ [37,38].

Taking into account all gluon ladder diagrams with n the intermediate gluon emissions equation (2.14) becomes [9]: (in what follows we use another notation for the factorisation scale: $\mu_f = Q_0$)

$$E \to E + \sum_{n=1}^{\infty}\left(\frac{\alpha_s}{2\pi}\right)^n \frac{1}{n!}\ln^n\frac{Q^2}{Q_0^2}\,P^n . \tag{2.26}$$

The terms $\ln^n\frac{Q^2}{Q_0^2}$ build up from the nested integrals over k_T arising when summing gluon ladder diagrams with n gluon rungs [9]:

$$\frac{1}{n!}\ln^n\frac{Q^2}{Q_0^2} = \int_{Q_0^2}^{Q^2}\frac{dk_{nT}^2}{k_{nT}^2}\int_{Q_0^2}^{k_{nT}^2}\frac{dk_{(n-1)T}^2}{k_{(n-1)T}^2}\cdots\int_{Q_0^2}^{k_{3T}^2}\frac{dk_{2T}^2}{k_{2T}^2}\int_{Q_0^2}^{k_{2T}^2}\frac{dk_{1T}^2}{k_{1T}^2} .$$

[3]Strictly speaking, splitting functions are not probability since they are not normalised to unity, but squared matrix elements of corresponding vertices, e.g $q \to gq$ in first α_s order, integrated over all kinematics variables apart from $z \equiv p_g^+/p_q^+$, where "+"- components of the momenta in light cone parametrisation are used . However the term "probability" is still used in literature. See e.g. page 213 of the classic book [36].

In fact this contribution comes from a region where the coordinates $(k_{1T}^2, \cdots, k_{(n-1)T}^2, k_{nT}^2)$ of the n-dimensional hypercube are strongly ordered

$$Q^2 \gg k_{nT}^2 \gg k_{(n-1)T}^2 \gg \cdots \gg k_{2T}^2 \gg k_{1T}^2 \gg Q_0^2 \,. \tag{2.27}$$

DLL approximation

The special case for which DGLAP equations can be solved analytically is the double leading log approximation (DLL) [39], which is based on the small x limit. At small x the parton content of the proton is dominated by gluons and a good approximation of the LO $g \to gg$ splitting function (2.24) is $P_{gg}(z) \sim \frac{2N_c}{z}$. If one assumes that the gluon distribution at factorisation scale Q_0, $xg_0 \equiv xg(x, Q_0)$, is a constant so that $g_0(x) = \frac{c}{x}$, the convolution with the n-degree of splitting function, $(P^n \otimes g_0)(x)$, in (2.20) can be calculated analytically:

$$\int_x^1 \frac{d\xi_n}{\xi_n} P(\frac{x}{\xi_n}) \int_{\xi_n}^1 \frac{d\xi_{n-1}}{\xi_{n-1}} P(\frac{\xi_n}{\xi_{n-1}}) \cdots \int_{\xi_2}^1 \frac{d\xi_1}{\xi_1} P(\frac{\xi_2}{\xi_1}) g_0(\xi_1) = \frac{(2N_c)^n}{n!} \ln^n \left(\frac{1}{x}\right) \cdot g_0(x) \,. \tag{2.28}$$

Similarly to (2.27), the $\ln^n\left(\frac{1}{x}\right)$ term comes from the region where the longitudinal momentum fractions are strongly ordered

$$1 \gg \xi_1 \gg \xi_2 \gg \cdots \gg \xi_n \gg x \,.$$

Applying (2.26) to the parton distribution function $g_0(x) = \frac{c}{x}$ at the scale Q_0 and taking into consideration (2.28), one derives the parton density at the scale Q

$$g(x, Q^2) = \left[\sum_{n=0}^{\infty} \frac{1}{(n!)^2} \left(\bar{\alpha}_s \cdot \ln \frac{Q^2}{Q_0^2} \cdot \ln \left(\frac{1}{x}\right) \right)^n \right] \cdot g(x, Q_0^2) \,, \tag{2.29}$$

where $\bar{\alpha}_s \equiv \frac{N_c \alpha_s}{\pi} = \frac{3\alpha_s}{\pi}$. This expression can be rewritten in exponential form by introducing a Bessel function, which for large arguments grows like an exponential: $I_0(2\sqrt{X}) \sim e^{2\sqrt{X}}$. Thus one obtains

$$g(x, Q^2) = e^{2\sqrt{\bar{\alpha}_s \cdot \ln \frac{Q^2}{Q_0^2} \cdot \ln \frac{1}{x}}} \cdot g(x, Q_0^2) \,, \tag{2.30}$$

which represents the DLL solution, valid for large Q^2 and small x, when both logarithms are large. Here the coupling $\bar{\alpha}_s$ is assumed to be constant. For a running coupling (2.11) the dressed parton density (2.30) is replaced by [39]:

$$g(x, Q^2) = e^{\sqrt{\frac{144}{33-n_f} \cdot \ln \left[\frac{\ln \frac{Q^2}{\Lambda^2}}{\ln \frac{Q_0^2}{\Lambda^2}} \right] \cdot \ln \frac{1}{x}}} \cdot g(x, Q_0^2) \,. \tag{2.31}$$

Equation (2.31) predicts at small x a fast rise of the gluon density with decreasing x.

Sudakov form factor

Both the $q \to qg$ (2.15) and the $g \to gg$ (2.24) splitting functions have the infra-red singularity $1/(1-z)$, which, as was mentioned above, is screened by taking into account virtual corrections to real emission diagrams (KLN theorem). Let us denote $xq(x,Q^2) \equiv a(x,Q^2)$. Then the evolution equation (2.20) can be rewritten as

$$\frac{da_r(x,Q^2)}{d\ln Q^2} = \frac{\alpha_s}{2\pi}\int_x^1 d\xi\; a_r(\frac{x}{\xi},Q^2)P_{qq}^{(0)}(\xi)\;, \tag{2.32}$$

where the subscript r means only real gluon emission. In the leading log approximation with virtual gluon contribution the evolution equation (2.32) is modified as follows

$$\frac{da_{r+v}(x,Q^2)}{d\ln Q^2} = \frac{\alpha_s}{2\pi}\left[\int_x^{1-\delta} d\xi\; a_{r+v}(\frac{x}{\xi},Q^2)P_{qq}^{(0)}(\xi) - a_{r+v}(x,Q^2)\int_0^{1-\delta} d\xi\; P_{qq}^{(0)}(\xi)\right]. \tag{2.33}$$

Straightforward check[4] gives the partial solution of (2.33)

$$a_{r+v}(x,Q^2) = \Delta_s(Q^2,Q_0^2)a_r(x,Q^2)\;, \tag{2.35}$$

where $a_r(x,Q^2)$ is the solution of the DGLAP evolution equation (2.32) with the only real gluons, whereas Δ_s, the so-called Sudakov form factor, is equal to

$$\Delta_s(Q^2,Q_0^2) = \exp\left(-\int_{Q_0^2}^{Q^2}\frac{dQ^{2\prime}}{Q^{2\prime}}\,\frac{\alpha_s(Q^{2\prime})}{2\pi}\times\int_0^{1-\delta} d\xi\; P_{qq}^{(0)}(\xi)\right). \tag{2.36}$$

It is said that Sudakov form factor arises from the resummation of the virtual corrections.

2.4.3 BFKL Evolution Equation

The DGLAP approximation leads to a resummation of leading logarithms $\alpha_s\ln(Q^2)$. This approximation, however, may become inadequate for small x, where $\ln(1/x)$ terms become important. In this region the Balitsky-Fadin-Kuraev-Lipatov (BFKL) [10–12] scheme is expected to be the appropriate approximation, where resummation includes only single logarithmic terms (the leading log approximation, LLA) of the form $\alpha_s^n\ln^n(1/x)$, and no strong ordering in k_T is assumed. The BFKL equation

[4]

$$\frac{d[\Delta_s a_r(x,Q^2)]}{d\ln Q^2} = \Delta_s\frac{da_r}{d\ln Q^2} + a_r(x,Q^2)\frac{d\Delta_s}{d\ln Q^2} =$$
$$\Delta_s\frac{\alpha_s}{2\pi}\int_x^1 d\xi\; a_r(\frac{x}{\xi},Q^2)P_{qq}^{(0)}(\xi) - a_r(x,Q^2)\Delta_s\frac{\alpha_s}{2\pi}\int_0^{1-\delta} d\xi\; P_{qq}^{(0)}(\xi) =$$
$$\frac{\alpha_s}{2\pi}\left[\int_x^{1-\delta} d\xi\; a_{r+v}(\frac{x}{\xi},Q^2)P_{qq}^{(0)}(\xi) - a_{r+v}(x,Q^2)\int_0^{1-\delta} d\xi\; P_{qq}^{(0)}(\xi)\right]. \tag{2.34}$$

takes into account diagrams in which the x_i are strongly ordered, $x_0 \gg ...x_i \gg x_{i+1} \gg .. \gg x$. Since the parton virtualities perform a random walk, the gluon density and the propagating partons can not be treated as collinear and have to depend on the transverse momentum. The unintegrated gluon density $f(x, k_T^2)$ is approximately related to the integrated gluon distribution $g(x, Q^2)$ by

$$xg(x, Q^2) \simeq \int_0^{Q^2} \frac{dk_T^2}{k_T^2} f(x, k_T^2) \; . \tag{2.37}$$

An additional effect of the fact that the parton virtualities perform a random walk is so-called "k_T diffusion". There is a possibility that the evolution diffuses into infrared region ($k_T < Q_0$) where perturbative theory cannot be applied, since α_s becomes large and is not usable as an expansion parameter.

The BFKL equation is an evolution equation in x and is written for the unintegrated gluon density [40]:

$$\frac{df_{r+v}(x, k_t^2)}{d \ln \frac{1}{x}} = \bar{\alpha}_s(k_t^2) \left[\int \frac{d\vec{p}_t}{\pi p_t^2} f_{r+v}(x, k_t'^2) - f_{r+v}(x, k_t^2) \int_{\mu^2}^{k_t^2} \frac{d\vec{p}_t}{\pi p_t^2} \right] \; , \tag{2.38}$$

where $\vec{p}_t = \vec{k}_t - \vec{k}_t'$ is the transverse momentum of the emitted real gluon and the first term is the contribution of its emission. The second contribution corresponds to the virtual correction in which the virtual transverse momenta $\vec{p}_t$ are bound by the total transverse momentum $\vec{k}_t$. The subscript $r+v$ means just real and virtual gluon emissions. The cut-off parameter μ^2 prevents from the singularity when $p_t \to 0$. Similarly to the Sudakov form factor one can resum the virtual corrections:

$$f_{r+v}(x, k_t^2) = \Delta_{ns}(x, k_t^2) f_r(x, k_t^2) \; , \tag{2.39}$$

where

$$\Delta_{ns}(x, k_t^2) \equiv e^{-\bar{\alpha}_s(k_t^2) \ln \frac{1}{x} \int_{\mu^2}^{k_t^2} \frac{d\vec{p}_t}{\pi p_t^2}} = e^{-\bar{\alpha}_s(k_t^2) \ln \frac{1}{x} \ln \frac{k_t^2}{\mu^2}} = x^{\alpha_s(k_t^2) \ln \frac{k_t^2}{\mu^2}} \tag{2.40}$$

is the so-called non-Sudakov form factor, the latter equation presenting its Regge-like form, and $f_r(x, k_t^2)$ is the gluon density originating from only real gluon emissions:

$$\frac{df_r(x, k_t^2)}{d \ln \frac{1}{x}} = \bar{\alpha}_s(k_t^2) \int \frac{d\vec{p}_t}{\pi p_t^2} f_r(x, k_t'^2) \; . \tag{2.41}$$

The BFKL equation can be solved analytically, if one assumes a fixed α_s, and with the help of (2.37) the series analogous to DLL (2.29) is derived:

$$g(x, Q^2) = \left[\sum_{n=0}^{\infty} \frac{1}{n!} \left(\bar{\alpha}_s \cdot 4 \ln 2 \cdot \ln \left(\frac{1}{x} \right) \right)^n \right] \cdot g(x, Q_0^2) = e^{\lambda \ln \left(\frac{1}{x} \right)} g(x, Q_0^2) = x^{-\lambda} g(x, Q_0^2) \; , \tag{2.42}$$

where $\lambda \equiv \bar{\alpha}_s \cdot 4 \ln 2$. That is the $\frac{1}{n!} \ln^n \frac{Q^2}{Q_0^2}$ in the sum (2.29) is replaced by the $(4 \ln 2)^n$. For $\bar{\alpha}_s = 0.19$ we obtain $\lambda = 0.55$. According to BFKL dynamics the gluon

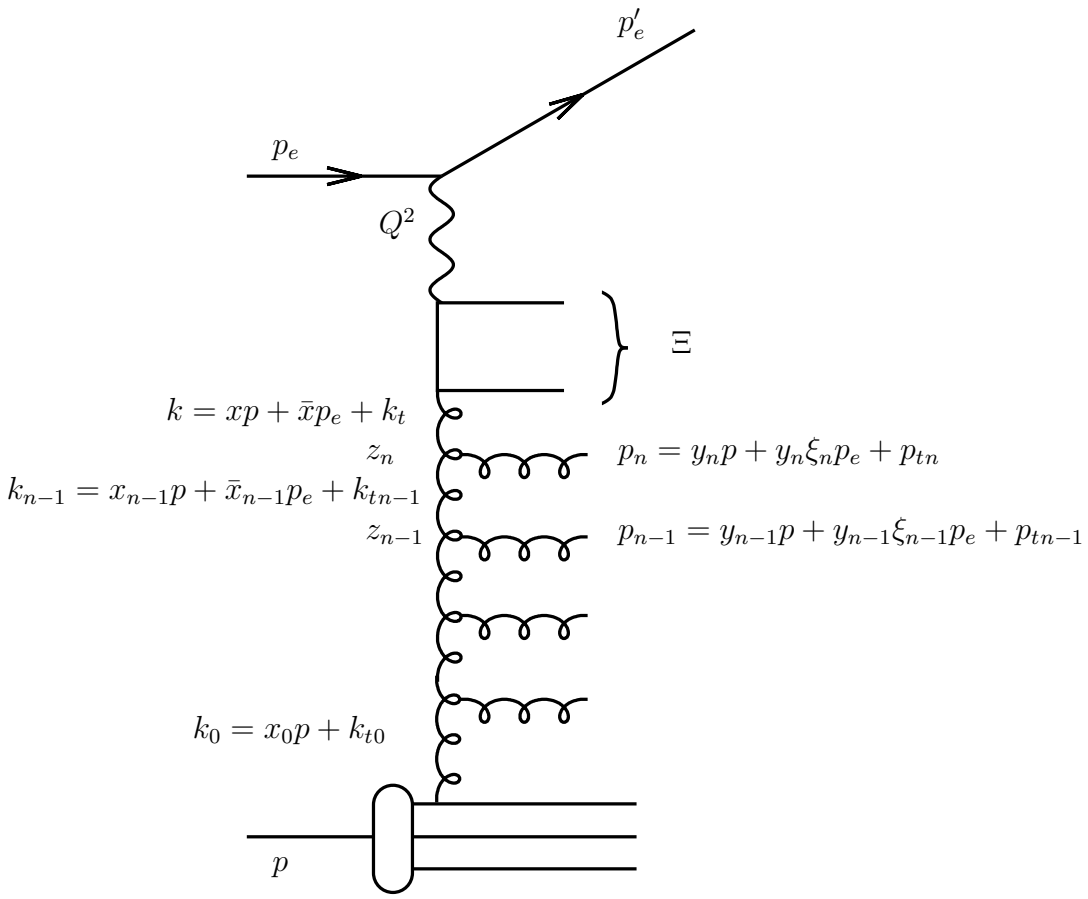

Figure 2.7: Hard process $\gamma^* g \to q\bar{q}$ along with preceding multigluon emission.

density is expected to rise like a power of $(1/x)$, faster than the DLL result at $x \to 0$. However, higher-order corrections and running α_s decrease the value of λ. BFKL predictions contain several uncertainties but are not in general inconsistent with the data. The DGLAP prediction, on the other hand, fits the data down to surprisingly small x, so it is hard to say whether any effects of the BFKL resummation can be seen in the data.

2.4.4 CCFM Evolution

The CCFM [41–43] approach attempts to cover both DGLAP and BFKL regions by considering color coherence phenomenon. At small x the gluons are the dominating partons of the proton, and a typical interaction can be illustrated by the diagram shown in figure 2.7, where k_i is the four-momentum of the evolved virtual gluon, $k_i^2 < 0$, and p_i is the four-momentum of the real emitted gluon, $p_i^2 = 0$. Sudakov parametrisation of the momenta of real emitted gluons (see Appendix A) looks like

$$p_i = y_i p_p + \frac{p_{ti}^2}{s y_i} p_e + p_{ti} \ , \tag{2.43}$$

so that the rapidities of the emitted gluons in ep centre of mass system are

$$\eta_i = -\frac{1}{2}\ln\frac{p_{ti}^2}{sy_i^2} \to e^{-\eta_i} = \frac{p_{ti}}{Wy_i} = \sqrt{\tan\frac{\theta_i}{2}}\ . \tag{2.44}$$

The important feature of the branching $k_{i-1} \to k_i + p_i$ is the *coherence* [44, 45] for $x \to 0$ and $x \to 1$, which means that the interference among soft gluons results in the angular ordering

$$\theta_0 < \theta_1 < \cdots \theta_n\ ,$$

or, equivalently, in the rapidity ordering

$$\eta_1 > \eta_2 > ... > \eta_n \tag{2.45}$$

of the emitted real gluons.

The lower limit in (2.45) is determined by the kinematics of the hard interaction $\gamma^* + g^* \to q\bar{q}$, namely by the rapidity of the interacting system $\gamma^* g^*$. Introducing $z_i \equiv \frac{x_i}{x_{i-1}}$ and $1 - z_i = \frac{y_i}{x_{i-1}}$ one can define a reduced transverse momentum of the emitted gluon

$$q_i \equiv \frac{p_{it}}{1-z_i} = x_{i-1}\frac{p_{it}}{y_i} = x_{i-1}We^{-\eta_i}\ , \tag{2.46}$$

and can show that the ordering requirement $\eta_{i-1} > \eta_i$ is equivalent to

$$q_i > z_{i-1}q_{i-1}\ . \tag{2.47}$$

Instead of the LO DGLAP splitting function

$$P_{gg}(z,\alpha_s) = \bar{\alpha}_s(Q^2)\left[\frac{1}{1-z} + \frac{1}{z} - 2 + z(1-z)\right]\ ,$$

where in fact only the first two terms are relevant for soft gluon emission and $x \to 0$, the CCFM splitting function P_{gg} is given by

$$P_{gg}(z_i, q_i, k_{ti}) = \frac{\bar{\alpha}_s(q_i^2(1-z_i)^2)}{1-z_i} + \frac{\bar{\alpha}_s(k_{ti}^2)}{z_i}\Delta_{ns}(z_i, q_i^2, k_{ti}^2)\ , \tag{2.48}$$

where the non-Sudakov form factor Δ_{ns} is introduced. The non-Sudakov form factor is generated by the resummation of virtual corrections, which are relevant, in contrast to Sudakov form factor, only for low x, and screens the singularity of the $g \to gg$ splitting function as $z \to 0$. In unfolded form these corrections are presented by the second contribution of right side of the BFKL equation (2.38) but with one reservation - the cut-off μ in (2.38) is replaced by $z'q_{ti}$ which follows from the angular ordering requirement $q > z'q_{ti}$.

As to the specific scales of $\bar{\alpha}_s$ in (2.48), it was argued in [46], that the proper hard scale is expected to be $(1-z_i)k_{ti}^2$, which tends to k_{ti}^2 as $z_i \to 0$ and to p_{ti}^2 as $z_i \to 1$. Therefore k_{ti}^2 is taken as the argument of $\bar{\alpha}_s$ in the non-Sudakov form factor (2.49) and in the $1/z_i$ term of (2.48), while the argument is p_{ti}^2 for the soft gluon emission term $1/(1-z_i)$ and in Sudakov form factor (2.53). This simplification allows to perform analytical calculation in some cases. In particular, one can derive from (2.38) that

$$\Delta_{ns}(z_i, q_i, k_{ti}) = \exp\left\{-\bar{\alpha}_s(k_{ti}^2)\ln\frac{1}{z_i}\ln\frac{k_{ti}^2}{z_i q_i^2}\right\}\ . \tag{2.49}$$

The expression (2.49) goes to 0 when $z \to 0$, screening thus the singularity at $z = 0$ in (2.48) ($\frac{\Delta_{ns}}{z} \to 0$ when $z \to 0$). Defining the constant C_i and introducing the variable τ as follows:

$$C_i \equiv \ln \frac{k_{it}}{q_i} , \qquad \tau \equiv C_i + \ln \frac{1}{z} \to z = e^{C_i - \tau} , \tag{2.50}$$

one can cast the expression (2.49) to the Gaussian form

$$\Delta_{ns}(\tau, C) = e^{\frac{(\tau_0 - C)^2}{2\sigma^2}} \, e^{-\frac{(\tau - \tau_0)^2}{2\sigma^2}} \tag{2.51}$$

with the mean and the standard deviation equal to

$$\tau_0 \equiv \frac{1}{2\bar{\alpha}_s(k_t^2)} , \qquad \sigma = \sqrt{\tau_0} = \frac{1}{\sqrt{2\bar{\alpha}_s(k_t^2)}} . \tag{2.52}$$

Equation (2.51) is convenient for Monte Carlo implementation (see below).

In accordance with the angular ordering the Sudakov form factor (2.36) is also modified in the CCFM approach[5]:

$$\Delta_s(q_i, z_i q_{i-1}) = \exp\left\{ - \int_{(z_{i-1}q_{i-1})^2}^{q_i{}^2} \frac{dq^2}{q^2} \int_0^{1-Q_0/q} dz \frac{\bar{\alpha}_s(q^2(1-z)^2)}{1-z} \right\} = \exp\left\{ \frac{6}{11 - \frac{2}{3}n_f} \left[t_i \left(\ln \frac{t_0}{t_i} + 1 \right) - t_{i-1} \left(\ln \frac{t_0}{t_{i-1}} + 1 \right) \right] \right\} , \tag{2.53}$$

where the explicit form with

$$t_0 \equiv \ln \frac{Q_0^2}{\Lambda^2} , \qquad t_i \equiv \ln \frac{q_i^2}{\Lambda^2} , \qquad t_{i-1} \equiv \ln \frac{z_{i-1}^2 q_{i-1}^2}{\Lambda^2} \tag{2.54}$$

is derived by use of (2.11). The upper limit in the integral over z keeps the argument of the running coupling constant out of the non-perturbative region ($(1-z)q > Q_0$) and regulates the $1/(1-z)$ singularity. The q integration region ($q > z_{i-1}q_{i-1}$) corresponds to the angular ordering constraint.

2.4.5 Hadronisation

The equations considered above reflect the various branchings of the quarks and gluons, as prescribed by QCD. The coloured objects form multiparton colour state which finally hadronises (fragments) into sets of charged particles detected in the experiment. It is thought that the global kinematic characteristics of the detected particles are generically connected with those of the original coloured partons.

There are few hadronisation (fragmentation) models: the Lund string model [47, 48], the area law string model [49], the independent jet model based on the Field-Feynman approach [50], and the cluster model [51]. Since there is no QCD description of the hadronisation, all these models are phenomenological.

[5]Note that it is customary to leave in the Sudakov form factor (2.53) in this case only the $\frac{2N_C}{1-z}$ term of the splitting function.

Lund string model

The Lund string model treats gluons as field lines, which are attracted to each other due to the gluon self-interaction and so form a narrow tube of strong color field. These flux tubes are approximated by relativistic massless strings, which break up producing the final state hadrons. The transverse dimension of the string is of typical hadronic sizes, roughly 1 fm. The assumption of the string model is that the tube-like field between an outgoing q and $\bar{q}$ contains a constant amount of field energy stored per unit length, i.e. that the potential between q and $\bar{q}$ is linearly rising: $V(r) \approx kr$, where r is the distance between the charges and $k \approx 1$ GeV/fm is the string constant, i.e. the amount of energy stored per unit length. As the charges move apart from each other their momenta and invariant mass are linearly growing with "time" τ and at some moment τ_0 this string break up to two new colour neutral strings, $q\bar{q'}$ and $q'\bar{q}$. Further breaks of the new strings may occur stochastically. The process is going on until all the available energy is used.

The string does not have any transverse degree of freedom, but the newly created $q'\bar{q'}$ pairs receive some p_T from the fragmentation process which can be described by Gaussian in p_x and p_y [52] with width σ:

$$\frac{d^2n}{dp_x dp_y} = \frac{1}{\sigma\sqrt{2\pi}}\exp\left(\frac{-\mathrm{p_x^2}}{2\sigma^2}\right)\frac{1}{\sigma\sqrt{2\pi}}\exp\left(\frac{-\mathrm{p_y^2}}{2\sigma^2}\right) . \tag{2.55}$$

The model predicts the suppression of heavy-quark production, $u : d : s : c \approx 1 : 1 : 0.3 : 11^{-11}$. Thus, charm and heavier quarks are not produced in hadronisation, but only in perturbative parton-showers $g \to q\bar{q}$.

Baryons can also be produced in the model. In the simple approach [53, 54] the string breaks by the production of a diquark-antidiquark pair, which later becomes the baryon and antibaryon. In this model the baryon and antibaryon are neighbors in rank and thus contain transverse momentum correlation. In the improved model, so-called "popcorn" model [55], one or few mesons can be produced in between the baryon and antibaryon. The experimental data tend to confirm the "popcorn" scenario.

The requirement, that the results of fragmentation are the same for the two scenario, mesons are produced starting from the quark edge and meson production starts from antiquark edge of the string, leads to the following $f(z)$, with z being the fraction of the remaining momentum taken by the new particle (*symmetric Lund model*):

$$f(z) = \frac{N}{z}(1-z)^a e^{-\frac{b\mu_T^2}{z}} , \tag{2.56}$$

where N, a and b are free parameters to be determined from the experiment, and $\mu_T = \sqrt{m^2 + p_T^2}$ is the meson transverse mass.

Model of cluster fragmentation

The mechanism of cluster fragmentation [51, 56], although being quite string-like, is however the alternative to the string fragmentation. The cluster model (used in

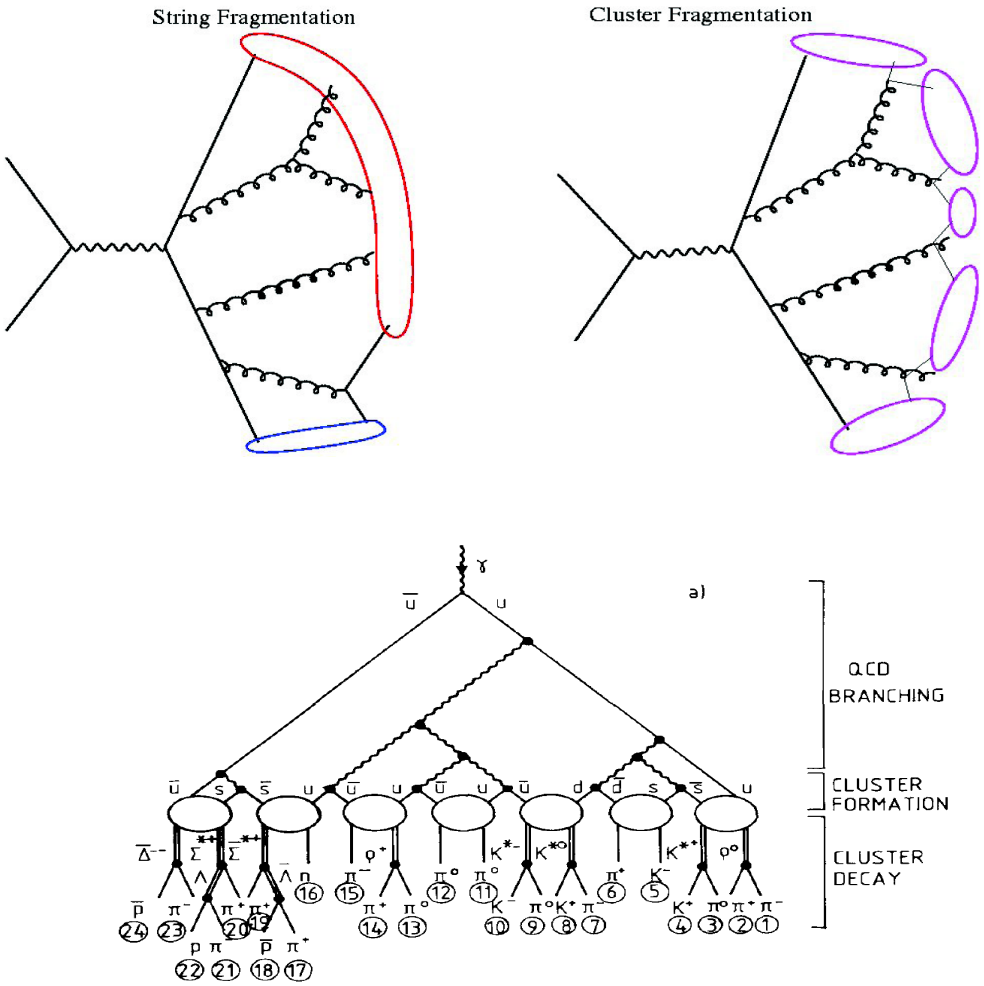

Figure 2.8: Upper: schematic mechanisms of string and cluster fragmentation [57]. Down: sample event demonstrating the cluster fragmentation of some Monte Carlo multiparton state [56].

particular in the parton cascade model of the Monte Carlo generator HERWIG) follows naturally from the "preconfinement" property already exhibited by jets at the perturbative level. Preconfinement is the tendency of the partons generated in the branching process to be arranged in colour-singlet clusters with limited extension in both coordinate and momentum space. It is natural to suppose that these clusters are the basic units out of which hadrons arise non-perturbatively. Their mass scale is controlled by the rather small value of the infra-red cut-off Q_0, so that most clusters have masses of a few GeV or less and may be regarded as superpositions of resonances, with phase-space dominated decay schemes into known resonances. In figure 2.8 the schematic mechanisms of string and cluster fragmentation (upper drawing) as well as a sample event, demonstrating the cluster fragmentation of some Monte Carlo multiparton state, are shown.

2.4.6 The Colour Dipole Model

The colour dipole model (CDM) [58–60] was originally developed for final-state parton cascades from a quark-antiquark system. It is the semiclassical model based on Lund string construction. In figure 2.9 a quark-antiquark-gluon event is shown.

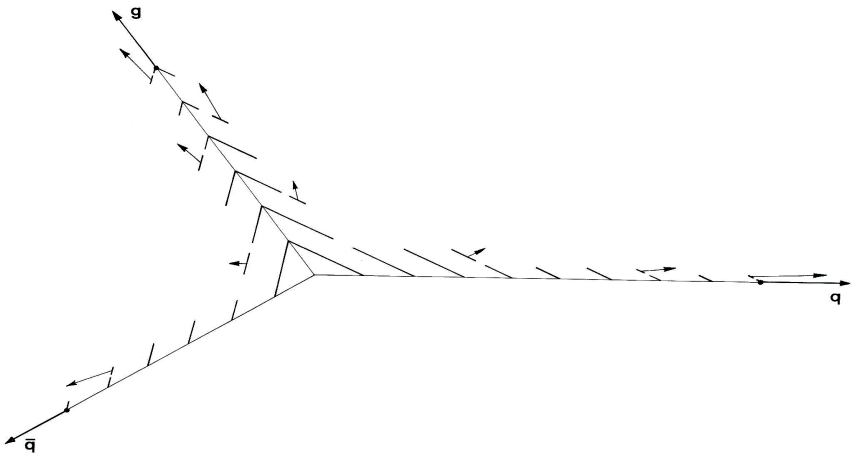

Figure 2.9: The space-time development of a quark-antiquark-gluon event [61].

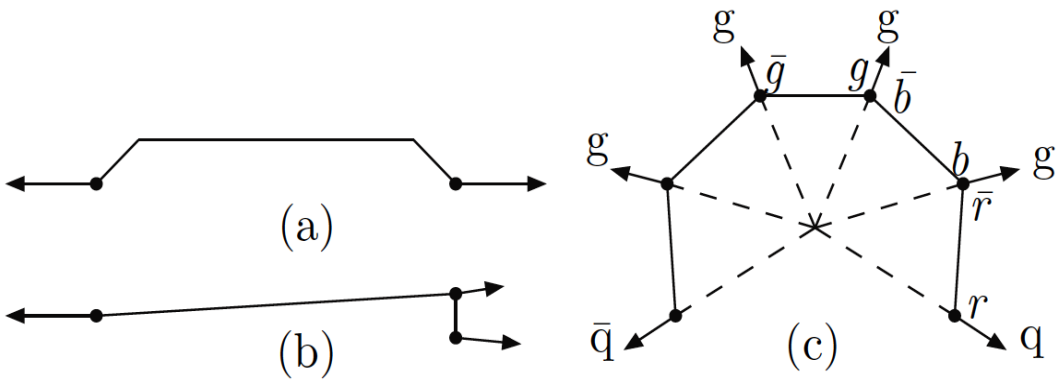

Figure 2.10: (a) A soft transverse gluon; (b) a collinear gluon; (c) a state with many gluons [61].

The string is stretched from the quark to the antiquark via the gluon, which moves like a point-like kink carrying energy and momentum. The string breaks by the production of new $q\bar{q}$ pairs, and the final state contains three jets. Soft particles formed in between the jets get a boost by the transverse motion of the string.

The situation in figure 2.9 can be directly generalised to many gluons. The string is here stretched from the quark to the antiquark via the colour-ordered gluons, as shown in figure 2.10(c). In a state with many gluons the string is stretched from the quark to the antiquark via the colour-ordered gluons, in the figure from red to antired, from blue to antiblue etc. Actually, the final state containing a set of dipoles has a strong similarity to the Lund string with a set of gluon excitations dragging out a set of straight string segments (corresponding to the dipoles) (c). As the masses of the dipoles quickly diminish, the corresponding gluons quickly become soft, i.e. the excitations on the string become smaller and smaller. A soft transverse gluon, shown in figure 2.10(a) will soon lose its energy. The kink on the string is split in two corners and a straight string piece is stretched in a way similar to a one-dimensional string. Also for a collinear gluon, figure 2.10(b), the energy in the string between the quark and the gluon is too small for a breakup of the string. A general rule in string fragmentation is that a gluon with less than a few GeV of transverse momentum does no longer really produce any noticeable effects. There

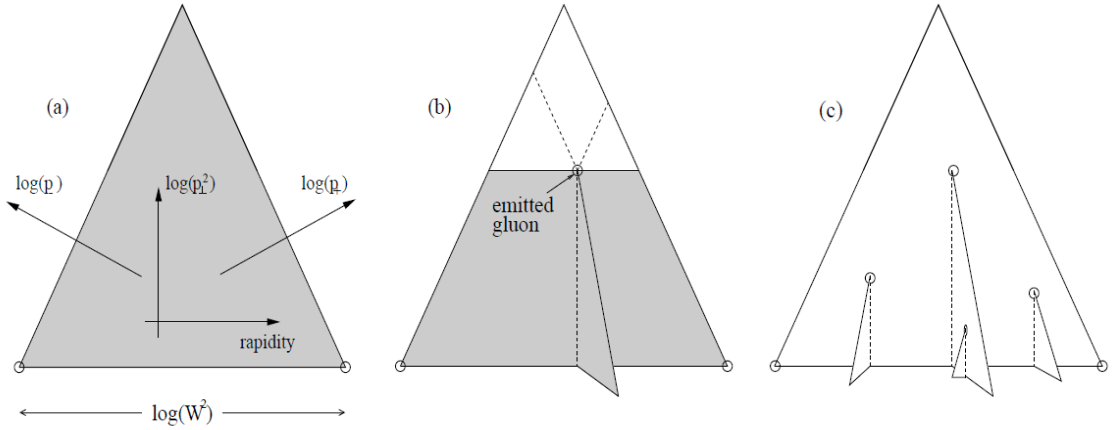

Figure 2.11: (a) The phase space of parton emission from a $q\bar{q}$ pair. (b) After the first emission, the phase space is split into two triangle which radiate gluons independently, but under a p_t ordering condition. (c) An event with four emissions [62].

is no "extra" particle production and the transverse momentum given away by the gluon to the string neighbourhood is drowning in the background noise. Therefore adding to the cascade the use of Lund string fragmentation means that the whole process is *infrared stable* .

The Sudakov parametrisation of the real gluons emitted from $(q\bar{q})$ string looks like

$$p = \frac{s_{g\bar{q}}}{s} p_q + \frac{s_{qg}}{s} p_{\bar{q}} + p_t \ , \tag{2.57}$$

where $s_{g\bar{q}} = 2(p_{\bar{q}}, p)$ and $s_{qg} = 2(p_q, p)$ are the squared masses of $(g, \bar{q})$- and (q, g)-dipoles respectively. Then p_t^2 and the rapidity in $q\bar{q}$ CMS are equal to

$$p_t^2 = \frac{s_{qg} s_{\bar{q}g}}{s} \ , \qquad y = \frac{1}{2} \ln \frac{s_{\bar{q}g}}{s_{g\bar{q}}} \tag{2.58}$$

and the kinematically allowed region is given by

$$p_t < \frac{\sqrt{s}}{2} \ , \qquad |y| \leq \ln \frac{\sqrt{s}}{p_t} = \frac{L - \kappa}{2} \ , \qquad L \equiv \ln s \ , \qquad \kappa \equiv \ln p_t^2 \ , \tag{2.59}$$

which corresponds to a triangle region shown in figure 2.11, where the phase space for gluon emission from a $q\bar{q}$ pair is shown in $(y, \ln p_t^2)$-plane.

The gluons are assumed to be radiated from a $q\bar{q}$ colour dipole and after each emission the dipole is split into smaller dipoles, which continue to radiate *independently*. Two independent dipoles with squared masses S_{qg} and $S_{g\bar{q}}$ emit a softer gluon independently, which means that the cross section of emission of one more, softer, gluon is factorisable into

$$dP(q\bar{q} \to q g_1 g_2 \bar{q}) = dP(q\bar{q} \to q g_1 \bar{q}) \left[dP(q g_1 \to q g_1 g_2) + dP(g_1 \bar{q} \to g_1 g_2 \bar{q}) \right] \ , \tag{2.60}$$

where all the terms dP on the right hand are equal to

$$dP = \frac{4}{3} \cdot \frac{\alpha_s}{\pi} \cdot d\kappa \cdot dy \ . \tag{2.61}$$

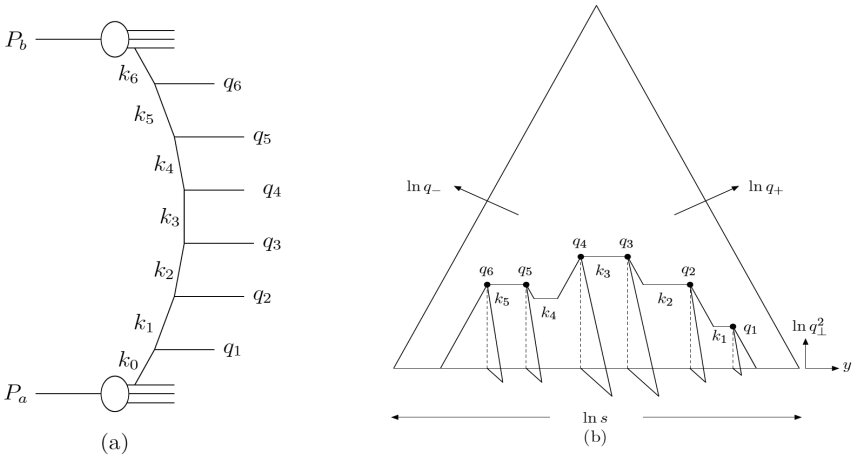

Figure 2.12: A parton-parton scattering chain (a) in the $(y, \ln q_t^2)$ plot (b). The real gluons q_i are ordered in p^+ and in p^-, and thus also in rapidity or angle [61].

Equation (2.61) follows from the radiation pattern of classic charge-anticharge system (dipole).

At fixed $p_{t\,1}^2$ of the first emitted gluon the rapidity range is equal to

$$\Delta y_1 = \ln \frac{s}{p_{t\,1}^2} \,. \tag{2.62}$$

In case of emission of a second gluon with $p_{t\,2}^2$ by two independent dipoles with the squared masses s_{qg_1} and $s_{\bar{q}g_1}$ the rapidity range is increased if $p_{t\,1}^2 > p_{t\,2}^2$:

$$\begin{aligned} \Delta y_2 = \ln \frac{s_{qg_1}}{p_{t\,2}^2} + \ln \frac{s_{\bar{q}g_1}}{p_{t\,2}^2} = \ln \left[\frac{s}{p_{t\,2}^2} \cdot \frac{s_{qg_1} s_{\bar{q}g_1}}{s} \cdot \frac{1}{p_{t\,2}^2} \right] = \\ \ln \left[\frac{s}{p_{t\,2}^2} \cdot \frac{p_{t\,1}^2}{p_{t\,2}^2} \right] = \ln \frac{s}{p_{t\,2}^2} + \ln \frac{p_{t\,1}^2}{p_{t\,2}^2} > \ln \frac{s}{p_{t\,2}^2} \,. \end{aligned} \tag{2.63}$$

Additional rapidity range $\ln \frac{p_{t\,1}^2}{p_{t\,2}^2}$ is drawn as the fold in figure 2.11(b). Each new emission has the same effect on the phase space. After several emissions one obtains a complex figure with many folds as in figure 2.11(c).

In [63, 64] a comparison of the semiclassical Dipole Cascade Model predictions with the ones of the conceptually very different approach of the Webber-Marchesini Cascade Model [65] based on the angular ordering of the emissions in the cascade (HERWIG [66]) is done. Surprisingly, both approaches give very similar results. As argued in [63, 64] the basic reason for this similarity is that the building of dipoles in the cascade is actually the same as the requirement of angular ordering in the emissions. The two different cascades developing along different lines nevertheless cover the same phase space region of figure 2.12 including the folds sticking out of the plane. In the dipole scheme it is searched from top to bottom, while in the Webber-Marchesini scheme it is searched sideways going from one rapidity end towards the other one.

Chapter 3

Event Generation

The measured transverse momentum distributions offers the possibility for discrimination of the various underlying parton dynamics. For these purposes the measured distributions are compared to the model distributions obtained with the help of series of Monte Carlo (MC) event generators. In the presented analysis in average six charged particles per event can be measured. Such multiplicity are not possible to generate by fixed-order calculations and therefore only Monte Carlo generators with applied hadronisation models are considered.

Monte Carlo event generators are computer programs used to simulate high-energy events. There are different MC generators which rely on different QCD models and particle collisions. They start with some given initial conditions and generate an event by random sampling of processes and final states.

As an example, the elements of an ep event generator are shown in figure 3.1.

A MC program starts with the hard scattering process, usually in leading-order. Then, the available phase space is filled by parton emissions in the initial/final state parton shower (PS). This can be done either for example according to the DGLAP/CCFM evolution equations (or by the CDM, see subsection 2.4.6). The generation of this cascade is often performed using so-called backward evolution, where we start from the hard scattering and go down in the ladder. The showering terminates at a cut-off scale Q_0, at this point the parton propagator is taken from

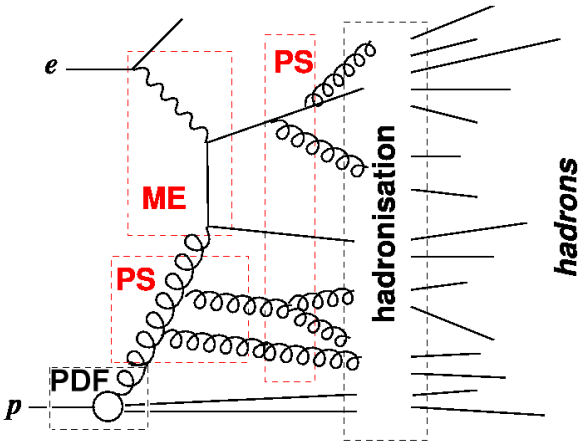

Figure 3.1: Elements of an ep event generator with the BGF matrix element.

the PDF. Before all produced partons undergo the hadronisation, corrections of their momenta have to be made such that the energy and momentum conservation is ensured. The most frequently used hadronisation models are Lung sting and cluster models (see section 2.4.5).

3.1 Monte Carlo Generators

In this section the MC generators used in this analysis are presented.

RAPGAP

The RAPGAP 3.1 MC generator [67] matches first order QCD matrix elements to DGLAP-based leading logarithm parton showers with strongly ordered transverse momentum of subsequently emitted partons. The factorisation and renormalisation scales are set to $\mu_f = \mu_r = \sqrt{Q^2 + p_T^2}$, where p_T is the transverse momentum of one of the outgoing hard partons from the matrix element in the centre of mass of the hard subsystem. The hadronisation is modelled with the Lund string fragmentation as implemented in PYTHIA [68]. QED radiative corrections are included through the HERACLES [69] program. Heavy quarks are treated as massive.

CASCADE

The CASCADE 2.2 program [70,71] uses off-shell leading order QCD matrix elements, supplemented with parton emissions based on the CCFM evolution equation requiring an unintegrated parton distribution function (uPDF) (see eq. (2.37)), which takes the transverse momenta of the propagators into account (see figure 3.2). It uses only gluon chains in the initial state cascade. For the hadronisation process the Lund string model is used. The light and heavy quarks are treated with masses. CASCADE has no QED corrections modelled.

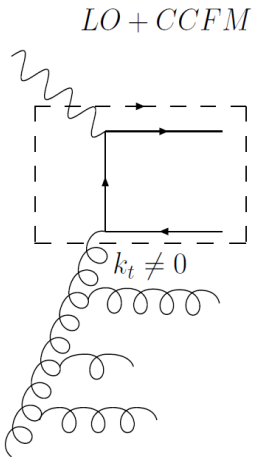

Figure 3.2: Leading order off-shell matrix element with CCFM parton shower.

DJANGOH

The DJANGOH 1.4 program [72] uses the Colour Dipole Model as implemented in ARIADNE [73], where dipoles are created between coloured partons. Gluon emission is treated as radiation from these dipoles. The hadronisation is modelled with the Lund string fragmentation and QED radiative corrections are included through the HERACLES program. DJANGOH uses on-shell leading order QCD matrix elements.

SHERPA

The SHERPA 1.3.1 Monte Carlo [74] program uses a parton shower algorithm based on Catani-Seymour dipole factorisation [75]. It contains tree-level multileg matrix elements for the calculation of hard scattering processes. For the current analysis, matrix elements with up to five partons in the final state are used. To consistently combine multiparton matrix elements with the QCD parton cascades the approach described in [76] is employed. SHERPA uses a modified cluster hadronisation model [77], but is also interfaced to the Lund string hadronisation and hadron decays provided by PYTHIA. In SHERPA only final-state QED radiations can be included, but not the initial-state ones.

Herwig++

The Herwig++ 2.5.2 Monte Carlo [66] program uses the Coherent Parton Branching [78, 79] algorithm which is based on colour coherence to suppresses branching outside an angular-ordered region of phase space. Here, final state radiation is angular ordered, initial state radiation is ordered in $E \cdot \theta$, where E and θ are energy and angle of the radiated parton. Herwig++ has now available the POWHEG (POsitive Weight Hardest Emission) method for DIS processes [80], which combines parton shower simulation and NLO calculation. Since the higher-order matrix element and the parton shower both radiate in some regions of the phase space, it leads to double counting. An approached, which match PS and NLO corrections, as POWHEG matching algorithm, is needed to remove this problem of double counting.

Choice of PDF

In this thesis, the RAPGAP, DJANGOH and SHERPA programs are used together with the CTEQ6L(LO) PDF [81]. The sensitivity to the choice of different LO and NLO PDFs is discussed. The predictions of Herwig++ were obtained with the default PDF MRST 08 LO** and with MRST 02 NLO [82] for POWHEG matched. The CASCADE uses uPDF set A0 [83].

3.2 Monte Carlo Tuning

All MC programs which use the Lund string fragmentation model are tuned to describe e^+e^- results. The tuning was performed by the ALEPH collaboration [84] using hadronic Z boson decay data and a PYTHIA 6.134 simulation with Bose-Einstein correlations included. The resulting tuned parameters are listed in table 3.1. In addition, the tune obtained by the Professor[1] tool using LEP data [85] is also compared to the data. The corresponding parameters are listed in table 10.1. This tune is the latest tune to LEP data using PYTHIA 6, which was prepared to be used at LHC. As discussed in [85] the Professor tool provides better accuracy and systematic control compared to the previous tuning system, used by ALEPH.

The parameter variation ranges used by Professor are shown in table 3.3.

[1] Acronym for "PROcedure For EStimating Systematic errORs".

MSTJ(11)	3	PARJ(54)	-0.040
MSTJ(12)	2	PARJ(55)	-0.0020
MSTJ(46)	0	PARJ(1)	0.108
MSTJ(51)	2	PARJ(2)	0.286
MSTJ(52)	9	PARJ(3)	0.69
MSTJ(53)	0	PARJ(11)	0.553
MSTJ(54)	2	PARJ(12)	0.470
PARJ(92)	1.11	PARJ(13)	0.65
PARJ(93)	0.341	PARJ(14)	0.12
PARJ(81)	0.299	PARJ(15)	0.04
PARJ(82)	1.54	PARJ(16)	0.12
PARJ(21)	0.382	PARJ(17)	0.20
PARJ(41)	0.437	PARJ(19)	0.55
PARJ(42)	0.85	PARJ(26)	0.276

Table 3.1: ALEPH tuned parameters.

MSTJ(11)	5
PARJ(21)	0.325
PARJ(41)	0.5
PARJ(42)	0.6
PARJ(47)	0.67
PARJ(81)	0.29
PARJ(82)	1.65

Table 3.2: Professor tuned parameters.

PARJ(21)	0.33	0.43	σ_q
PARJ(41)	0.4	1.5	Lund a
PARJ(42)	0.5	2.5	Lund b
PARJ(47)	0.4	1.0	r_b
PARJ(81)	0.23	0.35	Lambda
PARJ(82)	0.8	3.0	Parton shower cut-off

Table 3.3: Production ranges and settings for the Professor tune.

Chapter 4

Low-x Physics

4.1 The Structure Function F_2

In the previous section the evolution equations, describing the scaling violations of the proton structure function, were derived. There are two principal predictions for the rise of F_2, the DGLAP (or DLL) evolution equations, and the BFKL scheme. In principle it should therefore be possible to distinguish between these predictions by looking at the F_2 data from HERA. The observed rise of F_2 towards small x indicates the rise of the parton density in the proton. Is the NLO (or NNLO) DGLAP evolution equation sufficient to describe the data at small x or do BFKL effects play a role? Unfortunately this is not that simple to answer.

The H1 and ZEUS combined structure function data [86] from e^+p NC DIS scattering as function of Q^2 for different values of x are shown in figure 4.1. A steep rise towards small x, which flattens at smaller Q^2, is clearly seen.

To compare the DGLAP evolution results with the experimental data the parton densities at the starting scale have to be defined. This is usually done by parametrising the parton densities at the starting scale Q_0. By varying these parameters, the best fit to the data is produced. In figure 4.1 such a fit is performed by applying the DGLAP evolution equation in NLO. The scaling violation is well described by the DGLAP formalism over the whole range in Q^2 and x.

In [87] another PDF group doing the fit (MSTW) compared the description of the measured F_2 with a LO, NLO as well as NNLO DGLAP evolution fit. The results show that the LO fit is not able to give a good description of the data. The NLO and NNLO fits are very similar to each other and the overall fit quality is good.

Apart from the DGLAP evolution results, the effect of small x resummations was studied in [88]. This was done by resumming terms of the form $\ln(1/x)$ for the structure function based on the BFKL equation with next-to-leading logarithmic (NLL) corrections. The comparison of this prediction (labelled as 'NLL') with the measured F_2 for small x is shown in figure 4.2 together with the fit at NLO (labelled as 'NLO'). The results of the resummation of $\ln(1/x)$ also give a successful description of the measurement.

A unified BFKL and DGLAP description of the F_2 data using the unintegrated gluon distribution is also possible, with significant contributions from the $\ln(1/x)$ resummation [89].

The consequence of the above is that the present data on F_2 do not distinguish

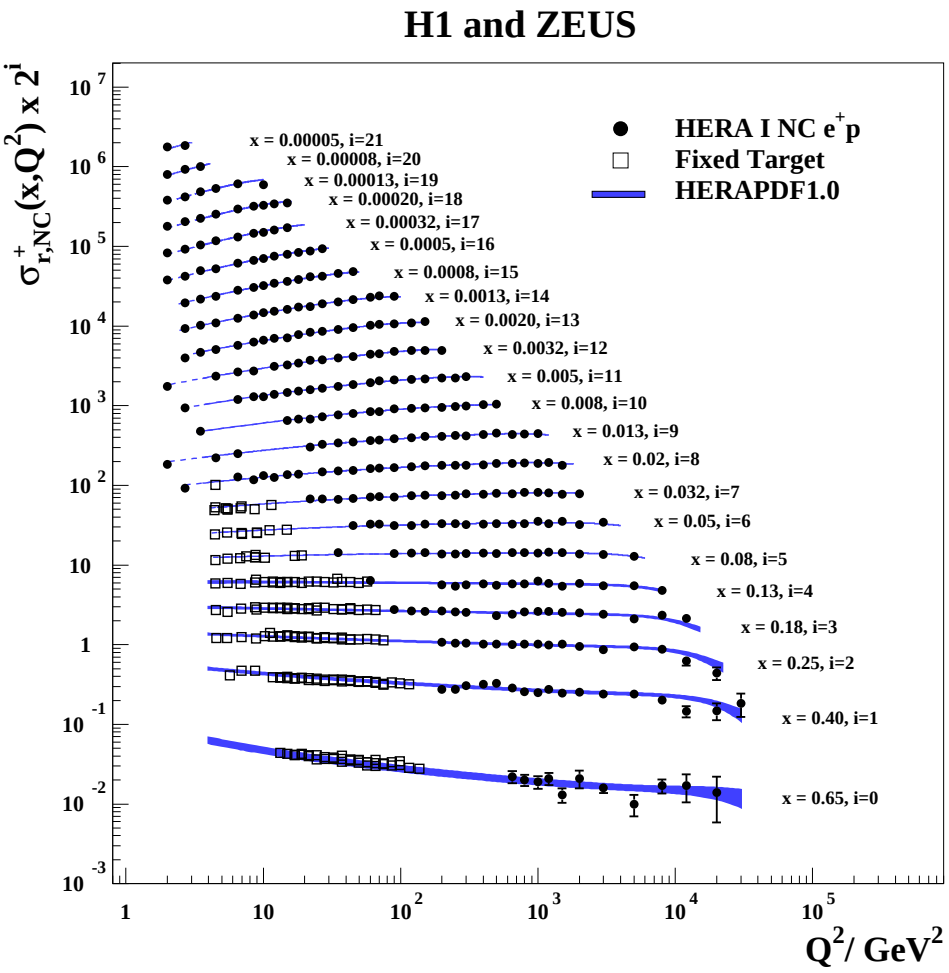

Figure 4.1: H1 and ZEUS combined structure function data from e^+p NC DIS scattering as function of Q^2 for different values of x [86].

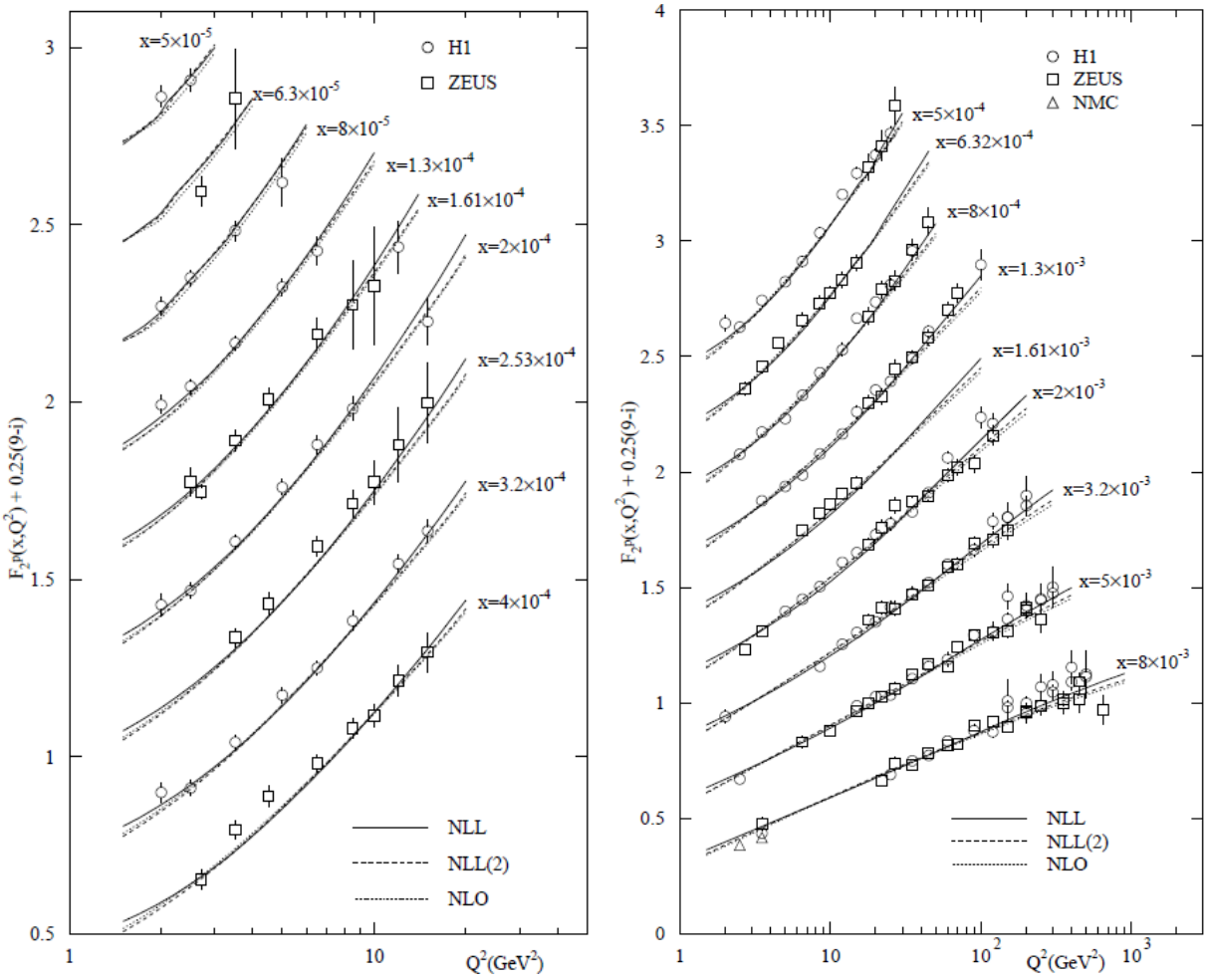

Figure 4.2: H1 and ZEUS combined structure function data from e^+p NC DIS scattering as function of Q^2 for $5 \cdot 10^{-5} \leq x \leq 4 \cdot 10^{-4}$ (left) and for $5 \cdot 10^{-4} \leq x \leq 8 \cdot 10^{-3}$ (right) together with theoretical predictions [88].

between the BFKL, DGLAP, and CCFM which embodies both, predictions.

4.2 Hadronic Final State

With structure function data alone one cannot distinguish between BFKL and DGLAP evolutions. Semi-inclusive measurements, where in addition to the scattered electron the hadrons emerging from the cascade are measured, are believed to provide a larger sensitivity to parton dynamics.

Reference frame

The hadronic final state is better studied in a frame where the transverse boost due to high Q^2 of the photon is removed, such that the virtual photon and proton are collinear. There are two appropriate frames: the hadronic centre of mass system (HCM), where the proton and photon are in the rest frame, $\vec{p}+\vec{q}=0$ ($\vec{p}$ and $\vec{q}$ are the momentum of the incoming proton and the virtual photon, respectively), and the Breit frame, where in addition to the collinearity it is required that the virtual photon does not transfer energy, but only momentum.

The transverse momentum and pseudorapidity of charged particles in the HCM frame are labeled as p_T^* and η^*, respectively[1]. In the HCM frame all hadronic final state particles which have $p_z > 0$ are said to belong to the current hemisphere, and all particles with $p_z < 0$ are assigned to the target or proton remnant hemisphere, as shown in figure 4.3. The forward direction, the direction of the incoming proton, is pointing to negative η^*.

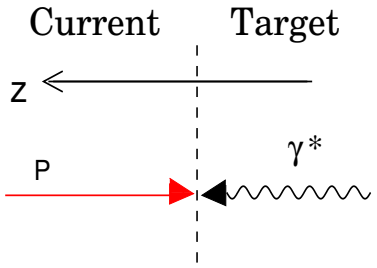

Figure 4.3: Illustration of the hadronic centre of mass system.

Some of the most dedicated measurements at small x at HERA which were concentrated on a search for deviations from DGLAP evolution are:

Transverse energy flow
The measurement of transverse energy flow [19–24] in the laboratory and HCM frames provides a rather generic signal, where the increased parton activity should result in an increased transverse energy. The measurements were found to agree with a BFKL-like CDM scenario and to disagree with the DGLAP predictions. Unfortunately, a final judgment in favour of BFKL in this experiment rested on the

[1] The definition of the pseudorapidity in HCM frame is $\eta^* = -\ln(\tan(\theta^*/2))$, where θ^* is the angle with respect to the virtual photon direction, i.e. to the positive z^* direction

impossibility to disentangle the perturbative parton radiation from non-perturbative hadronisation effects. The hadronisation effects were estimated by MC, and it was shown that hadronisation adds relatively little to the partonic E_T for CDM, most of the E_T is generated by hadronisation for the k_t ordered cascades.

Forward jet production
Measurements of forward jet production [90,91] (or measurements of forward π^0 production [92]), that is energetic jets of high transverse momentum produced close to the proton direction in the laboratory frame, at low x are considered to be sensitive to BFKL dynamics [93]. The selection criteria can be constructed in such a way as to suppress the contribution of k_T-ordered DGLAP cascades by the restriction $P^2_{T,\text{fwdjet}} \approx Q^2$, and to maximize the phase space for BFKL evolution by requiring $x_{\text{fwdjet}} = E_{\text{fwdjet}}/E_p$ to be as large as possible to allow for strong ordering $x_i \ll x_{i-1}$ along the ladder.

In addition, measurements of the azimuthal correlation between the forward jet and the scattered electron were performed [94]. The additional parton emissions partially decorrelate the jet from the electron. As a consequence, for evolution schemes without ordering in transverse momentum, the decorrelation is expected to increase with the electron-jet rapidity distance, since the phase space for additional parton emissions increases. Again the best description of the data is achieved by the BFKL-like CDM model, while the DGLAP-based model is below the data.

Transverse momentum spectra
Measurements of transverse momentum spectra were proposed in [26] as a more direct probe of the underlying parton dynamics and were measured by H1 [25] and ZEUS [95, 96]. Hadrons with large transverse momentum are disfavoured by the strong k_T ordering in DGLAP. It has been shown that the high-p_T tail is sensitive to parton radiation, while the contribution from hadronisation is small.

4.2.1 Transverse Momentum Spectra

The transverse momenta of final-state hadrons are expected to come not only from QCD radiation, but also from an intrinsic p_T of the initial parton in the proton (p_T^{intr}) and from fragmentation, see (2.55).

Measurements of the transverse momentum of charged particles have been performed earlier by the H1 collaboration, and one of the results of this publication is shown in figure 4.4. The measurements are shown in different x and Q^2 bins for $0 < \eta^* < 1.5$, where the largest deviation from DGLAP is expected, since in this region the forward direction to the maximum limit allowed by the H1 detector tracking system is reached. The lower limit of the pseudorapidity interval is given by the approximate acceptance of the detector and the upper limit suppresses the current fragmentation region.

The data are compared to DGLAP-like models (LEPTO, HERWIG) and to an other model which performs a random walk in k_T (ARIADNE). At small x and high p_T^* a deviation from the DGLAP model is seen, but the low statistics available at that time did not allow systematic differential investigations.

The high statistics of the data taken at HERA II and the substantial improve-

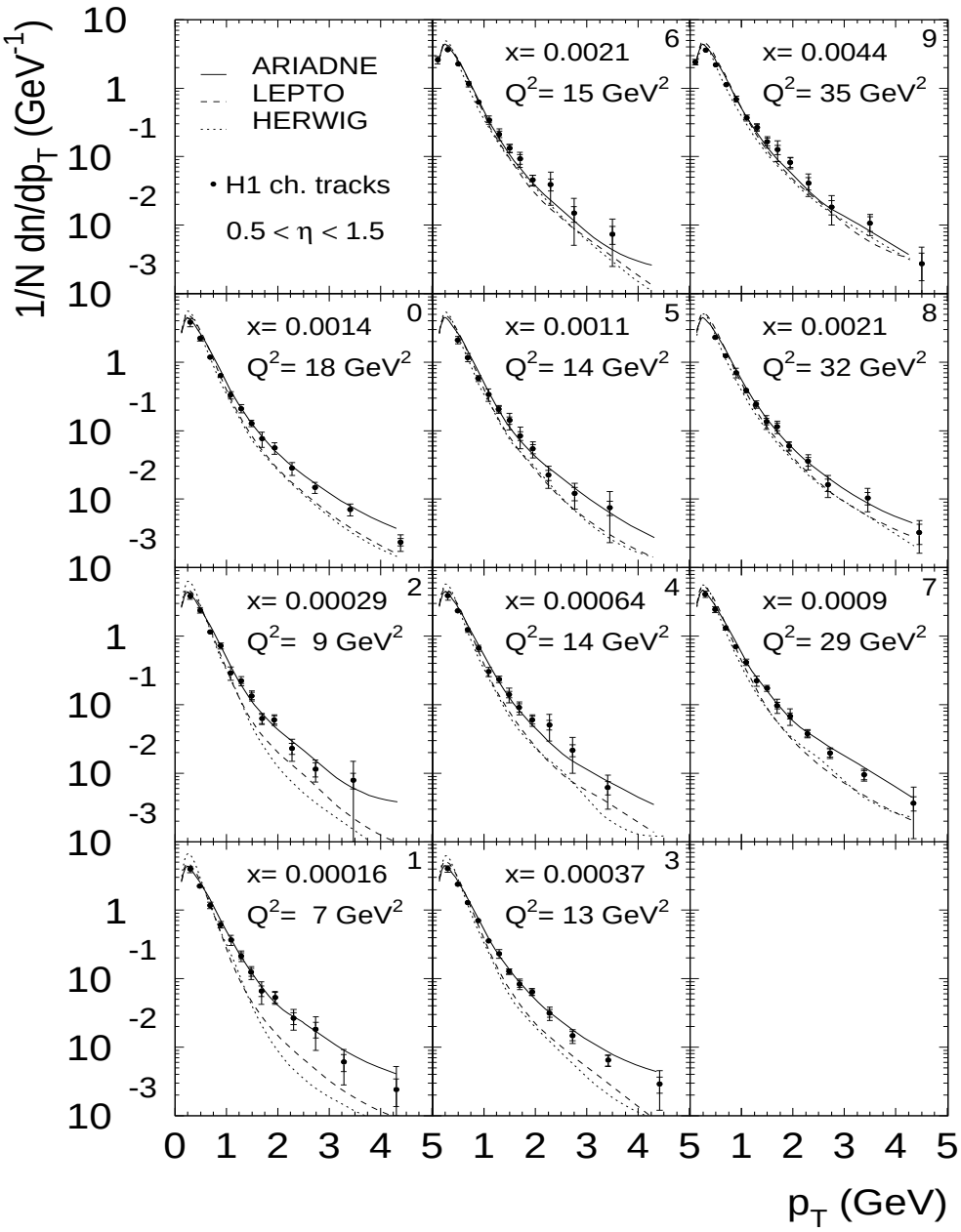

Figure 4.4: Measured p_T^* spectra of charged particles in the HCM in $0 < \eta^* < 1.5$ range for eight intervals of Q^2 and x together Monte Carlo predictions [25].

ment of the track reconstruction and calibration by H1 collaboration allowed to measure charged particle distributions with much better precision compared to the measurements performed by H1 collaboration in 1996.

Chapter 5

HERA and H1 detector

5.1 The HERA Ring

The Hadron Electron Ring Accelerator (HERA) at Deutsches Elektronen-Synchrotron (DESY) in Hamburg was the first and so far the only colliding beams facility in the world where electrons or positrons[1] were colliding with protons. The circumference of the machine was 6.3 km. There were four experimental halls along the HERA ring. Since the startup of HERA in 1992 up to 2007 two detectors measured interactions of the colliding beams: H1 and ZEUS. The aims of both experiments were to probe the structure of the proton, study the fundamental interactions between particles and search for new physics beyond the standard model. Besides these two experiments two more fixed-target experiments were taking data: HERMES and HERA-B. At HERMES interactions between longitudinally polarised electrons and a stationary polarised gas target were studied. HERMES operated from 1995 to 2007. Its main research programme was to study the spin structure of nucleons. At HERA-B the proton beam collided with a stationary wire target to study CP violation in the decay of B-mesons and was in operation between 1998 to 2003.

Being injected into the HERA ring, electrons and protons were accelerated in several steps (see figure 5.1) from the initial linear accelerators and synchrotrons to the storage ring Positron-Elektron-Ring-Anlage (PETRA), which was the final pre-accelerator in the chain and was used for both electrons and protons. PETRA delivered electrons of 14 GeV into HERA, while the protons were injected at 40 GeV. After injection the beam particles were stored in bunches separated by a distance of 28.8 m corresponding to a bunch crossing time of 96 ns. In HERA the electrons obtained a final energy of 27.6 GeV and the protons a final energy of 820 GeV (HERA I). In 1998/99 an upgrade of the HERA led to an increase of the proton energy to 920 GeV (HERA II), resulting in a centre of mass energy of $\sqrt{s} \approx 319$ GeV. Data taking after the upgrade started in 2003. To keep high momentum protons on the circular orbit superconducting magnets were required with a magnetic field of 4.7 T, the electrons were controlled by conventional magnets.

An important quantity that characterises the performance of a collider is the luminosity. For the collision of n bunches having N_e and N_p of electrons and protons

[1] further the term electron refers to both the electron and the positron.

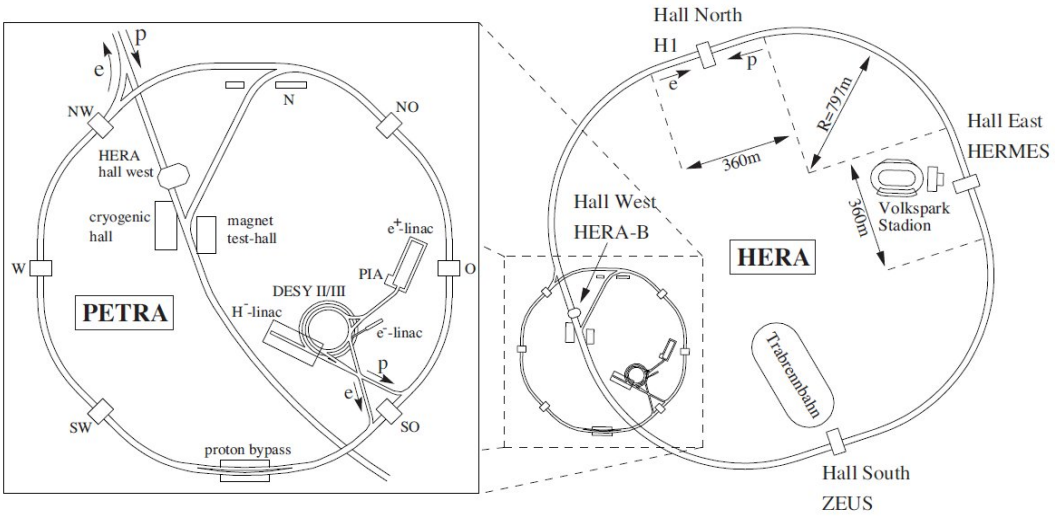

Figure 5.1: The HERA ring and acceleration system.

in a single bunch the luminosity is calculated as:

$$L = f\frac{nN_eN_p}{4\pi\sigma_x\sigma_y} \quad [\mathrm{cm}^{-2}\mathrm{s}^{-1}], \tag{5.1}$$

where f is the revolution frequency and σ_x and σ_y denotes the Gaussian transverse beam profiles in horizontal and vertical directions. The total (integrated) luminosity is

$$L = \int Ldt = \frac{N}{\sigma}, \tag{5.2}$$

where N is the number of detected events and σ is the interaction cross section. In figure 5.2 the integrated luminosity collected by the H1 detector is shown. With

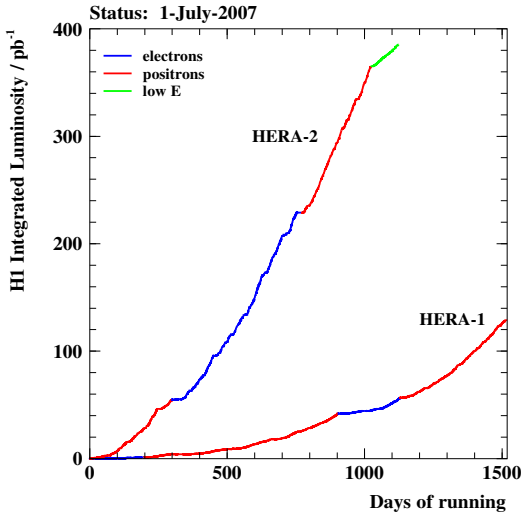

Figure 5.2: Integrated luminosity collected by the H1 detector during HERA I and HERA II running period [97].

the HERA upgrade the luminosity was increased by a factor of five, which was achieved by introducing new superconducting focusing magnets well inside the H1 and ZEUS detectors and thus compress the beam size (HERA II period). The total integrated luminosity of HERA II data taking period is around 400 pb^{-1}. In last month of operation the proton beams were accelerated to lower energies of 460 GeV and 575 GeV to perform a measurements of the longitudinal structure function F_L, this region is marked as a "low E" in figure 5.2. The HERA II data taking continued until the end of June 2007 when HERA closed its operation.

5.2 The H1 Detector

Figure 5.3 shows the general layout of the H1 detector. In this figure the electron enters from the left and the proton from the right. The direction of the proton beam is defined as positive z-axis. The nominal interaction point is the centre of a right-handed coordinate system. In the spherical coordinate system the polar angle is chosen such that the electron beam direction is at $\theta = \pi$ (negative z direction). Since the energy of the proton is much higher than the energy of the electron, charged particles are produced at small angles with respect to the incident proton (forward) direction which corresponds to $\theta = 0$. This requires an asymmetric detector design and therefore the detector in the forward region was more massive and segmented.

From the center outwards, H1's most important systems are silicon trackers for the determination of primary and secondary vertices, jet chambers for the measurement of charged particle tracks, the liquid argon (LAr) calorimeter for the measurement of electromagnetic and hadronic showers and the lead/scintillating fiber calorimeter (SpaCal) in the backward direction for the measurement of the scattered lepton. Some undetectable particles, mostly muons, escaping the inner part of the detector enter the muon chambers and instrumented iron in which the small fraction of hadronic shower leaking out from the LAr calorimeter may also be detected. To measure highly energetic muons in the forward direction, the forward muon detector was installed. A uniform magnetic field of 1.15 T was generated by a superconducting solenoid positioned outside the tracking and calorimeter systems.

A detailed description of the H1 detector can be found elsewhere [98, 99] and in following subsections only components relevant for the analysis is described.

5.2.1 Tracking System

The tracking system of the H1 detector provided track reconstruction and particles identification. To maintain good efficiency for event triggering and reconstruction over the whole solid angle, the tracking system has been divided between the central and forward regions (see figure 5.4). Each was optimised for tracking and triggering in its angular region.

Central Tracking System

The Central Tracking Detector (CTD) consisted of six chambers shown in figure 5.4. Track reconstruction in the central region was based on two large concentric drift chambers, CJC1 and CJC2, where the charge and momenta of charged particles

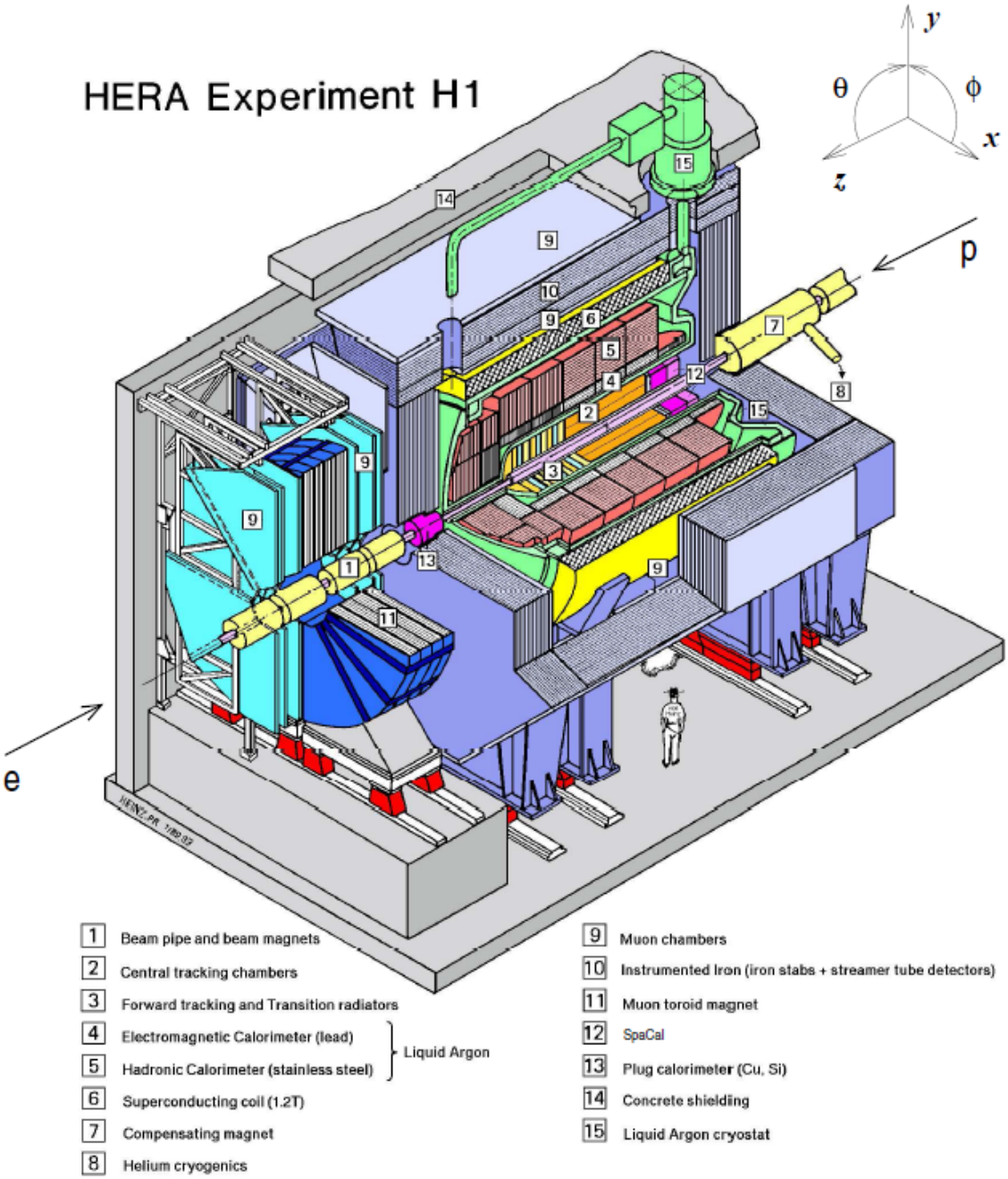

Figure 5.3: Schematic layout of the H1 detector [98].

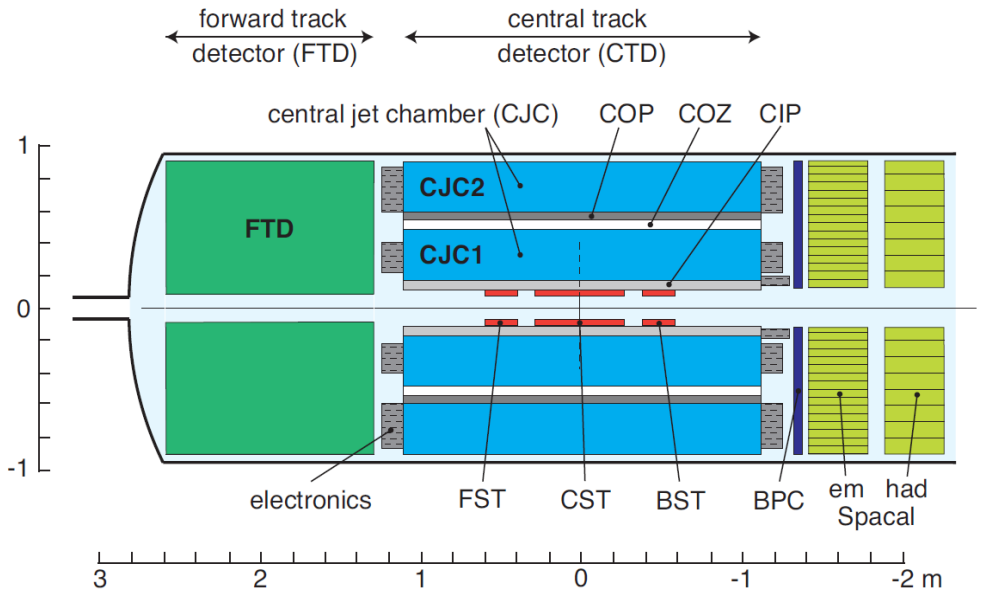

Figure 5.4: Schematic side view of H1 tracking system, divided into forward, central and backward systems [100].

are measured. In addition the specific energy loss, $\frac{dE}{dx}$, is used to improve particle identification.

The CJC1 had inner radius of 203 mm and outer radius of 451 mm, and consisted of 30 drift cells with 24 sense (anode) wires each. The CJC1 covered the polar angular range $11° < \theta < 169°$. The CJC2 comprised of 60 drift cells with 32 sense wires each and covered $25° < \theta < 160°$. The sense wires stretched parallel to the beam pipe and the magnetic field, and the drift cells were tilted by 30° with respect to the radial direction. This is due to the fact that the existence of the magnetic field tilts drift lines of the ionisation electrons by the Lorentz angle with respect to the electric field direction. The angle of 30° is approximately equal to this Lorentz angle in the presence of the 1.5 T magnetic field, thus the ionisation electrons from a high momentum track, so-called stiff track, drift approximately perpendicular to radial direction (see figures 5.5 (left) and 5.6). This gave few advantages on track reconstruction:

- High momentum charged particle crossing several cells produce ionisation electrons, which drift on both sides of the wire give mirror hits (wrongly assigned) (see figure 5.6). Such wrong mirror track segments are easy to determine since they do not result in a smooth track and do not point to the vertex.

- Every stiff track crosses the sense wire plane in the CJC1 and CJC2 at least once. From the matching with the beam crossing the passing time of a particle can be determined with an accuracy of approximately 0.5 ns which allowed an easy separation of tracks from different bunch crossings.

The spatial resolution of the hit position measurement in the $r\varphi$ plane was $\sigma_{r\varphi} = 170\ \mu$m obtained from the drift time measurements. The trajectories of charged particles were measured with a transverse momentum resolution of $\sigma_{p_T}/(p_T^2) = 0.005\text{GeV}^{-1} \oplus 1.5\%$ [101].

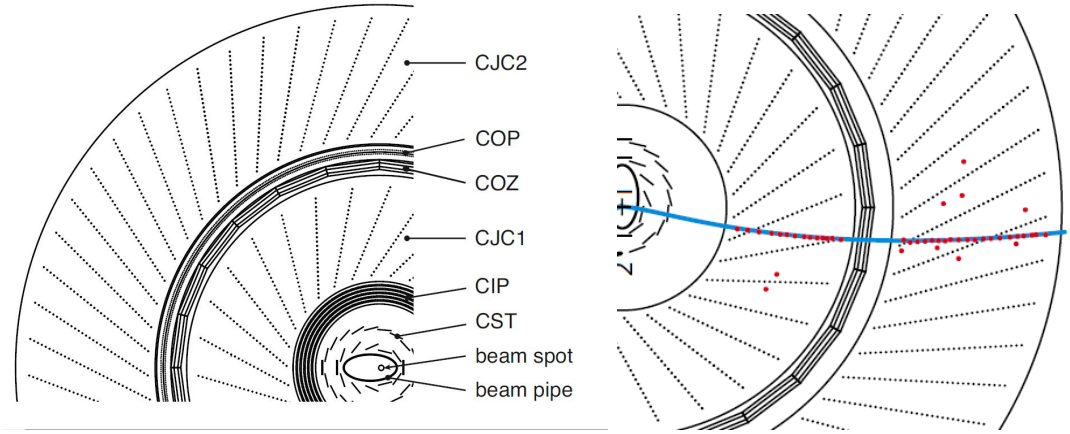

Figure 5.5: The H1 tracking system in xy-plane.

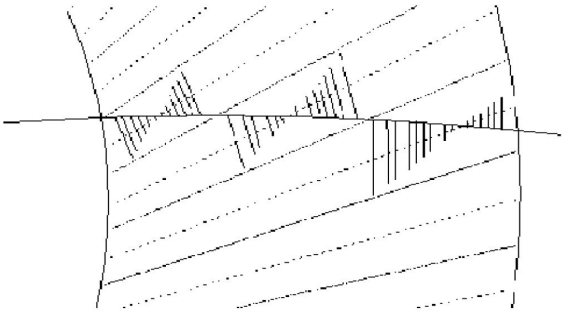

Figure 5.6: Track reconstruction in CJC2.

By measuring the signal propagation time on both wire ends the z-coordinate could be measured with a resolution of $\sigma_z = 22$ mm. The z-chambers provided higher precision for the measurements.

The central outer z-chambers (COZ)

To obtain an exact measurement of the z-coordinate the central outer drift z-chambers (COZ) were used (for HERA I two sets of outer and inner drift z-chambers, CIP and COP). Its sense wires were perpendicular to the beam pipe, resulting in a drift direction along z-direction. The achieved resolution was $\sigma_z = 200$ μm.

The central inner and outer proportional chambers (CIP, COP)

Triggering and timing information for the central trackers was supplied by two multiwire proportional chamber, the central inner proportional chamber (CIP) and the central outer proportional chamber (COP) (see figure 5.5 (left)). The CIP was modified during the HERA upgrade and redesigned to CIP2000 (or CIP2k) [102] with higher response time and was therefore used for online event selection. The CIP and COP were used for measurement of the z-position of the event vertex. This was used in the first level of the H1 trigger system [103, 104].

The Silicon track detectors (CST, FST, BST)
The silicon tracker [105] consisted of the central silicon tracker (CST), the forward silicon tracker (FST) [106] and the backward silicon tracker (BST) [107], shown in figure 5.4. The CST consisted of two concentric cylindrical layers of silicon sensors. It surrounded the elliptical beam pipe at the nominal interaction point (IP) such that particle trajectories originating at the IP were perpendicular to the silicon layers. It was built to provide a precise vertex information as well as the identification of displaced secondary vertices. A polar angular coverage of CST was $30° < \theta < 150°$. The achieved resolution was 12 μm in $r\varphi$-plane and 22 μm in the z-direction. The impact parameter resolution was 37 μm for high momentum track. The BST and FST were used to extend the angular coverage of the CST and to improve the reconstruction of small angle tracks in the backward and forward regions. The FST covered a forward polar angular range of $7° < \theta < 19°$ and the BST covered a backward region of $165° < \theta < 176°$.

The backward proportional chamber (BPC)
The backward proportional chamber (BPC) was located in front of the SpaCal and provided the angular measurement of the electron together with its track. The BPC consisted of six wire layers at three different azimuthal orientations and measured the angle of a particle with a precision of 0.5 mrad.

The forward track detector (FTD)
The forward tracking detector (FTD), which was built in three supermodules, covered a polar angle range of $5° < \theta < 25°$. The forward detector was rebuilt to host five additional planar drift chambers. Each of the supermodules contained three planar (P) chambers, which remained from the HERA I running period and a new (Q) planar chamber added during the HERA upgrade to increase the efficiency at high track multiplicity (see figure 5.7). New chambers reduced the amount of the material to minimise the effects of multiple Coulomb scattering. In addition, the number of sense wires was increased in the new planar chambers. The P-chambers had 32 drift cells with four sense wires each and oriented with respect to the y-axis at $\phi = +60°, -60°, 90°$ and $0°$. The Q-chambers contained 30 drift cells with eight wires at $30°$ and $90°$. A combination of hit information from each planar chamber in a supermodule defined a planar track segment. The achieved resolution was 210 μm in $r\varphi$-plane and radial resolution was about 3 cm. The momentum resolution depends on the track length and the track's polar angle and varies in the range of $\sigma_p/p^2 \sim 0.1 - 0.02$ GeV^{-1}. The track finding efficiency was about 70% in each supermodule.

5.2.2 Calorimeters

In DIS events scattered electrons could be observed in the backward calorimeter SpaCal (Spaghetti Calorimeter) for $Q^2 \leq 100$ GeV^2 and in the LAr (liquid argon) calorimeter for larger values of Q^2. The SpaCal and LAr were sampling calorimeters, where the material which produces the particle shower (passive layer) is distinct from the material which collects and measures the signal (active layer). Both calorimeters had an electromagnetic and a hadronic part.

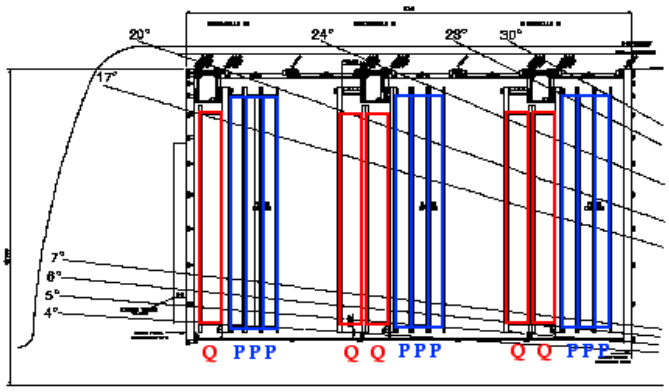

Figure 5.7: Side vies of the forward track detector (FTD).

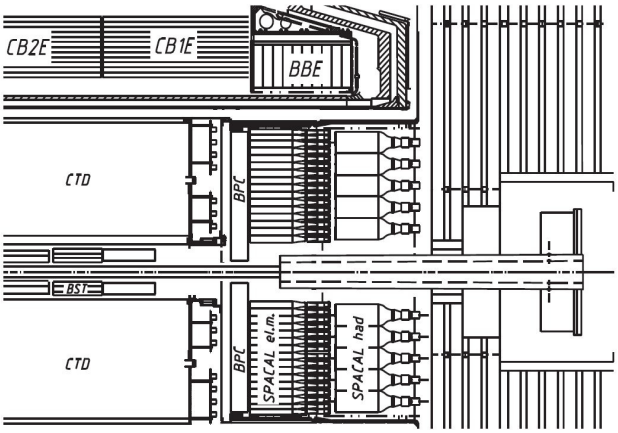

Figure 5.8: Side vies of the SpaCal calorimeter together with the backward proportional chambers in front of electromagnetic part of the SpaCal.

The SpaCal calorimeter

The SpaCal calorimeter was a backward lead/scintillating fibre calorimeter and covered the range of $154° < \theta < 174°$. It was used for identification and precise reconstruction of the scattered electron in the backward region. The SpaCal consisted of the inner electromagnetic and outer hadronic sections (see figure 5.8). The absorbing material was lead for both electromagnetic and hadronic parts. The active material was plastic scintillating fibres. Shower particles produced light in scintillating fibers which were oriented parallel to the beam direction. The signal was collected by photomultiplier tubes. The active length of the electromagnetic SpaCal corresponded to 28 radiation lengths and 1 hadronic interaction length. The energy resolution for positrons in the electromagnetic section was $\sigma(E)/E \approx 7.1\%/\sqrt{E/\mathrm{GeV}} \oplus 1\%$, as determined in test beam measurements [108]. The SpaCal provided energy and time-of-flight information used for triggering purposes.

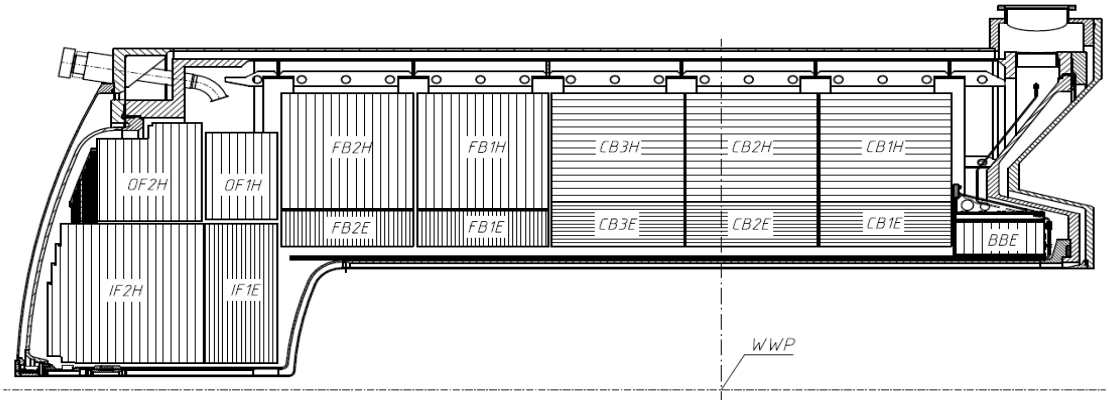

Figure 5.9: Side view of the liquid argon calorimeter (LAr).

The LAr calorimeter

The liquid argon (LAr) [109] calorimeter covered the range $4° < \theta < 154°$ as shown in figure 5.9. It was designed for measurement of electromagnetically as well as hadronically interacting particles. The LAr was used in this analysis for the reconstruction of the hadronic final state. The active material of LAr was liquid argon. The passive material was lead in the electromagnetic part and stainless steel in the hadronic part. The LAr calorimeter was segmented in eight concentric wheels with absorber plates orientated such that the incident particles entered the LAr as perpendicular as possible. An incoming particle entering the active layer created a shower, and a signal was produced by ionisation in the liquid argon. The response to the hadronic shower and electromagnetic one was very different due to undetectable energy in case of hadronic shower. The efficiency of collecting energy from electromagnetic showers in LAr is about 30% larger than for hadrons. Such energy imbalance had to be corrected during the reconstruction.

The LAr calorimeter had an energy resolution of $\sigma(E)/E \approx 50\%/\sqrt{E/\mathrm{GeV}} \oplus 2\%$ for hadronic showers, as obtained from test beam measurements [110] . For electrons the achieved resolution was $\sigma(E)/E \approx 12\%/\sqrt{E/\mathrm{GeV}} \oplus 1\%$. [111].

5.2.3 Time-of-Flight Counters

To reject background events induced by interaction of beam particles with residual gas molecules in the beam pipe and stray protons interacting with the walls of the beam pipe the Time-of-Flight (ToF) detectors were used. The ToF system, shown schematically in figure 5.10, consisted of several detectors. In the forward region three Forward Inner ToF (FIT) detectors were installed at 1.3 m (FTi1), 2.5 m (FTi2) and 2.7 m (FIT) from the IP, as well as the Plug detector (PToF) at 5 m. In the backward region the ToF system consisted of the SpaCal ToF (SToF), the backward ToF (BToF) at -4 m and the large and small veto walls, LVeto and Veto, at -6.5 m and -8.1 m, respectively. Each of these detectors consisted of scintillator arrays which were used to compare the time of arrival of the signal. The background processes occur at different times compared to the actual ep interaction and were

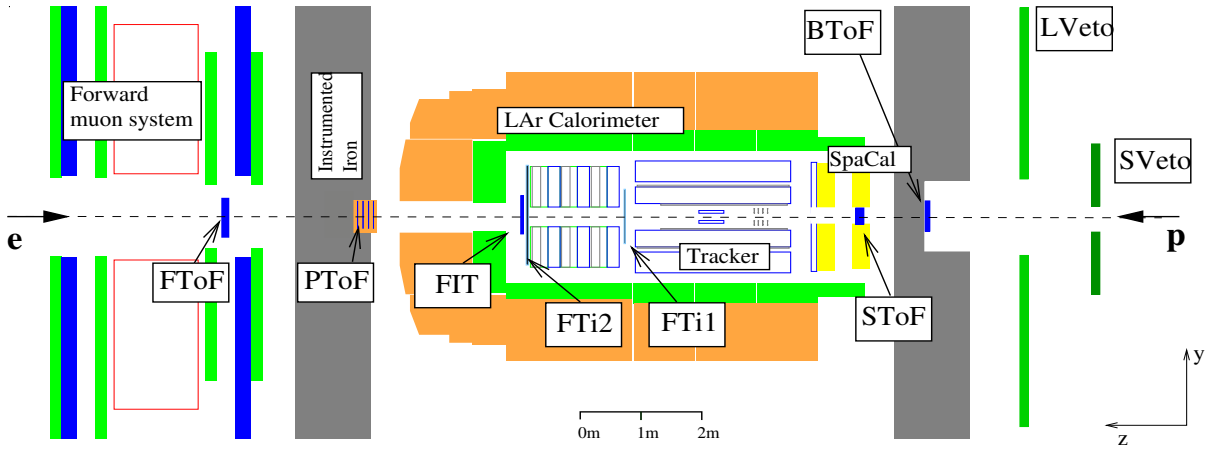

Figure 5.10: The Time-of-Flight systems.

rejected. The time resolution of ToF system was of about 1 ns.

5.2.4 Luminosity System

The luminosity measurement in the H1 experiment is based on the Bethe-Heitler process, $ep \to ep\gamma$, where the electrons and photons are scattered at very low angles.

Theoretically, the Bethe-Heitler process is very precisely calculable in QED, and therefore well suited for the determination of the luminosity in an electron-proton colliding beam experiment.

The scattered photon from the Bethe-Heitler process is detected with the Photon Detector, situated at $z = -101.8$ m near the beam pipe along the electron beam direction. The Photon Detector is a sampling calorimeter consisting of scintillating fibres and tungsten absorbers. For the background suppression a beryllium filter and a water Cherenkov counter are mounted in front of the Photon Detector.

In a certain energy range, the scattered electron from the Bethe-Heitler process is detected with the Electron Tagger, placed at $z = -5.4$ m along the electron beam direction. This measurement is used for the calibration of the luminosity system and as a cross check of the luminosity determination.

5.2.5 Trigger System

The bunch crossing rate at HERA was about 10.4 MHz, which is much higher than the storage capabilities and the readout rates of the detectors. The overwhelming amount of the events were background. The purpose of a four-level trigger system was to efficient reject background events, such that the ep collisions could be recorded with a maximal frequency of about 50 Hz at which data could be written out. Each trigger level consisted of several sub-triggers and different decision algorithms. Some sub-triggers had a very high trigger rate and had to be prescaled, i.e. some triggered events were rejected while the events that were kept were given a weight.

Level 1
The first level of the trigger system analysed bunch crossing information stored in a pipeline and was based on the information from 256 trigger elements combined into 128 sub-triggers named S0 to S127. As an example of the trigger element is the one that requires the energy deposited in the SpaCal to be large enough to be a scattered electron, or is the one that requires the position of the scattering vertex to be within some reasonable distance from the nominal interaction point. At the first level trigger system a decision to keep or reject the event was taken within 2.3 μs, corresponding to 24 bunch crossings. If at least one of the sub-triggers accepts the event the event is taken to the second level trigger.

Level 2
With a decision time of 20 μs a more sophisticated analysis of the event could be made at the second level. At L2 an event was analysed by either a topological trigger system (L2TT) or by a neural network (L2NN). The L2TT provided reduction of background based on topological event signatures, while the L2NN was trained to select events based on sub-detector information.

Level 3
The third trigger level was implemented in 2005. The L3 trigger system mainly used track based information to search for heavy quark decays. The decision took place within 100 µs and reduced the event rate to 50 Hz.

Level 4
In the fourth level trigger the full information of the event was used and a fast online reconstruction of the event was performed. After all the levels the event could be prescaled again at the fourth level due to the limited storage volume. In this final step all events which passed the fourth level trigger were classified into classes, which are available for further physics analysis (for example, DIS, electron in the SpaCal or jets classes).

5.2.6 Detector Simulation

For the simulation of effects of H1 detector, such as detector geometry, interaction of particles in matter and tracking and hit management, the programme H1SIM based on GEANT 3 [112] was developed. To simulates the behaviour of the detector, GEANT creates tracks and energy deposits from four-momenta of particles generated by Monte Carlo generators and simulates electromagnetic and hadronic showers. The events created by H1SIM are reconstructed and analysed using the same programmes as for the data.

Chapter 6

Reconstruction

6.1 Track Reconstruction

Detailed information on track reconstruction in H1 can be found in [113], and in this chapter only a brief description is given.

The trajectory of a particle moving in a uniform magnetic field, $\vec{B} = (0, 0, B_z)$, parallel to the beams is ideally a helix. To reconstruct particle momentum one performs the general strategy: first, the track trajectory is parametrised, second, a fit of the given parametrisation to the point measured in a tracking chamber is performed.

Track parametrisation
The helical parametrisation contains five parameters (see figure 6.1):

- the azimuth angle, φ - an angle between x-axis and transverse momentum vector at the point of closest approach;
- the polar angle, θ - an angle between z-axis and momentum vector at the point of closest approach;
- the curvature which is signed inverse radius $k = \pm r^{-1}$. It is positive if the direction of the azimuth angle coincides with a counter-clockwise rotation as seen from the $+z$ direction.
- the signed closest distance from z-axis in the (x, y) -plane, $d_{ca} = \pm|\vec{d_{ca}}|$, which is positive if $\vec{d_{ca}}$ and the trajectory direction form a right-handed system;
- the z-position (z_0) at the point of closest approach;

The helix is a circle in the (x, y)-plane:

$$\frac{1}{2}(r^2 + d_{ca}^2) + (1 - kd_{ca})r \cdot \sin(\varphi - \phi) - d_{ca} = 0, \tag{6.1}$$

and a straight line in the (y, z)-plane:

$$z_i = z_0 + (\frac{dz}{dS})s_i^{xy}, \tag{6.2}$$

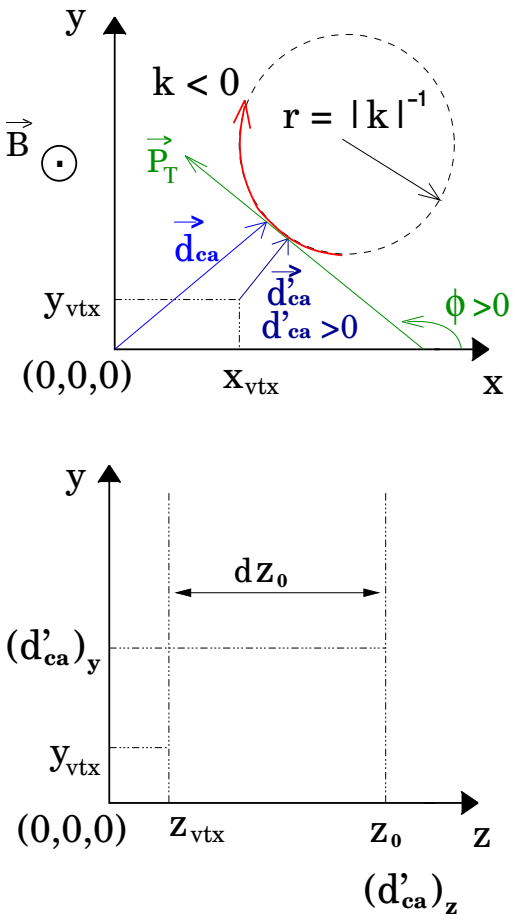

Figure 6.1: Parameters of the track helical trajectory. Upper plots - (x,y) -plane, bottom plot - (y,z)-plane.

where s_i^{xy} is the track length for the point z_i in the (x,y). At the point of closest approach we have $s_i^{xy} = 0$. The slope $\frac{dz}{dS}$ is related to the polar angle angle by:

$$\theta = \arctan\left(\frac{1}{(dz/dS)}\right) \tag{6.3}$$

Track fitting

The helical parametrisation is valid only as an approximation. In reality various effects can result in a deviation from the ideal helix trajectory. Such deflections are caused by multiple scattering, by inhomogeneities of magnetic fields and energy loss along the particle's trajectory. For such situations, a simple 2D fit of the circle (6.1) and of a straight line (6.2) may lead to large χ^2 and cannot be used to decide whether the hit is acceptable or not. To take into account these effects the H1 track reconstruction uses a track-fit method similar to algorithm based on broken lines [114]. In H1 two sets of parameters were needed with the constraint that both join at the point between CJC1 and CJC2. Track parameters obtained in simple 2D fit of the circle and of a straight line are used as starting values in a broken-helix fit. The required criteria of the fit are: optimal track parameters at track start (vertex) and at track end for extrapolation to other detectors, good overall χ^2 of track and χ^2 of each single hit for improvement of hit selection.

After track is fitted and parameters are determined the track momentum is found via track's curvature

$$k = \frac{1}{r} = \frac{0.3 \cdot B_z}{p_T}, \tag{6.4}$$

and the following expressions

$$p_x = p \cdot \sin\theta \cdot \cos\varphi, \tag{6.5}$$
$$p_y = p \cdot \sin\theta \cdot \sin\varphi, \tag{6.6}$$
$$p_z = p \cdot \cos\theta. \tag{6.7}$$

When tracks are found, the primary event vertex can be calculated from the z_0 parameter. The more precise determination can be obtained not only from CJC or FTD tracks, but also from tracks measured by the silicon track detectors (CST, FST and BST) and event timing t_0 information. The details on the determination of z-coordinate of the primary vertex can be found in [115]. When the vertex position is known the tracks are refitted using the vertex position as an input. In the region where the acceptance of CJC and FTD overlaps a combined fit using hits from both detectors is tried, in case of fail only FTD tracks are fitted to the primary vertex.

6.2 Hadronic Final State

The momenta of the charged particles can be measured either from the tracker device or through the energy deposit in the calorimeter. The algorithm described in this section estimates the resolution for these two measurements and decides which one to use to define a charged particle. If the tracks measurements are better, it is used in further reconstruction. If the cluster measurements are better, only this information is used to define a charged particle. The output objects are then calibrated and used in the analysis.

The Hadronic Final State (HFS) consist of all particles except isolated electrons and muons. The HFS finder algorithm used in this analysis was Hadroo2 (Hadronic Reconstruction in H1OO[1]) [116], where information from the tracks and cluster were combined.

Further, the description of the input for the algorithm, tracks and clusters, is discussed, and then the details of comparison of track and cluster information are presented.

6.2.1 Tracks

The Hadroo2 algorithm uses vertex-fitted tracks measured by the central tracker (central tracks), forward detector (forward tracks) or their combination (combined tracks), see chapter 8 and figure 8.1. The selection criteria on the tracks are based on studies made by Lee West [117] and listed in table 8.1 and refereed as "Lee West selection". After the selection of good tracks, isolated electrons[2] and muons are

[1] H1OO is the Object Oriented framework developed in H1.

[2] The electron is defined as isolated if the energy in the calorimeter in a cone around the electron $R_{\eta-\varphi} = 0.5$ is less than 3% of the electron energy, excluding the energy associated to any other identified electron in this cone.

identified. Finally HFS tracks include all particles except isolated electrons and muons.

After all selected tracks were used to reconstruct HFS, the remaining clusters are still used to make other particle candidates. These particles correspond to neutral particles.

6.2.2 Clusters

Calorimeter clusters are made out of LAr and SpaCal energy deposited cells. The H1 offline reconstruction algorithm identifies clusters originating from electromagnetic particles or from hadrons. In Hadroo2 a particle is considered as electromagnetic if 95% or more of its energy was deposited in the electromagnetic part of the calorimeter, with 50% of this energy in the fist two layers. All other clusters are considered as hadrons.

6.2.3 Tracker and Calorimeter Measurements Comparison

To make a decision which measurement, either from the track or from the cluster, has to be used, the algorithm compares the energy resolution obtained from the track fit with the resolution of calorimeter measurements. The energy of the track which is under the hypothesis to belong to a pion, π, is calculated according to

$$E^2_{\text{track}} = P^2_{\text{track}} + m^2_\pi = p^2_T/\sin^2\theta + m_\pi. \tag{6.8}$$

The uncertainty on the energy can be written as

$$\frac{\sigma(E)_{track}}{E_{\text{track}}} = \frac{1}{E_{\text{track}}}\sqrt{\frac{p^2_T}{\sin^4\theta}\cos^2\theta\sigma^2_\theta + \frac{\sigma^2_{p_T}}{\sin^2_\theta}} \tag{6.9}$$

where σ_θ and σ_{p_T} are uncertainties of the track transverse momentum and its polar angle, respectively, obtained from a track fit.

The evaluation of the corresponding uncertainty on the calorimeter measurement is only based on the track, since the number of induced clusters by the incident particle is a priori not known. For the resolution on the LAr the following expression is used [118]

$$\left(\frac{\sigma(E)}{E}\right)_{\text{LAr}} = \frac{\sigma(E_{\text{track}})_{\text{LAr}}}{E_{\text{track}}} = \frac{0.5}{\sqrt{E_{\text{track}}}} \tag{6.10}$$

Then the relative resolution of the tracks and calorimeter measurements are compared and the measurement with the best resolution is taken. It was shown that the track measurements are better than calorimeter up to an energy of 25 GeV for central tracks, up to 13 GeV for combined tracks and up to 12 GeV for forward tracks.

To avoid double counting the measurements which were not preferred have to be removed. How it performs, as well as the details of work of the algorithm, are discussed below.

Track measurement

In case the track measurements are taken, the energy in the calorimeter originating from a track has to be removed to avoid double counting of the track energy. To estimate the amount of the energy in the calorimeter, which corresponds to a certain track, the track is extrapolated up to the surface of the calorimeter as an helix, and inside the calorimeter as a straight line, see figure 6.2. The volume for the clusters

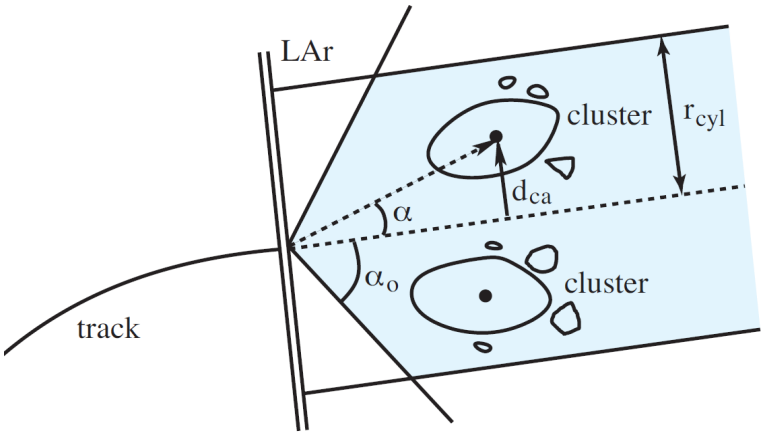

Figure 6.2: The volume in the calorimeter within which the clusters are summed up [100].

is defined by a cone with opening angle of 67.5° and cylinders of radius 25 cm in the electromagnetic part and 50 cm in the hadronic part of the calorimeter. The sum of the cluster energies inside this volume is denoted with E_{cylinder} and this energy is compared to the track energy E_{track}. The E_{cylinder} is set to zero and removed from the list if the following condition is fulfilled (see first line in figure 6.3):

$$E_{\text{cylinder}} < E_{\text{track}} \cdot \left(1 + 1.96\sqrt{\left(\frac{\sigma(E)}{E}\right)^2_{\text{track}} + \left(\frac{\sigma(E)}{E}\right)^2_{\text{LAr}}}\right) \tag{6.11}$$

This expression takes into account possible fluctuations of both measurements. If this condition is not fulfilled only the energy E_{track} is removed. The cluster with remaining energy is associated to a neutral particle or another track and kept for further steps of the algorithm.

Calorimeter measurement

In the case of the calorimeter measurement, E_{cylinder} and E_{track} are compared and if

$$E_{\text{track}} \in [E_{\text{cylinder}} - 1.96\sigma_{E_{\text{cylinder}}}, E_{\text{cylinder}} + 1.96\sigma_{E_{\text{cylinder}}}], \tag{6.12}$$

with $\sigma_{E_{\text{cylinder}}} = 0.5\sqrt{E_{\text{cylinder}}}$, the calorimeter measurements are used and track is removed from the list.

If the condition 6.12 is not fulfilled and $E_{\text{track}} < E_{\text{cylinder}} - 1.96\sigma_{E_{\text{cylinder}}}$ then it is assumed that E_{cylinder} consists of a few clusters originating from several particles, see second line in figure 6.3. In this case the track measurements are used.

On the other hand, if $E_{\text{track}} > E_{\text{cylinder}} - 1.96\sigma_{E_{\text{cylinder}}}$, the calorimeter measurements are used, since highly energetic tracks usually are less accurately measured (see third line in figure 6.3).

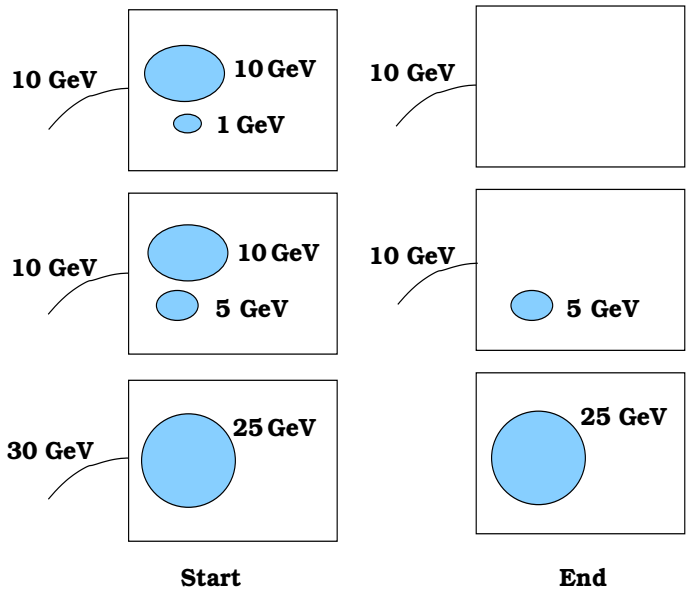

Figure 6.3: Example of the Hadroo2 algorithm behaviour in three different situations [116].

6.3 Calibration

The measurements presented in this thesis depend on the reconstruction of the scattered electron energy and of the energy of the hadronic final state particles, and therefore demand a precise calibration of the SpaCal, where the scattered electron is measured, and LAr calorimeter, where the HFS is measured. The energy of the scattered electron is measured only with calorimeter, while the HFS is reconstructed by combination of the tracks with the measurement of calorimeter, as discussed in the previous section. The general idea of the calibration is to compare the measured energy with the expected one and thus derive calibration functions, which are different for the data and the simulation.

6.3.1 Electron Calibration

The event kinematics reconstruction uses information of the scattered electron and thus the resolution in the kinematic variables depends on the energy measurement of the final state electron. Therefore the SpaCal calibration is demanded to be as precise as possible. The largest uncertainty in the electromagnetic energy calibration is from fluctuations of the charge collection efficiency, which lead to small deviations from the electromagnetic scale over time. The aim of the electron calibration is to correct for this effect. In addition, the electron may lose part of its energy due to interaction in dead material, in front of the SpaCal, before it enters the active part of the calorimeter. To well simulate this effect, the electron calibration determines the radially dependent corrections.

The most accurate method for the SpaCal electromagnetic energy scale is the double angle (DA) method [119], where the the electron energy E'_{DA} is expressed by the two angles, scattered lepton angle, θ_e, and the hadronic scattering angle, θ_h. Deviations of the ratio E'_e/E'_{DA} from one are used to determine the calibration constants for the individual SpaCal cells. The calibration has been finally applied to the data and simulated events during the offline analysis. The achieved uncertainty on the electron energy is less than 1% [120].

6.3.2 Hadronic Final State Calibration

As discussed in the previous section the HFS object is reconstructed either from track or from clusters. Tracks are well measured and do not need to be calibrated. The measured calorimeter energy is not precisely the particle energy and the number of induced clusters by the incident particle is not known. A hadronic shower consists of both an electromagnetic and hadronic parts. The response of the electromagnetic section is very similar to the pure electromagnetic shower, where positrons, electrons and photons are detected. In the hadronic part, a relatively large fraction of the energy can not be measured. Such undetectable energy is related to the energy dissipating into the recoil of the target nuclei, nuclear binning energy and to the not measured neutrinos and muons. Thus the measured energy will be significantly lower compared to the true energy of the hadrons initiating the cascade. A correction of the energy is needed to compensate for such losses and bring the measured energy to the true energy, i.e. the absolute energy scale. Apart from a correction of the energy, the calibration procedure is aimed to reduce the uncertainty in determination of the absolute energy scale, as much as possible.

For the current analysis the low p_T HFS Iterative Calibration method [121] is used. Here, low p_T means the method was used in events where the transverse momentum of the hadronic system is lower than 10 GeV. The principle of the calibration is to find reference measurements independent of the hadronic energy measurement. In ep collision, in the laboratory frame, the transverse momentum of the scattered electron is balanced by the other final state particles (HFS particles plus isolated electron and muons). Since the scattered electron is measured with high precision, it can be used as a reference. The transverse momentum of the electron, P_T^e, is compared with the transverse momentum of the hadronic final state, $P_T^h = \sqrt{(\sum P_x^i)^2 + (\sum P_y^i)^2}$. To study how they are balanced, the quantity $P_T^{bal} = P_T^h/P_T^e$ is used. The deviation of P_T^{bal} mean value from unity determines the corrections to the calibration constants.

To know how well the detector response is simulated, the double ratio $\left(\frac{P_T^h}{P_T^e}\right)_{\text{data}} / \left(\frac{P_T^h}{P_T^e}\right)_{\text{MC}}$ is defined. These quantities are used to define the systematic uncertainty on the measured energy. From the methods described in [116, 122, 123] it was shown that the uncertainty is less than 2%.

6.4 Event Kinematic Reconstruction

The kinematics of an ep scattering process is characterised by a set of two of the three variables x, y and Q^2 at a fixed centre of mass energy $\sqrt{s}$. At HERA, the DIS

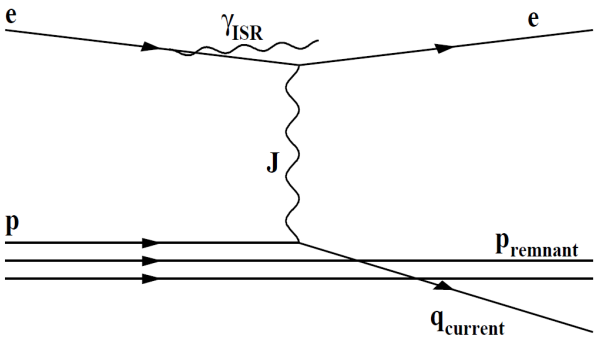

Figure 6.4: Initial state QED Radiation (ISR) in $ep \to eX$ reaction.

kinematics can be reconstructed using the scattered lepton (electron method), the hadronic final state (Σ method) or a combination of both (electron-Σ method). The resolution of each of them depends on the kinematical region.

Before the details of each reconstruction method are discussed it is important to mention how the scattered electron was measured. The electron cluster position might be associated with a track. The azimuthal angle of the electron, φ_e is determined from the track if a vertex-fitted track was found, otherwise the φ_e is obtained from the cluster. The polar angle, θ_e, is always calculated form the cluster information. Since the CTD was removed during HERA upgrade from the H1 detector for maintenance and then reinstalled, a realignment of the CTD with respect to the calorimeters was necessary. The procedure leads to consistency between the measurements of φ_e and θ_e obtained from cluster position and tracks within 1 mrad. The energy of the scattered electron is obtained from calorimeter energy deposit with an energy scale uncertainty of 0.5%.

Electron method. The kinematic variables are calculated using only information of the scattered lepton, its energy E'_e and its angle θ_e:

$$y = 1 - \frac{E'_e}{E_e}\sin^2\frac{\theta_e}{2} \tag{6.13}$$

$$Q^2 = 4E_eE'_e\cos^2\frac{\theta_e}{2} \tag{6.14}$$

$$x = \frac{Q^2}{sy} \tag{6.15}$$

At high Q^2 and low y this method is affected by the initial state QED radiation (see figure 6.4), which leads to lower collision energy than the nominal one and thus to wrong determination of the kinematical variables. To reduce the effect of QED corrections the hadronic final state particles can be used to calculate the kinematic variables.

The Σ method and the e-Σ method. The idea is to reduce the effect of initial state QED radiation by reconstruction of the scattered electron energy using the final state information. Energy and momentum conservation requires that $\sum_i(E_i - p_{z,i})$, where i runs over all final state particles including the scattered electron, is equal

to two times the incident electron energy, $2E_e$

$$E - P_z \equiv \sum_i (E_i - p_{z,i}) = \Sigma + E'(1 - \cos\theta_e) = 2E_e. \tag{6.16}$$

Thus $(E-P_z)/2$ can be used to redefine the electron beam energy and thus giving the possibility to correct for effect of initial state radiation. The kinematical variables in the Σ method are defined as:

$$y_\Sigma = \frac{\Sigma}{E - P_z}, \tag{6.17}$$

$$Q^2_\Sigma = \frac{E'^2_e \sin^2(\theta_e)}{1 - y_\Sigma}, \tag{6.18}$$

$$x_\Sigma = \frac{Q^2_\Sigma}{s y_\Sigma} \tag{6.19}$$

The term Σ is calculated using the hadrons measured by LAr calorimeter and thus the method suffers from the poor resolution of the calorimeter.

In e-Σ method [124] the mixture of electron and Σ methods is used. The kinematical variables in the e-Σ method are defined as:

$$Q^2_{e\Sigma} = Q_e, \tag{6.20}$$

$$x_{e\Sigma} = x_\Sigma = \frac{Q^2_\Sigma}{s y_\Sigma}, \tag{6.21}$$

$$y_{e\Sigma} = \frac{Q^2_e}{s x_\Sigma} \tag{6.22}$$

The e-Σ method has better resolution than Σ method and is used to reconstruct the kinematical variables in this analysis.

6.5 Reconstruction of the Boost to the HCM Frame

The Lorentz Boost to the hadronic centre of mass (HCM) system (introduced in section 4.2) can be reconstructed for each event using the four-vector of the virtual photon, which can be calculated from kinematical variables y and Q^2 as well as the azimuthal angle of the scattered electron. It was shown in [125] that the most precise measurement of boost vector is obtained from kinematic variables reconstructed by the e-Σ method, which is less affected by QED radiation. The energy E_e^{reco}, polar angle θ_e^{reco} and azimuthal angle ϕ_e^{reco} of the scattered electron are calculated as following:

$$E_e^{reco} = \frac{Q^2_{e\Sigma}}{4E_e} + E_e(1 - y_{e\Sigma}), \quad \theta_e^{reco} = \arccos\frac{1-b}{1+b}, \tag{6.23}$$

where

$$b = 4E_e^2 \frac{1 - y_{e\Sigma}}{Q^2_{e\Sigma}} \quad \text{and} \quad \phi_e^{reco} = \phi_e. \tag{6.24}$$

The ϕ_e^{reco} is calculated from the electron method and is used to rotate the HCM frame such way the x-axis is parallel to p_x of the scattered electron in the HCM frame.

Chapter 7

Event Selection

The measurement of the charged particle transverse momentum spectra is based on a selection of NC DIS events, which are defined through the scattered electron. The selection described in this chapter is optimised to reduce the background from ep and non-ep interactions and to ensure a well identified scattered electron well inside the detector acceptance and within the region where the trigger efficiency is high.

In section 7.2 the event triggers are introduced. In sections 7.5 and 7.6 the physics selection, which restricts the phase space of the analysis, as well as detector-related cuts to optimize the event reconstruction are presented. In addition, the exclusion of non-functioning and inefficient parts of the detectors is discussed. In section 7.7 the trigger efficiencies are shown.

The chapter is complemented with control distributions comparing the data with simulated events. This comparison illustrates the quality of the event simulation including the detector performance.

7.1 Run Sample Selection

The analysis utilises the e^+p data collected with the H1 detector in 2006. The proton beam energy was 920 GeV and the positron energy was 27.6 GeV resulting in a centre of mass energy of $\sqrt{s} = 319$ GeV. The data recorded at similar detector and accelerator conditions are grouped into run periods. From run to run the detector conditions might change, for example because of a sudden drop of the high voltage (HV) for a detector component. The run selection is chosen to obtain a subset of events where the following detector components, relevant to this analysis, were switched on and the corresponding HV was on: LAr, SpaCal, CJC1, CJC2, FTD, CIP, ToF and Luminosity system. In case of studies with forward tracks, the FST is also required to be on. Runs with a total luminosity less than 0.1 nb^{-1}, with poor run quality or with shifted z-vertex are ignored.

7.2 Event Triggering

Only events satisfying certain trigger conditions are read out and analysed. In the current analysis the event must fulfill the requirements of the s1 and s2 SpaCal triggers (based on the energy depositions in the SpaCal calorimeter as counted by

the Inclusive Electron Trigger (IET)). The level 1 trigger elements of s1 and s2 are defined as

$$\text{s1} = (\text{SPCLe\_IET} > 2 || \text{SPCLe\_IET\_Cen\_3}) \wedge (\text{BG}), \tag{7.1}$$

$$\text{s2} = (\text{SPCLe\_IET} > 2) \wedge (\text{BG}). \tag{7.2}$$

The trigger element SPCLe_IET > 2 means that the energy deposition in one of the outer[1] SpaCal trigger towers has to be larger than 9 GeV. The trigger element SPCLe_IET_Cen_3 is similar to SPCLe_IET > 2 but for the central part of the SpaCal (also with a cluster of energy above 9 GeV). The BG is a collection of background rejection trigger elements including requirements on the time-of-flight measurement. Trigger s1 allows to trigger low Q^2 events and has very high efficiency, which leads to a high trigger rate. In order to reduce the rate, integer prescales are applied run-by-run. Mean prescale factor of s1 for 2006 is about 23. To avoid a loss in statistics at low Q^2 the trigger s1 was used in combination with the trigger s2. Trigger s2 has a SpaCal radius cut ($R > 20$ cm), as a level 2 trigger requirement, cutting very low Q^2 events. It has a low prescale factor of 1.2 averaged over 2006 running period.

Since two subtriggers are used and each of them has its own prescale factor, one needs to combine their weight in such a way that no events are missed or double counted. The detailed explanation of such a combination is presented in [126]. In case of two subtriggers with prescale factors $pf_{1,jk}$ and $pf_{2,jk}$, which trigger the event j in the run k, the weight is defined as:

$$w_{jk} = P_{jk}^{-1} = \left(1 - (1 - \frac{1}{pf_{1,jk}})(1 - \frac{1}{pf_{2,jk}})\right)^{-1}. \tag{7.3}$$

7.3 Interaction Vertex

One of the basic requirement for reconstructing a DIS event is that there should be a primary interaction vertex reconstructed from the tracks. Since the particle density in the bunches follows a Gaussian distribution ($\sigma_z^P \sim 13$ cm, $\sigma_z^2 \sim 2$ cm, for the proton and electron beam respectively) along the z-direction, the frequency of the collisions between beam particles is also distributed according to a Gaussian around the nominal vertex position. Some of the beam particles will depart from the ideal beam orbit. For example, beam-wall and beam-gas collisions will be evenly spread out along the beam direction and some of these collisions will give tracks in the detector. Also, so-called shifted z-vertex events might be seen in case of collisions of electrons with proton satellites, which are small bunches shifted with respect to the main bunch. In order to suppress such backgrounds the z coordinate of the primary vertex is required to be within 35 cm of the nominal interaction point. The spread in the x- and y-coordinates of the primary vertex is expected to be small due to the small transverse size of the beams of $\sigma_x \times \sigma_y = 112 \times 30$ μm. In figure 7.1 (left) the distribution of the z coordinate of the primary vertex is shown together with detector simulated MC predictions of DJANGOH and RAPGAP. A

[1] The SPCLe_IET trigger is divided into a central ($-16 < x < 8$ cm and $-8 < y < -16$ cm) and an outer region.

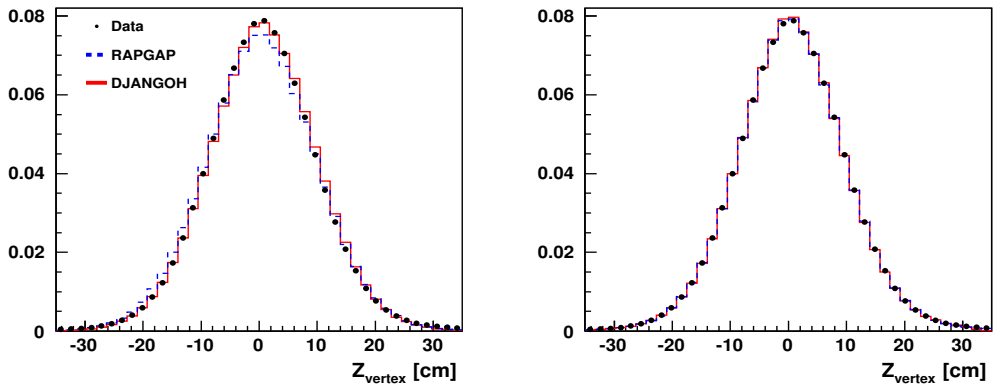

Figure 7.1: z_{vertex} distribution before (left) and after (right) reweighting.

small shift between the data and the MC simulations can be seen. The difference between data and MC is due to the fact that the position of the actual collision point is normally not exactly at the nominal vertex position and that it varies from run to run. In addition, it depends on the beam conditions, which have not been taken into account for the detector simulation. To match the data, the simulated events were reweighted using a polynomial fit function of fifth order. The resulting distribution is shown in figure 7.1 (right), where a good agreement between data and MC is observed.

The following reweighting procedure is performed in this analysis. A reweighting function is the fitting function, f, (usually polynomial) to the ratio of data and MC. The event weight, w, is calculated from the generated level value of the particular quantity:

$$f(x) = \frac{x_{\text{data}}}{x_{\text{MC,rec}}}, \quad w = f(x_{\text{MC,gen}}). \tag{7.4}$$

The weight is applied to both reconstructed and generated level, used for the data correction.

7.4 The Final State $\sum(E - p_z)$

Due to energy and momentum conservation, $E - P_z$ defined in eq. (6.16), is equal to two times the incident electron energy, $2E_e = 55.2$ GeV. In a real measurement, the energy of the final state can only be determined to a certain degree of accuracy and therefore a cut on this variable must cover a certain region correlated to the detector performance. For the event reconstruction the following cut was applied: $35 < E - P_z < 75$ GeV. This cut suppresses radiative background, where photons radiated collinear to the electron beam, escaping the detector. In addition, the lower cut suppresses photoproduction events, in which the scattered lepton escapes in the beam pipe and a particle from hadronic final state is misidentified as the scattered lepton.

In figure 7.2 the measured $E - P_z$ distribution is shown before and after the calibration of the hadronic final state energy, discussed in subsection 6.3.2. It can

be seen that before the calibration the $E - P_z$ distribution does not peak at $2E_e$. This is however the case after the corrections from the calibration have been applied and the distribution peaks exactly at 55.2 GeV, shown by the vertical line in the figure.

The comparison with the simulated events is shown in figure 7.3 (left). The MC does not reproduce well the shape of the distribution. The difference might be partly explained by the uncertainty of the hadronic energy scale, which is 2%, see figure 7.3 (right). The remaining discrepancy can be covered be increasing the value of the energy shift roughly by two. Since the effect of the hadronic energy scale uncertainty on the measurement is rather small (see table 9.2), the total systematic uncertainty will not change in this case.

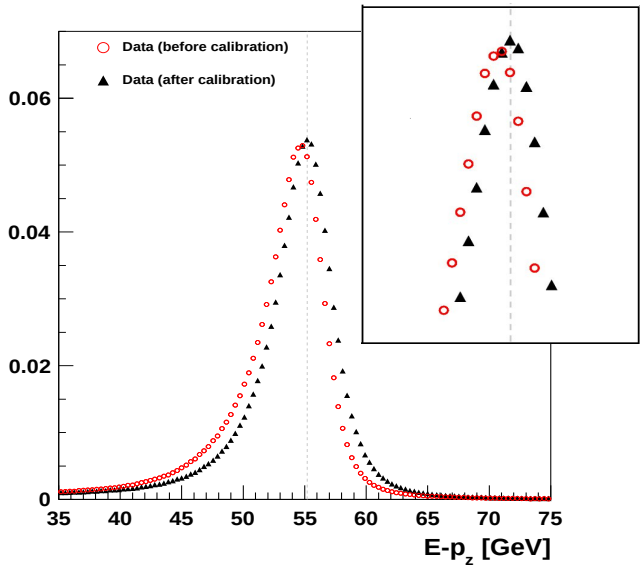

Figure 7.2: Sum of $(E_j - p_{z,j})$, for the data compared to detector simulated DJANGOH and RAPGAP. Zoomed peak is shown in the overlap frame.

7.5 Physics Selection

According to the four-momentum Q^2 of the photon participating in the interaction, the scattered lepton might be detected either by SpaCal or by the LAr calorimeters. In this analysis only the SpaCal has been used, where the scattered lepton is identified as the cluster with the highest E_T. Such a cluster is required to fulfill all selection criteria and identification cut listed below.

The scattered lepton is required to have an energy E'_e larger than 12 GeV. For lower energies the contribution of photoproduction might become significant.

The event kinematics is reconstructed by the e-Σ method (see section 6.4). The kinematical phase space is defined by requiring Q^2 to be in the range $5 < Q^2 < 100$ GeV^2 and the inelasticity y to be in the range $0.05 < y < 0.6$. The cuts ensure high acceptance. The lower cut on Q^2 and upper cut on y reduce background from photoproduction. In addition, x is required to be in the range $0.0001 < x < 0.01$. This

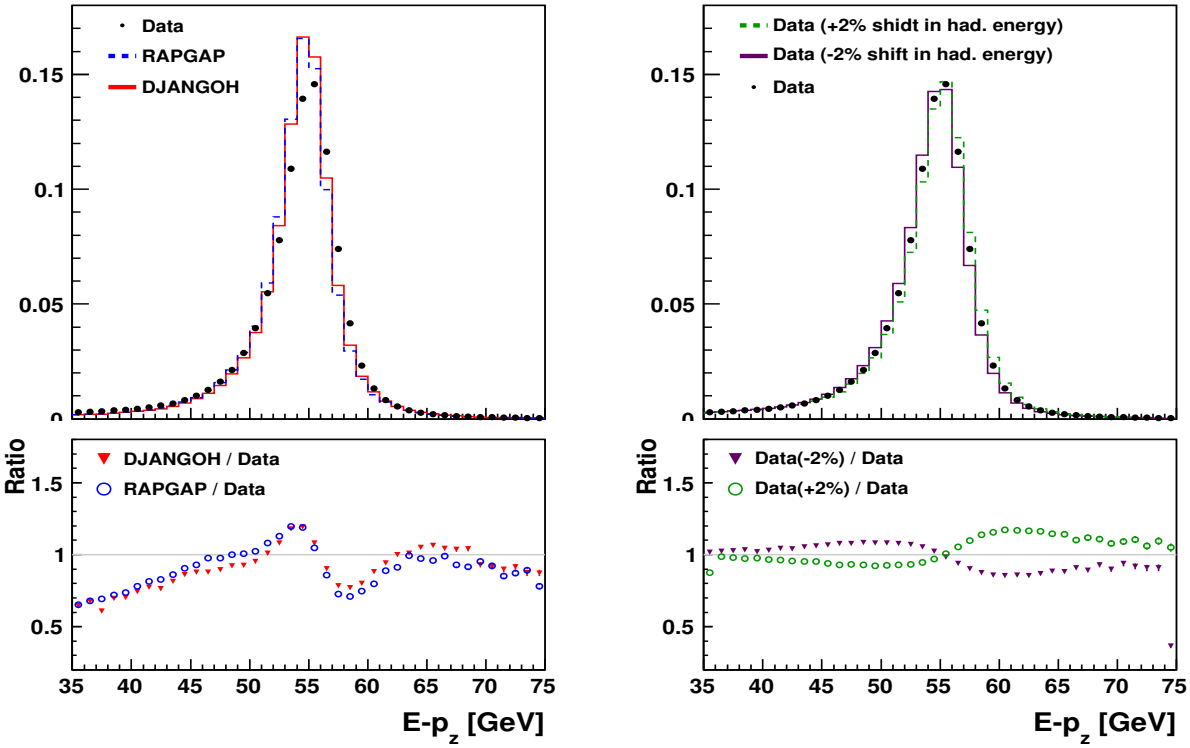

Figure 7.3: Sum of $(E_j - p_{z,j})$, for the data compared to detector simulated DJANGOH and RAPGAP (left). On the right figure the effect of the uncertainty of the hadronic energy scale is shown.

restriction is slightly harder compared to the cut in Q^2 and y. In figure 7.4 the analysis kinematic region in the (x, Q^2)-plane is shown.

7.6 Detector Level Selection

In addition, a few other detector-related cuts were applied to ensure a well identified scattered electron and to suppress background. Since one expects that the scattered electron should be fully absorbed in the electromagnetic part of the SpaCal, the energy in the hadronic part behind the electromagnetic cluster is required to fulfill $E_{\text{had}} < 0.5$ GeV.

Scattered electron hitting the SpaCal close to the edge of the detector may not deposit their full energy in the SpaCal. This effect is especially severe at the beam hole edge since most of the electrons are scattered at small angles. Hence, in order to obtain a good energy measurement, one requires that the total energy deposit in the four layers, positioned in the SpaCal, closest to the beam pipe (E_{veto}) is not allowed to exceed 1.0 GeV.

To reduce background from hadronic showers, the fact that hadronic showers have a broader spatial extension compared to electromagnetic shower is used. Therefore, the radius of the electron candidate cluster in the SpaCal is required to be smaller than 4 cm.

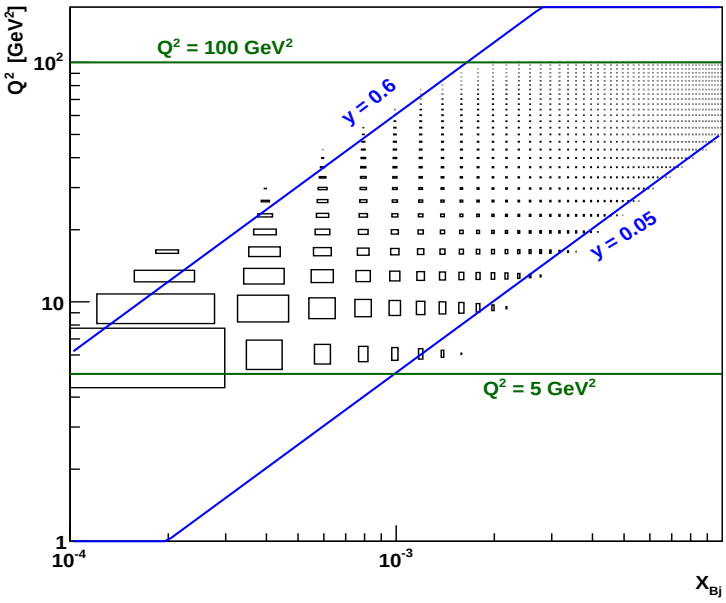

Figure 7.4: The phase space in the (x, Q^2)-plane covered in this analysis.

7.6.1 Fiducial Cuts

To have a precise identification of the scattered electron some inefficient regions of the SpaCal have to be excluded. The following regions were removed for the 2006e$^+$ running period in the data and in the detector simulated Monte Carlo samples:

$$\begin{aligned} -16.2 < x < 16.2 \text{ cm} \quad &\text{and} \quad -4.05 < y < 4.05 \text{ cm}\,, \\ 0 < x < 17 \text{ cm} \quad &\text{and} \quad -5 < y < 5 \text{ cm}\,, \\ 10 < x < 15 \text{ cm} \quad &\text{and} \quad 5 < y < 8 \text{ cm}\,, \\ 5 < x < 16 \text{ cm} \quad &\text{and} \quad 8 < y < 13 \text{ cm}\,, \\ -10 < x < 10 \text{ cm} \quad &\text{and} \quad -17 < y < 10 \text{ cm}\,, \end{aligned}$$

where (x, y) are the electron coordinates in the SpaCal.

To avoid transverse energy leakage in case the electron hits the edges of the SpaCal, restrictions on the radius for the inner and outer regions of the SpaCal are applied:

$$R_{\text{SpaCal}} > 15 \text{ cm}, \quad R_{\text{SpaCal}} < 70 \text{ cm}.$$

Dead cells were excluded by requiring

$$\begin{aligned} -28.35 < x < -24.3 \text{ cm} \quad &\text{and} \quad -52.65 < y < 44.55 \text{ cm}\,, \\ 60.75 < x < 64.8 \text{ cm} \quad &\text{and} \quad 20.25 < y < 24.5 \text{ cm}\,, \\ 64.8 < x < 68.85 \text{ cm} \quad &\text{and} \quad -20.25 < y < -16.2 \text{ cm}\,, \\ -68.85 < x < -64.8 \text{ cm} \quad &\text{and} \quad 0 < y < 8.1 \text{ cm}\,. \end{aligned}$$

In addition, to ensure high efficiency of the analysis triggers, the region of low s2 trigger efficiency was also excluded:

$$-16.2 < x < 8.1 \text{ cm} \quad \text{and} \quad -8.1 < y < 16.2 \text{ cm}\,.$$

Figure 7.5 shows the distributions of the electron in the SpaCal in (x,y)-plane after all fiducial volume cuts. The full set of offline cuts is listed in table 7.1.

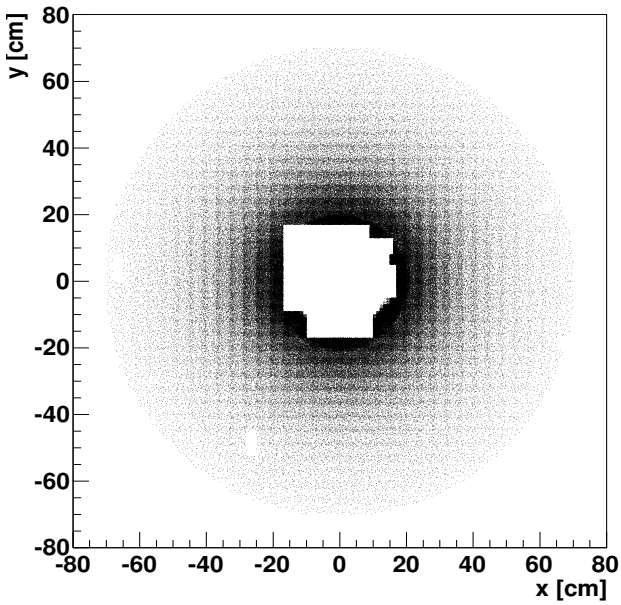

Figure 7.5: SpaCal after fiducial cuts.

Selection criteria	
z-coordinate of vertex	$\lvert z_{\text{vertex}}\rvert < 35$ cm
Scattered lepton energy	$E'_e > 12$ GeV
Energy in hadronic section	$E_{\text{had}} < 0.5$ GeV
Cluster radius in the SpaCal	$R_{\text{clus}} < 4$ cm
Energy in a "veto"-region	$E_{\text{veto}} < 1$ cm
Fiducial volume cut	see subsection 7.6.1
Longitudinal momentum balance	$35 < E - P_z < 75$ GeV
Kinematic range	$5 < Q^2 < 100$ GeV^2 $0.05 < y < 0.6$ $0.0001 < x < 0.01$

Table 7.1: Selection criteria on reconstruction level used for this analyses.

7.7 Trigger Efficiency

The trigger efficiency, ϵ, is calculated using independent triggers, so-called monitor triggers, which have no common requirements with the investigated trigger. For the

SpaCal triggers s1 and s2, the monitor triggers s65 and s64 are chosen, which are based on LAr calorimeter information. The efficiency is calculated bin-by-bin in the analysis bins according to

$$\epsilon = \frac{N_{\text{true}\wedge\text{monitor}}}{N_{\text{monitor}}} \ ,$$

where $N_{\text{true\&\&monitor}}$ is the number of the events after the event selection, accepted by both investigated and monitor triggers, and N_{monitor} is the number of the events after the event selection accepted only by the monitor trigger.

For the phase space defined in the previous section, the trigger efficiencies for the combination of s1 and s2, as used in the analysis, are shown in figure 7.6 as a function of kinematic variables, Q^2, y, $\log_{10} x$, and as a function of reconstructed electron quantities, E', θ_e and φ.

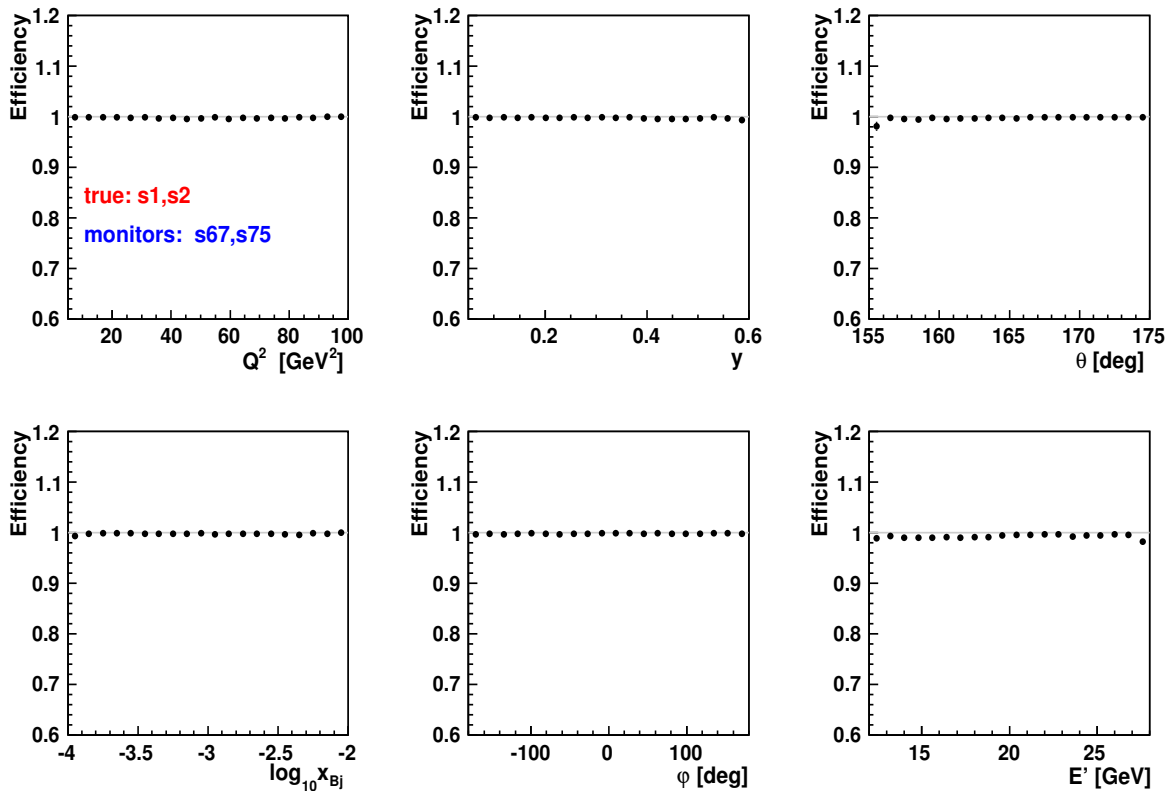

Figure 7.6: Efficiencies for the combination of subtriggers s1 and s2 measured as a function of the DIS variables.

The efficiency is close to 100% for all variables. The trigger information is also implemented in the H1 simulation. The trigger efficiency in MC is 100%.

7.8 DIS Control Plots

The comparison of data with predictions from RAPGAP and DJANGOH MC of the following variables are presented in figure 7.7: θ, Q^2, E', $\log_{10} x$, y and φ. All distributions are normalised to the total number of events. The weight from the

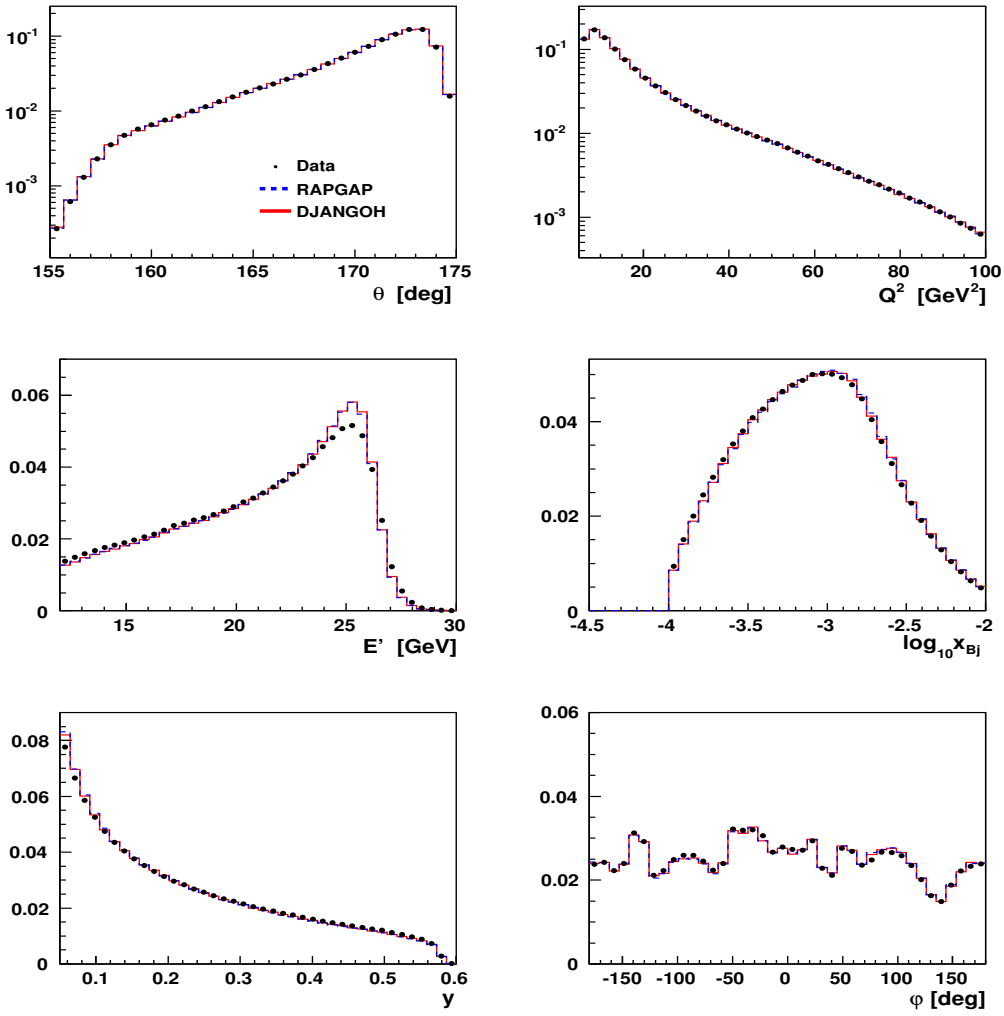

Figure 7.7: Control distributions for the DIS variables before the reweighting and energy smearing procedure.

z_{vertex} reweighing procedure for MC is applied here. As seen from the figures, both MCs fail to describe the data at high values of the energy of the scattered electron as well as at low values of y. The reweighting of one of these variables does not lead to a good description of the other, since in the e-Σ reconstruction method they are not directly correlated. To achieve a good description of the data in both variables, first of all only the reweighting of the y distribution was performed, after that corrections for the predicted energy of the scattered electron were made. These corrections include SpaCal radius-dependent corrections to smear the energy resolution of the MC. Apart from that a global -0.3% energy correction is applied to the MC. The resulting distributions are shown in figure 7.8, where the MC describes the data well for all variables.

In this chapter it was shown that DIS control distributions are well described by the MC simulations and thus the track qualities can be considered in the next chapter. Total number of DIS events in the analysed phase space is about 6.8 millions. The photoproduction background is estimated in the analysis with a similar phase space to be less than 0.2% [127].

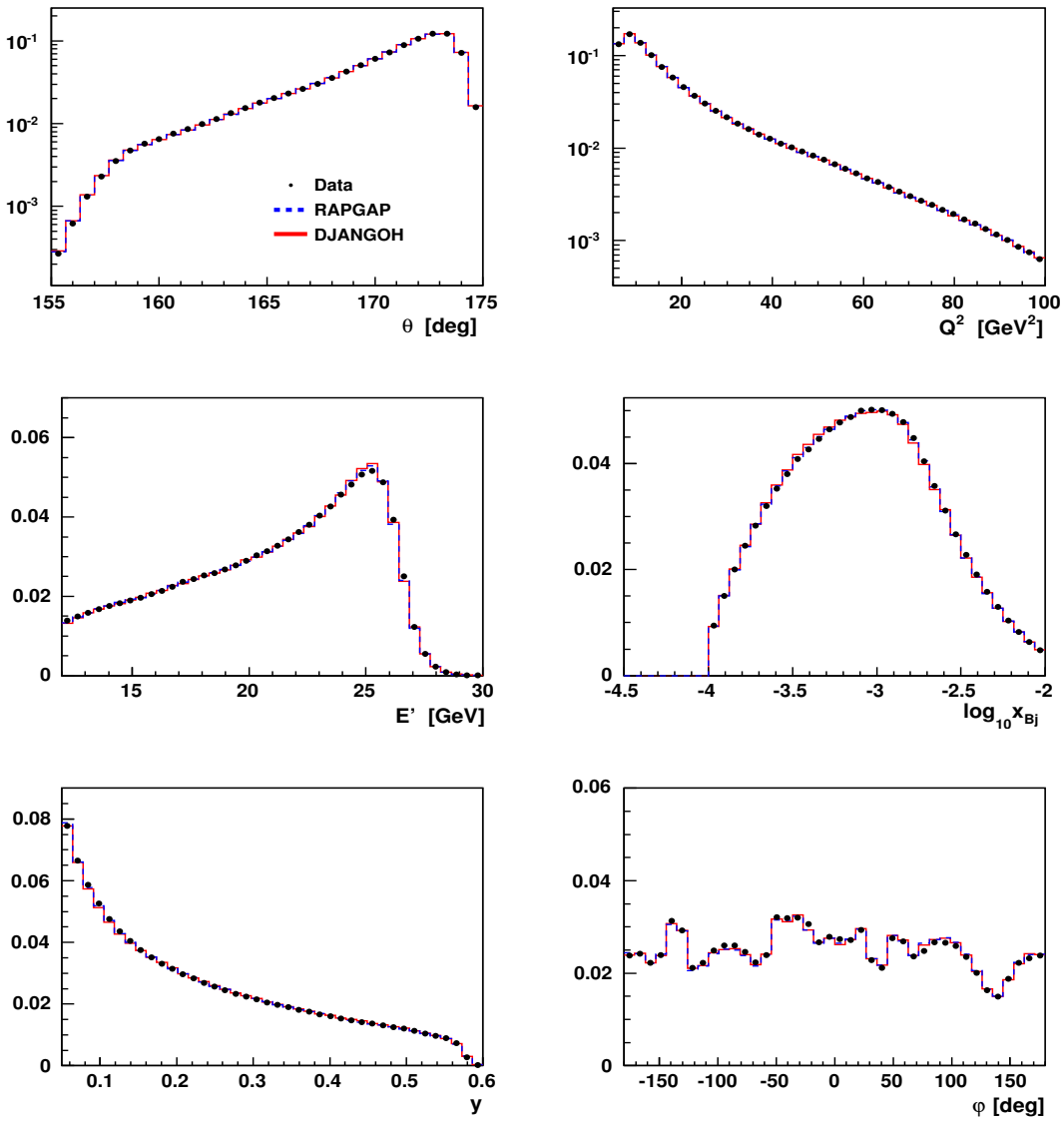

Figure 7.8: Control distributions for the DIS variables after the reweighting and energy smearing procedure.

Chapter 8

Tracks and Track selection

There are several types of track candidates available in the H1 reconstruction software, see figure 8.1 (left): the track measured only in central devices (CJC, CST, z-chambers) - central tracks (C); the tracks measured only with FTD - forward tracks (F); and combined tracks (K), measured in central and forward trackers. Furthermore, tracks can be reconstructed assuming their origin at the primary vertex (1) or at the secondary vertex (2), see figure 8.1 (right).

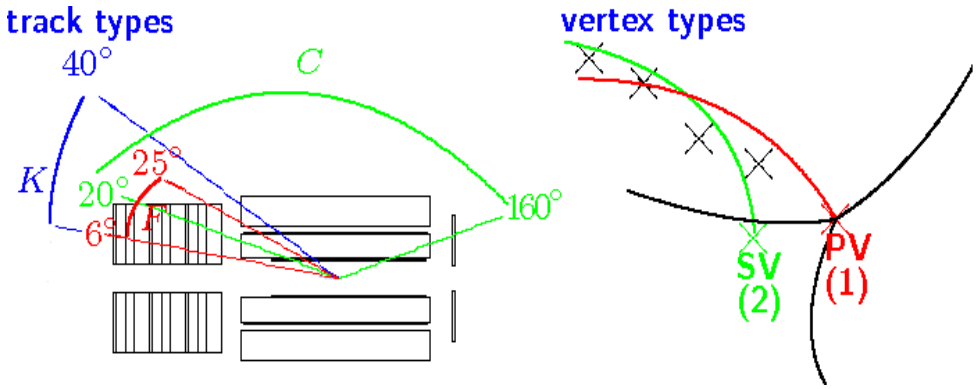

Figure 8.1: Different track and vertex types in the H1 reconstruction procedure.

Since a track might be assigned to more than one type, double counting is possible. This issue can be resolved by the following procedure. First, only "good" tracks are selected, which pass the default tracks cuts, so-called "Lee West track selection". The cuts are different for each track type and are listed in table 8.1. In the second step the preference for one track type over the others for a selected track is taken, thus the double counting is removed. The choice of the best track type is discussed below.

All reconstructed data after the fourth level trigger but before the physics analysis selection are stored in the lowest level of the storage system - ODS (Object Data Store). The selected data are stored in the next level of the storage system (μODS - Micro Object Data Store), which is smaller in size than the ODS and essentially stores the final state information allowing a substantially faster event selection.

On μODS the following strategy for the selection of the best track hypothesis is applied:

Central tracks	
$p_T > 0.07$ GeV	Track transverse momentum
$\lvert dca' \cdot \sin(\theta)\rvert \leq 2$ cm	dca'- distance of closest approach of the track in the $r\varphi$ plane to the primary vertex
$R_{\text{start}} \leq 50$ cm	Start point of first hit
$R_{\text{length}} \geq 10$ cm for $\theta \leq 150^o$ $R_{\text{length}} \geq 5$ cm for $\theta > 150^o$	Radial distance between first and last hits
$N_{\text{CJC hits}} \geq 0$	Number of hits in CJC
Combined tracks	
$p_T > 0.12$ GeV	Track transverse momentum
$p > 0.5$ GeV	Track momentum
$10^\circ < \theta < 30^\circ$	Track polar angle
$\lvert dca'\rvert \leq 5$ cm	Distance of closest approach of the track in the $r\varphi$ plane to the primary vertex
$R_{\text{start}} \leq 50$ cm	Start point of first hit
$N_{\text{CJC hits}} \geq 0$	Number of hits in CJC
$\frac{\Delta p}{p} < 99999.9$	Track momentum resolution
Fit $\chi^2 < 50$	χ^2 of vertex fit
$\chi^2_{c-f} < 50$	χ^2 of link between central and forward tracks
Forward tracks	
$p_T > 0.12$ GeV	Track transverse momentum
$p > 0.5$ GeV	Track momentum
$6^\circ < \theta < 25^\circ$	Track polar angle
$R_{\text{start}} \leq 25$ cm	Start point of first hit
$z_{\text{length}} \geq 10$ cm	z distance between first and last hits
$R_0 \leq 20$ cm	Radial distance of the track from the beamline
$\frac{\Delta p}{p} < 99999.9$	Track momentum resolution
Fit $\chi^2 < 25$	χ^2 of vertex fit
$\chi^2 < 10$	χ^2 of track fit

Table 8.1: Cuts for the "good" central, combined and forward tracks (Lee West criteria).

- if a central track passes the track selection, combined and forward tracks are ignored, and the central track is used
- if the central track fails the track selection, the combined track is tried, if it passes the combined track selection it is used
- if both the central and combined tracks fail the selections, the forward track is tried and if that passes the selection then it is used

One of the reasons for such preference is the momentum resolution, which is getting worse in the forward direction. Furthermore, if no special constraint on the track vertices is made in an analysis, the tracks from the primary vertices are preferred to tracks from secondary vertices. In this analysis the tracks only from primary vertices have been considered.

In the next two sections, a study of the track qualities is presented. The central tracks are taken from μODS. Combined and forward tracks are studied on ODS level, since it was a first attempt to include these tracks into a H1 analysis after the HERA upgrade and thus a very detailed study of basic track variable description, track quality and modelling of overall efficiency were needed.

8.1 Central Track Selection on μODS

In addition to the default "Lee West track selection" (see table 8.1) slightly harder cuts were applied in order to provide a higher efficiency of the track reconstruction:

- The transverse momentum, p_T, is required to be larger than 0.15 GeV. Tracks with lower momenta suffer from significant scattering in the dead material between the interaction point and the CJC. In addition, this cut ensures reconstruction in the region of the CJC with high efficiency, where a track reaches the outer CJC, which improves the reliability of the track reconstruction.
- Tracks are required to have a radial length, R_{length}, (the radial distance between the first and the last hit) larger than 10 cm independently of θ to avoid short tracks and to ensure good momentum resolution. This cut is equivalent to the restriction on the polar angle of the tracks.
- To exclude tracks originating from the electron due to showering in the material in front of CJC1, the minimum angle of a track w.r.t. the scattered electron has to be larger than 0.2 rad. In figure 8.2 this angle is shown for all central tracks (left) and for those which have transverse momentum in HCM frame larger than 4 GeV (right). One clearly sees the peak at zero from showering with photon conversions for high p_T^* tracks.

The "Lee West track selection" together with the additional cuts listed above are further referred to as "track selection" and are applied in all further distributions where central tracks are used.

In figure 8.3 (a) the central track multiplicity distribution is shown after event and track selection. On average six central tracks are observed per event. As seen from the plot, both MCs fail to describe the data and do not agree with each other.

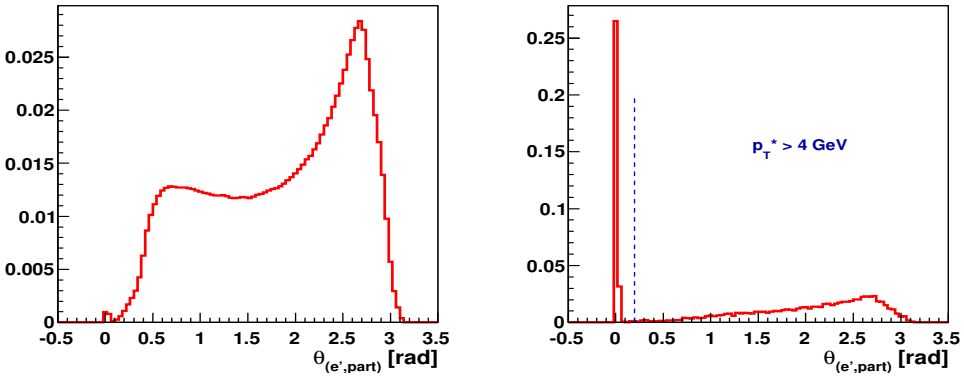

Figure 8.2: Angle of tracks w.r.t. the scattered electron: for all central tracks (left) and for those which have transverse momentum in HCM frame larger than 4 GeV (right).

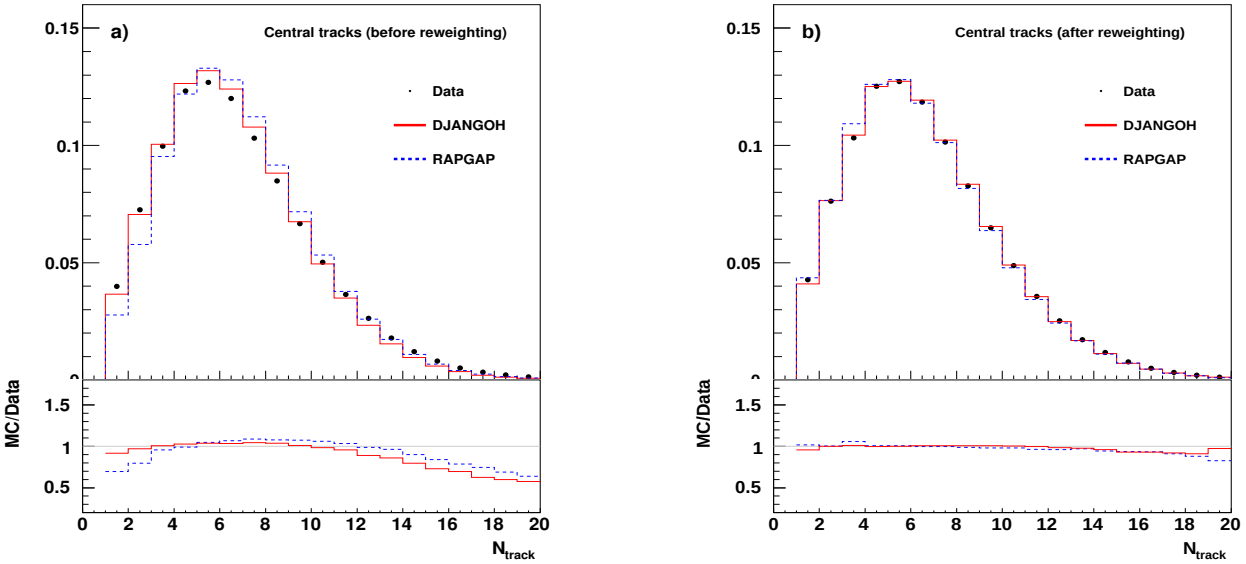

Figure 8.3: Number of central tracks in the event before reweighting (a) and after reweighting (b).

The MC distributions were thus reweighted to the data, and the result is presented in figure 8.3 (b). The reweighting is done using the procedure explained in the end of section 7.3. The obtained event weight, evaluated as a function of multiplicity on generated level, is applied for all further distributions. As one can see in the plot still 10% difference in seen after the reweighting procedure, this is due to a non-ideal fit function and to a not perfect correlation between multiplicity on reconstructed level and multiplicity on generated level.

One more weight is applied for further track control distributions, which is related to the different probabilities of nuclear interactions in the detector material of pions and kaons seen in data and MC. The MC shows less interactions of pions and kaons in material between the beam line and CJC1 as well as between CJC1 and CJC2 than in data [128]. To take into account this difference the pion and kaon correction functions were implemented in H1 software and were applied as a particle weight on

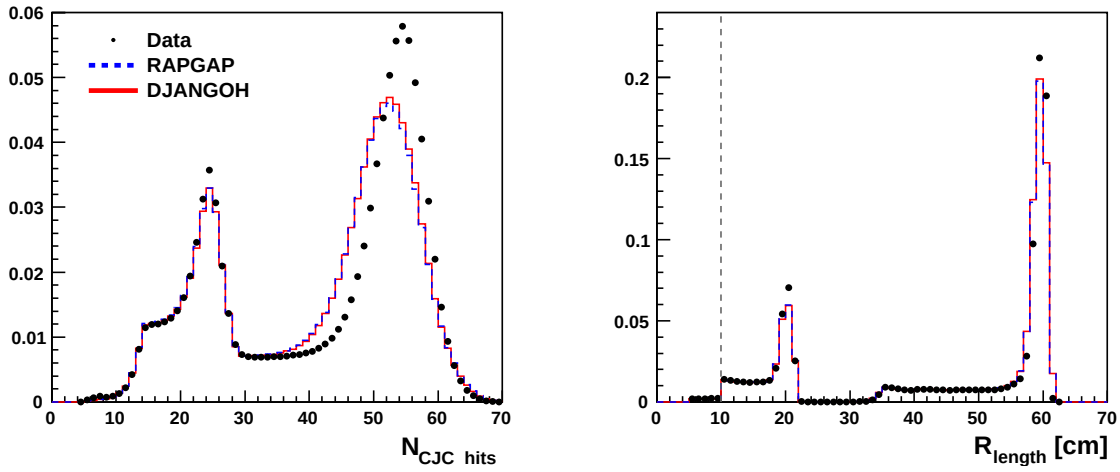

Figure 8.4: Central track control plots for the number of hits in CJC, $N_{\text{CJC hits}}$, (left) and for the track length, R_{length}, (right).

reconstruction level.

Figure 8.4 shows the control distributions for the number of hits in CJC, $N_{\text{CJC hits}}$, (left) and the track radial length R_{length} (right). Two peaks in both distributions represent the tracks which traverse only CJC1 (left peak) or both chambers (right peak). The gap between them corresponds to the joint of CJC1 and CJC2. As seen from the plot, both MCs predict a shift of the peak in the $N_{\text{CJC hits}}$ distribution for the tracks which pass both chambers. This discrepancy is not so important for the analysis since for "long" tracks the efficiency and momentum resolution do not depend so much on the number of hits.

Central track control distributions for the transverse momentum, pseudorapidity, polar angle, and azimuthal angle are presented in figure 8.5. All distributions are normalised to the area. The peak in the θ distribution at $\theta \approx 20^\circ$ is typical for central tracks due to the fact that the particle density at small angles, i.e. in the forward region, is large. A satisfactory description is observed for all kinematical quantities. A difference between data and MC is seen at low θ (high η) and at the tail of the p_T spectrum. To achieve a good description of the data, the predicted η and p_T distributions were reweighted to the data using the reweighting procedure described above. The resulting distributions are shown in figure 8.6.

8.2 Forward and Combined Tracks on ODS

One of the challenging task of this analysis was to reach the forward (towards the proton remnant) direction to the maximum limit allowed by the detector tracking system. Compared to the DGLAP scheme, more gluons with sizable transverse momentum are emitted near the proton direction. For this reason, charged particles with high transverse momentum produced close to the proton direction, are considered to be especially sensitive to QCD dynamics at low x. This was a first attempt to include forward and combined tracks into a H1 analysis after HERA upgrade. Issues such as large amount of material in front of the FTD, worse p_T resolution of

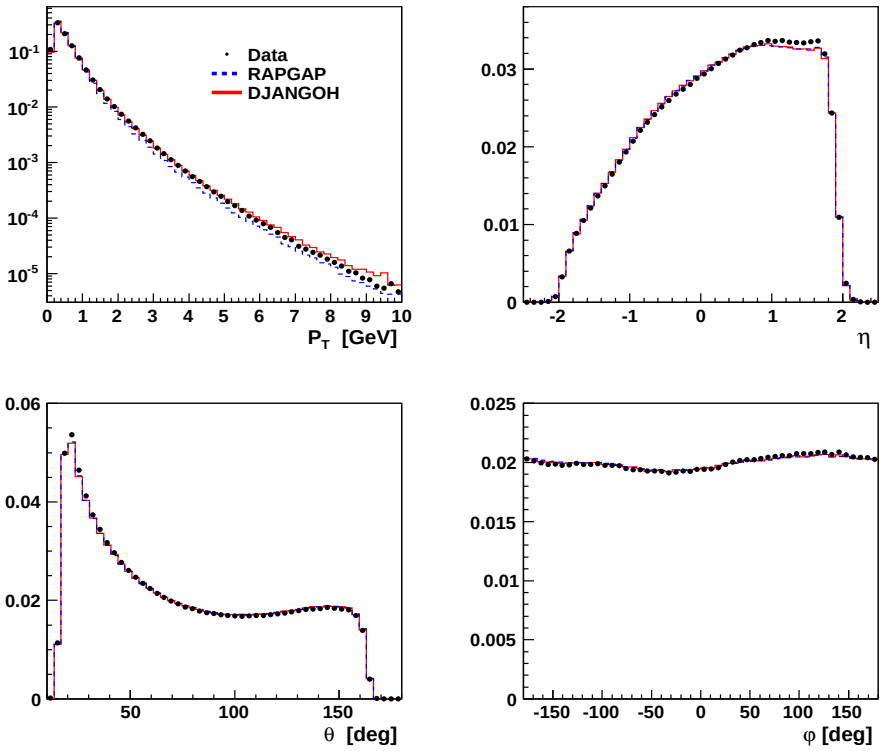

Figure 8.5: Central track control plots for the transverse momentum, p_T, pseudorapidity, η, polar angle, θ and azimuthal angle, φ.

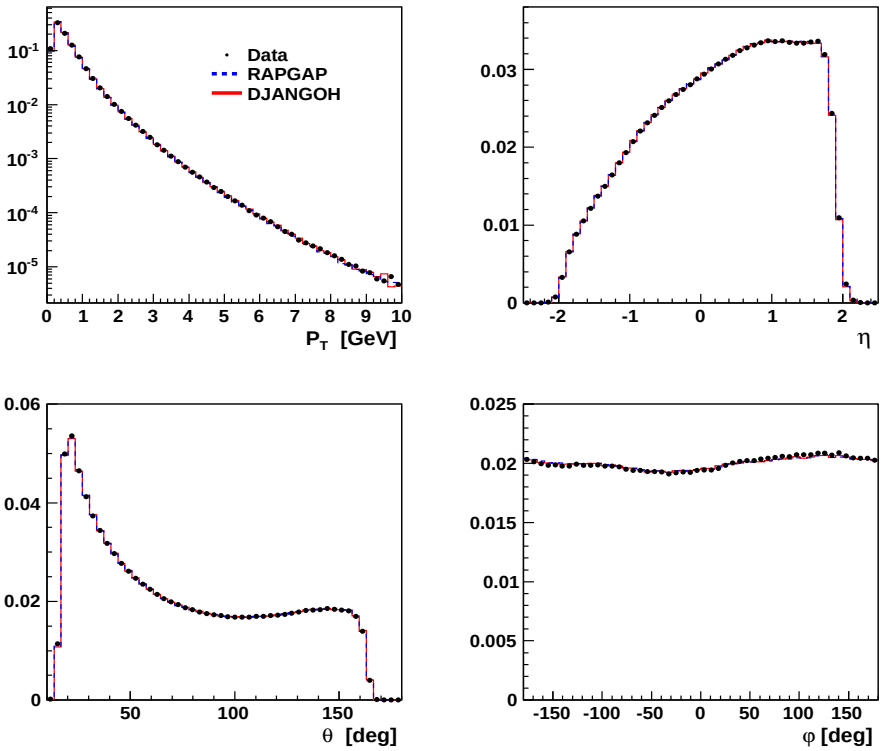

Figure 8.6: Central track control plots for the transverse momentum, p_T, pseudorapidity, η, polar angle, θ and azimuthal angle, φ, after the reweighting.

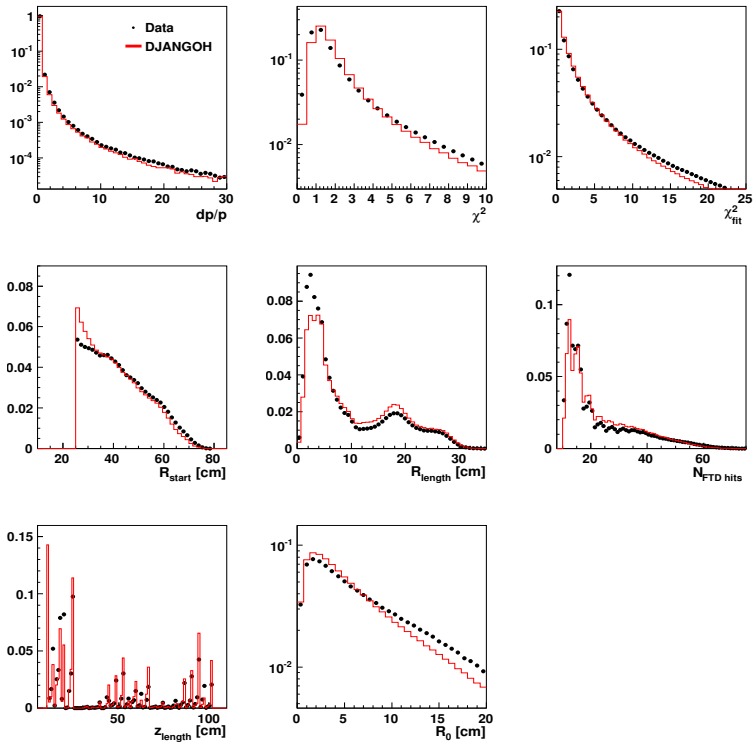

Figure 8.7: The forward track parameter control distributions. The definition of these parameters is presented in table 8.1.

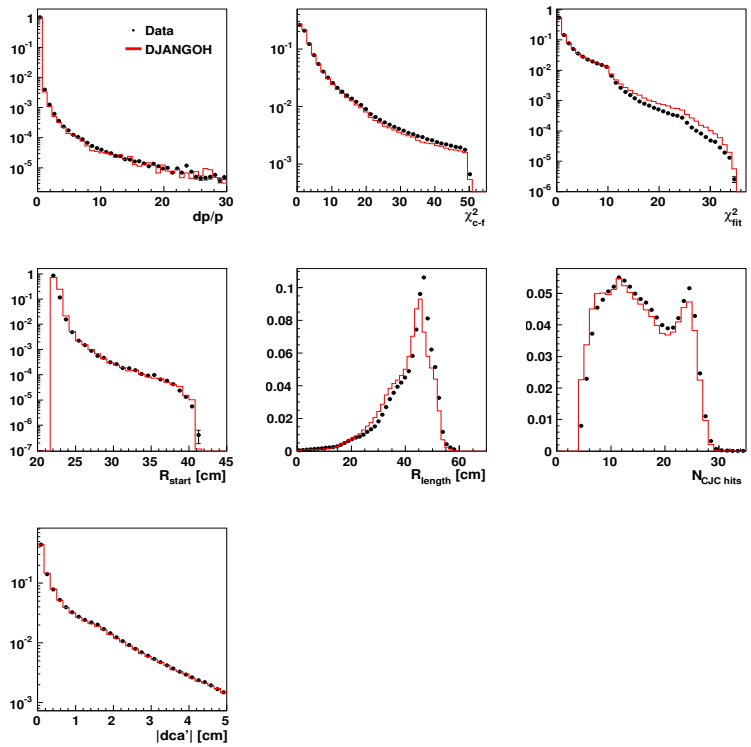

Figure 8.8: The combined track parameter control distributions. The definition of these parameters is presented in table 8.1.

the forward tracks compared to the central ones as well as the general problems of reconstruction of forward going tracks make the measurement difficult.

The HERA-II FTD track selection criteria used in the analysis are listed in table 8.1. Some of these technical quality criteria of the tracks were optimised particularly for the current analysis. The description of the forward and combined track variables characterising the track quality, such as χ^2 of track and vertex fit, radial length, start point of first hit and etc., is shown in figures 8.7 and 8.8. The definition of these variables was introduced in table 8.1.

As seen from the plots, the MCs do not describe all quantities. Since for the presented analysis the most important track variables are p_T and θ, one especially needs to calculate and understand the track finding efficiency as a function of these variables. Almost all studies described in the next few sections are dedicated to the understanding of the systematic uncertainties associated with the track reconstruction efficiency.

8.2.1 Efficiency Study: Inclusive Sample

The main technical issue for the analysis extension is to control the modelling of the forward tracker efficiency by the MC and to define a systematic uncertainty associated with the track reconstruction efficiency. The main problem of the FTD was the ageing of the detector. The ageing reduced the likelihood of observing hits in the detector, which consequently reduced the track finding efficiency. This effect has to be well modeled in the MC, if it is used to correct the data from reconstructed to generated level.

In the MC, one can define the efficiency using the original simulated track as the "truth". This is impossible for data, but an independent detector can be used to provide the control sample. The FST provides a good definition of true information, as it has low noise and little dead material causing fake tracks, and it does not suffer from the nuclear interactions problems that the CJC sees for forward going tracks.

For the efficiency calculation, FST tracks are required to be in the acceptance of the FTD and to have a momentum larger than 0.5 GeV, which is mainly to ensure that the track has enough momentum to pass through the end-wall of the CJC (which is approximately 0.5 X_0 thick) and to be visible in the FTD. Then for such a high momentum FST track, the FTD track closest in (θ, φ)-space is considered. The matching criteria for the FST-FTD association are: $\Delta\theta < 0.02$, $\Delta\varphi < 0.1$.

The forward track finding efficiency as a function of the track's polar angle is shown in figure 8.9 for different running periods of 2006. At small angle ($\theta < 10°$) the sharp drop in the efficiency is seen, at higher angles the efficiency is about $30-35\%$. The value of absolute efficiency strongly depends on the track selection and the matching criteria for the FST-FTD association (for the current plots $\Delta\theta < 0.02$, $\Delta\varphi < 0.1$ is taken). The degrading of the efficiency with time is observed, which shows the ageing of the chambers. As seen from the plot this effect is not modelled in the MC. Here and in all further plots, only DJANGOH is used to study the efficiency, since no model difference was observed. The reasonable description of the data which observed in early 2006 was achieved by better estimation of the wire and module-wise efficiencies of the detector. In the end of 2006 running period the difference between measured and modelled efficiency raised quite significantly. At high angles

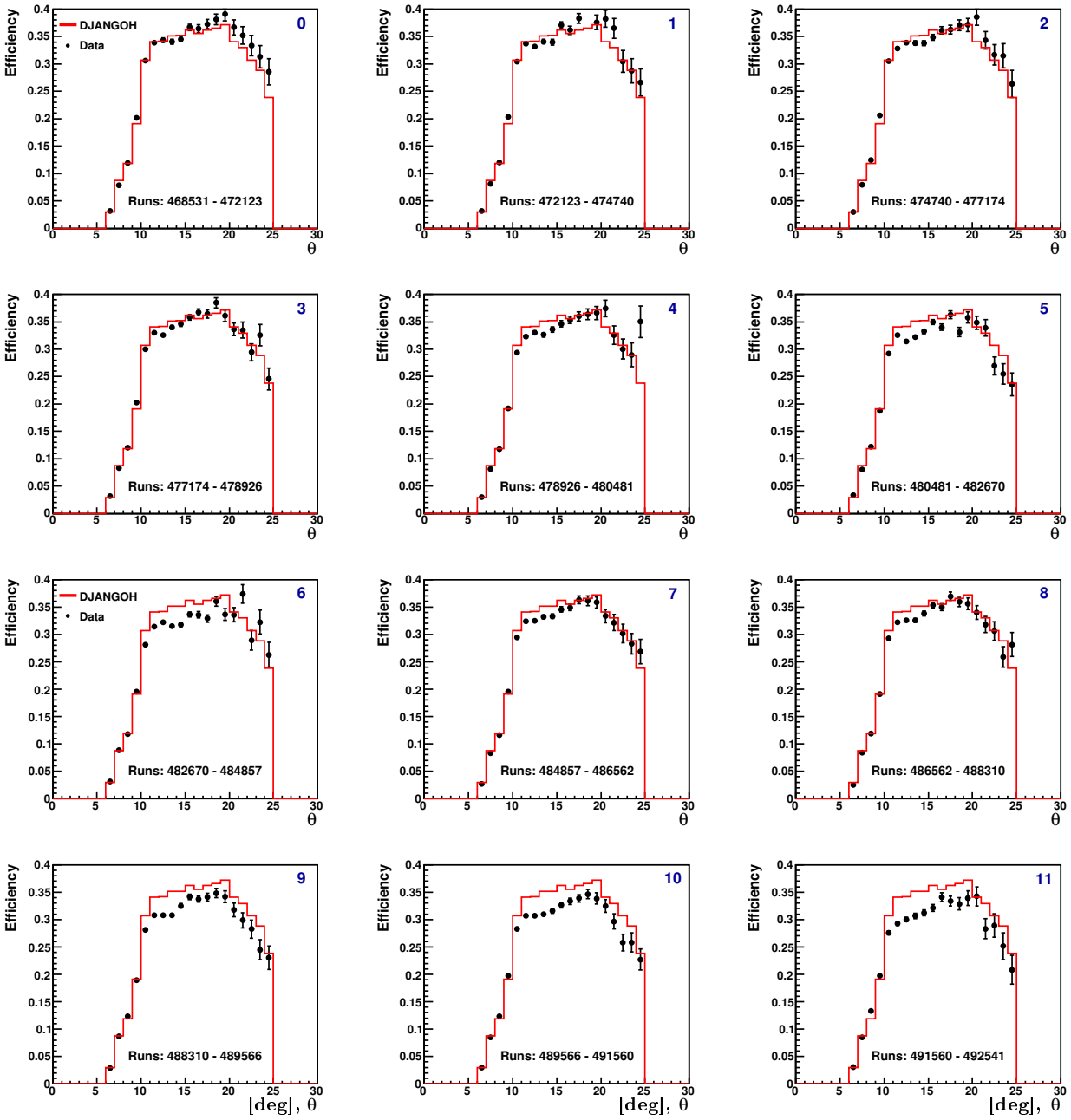

Figure 8.9: The measured and predicted track finding efficiency of FTD probed by FST tracks for 12 different run ranges.

the statistical uncertainty becomes larger due to the FST acceptance, which covers a polar angular range of $7° < \theta < 19°$. For higher θ the central tracks can be used as a truth probe. The absolute efficiency of the FTD in case of probing it by FST and central tracks is not required to be identical (as the definition of efficiency depends on the track selection and matching criteria), but the level of agreement between data and MC can be estimated. The idea is to derive a correction function for MC in the whole angular range covered by FTD, thus using both FST and CJC tracks.

The ratio of the efficiency measured in data over the one predicted by the MC

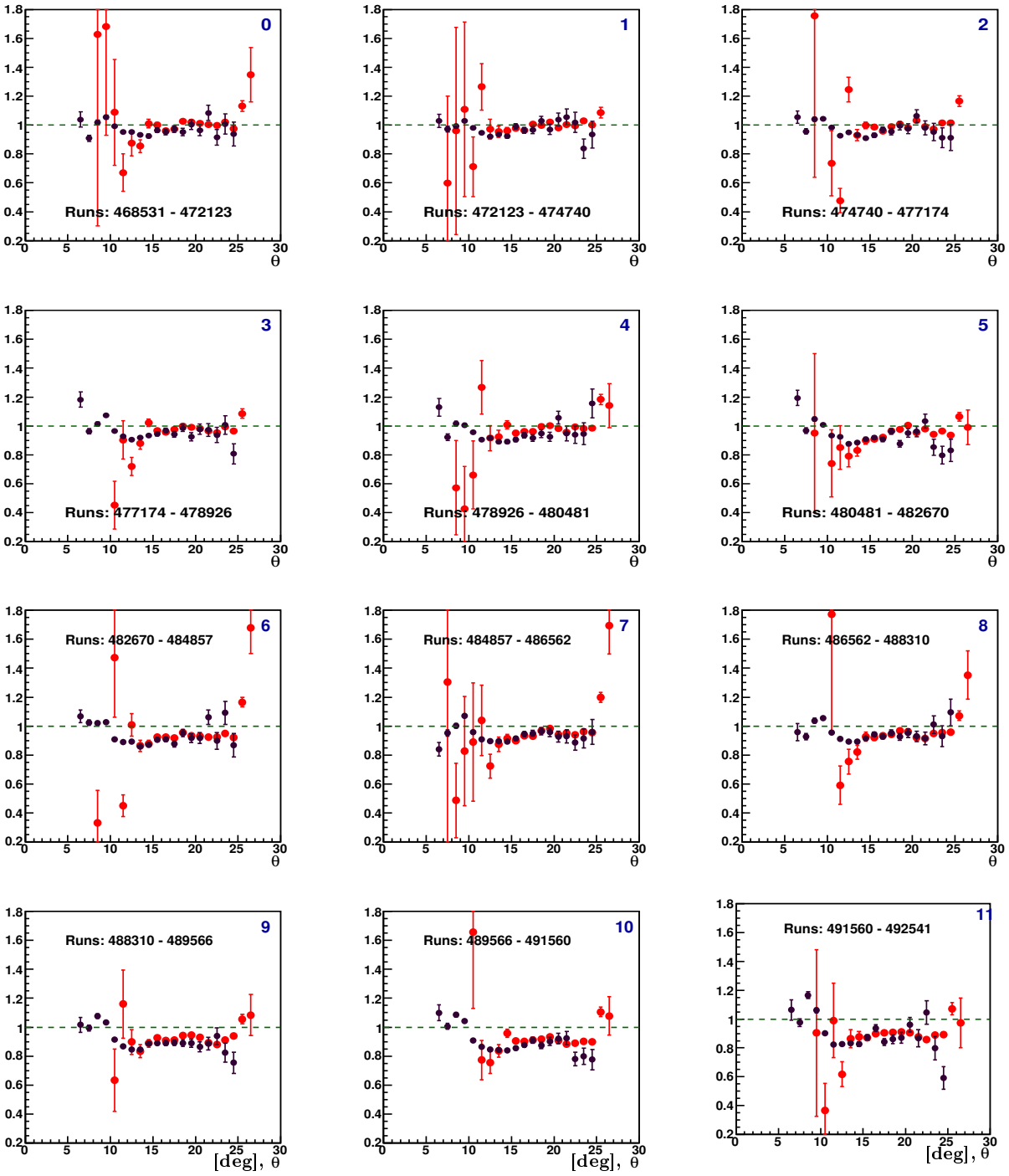

Figure 8.10: The ratio of the measured efficiency over the one predicted by the MC simulation for 12 different run ranges.

simulation is shown in figure 8.10 for both samples, using FST and CJC tracks, and for different running periods. Since these ratios, as will be discussed later, are used to derive the θ-dependent functions for rejection the necessary amount of tracks in MC to describe the measured efficiency (further referred to as "MC downgrading"), the previous rough θ-independent MC downgrading by 5% has been removed here to make a new fit of the shown distributions. It is seen that the difference rises up

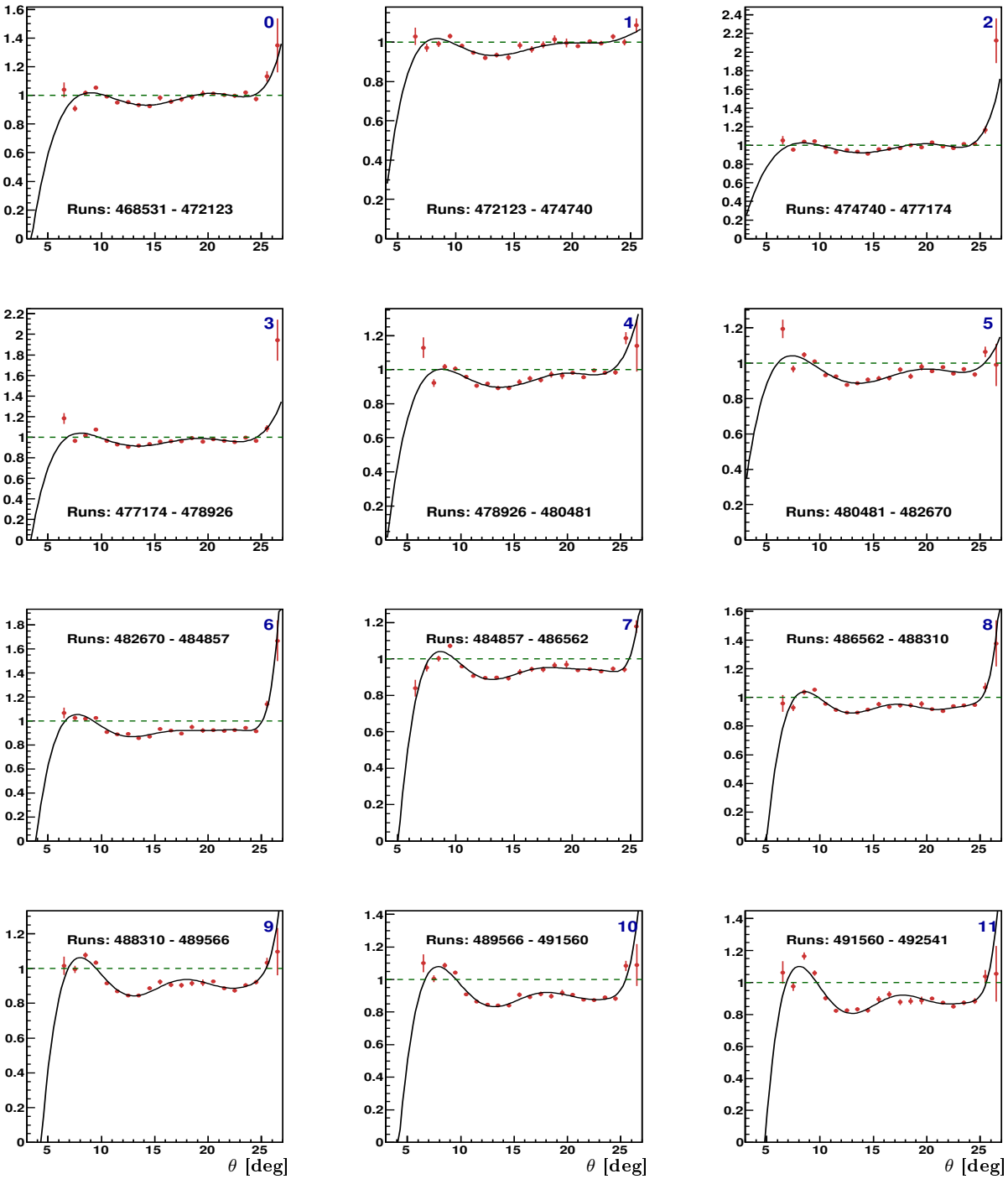

Figure 8.11: The ratio of the measured efficiency over the one predicted by the MC simulation using both FST and central tracks. The measurements are combined as explained in the text.

to 20% for the last runs of 2006. In the overlap region between FST and central tracks the data over MC ratios agree within few present. These ratios were fitted by a polynomial curve to derive a correction function for each running period. To do that the two samples were combined in the following way: for $\theta < 15°$ the ratio of efficiencies obtained using FST tracks is used; for $15° \leq \theta < 20°$, the average between two ratios (using FST and central tracks) is taken; for $\theta \geq 20°$ the ratio

of efficiencies using central tracks is considered. The result of this combination procedure together with the fitted curve is shown in figure 8.11. The fit functions were used to define the necessary amount of tracks in MC which have to be rejected to describe the measured efficiency.

In figure 8.12 the final FTD efficiency probed by FST and CJC tracks is demonstrated for all runs in 2006. The described above MC downgrading procedure leads to a good description of the data for both samples, using FST and CJC tracks. The vertical lines show the acceptable region in θ: in case of FST tracks the cut $\theta > 10°$ is applied to guarantee high enough efficiency and for the central tracks $\theta > 15°$ is required since for lower values of θ the statistics is poor.

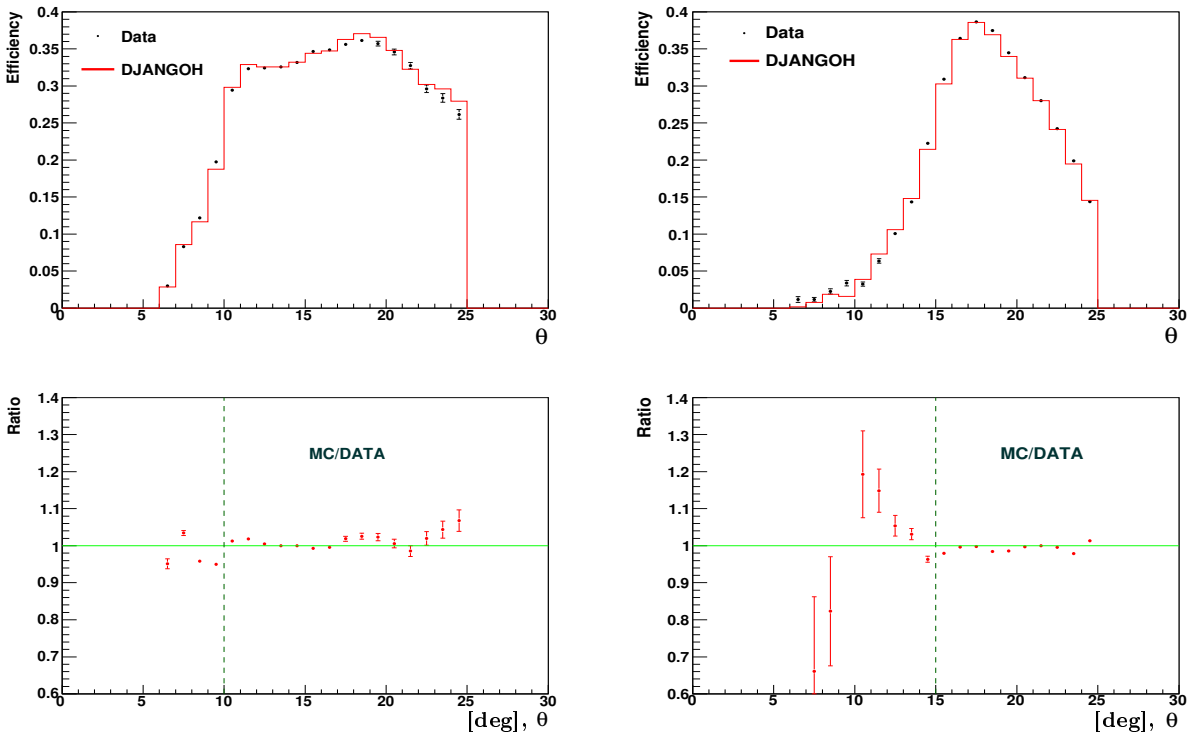

Figure 8.12: The measured efficiency of FTD and the one predicted by the MC simulation as a function of θ track probed by FST tracks (left) and by central tracks (right).

To estimate the systematic uncertainty, in figure 8.13 the data and the MC efficiencies are compared for other variables as the transverse momentum, the azimuthal angle and the number of FST, N_{FST}, tracks in the event. N_{FST} is the average number of FST tracks in the event which are matched with FTD tracks. The efficiency as a function of φ shows the positive/negative asymmetry. In figure 8.13 the MC is shown before and after the reweighting procedure. After the reweigting all variables are described by the MC within 10%. The FTD efficiency using central tracks for the same three variables is shown on figure 8.14. The same level of agreement between data and MC of about 10% is observed.

The modeling of the efficiency also improves the description of the kinematical variables of the FTD tracks. In figure 8.15 the transverse momentum and angular distributions of forward tracks are shown. DJANGOH provides a reasonable description of the data.

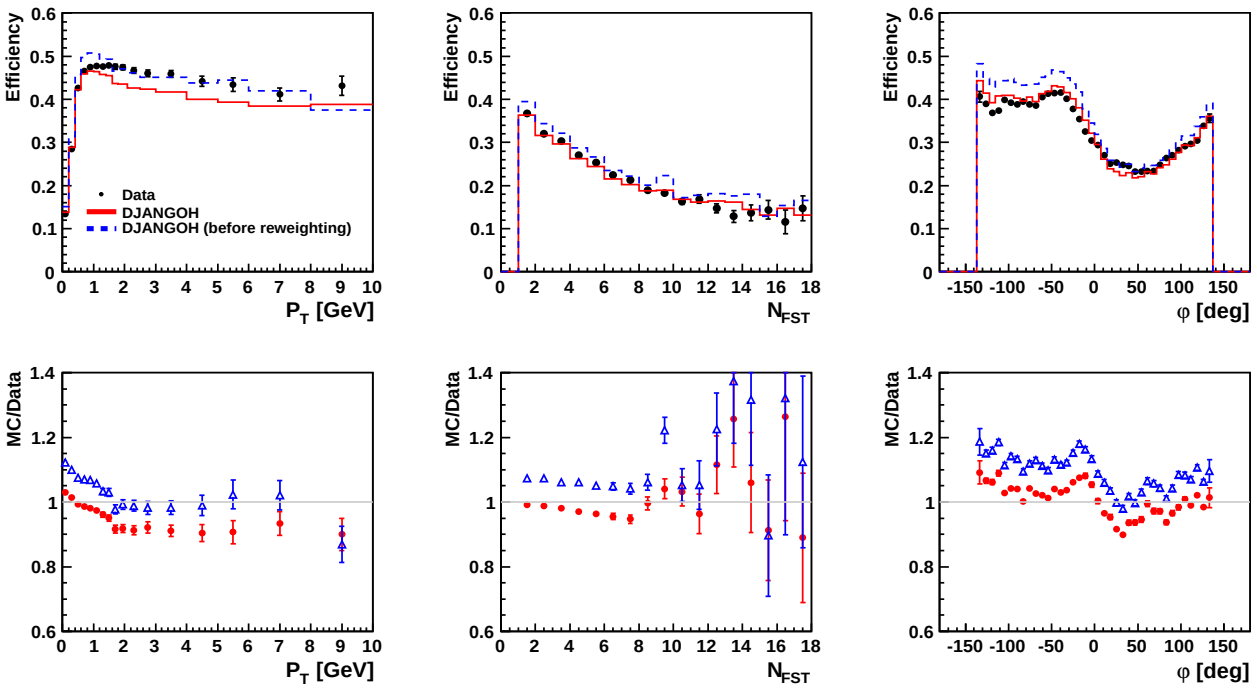

Figure 8.13: The measured efficiency of FTD probed by FST tracks and the one predicted by the MC simulation as a function of transverse momentum (p_T), multiplicity of FST tracks (N_{FST}) and azimuthal angle (φ) before and after the MC downgrading.

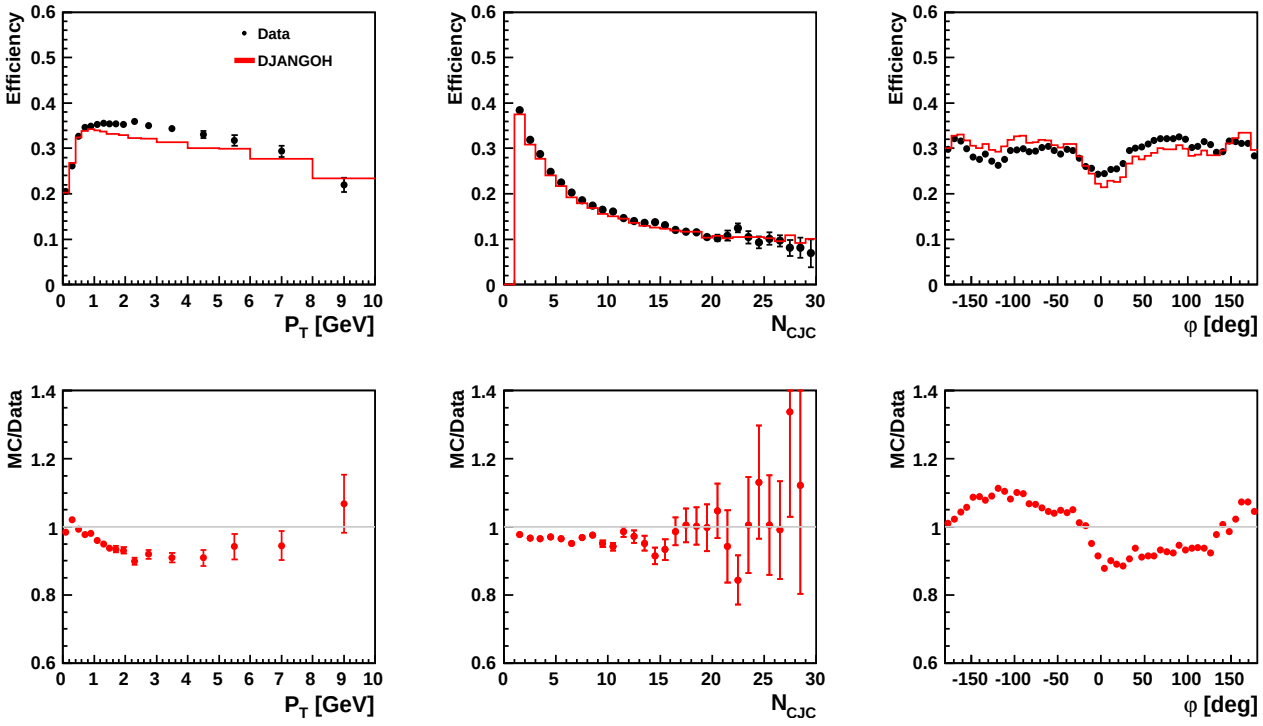

Figure 8.14: The measured efficiency of FTD probed by CJC tracks and the one predicted by the MC simulation as a function of p_T, N_{CJC} and φ.

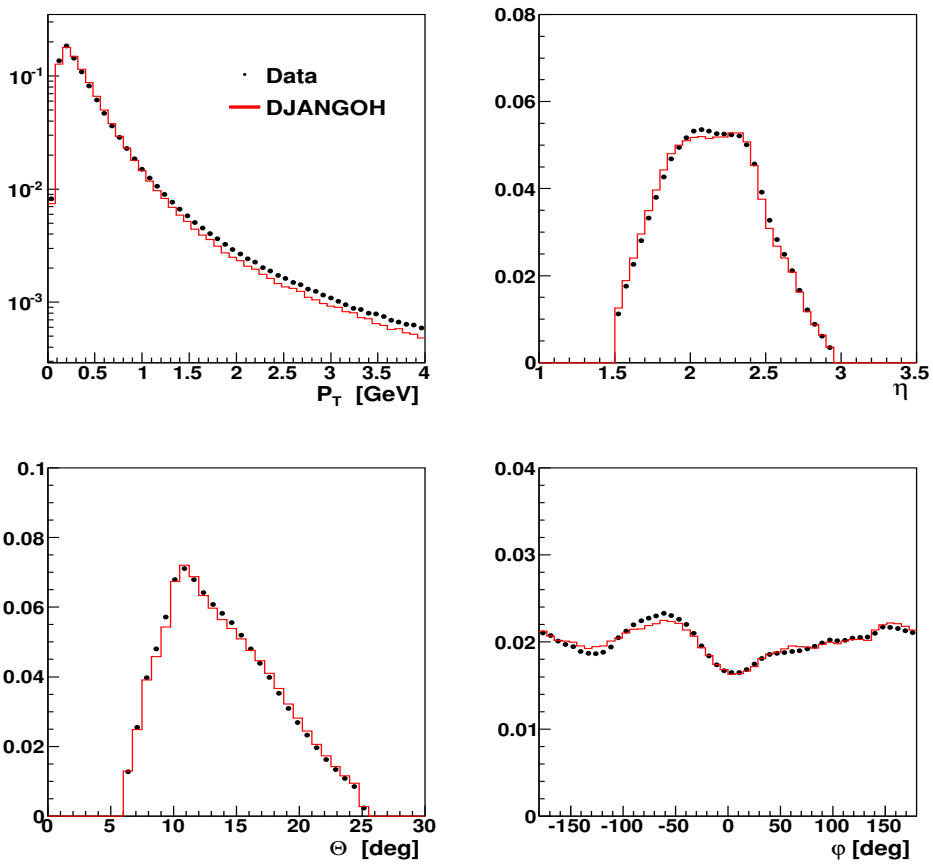

Figure 8.15: Distribution of transverse momentum (p_T), the pseudorapidity (η), the polar angle (θ), and azimuthal angle (φ) for the forward tracks.

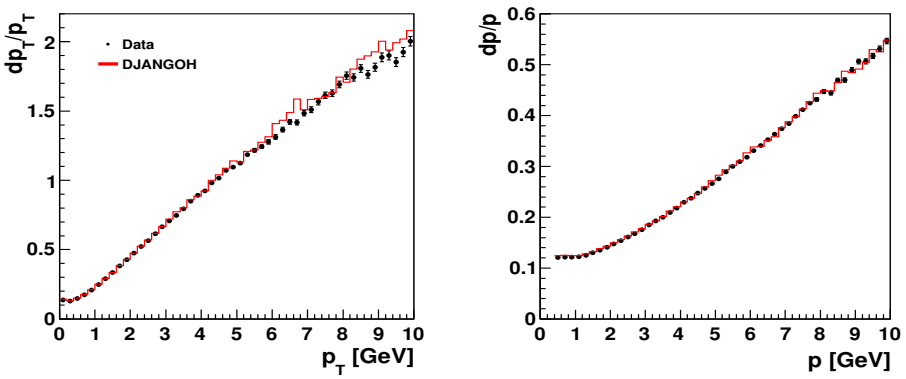

Figure 8.16: Momentum resolution of the vertex fitted FTD tracks.

A good description of the data allows to use the MC to correct the data. To include forward tracks, also the momentum resolution should be good to guarantee high purity for each bin of the final measurements. The momentum and transverse momentum resolutions of the FTD are shown in figure 8.16. A good description of the data by the MC is observed. The possibility of an inclusion of forward tracks in the final measurements is discussed in section 9.2, where the purity in each bin of the final measurement using forward tracks is presented.

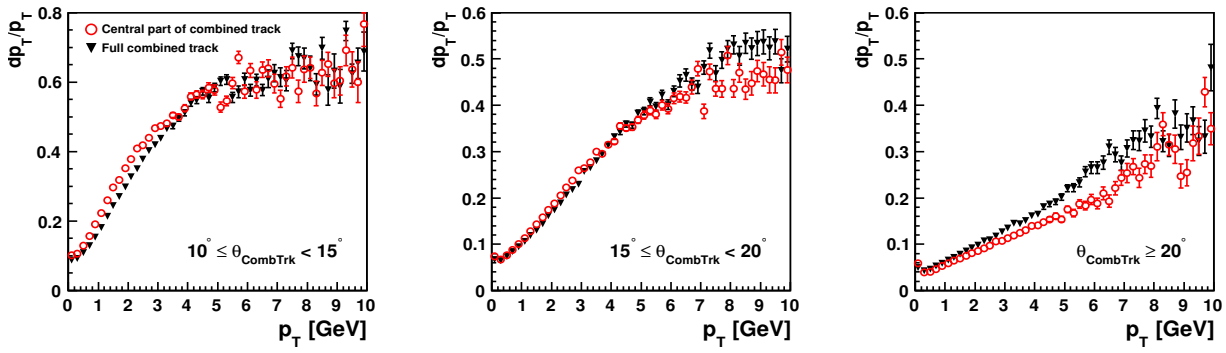

Figure 8.17: Momentum resolution of the combined tracks and its central part depending on the polar angle, obtained from simulated data.

These distributions look different if one looks in different θ ranges. The best achieved resolution for FTD is $dp_T/p_T = 9\% \oplus 6.5\% \cdot p_T/\text{GeV}$ in a region between 15 and 20 degrees.

A combined track in the H1 reconstruction software consists of a vertex-fitted central track and a non-vertex-fitted forward track. To study combined tracks the same techniques as for forwards tracks were used. It is more difficult to draw conclusions about the MC description of the combined tracks as well as their finding efficiency since any discrepancy in the central or the forward tracker description will lead to discrepancies in the combined tracks. Nevertheless, combined tracks will allow an extension of the phase space and are preferred over forward tracks. A comparison of the transverse momentum resolution of combined tracks and their central parts is performed in figure 8.17 for three different θ intervals: $10^\circ \le \theta < 15^\circ$, $15^\circ \le \theta < 20^\circ$ and $\theta \ge 20^\circ$. The central tracks have slightly better resolution for $\theta \ge 20^\circ$ compared to the combined tracks, but on μODS for such large θ no combined tracks will be found, as central tracks are preferred to combined ones there. At low angles, where the combined tracks are expected to contribute, the transverse momentum resolution of combined tracks is slightly better compared to its central part.

To study the combined track finding efficiency the central tracks were used. They cover the same θ range as combined ones and the inclusion of the FST tracks is not needed. In addition, the usage of FST tracks will demand further control of the z_{vtx} distribution by MC, since in order for a track to go through the FST and the CJC and the FTD, the acceptance will depend more strongly on z_{vtx}, which will affect the number of tracks for a given θ. The measured efficiency of combined tracks and the one predicted by the MC simulation as a function of θ, p_T and φ are shown in figure 8.18. The MC describes the data within 10%.

Figure 8.19 shows the distribution of transverse momentum, the pseudorapidity, the polar angle, and azimuthal angle for the combined tracks. A discrepancy between data and MC is observed. The polar angle distribution is shifted for MC, and it does not reproduce the azimuthal angle. The predicted distributions have to be reweighted to the data on μODS, see section 8.3.

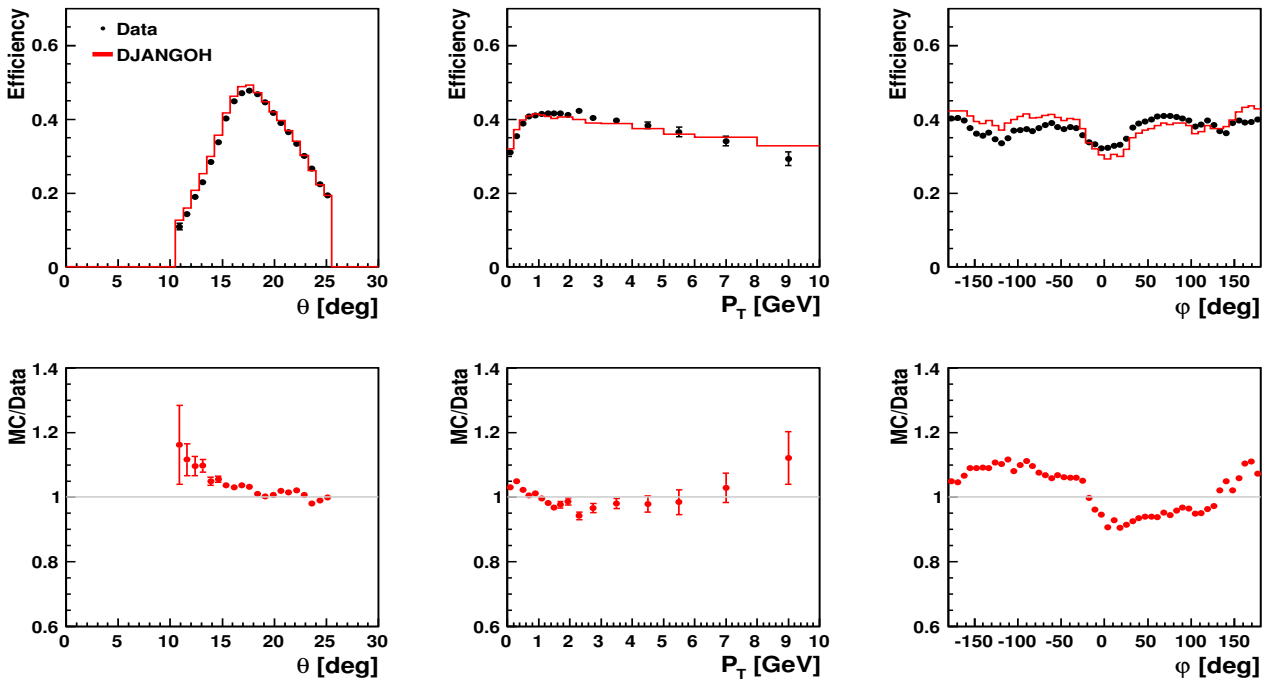

Figure 8.18: The measured efficiency of combined tracks probed by CJC tracks and the one predicted by the MC simulation as a function of θ, p_T and φ.

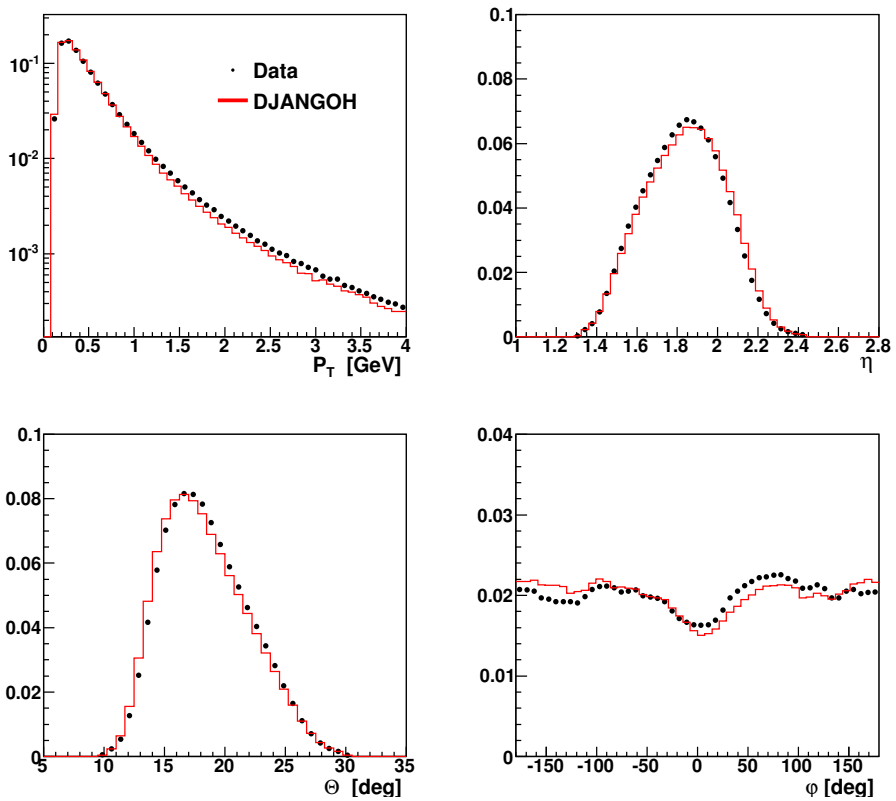

Figure 8.19: Distributions of the transverse momentum (p_T), the pseudorapidity (η), the polar angle (θ), and azimuthal angle (φ) for the combined tracks.

8.2.2 Efficiency Study: K_S^0 Method

To draw conclusions about the description of the measured efficiency by the MC and to estimate the systematic uncertainty related to this, an independent method for the efficiency determination, which uses π mesons from K_S^0 decay is used. The idea is to have a clean definition of "truth" in the data by using a track that is definitely a physical track because it originated from a K_S^0 which can be reconstructed.

The channel $K_S^0 \to \pi^+\pi^-$ is used to reconstruct the K_S^0 because it has a high rate and contains only charged particles in the final state. The pion candidates are required to have tracks in the central detectors, with opposite charges and pass the central track "Lee-West" selection (see table 8.1 for central tracks). The K_S^0 meson has a long lifetime, which means it travels some distance before it decays. Its vertex, displaced from the primary vertex, can be reconstructed and is referred to as secondary vertex V^0. The number of hits for a track candidate is required to be larger than 10, to ensure a good determination of dE/dx.

The requirements listed in table 8.2 are applied to select K_S^0 candidates.

$\boldsymbol{K_S^0}$ **cuts**
Number of K_S^0 >0
Nr. of daughters =2
Decay length > 2 cm
$p_T(K_S^0) > 0.5$ GeV
χ^2 of the fit of the daughter particles to the secondary vertex < 5.4
$\Delta_{\text{dca}} > 0.5$
Number of hits to determine $dE/dx > 10$

Table 8.2: Selection criteria for K_S^0 candidates.

Typical K_S^0 produced in the H1 detector have so small momenta that the both pion candidates can not be detected in FTD, but only one of them. To isolate a signal involving forward tracks one of the decay pions must leave hits at wide angles in the CJC, corresponding to the FTD acceptance. For such a situation a harder cut on the momentum ($p > 0.5$ GeV) has to be required in addition to the central track "Lee-West" selection, in order to ensure that the tracks can pass through the CJC end-wall material and be detected in the FTD. A track found in the FTD acceptance has a shorter track in CJC, thus the cut on the number of hits to determine dE/dx is modified for this situation and is required to be larger than 5 for such "short" tracks and larger than 15 for other daughter track.

The invariant mass, M, is calculated under the hypothesis of the π mass for both negative and positive tracks according to:

$$M(\pi^+\pi^-) = \sqrt{(E_{\pi^+} + E_{\pi^-})^2 - (\vec{p}_{\pi^+} + \vec{p}_{\pi^-})^2}\,, \tag{8.1}$$

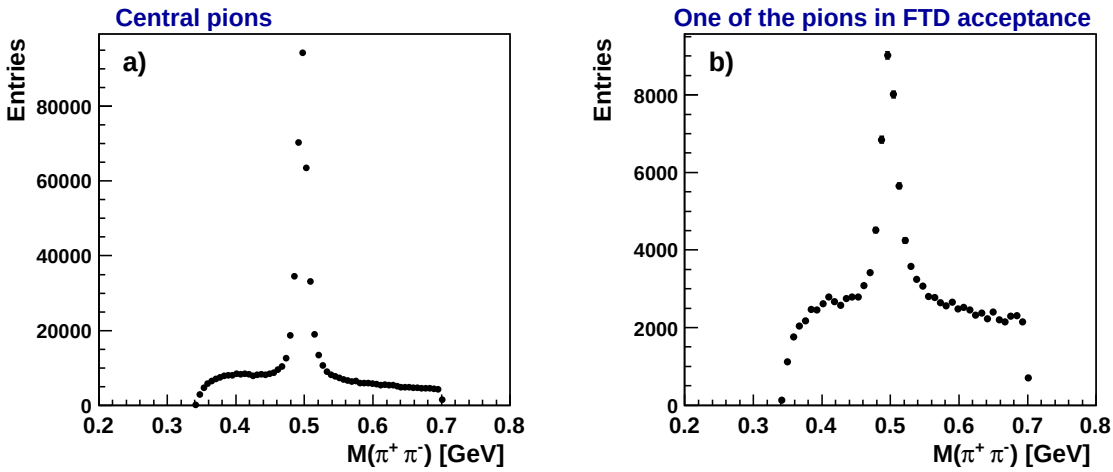

Figure 8.20: The $(\pi^+\pi^-)$ invariant mass distributions for different requirements on the central tracks and different track types as explained in the text.

where $\vec{p}_{\pi^i}$ is the momentum vector, $E_{\pi^i} = \sqrt{\vec{p}^2_{\pi^i} + m_{\pi^i}}$ the energy for negative $(i = -)$ or positive $(i = +)$ charged pions; m_{π^i} is the pion mass [129].

The invariant mass distributions of the K^0_S candidates reconstructed from the $K^0_S \to \pi^+\pi^-$ channel are shown in figure 8.20. In figure 8.20 (a) the invariant mass distribution is shown for the case when both daughter pions are detected in CJC without additional restriction for one of them to be in the FTD acceptance, while in figure 8.20 (b) one of the pions is required to have $\theta < 25°$ and $p > 0.5$ GeV to reach the forward detector. As can be seen from figure 8.20 (b) this requirement increases the background contribution. The high momentum central track (with $p > 0.5$ GeV) can be matched in (η, φ)-space with a forward track and thus can be used to construct a combined track. The second daughter track which is not matched with signals in FTD will be called the central track. One can form the $(\pi^+\pi^-)$ invariant mass not only between the central track and combined tracks (C+K), but also between central track and central part of the combined track (C+C), or between central track and forward part of the combined track (C+F), separately. These three cases are illustrated in figure 8.21. Such measurements provide a possibility to make

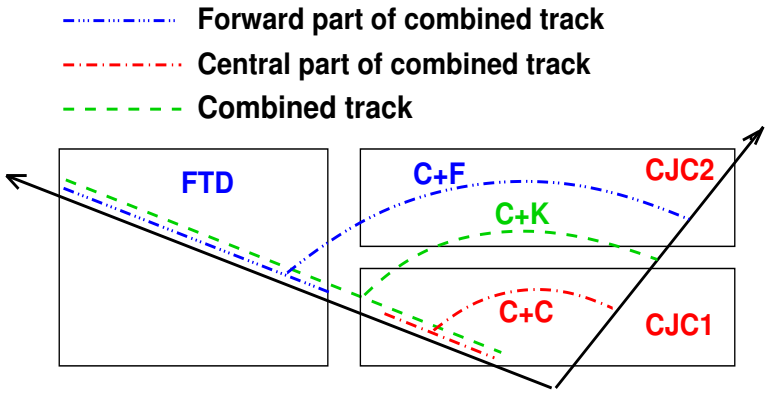

Figure 8.21: Three different methods to form the $(\pi^+\pi^-)$ invariant mass: C+C - central track plus central part of the combined track, C+F- central track plus forward part of the combined track, C+K - central plus combined tracks.

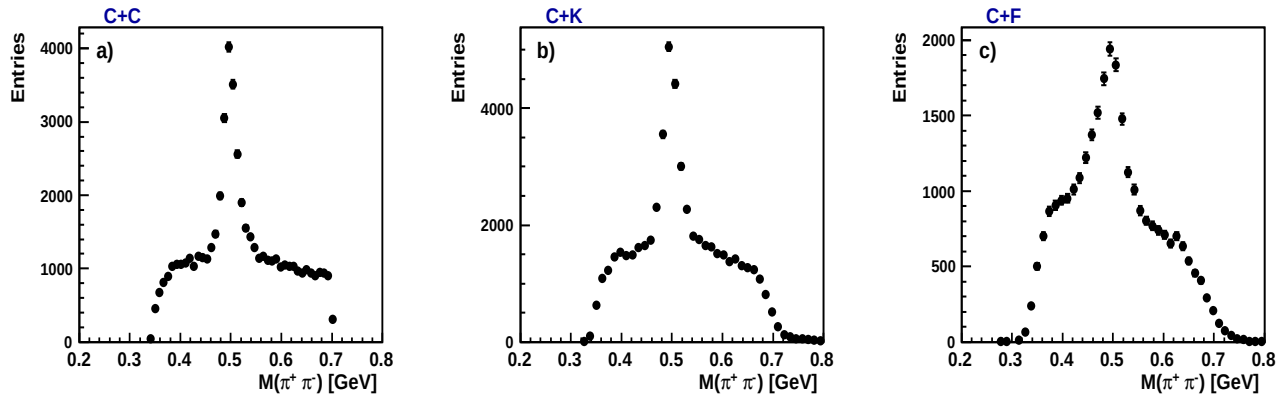

Figure 8.22: The $(\pi^+\pi^-)$ invariant mass distributions for different requirements on the central tracks and different track types as explained in the text.

direct comparison of combined and central tracks, or of the forward and central parts of the combined track. The decay width of K^0_S reflects the momentum resolution of the particular tracks type. The C+C situation is shown in figure 8.22 (a), C+K - figure 8.22 (b) and C+F - in figure 8.22 (c). The C+C and C+K invariant mass distributions have similar signal peak and width values. A comparison of the fit parameters will be discussed below. The invariant mass distribution for the C+F case shows approximately the correct position of the mass peak, but a wider signal width. Here not only angular matching to build the combined track, but also matching in momentum ($\Delta p < 0.2$ GeV) is applied, which slightly improves the signal-to-background ratio. In addition, the increased background is seen close to the mass $(\pi^+\pi^-)$ threshold.

A detailed comparison of invariant mass distributions for C+C and C+K samples are shown in figure 8.23. The distributions were fitted to extract the mass of the K^0_S. The fit function, $f_{\rm tot}(\pi^+\pi^-)$ was taken to be a sum of the signal and the background functions:

$$f_{\rm tot}(\pi^+\pi^-) = f_{\rm sig}(\pi^+\pi^-) + f_{\rm bgrd}(\pi^+\pi^-). \tag{8.2}$$

A quadratic polynomial is used to describe the background and a Lorentz function for the signal. The invariant mass distributions and their fit functions are shown for the data (top plots in figure 8.23) and for the MC (bottom plots in figure 8.23). The reconstructed K^0_S mass is in agreement with the Particle Data Group value of 0.497648 ± 0.0022 GeV [129] for both samples. The width of the signal is slightly wider in the C+C than in the C+K case. The vertical lines show $\pm 2.5\sigma$ interval around the peak, in these intervals the reconstructed π are taken for the determination of the forward and combined track finding efficiency.

The measured and the predicted efficiency of the FTD using π from K^0_S decays is shown in figure 8.24 as a function of the polar angle, θ, the transverse momentum, p_T, and the azimuthal angle, φ. The level of agreement between data and MC is about $5-10\%$. The comparison with the FTD efficiency obtained in subsection 8.2.1 using all CJC tracks can be made, see figure 8.12 (right) and figure 8.14. The similar level of agreement between data and MC is seen there.

The efficiencies of combined tracks using π from K^0_S decay are presented in figure 8.25. The level of agreement between data and MC is about $5-10\%$. Again,

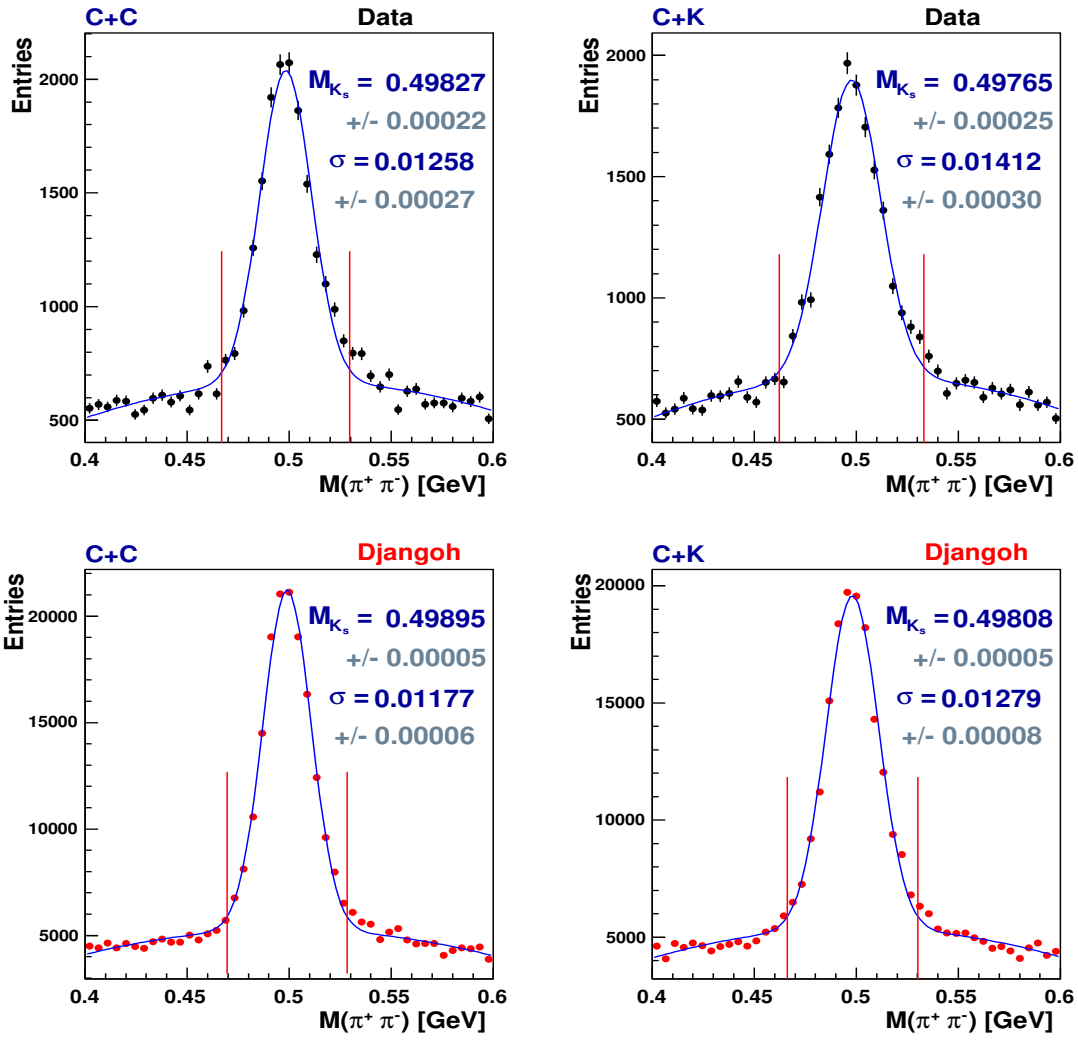

Figure 8.23: Comparison of invariant mass distributions for C+C and C+K samples in the data (top) and in the MC (bottom).

the results might be compared to the inclusive sample where all CJC tracks were used to study the efficiency, see figure 8.18.

The comparison of the efficiency using the K^0_S and the inclusive samples gives consistent results showing agreement of data and MC within 10%. Thus this number is taken as a systematic uncertainty.

Apart from the efficiency studies, the K^0_S method might be used to study the probability of finding more than one matched FTD-central track. An extra track can originate in the material in front of FTD. The idea is to check how well the MC describes this probability. For this purpose the isolated track that comes from the K^0_S decay is used and the number of matched FTD tracks is counted. Figure 8.26 shows how many FTD tracks were found within chosen matching criteria ($\Delta\eta < 0.07$, $\Delta\varphi < 0.25$). As seen from the plot the probability of associating two FTD tracks with a central one is small and is well described by the MC.

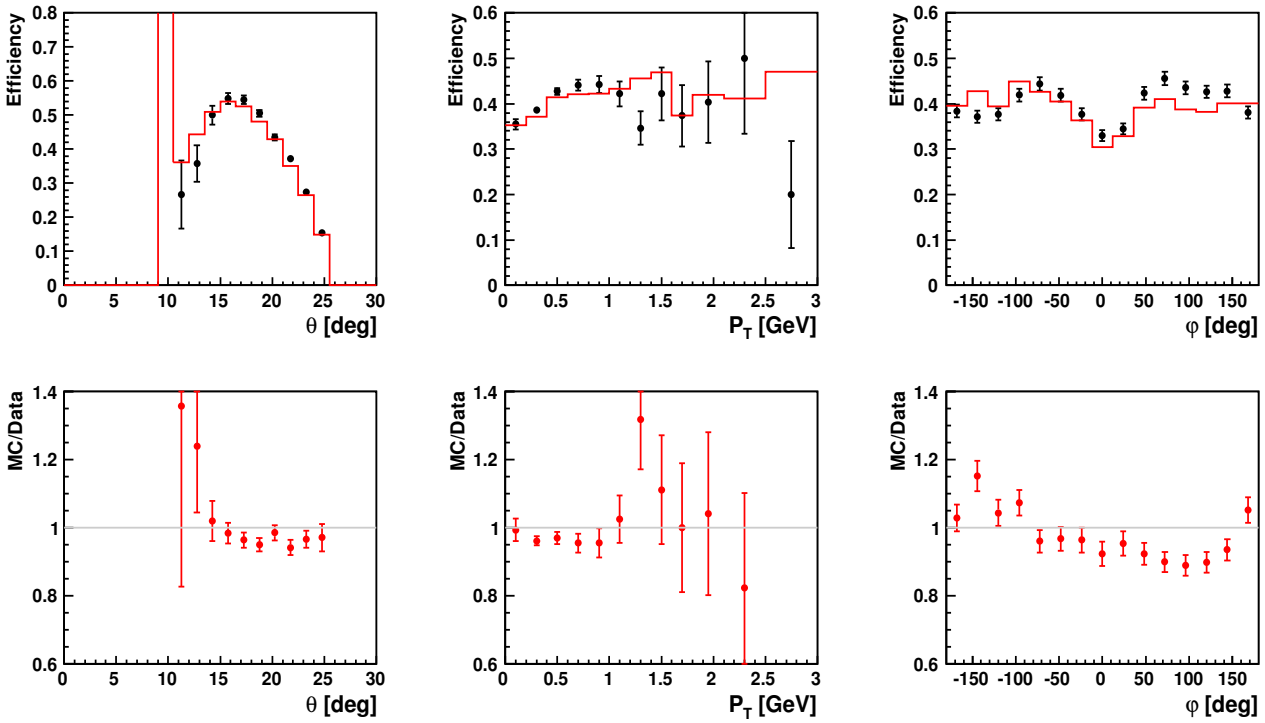

Figure 8.24: The measured efficiency of FTD using π from K^0_S and the one predicted by the MC simulation as a function of polar angle, θ, transverse momentum, p_T, and azimuthal angle, φ.

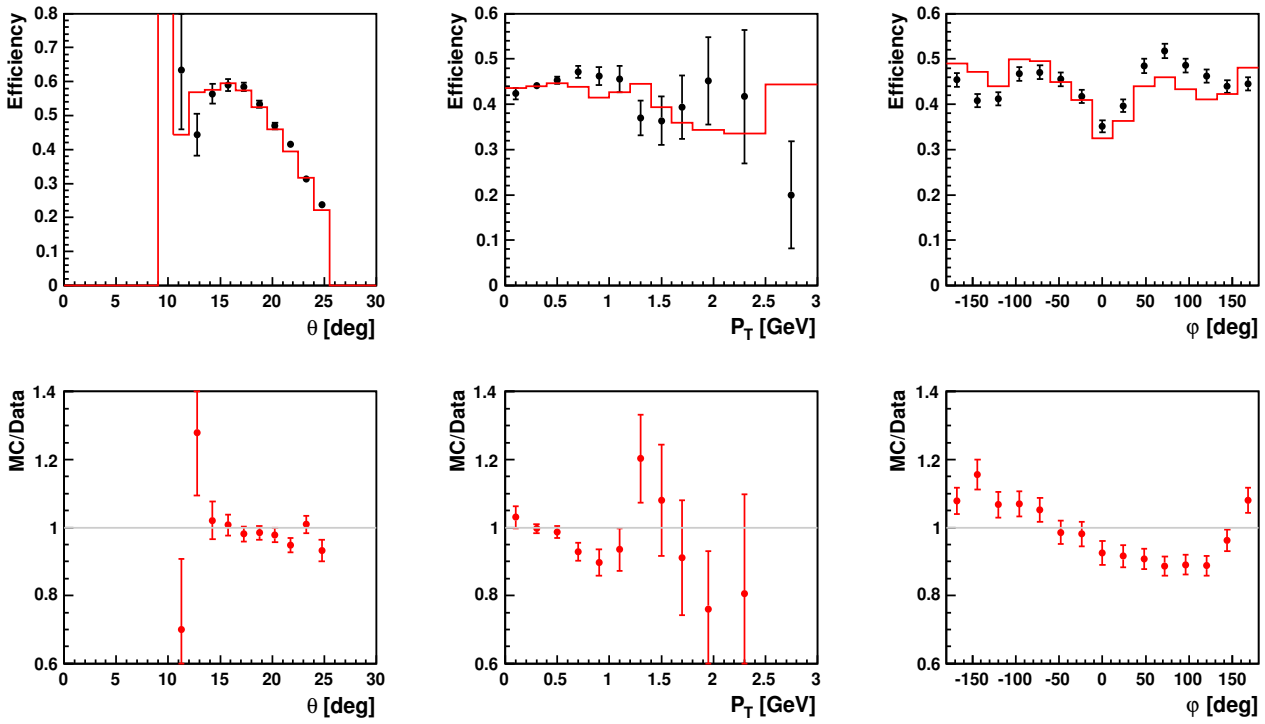

Figure 8.25: The measured efficiency of combined tracks using π from K^0_S and the one predicted by the MC simulation as a function of polar angle, θ, transverse momentum, p_T, and azimuthal angle, φ.

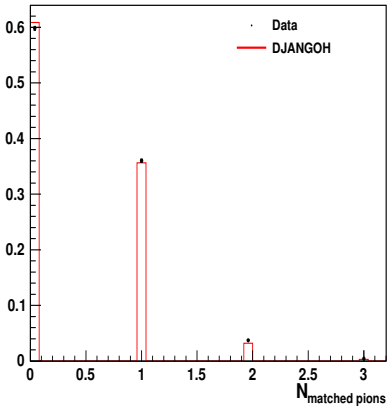

Figure 8.26: Number of tracks in the FTD associated with a single pion candidate in the central tracking detector.

8.3 Forward and Combined Tracks on μODS

After the forward and combined track finding efficiency was studied and the corresponding systematic uncertainty is derived, these tracks can be added to the HFS on μODS, where the double counting of the tracks is resolved by a track's type preferences, see beginning of chapter 8. To judge about the possibility to include these tracks into the analysis, migration effects in each bin of the final measurement, represented by the bin purity, have to be studied. The MC efficiency downgrading which was performed in previous section decreases the purity for forward and combined tracks. In the forward direction the migration effect is expected to be larger compared to the central region due to the worse momentum resolution. In section 9.2 a detailed study of the migration effects is presented, where it is shown that only combined tracks can be considered in the present analysis. Due to this reason in present section only control plots for combined tracks are presented, but not for forward tracks.

Figure 8.27 shows the control distributions for combined tracks for the transverse momentum, pseudorapidity, polar and azimuthal angles. The MC distribution of the polar angle is slightly shifted in the forward direction with respect to the data. The φ distribution shows positive/negative asymmetry, because of the dead regions of the detector. To obtain a weight for MC, which fits it to the data, a combined sample of central and combined tracks has to be reweighted. The reweighting is performed in η and p_T. The resulting distributions of central and combined tracks are shown in figure 8.28. Obtained weights are also applied on the generated level.

In section 8.1 the multiplicity distribution of central tracks was discussed (figure 8.3). The inclusion of combined tracks will slightly change this distribution. In figure 8.29 number of central and combined tracks in the event is shown after the same reweighting was applied as for central tracks only. As seen from the plots, the MCs describe the data within 10%.

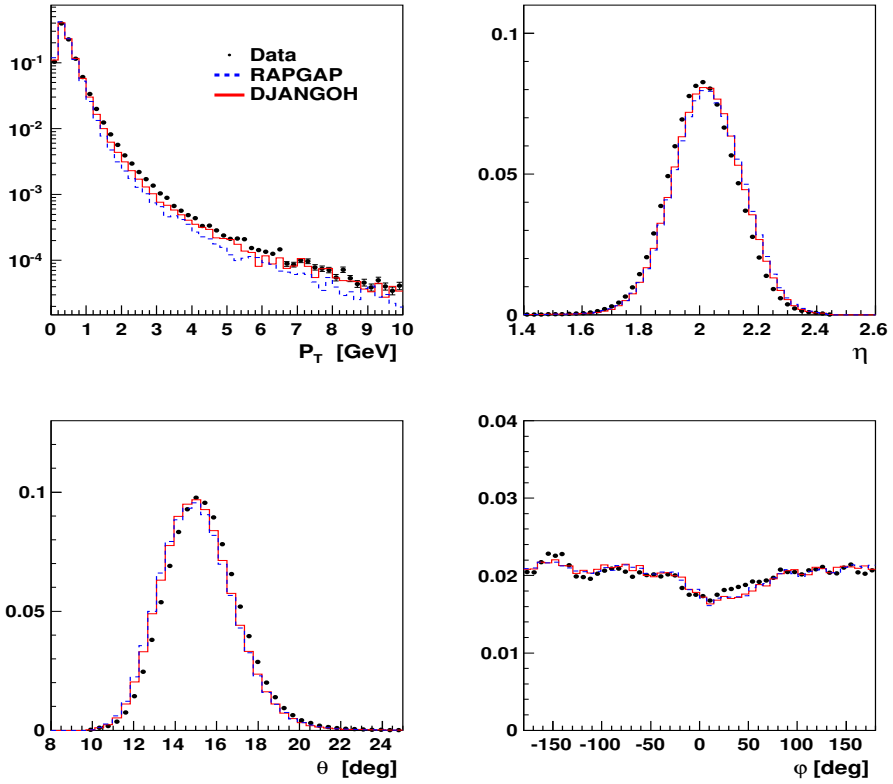

Figure 8.27: Distributions of the transverse momentum (p_T), the pseudorapidity (η), the polar angle (θ), and azimuthal angle (φ) for the combined tracks on μODS before reweighting.

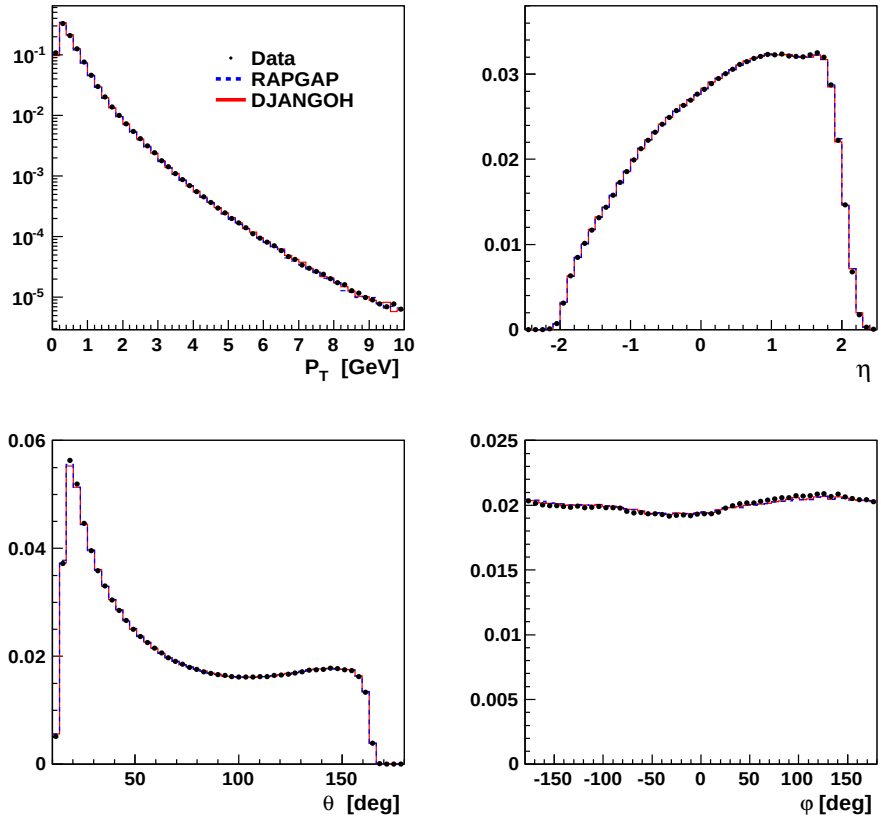

Figure 8.28: Distributions of the transverse momentum (p_T), the pseudorapidity (η), the polar angle (θ), and azimuthal angle (φ) for the combined and central tracks on μODS after the reweighting in η and p_T.

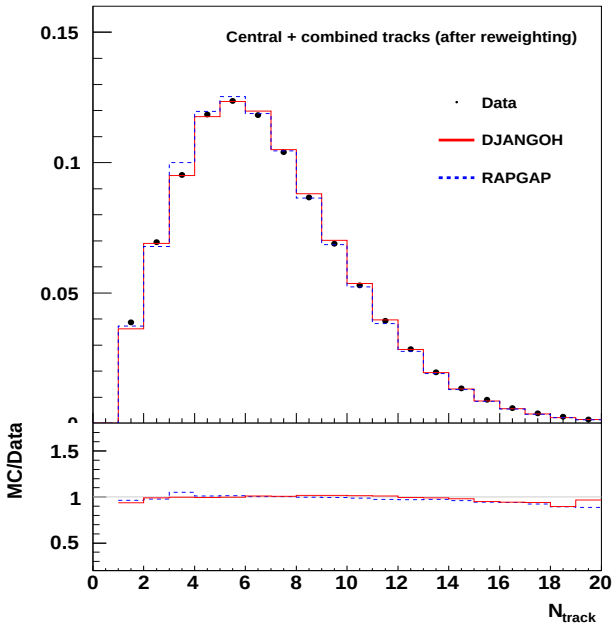

Figure 8.29: Number of central and combined tracks in the event after reweighting.

Chapter 9

Detector Effects

In previous sections the control distributions for DIS events as well as for tracking variables were presented. Good overall agreement between data and MC was achieved, and thus the models can be used to correct the data for detector acceptance, efficiency and resolution effects. To do that the detector effects must be studied in each bin of the final measurements.

In section 9.1 the observables, which are of interest for the analysis, are introduced.

In section 9.2 a detailed study of purities is presented and the effect of including forward and combined tracks is discussed.

In section 9.3 the factors used to correct for detector effects are presented.

In section 9.4 the systematic uncertainties of the measurement are presented.

9.1 Observables

The results are presented in the hadronic centre of mass system (HCM), i.e. in the photon-proton rest frame (see section 4.2). The transverse momentum and pseudorapidity of charged particles in the HCM frame are labeled as p_T^* and η^*.

The event-normalised charged particle transverse momentum and rapidity distributions are defined as:

$$D(p_T^*) = \frac{1}{N}\frac{dn}{dp_T^*}\,, \qquad D(\eta^*) = \frac{1}{N}\frac{dn}{d\eta^*}\,, \tag{9.1}$$

where N is the total number of selected DIS events and dn is the total number of charged particles with transverse momentum (pseudorapidity) in the interval dp_T^* ($d\eta^*$). Summing up all bins dp_T^* ($d\eta^*$) we obtain: $\frac{n}{N}$ - the average multiplicity of charged particles in the event.

The event-normalised transverse momentum spectra of charged particles are measured in two pseudorapidity intervals: $0 < \eta^* < 1.5$ and $1.5 < \eta^* < 4$. A two-dimensional plot of the boosted η^* vs. η of the tracks in the laboratory frame is shown in figure 9.1. In this plot central and combined tracks are included. Two horizontal lines show the regions under the investigation. A Feynman diagram with a schematic representation of these pseudorapidity regions is shown in figure 9.2.

In the region $1.5 < \eta^* < 4$, where the current fragmentation is strongly dominating, the sensitivity to the hard scattering is expected. In the range $0 < \eta^* < 1.5$,

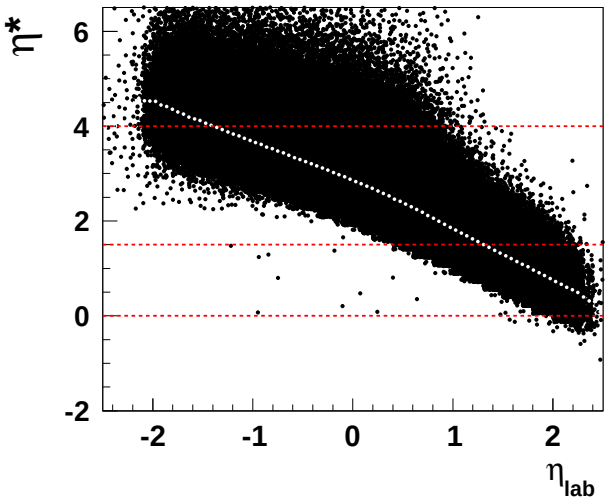

Figure 9.1: The correlation between boosted pseudorapidity, η^*, and the pseudorapidity in the laboratory frame η_{lab}. The white line indicates the mean of the two-dimensional distribution.

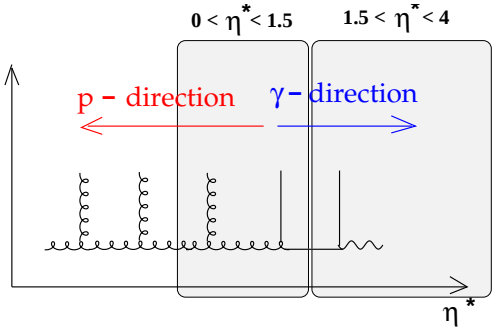

Figure 9.2: Schematic representation of the two measured pseudorapidity regions, $0 < \eta^* < 1.5$ and $1.5 < \eta^* < 4$.

where the target fragmentation is also playing a role, the sensitivity to the parton shower might be studied.

As seen from figure 9.1, the interval of $1.5 < \eta^* < 4$ covers mostly the central region of the detector and is called the "central region". The interval $0 < \eta^* < 1.5$ partly covers the forward region and is referred to as "forward region".

In addition, the transverse momentum spectra and pseudorapidity distributions are measured in different x and Q^2 bins. The binning of the phase space is shown in figure 9.3 and the bin sizes are indicated on the plots and in table 9.1. The binning was chosen to have approximately the same number of events in each bin.

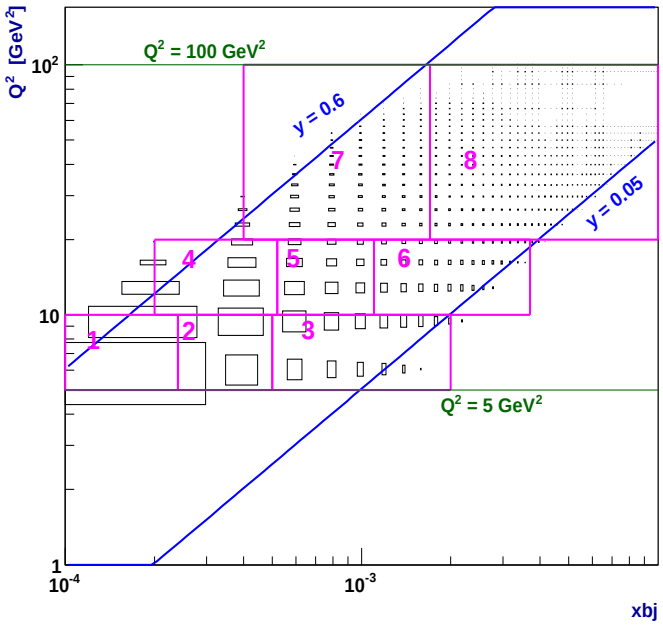

Figure 9.3: The binning of the phase space in the (x, Q^2)-plane covered in the analysis.

Kin. bin	$x/10^{-3}$	Q^2 / GeV^2
0	0.10 - 10.0	5-100
1	0.10 - 0.24	5-10
2	0.24 - 0.50	5-10
3	0.50 - 2.00	5-10
4	0.20 - 0.52	10-20
5	0.52 - 1.10	10-20
6	1.10 - 3.70	10-20
7	0.40 - 1.70	20-100
8	1.70 - 10.0	20-100

Table 9.1: The kinematic bins.

9.2 Purity

The purity is a variable used to study effects of migration between individual bins of the measurement. Let us consider some kinematic variable in a fixed bin and let N_{rec} and $N_{\text{gen}\wedge\text{rec}}$ be the numbers of the MC events reconstructed and both generated and reconstructed in this bin, respectively. Here, the stable generated level is considered. "Stable" means all particles with an average proper lifetime $c\tau$ larger than 10 mm. The purity (P) is defined as

$$P = \frac{N_{\text{gen}\wedge\text{rec}}}{N_{\text{rec}}} , \tag{9.2}$$

and shows the fraction of the events both generated and reconstructed in the bin with respect to the total number of events reconstructed in this bin. For example, a purity of 80% means that 80% of the events measured in the bin on the detector level are also found in that same bin on the generated level, and 20% of the events have migrated into that bin from other generated level bins. Such migrations might originate from the following sources:

- migrations from outside the phase space N_a;
- migration from neighbouring bins to a given bin N_b;
- other migration from inside the phase space N_c.

The purity might be rewritten explicitly showing these contributions:

$$P = \frac{N_{\text{gen}\wedge\text{rec}}}{N_{\text{gen}\wedge\text{rec}} + N_a + N_b + N_c} , \tag{9.3}$$

For the bin-by-bin correction method to be applicable, the purity should be high, otherwise the method would not deliver a reliable result and may introduce large biases, in which case a full unfolding procedure should be performed. As discussed in [130] the "simple" bin-by-bin method has a sizable bias to the input MC distribution, particularly if migrations from outside the analysis phase space are large. An "improved" bin-by-bin method, where the migrations from outside of the phase-space are subtracted, was introduced in [130].

A modified purity (inside the analysis phase-space) is defined as:

$$\tilde{P} = \frac{N_{\text{gen}\wedge\text{rec}}}{N_{\text{gen}\wedge\text{rec}} + N_b + N_c} , \tag{9.4}$$

The way the "improved" bin-by-bin method modifies the correction factor calculations and the statistical errors treatment is discussed in the next section. The "improved" bin-by-bin correction procedure still suffers from biases, but these can be controlled by tuning bin sizes such that purities inside the analysis phase-space are high. By H1 convention, the bin-by-bin method might be used for modified purity (further on referred to as purity) larger than 0.8.

The purities for the p_T^* spectra in the interval of $0 < \eta^* < 1.5$ for the whole analysis phase space and in the different (x, Q^2)-bins are presented in figures 9.4 and 9.5, respectively. Since in the $0 < \eta^* < 1.5$ pseudorapidity region a contribution from central and forward tracks is expected (see figure 9.1), the purities are shown separately for the central, combined and forward tracks as well as for their combinations: central and combined tracks (in the plots labelled as 'C and K tracks'); central, combined and forward tracks (in the plots labelled as 'C,K and tracks'). One should remind that the selection of the best track hypothesis for a selected track is considered to avoid double counting (see beginning of chapter 8). Therefore in case 'C,K and tracks' central tracks are taken in preference to combined and forward tracks and combined tracks are taken in preference to forward tracks. Shown distributions were obtained using the DJANGOH MC. As seen from the plots the forward tracks have purity lower than 0.4 almost in all p_T^* bins, and the combined track purity is varying between 0.55 and 0.75. The purity of the combination of central tracks

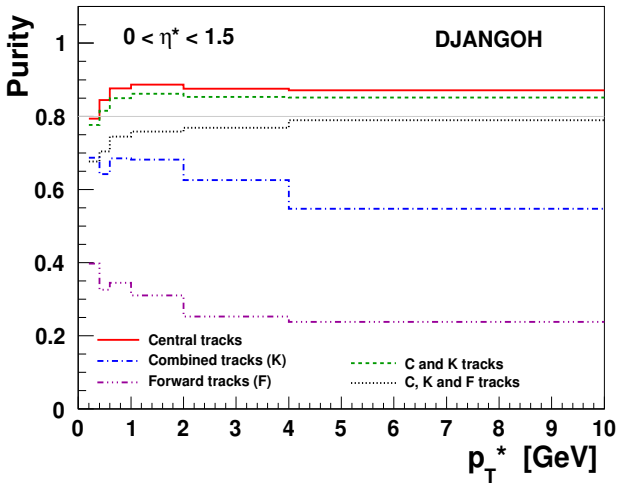

Figure 9.4: Purity as a function of the p_T^* in $0 < \eta^* < 1.5$ range.

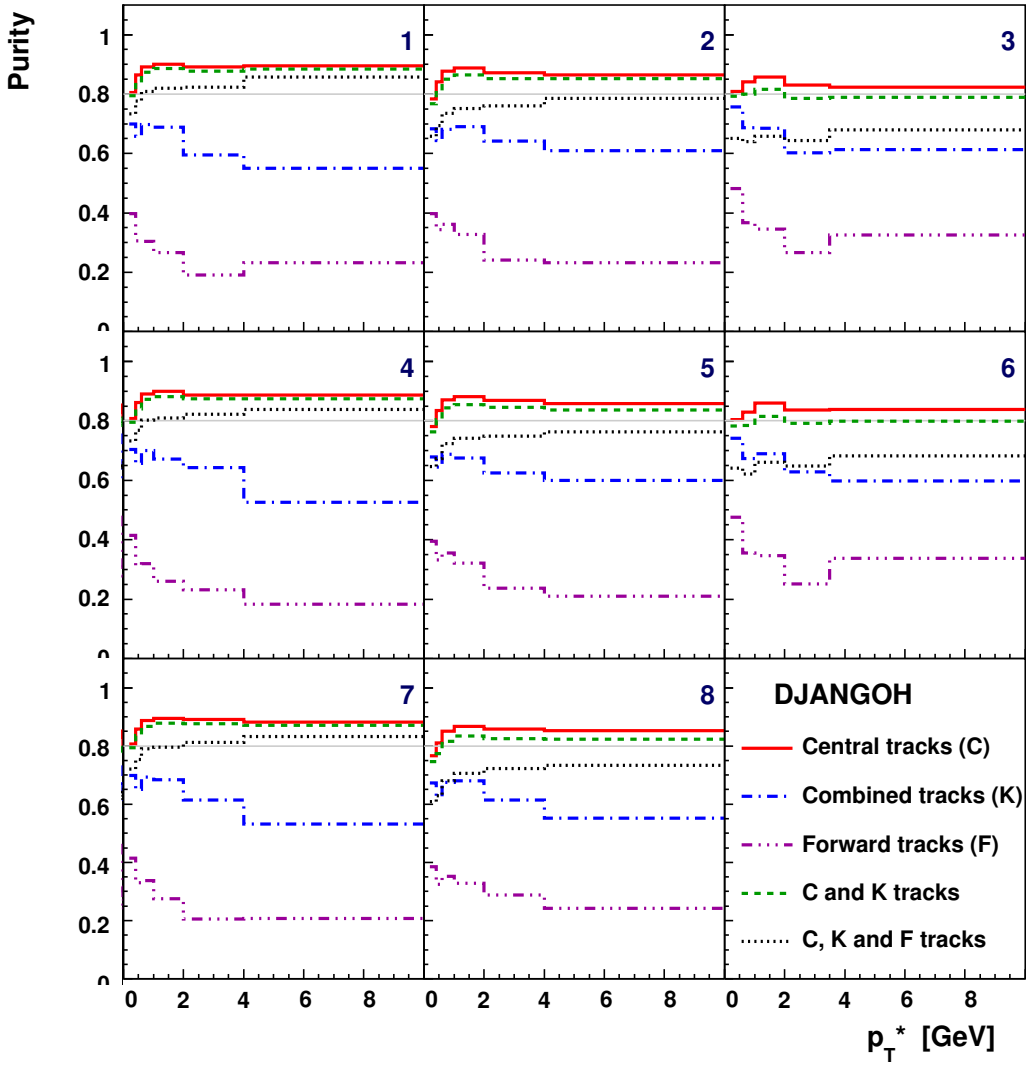

Figure 9.5: Purity as a function of the p_T^* in $0 < \eta^* < 1.5$ range for eight different (x, Q^2)-bins.

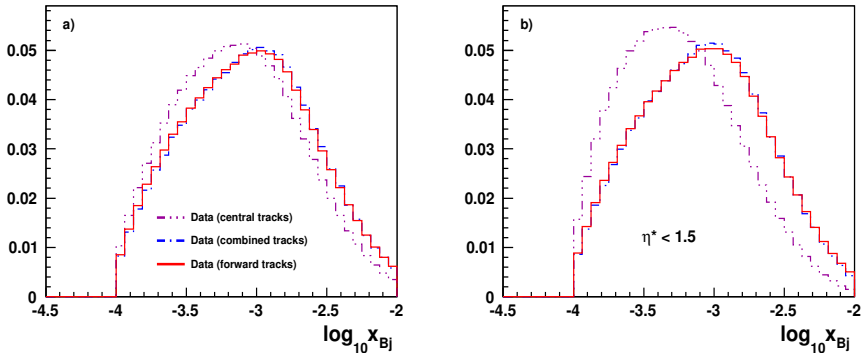

Figure 9.6: The distribution of x for the central, combined and forward tracks.

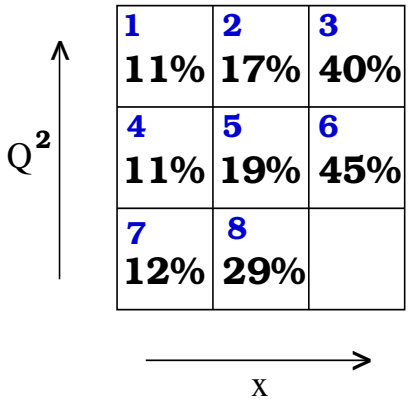

Figure 9.7: Contribution of the combined tracks in each (x, Q^2)-bins for the p_T^* spectra in the region $0 < \eta^* < 1.5$ (see figure 9.5).

with combined ones or with the combined and forward tracks shows the possibility of including these tracks in the measurements. If it is below 0.8 and no reasonable rebinning can improve it, then we can not include these tracks in the measurements. The p_T^* bin size in figures 9.4 and 9.5 was adjusted for the C+K sample to guarantee purity to be higher than 0.8 in all p_T^* bins and in all eight (x, Q^2)-intervals. A different p_T^* binning is used for the different (x, Q^2)-bins.

To see which value of x forward and combined tracks prefer, the x distribution of these tracks together with central ones is shown in figure 9.6. In figure 9.6 (b) tracks are required to have $\eta^* < 1.5$. As seen from the plot, the forward and combined tracks prefer larger x value, thus in the (x, Q^2)-bins with larger x values, as bin 3 and 6 (the bin number is indicated in the top right corner in figure 9.5), the contribution of the forward tracks is maximal, and in order to achieve the purity larger than 0.8 even wider binnings have to be chosen. In particular, this means that for bins $2, 3, 5, 6, 8$ only two to three bins in p_T^* might be obtained. For the low-x bins $1, 4$ and 7 the contribution of the forward tracks is not so high and the purity is not not affected much by including forward or combined tracks. Based on these studies it was decided not to include forward tracks in the p_T^* distributions. The combined tracks are successfully included in the analysis and their statistical contribution (in percent) in each (x, Q^2)-bin of figure 9.5 is illustrated in figure 9.7.

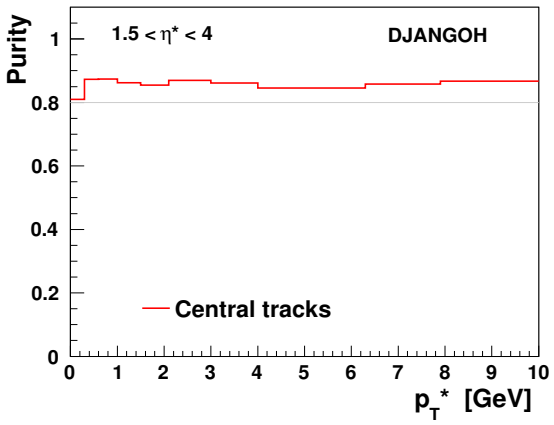

Figure 9.8: Purity as a function of the central track p_T^* in $1.5 < \eta^* < 4$ range.

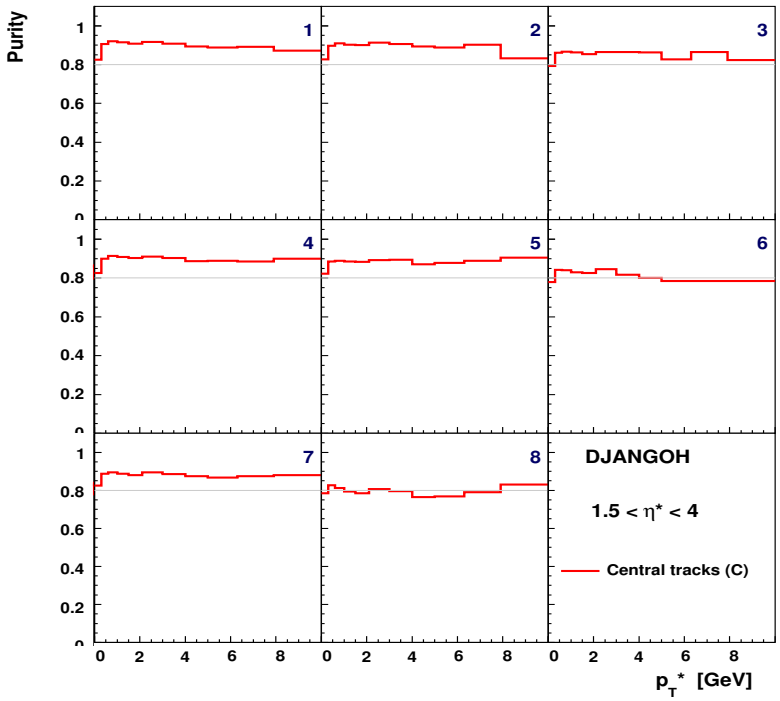

Figure 9.9: Purity as a function of p_T^* in $1.5 < \eta^* < 4$ range.

Figures 9.8 and 9.9 show the purity as a function of p_T^* in the $1.5 < \eta^* < 4$ region, for the whole analysis phase space and in the different (x, Q^2)-bins, respectively. Here, only central tracks are shown, since they are strongly dominant in that region, see figure 9.1.

A more narrow binning in p_T^* was used compare to the forward region, due to the better resolution. Purity is above 0.8 almost in all bins. Despite the fact that in some p_T^* bins it achieves only 0.75, those bins were still accepted.

Figure 9.10 shows the purity as a function of η^* for $p_T^* < 1$ GeV. In the HCM frame the proton direction points to the left, so forward and combined tracks are found for $\eta^* \lesssim 2$. The contributions of central, combined and forward tracks are shown separately in figure 9.10. A rather wide binning was used to guarantee purities of about 0.8 for the central tracks. The acceptable (high purity) region for the final

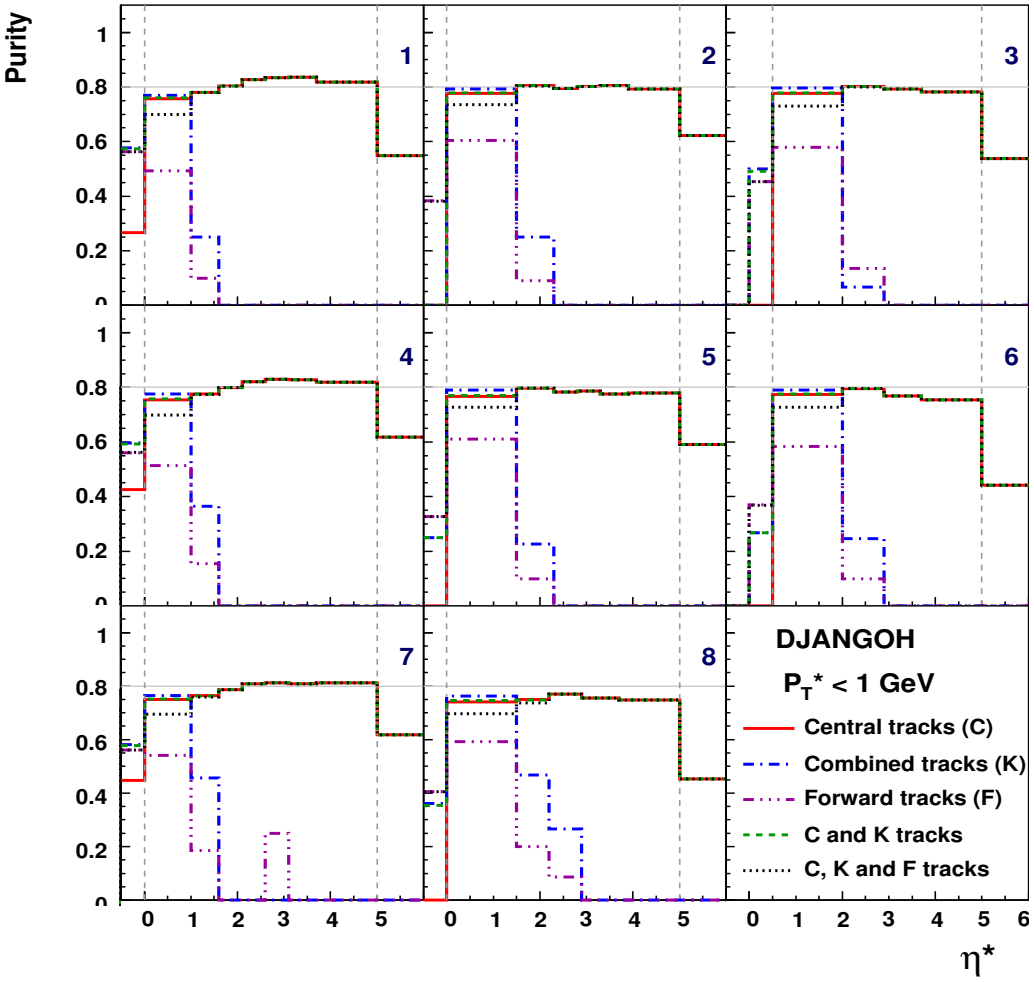

Figure 9.10: Purity as a function of charged particle η^* for $p_T^* < 1$ GeV.

measurements is shown with two dashed vertical lines. As seen from the plots, in the region $0 < \eta^* < 1$ purities for the central and combined tracks are similar. For the more forward region, $-0.5 < \eta^* < 0$, central tracks almost do not contribute, but purities of the combined and forward tracks are too low to include this region in the analysis. Including the forward tracks for the $\eta^* > 0$ region will need an even wider binning, which will lead to a decrease of the forward track fraction in such wide bins due to the strong dominance of the central tracks. Due to that reason the forward tracks are also not included in the η^* distribution.

Figure 9.11 shows the purity as a function of η^* for particles with transverse momentum, $p_T^* > 1$ GeV. A narrow binning was used due to higher purity compared to the soft p_T^* sample.

The purity as a function of η^* for $p_T^* < 1$ GeV and $p_T^* > 1$ GeV for the whole analysis phase space is shown in figure 9.12. Only the final combination of central and combined tracks is shown.

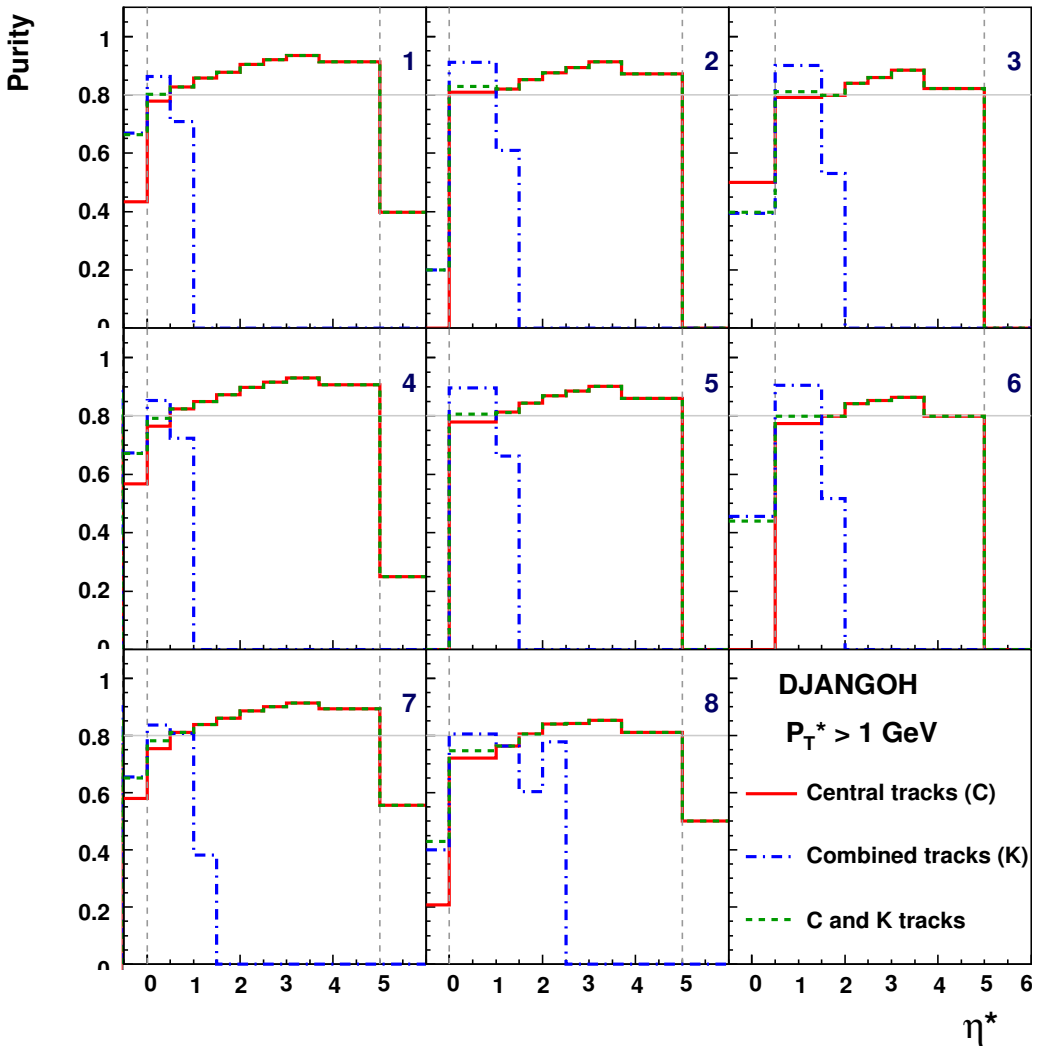

Figure 9.11: Purity as a function of charged particle η^* for $p_T^* > 1$ GeV.

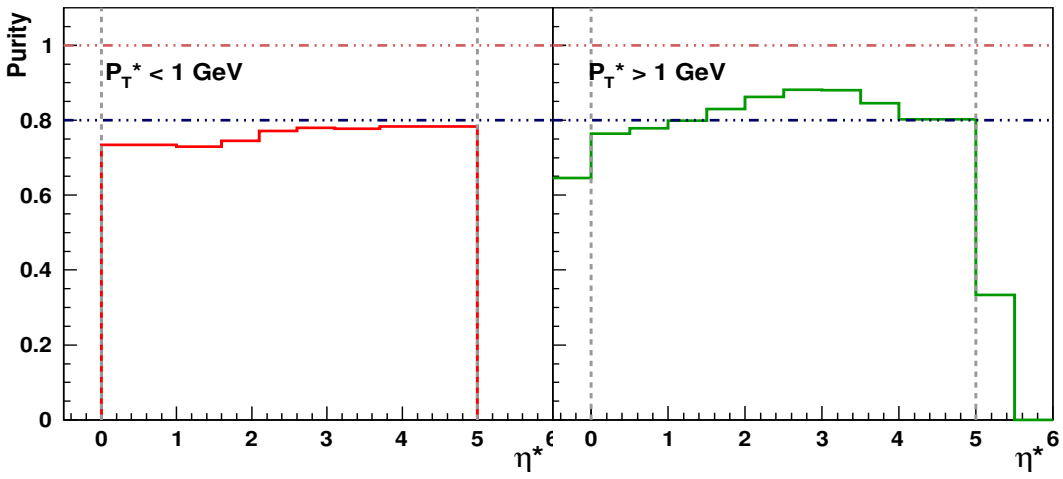

Figure 9.12: Purity as a function of charged particle η^*.

9.3 Correction Factors

High purities in each bin of the measurements allow to use the bin-by-bin method to correct the data. The correction factors, c_i, are used to correct the data from the reconstructed level to the stable non-radiative generated level. "Stable" means that all the particles with an average proper lifetime $c\tau$ larger than 10 mm are considered as stable (K^0_S, Λ, $\Sigma^{\pm}$, Ξ^-, Ξ^0, Ω^-), since most of them will not decay before reaching the detector. "Non-radiative" means that the effects of QED radiation are corrected for.

The correction factor, c_i, for bin i for a particular distribution is given by:

$$c_i = \frac{D_{\text{nonrad gen},i}}{D_{\text{rec},i}} \ ,$$

where $D_{\text{nonrad gen},i}$ is the observable defined in equation 9.1 on the stable non-radiative generated level, and $D_{\text{rec},i}$ is the same observable in the same bin i but on reconstructed level. Thus, the final event-normalised measurements have to be multiplied bin-by-bin by these corrections:

$$\left(\frac{n_i}{N}\right)^{data} \quad \rightarrow \quad \left(\frac{n_i}{N}\right)^{data} \cdot c_i \ , \tag{9.5}$$

where n_i is a number of charged particles observed in bin i and N is the number of DIS events fulfilling the analysis selection criteria. The statistical uncertainty in each bin of the measurement is calculated as:

$$\delta_{i,\text{stat}} = \frac{\sqrt{n_i}}{N} \cdot c_i \ , \tag{9.6}$$

As discussed in the previous section the "improved" bin-by-bin method was introduced to subtract the migrations from outside the analysis phase space using simulations and thus to reduce the bias to the input MC distribution. This leads to a modification of (9.5):

$$\left(\frac{n_i - n_i^{out}}{N}\right)^{data} \cdot c'_i = \left(\frac{n_i - n_i^{out}}{N}\right)^{data} \cdot \frac{n_{\text{nonrad gen},i}}{n_{\text{rec},i} - n^{\text{out}}_{\text{rec},i}} \cdot \frac{N_{rec}}{N_{\text{nonrad gen},i}},$$

where n_i^{out} is number of charged particles from outside the analysis phase space. This expression is equal to expression (9.5), since the fraction of the samples is subtracted for the data is the same as for MC on reconstructed level:

$$\left(\frac{n_i^{out}}{n_i}\right)^{data} = \frac{n^{\text{out}}_{\text{rec},i}}{n_{\text{rec},i}}. \tag{9.7}$$

Assuming the relative statistical error on n_i^{out} is small compared to that on n_i the the statistical error in each bin of the measurement is recalculated as:

$$\delta^{\text{improved}}_{i,\text{stat}} = \frac{\sqrt{n_i}}{N} \cdot c'_i \ , \tag{9.8}$$

Thus the "improved" bin-by-bin method increases the statistical uncertainty in bin i by a factor:

$$\frac{c_i}{c'_i} = \frac{n_{\text{rec},i} - n^{\text{out}}_i}{n_{\text{rec},i}}. \tag{9.9}$$

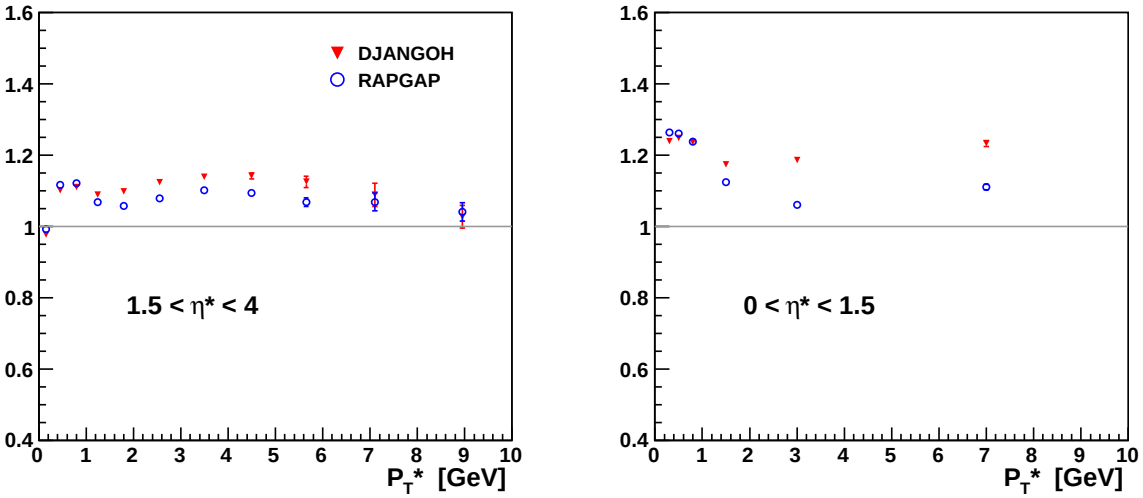

Figure 9.13: Correction factor as a function of p_T^*

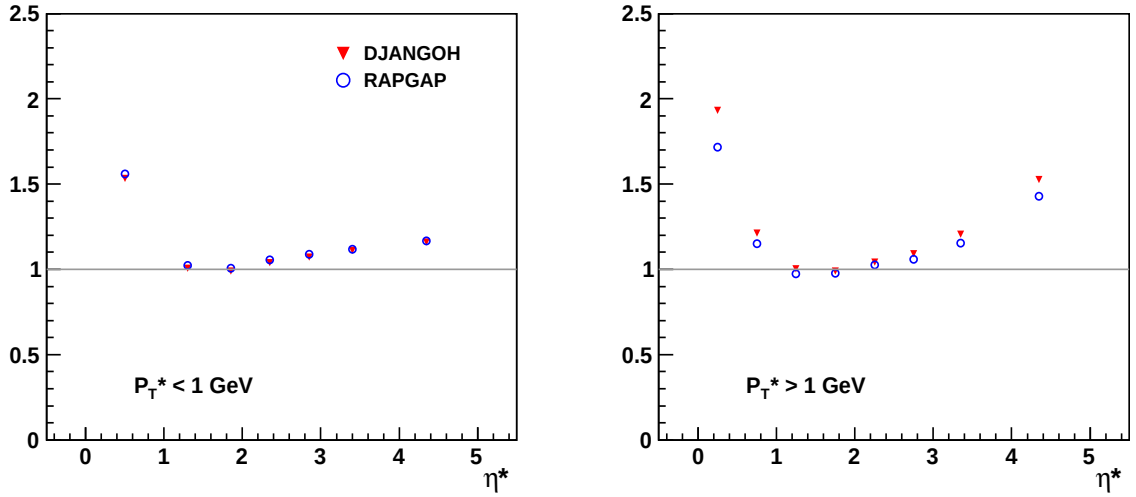

Figure 9.14: Correction factor as a function of η^*

The correction factors for the transverse momentum distributions of charged particles in the two pseudorapidity intervals $0 < \eta^* < 1.5$ and $1.5 < \eta^* < 4$ are shown in figure 9.13. The correction factors for rapidity distributions in case of soft, $p_T^* < 1$ GeV, and hard, $p_T^* > 1$ GeV, particles are shown in figure 9.14 separately for DJANGOH and RAPGAP.

The value of correction factors strongly depends on η^* and less on p_T^*. In the central region it is never larger than 1.5 or smaller than 0.95, where the largest values are seen at high p_T^* and large η^*. For the forward region it reaches a value of 2 at high p_T^* mostly due to limited detector acceptance in that region.

A model dependence of the correction factors is observed at larger p_T^*. In general both models (DJANGOH and RAPGAP) agree within few percent, but the difference rises up to 7% in the forward region.

9.4 Systematic Uncertainties

The following sources of systematic uncertainties are considered for all measured quantities.

- The systematic uncertainty on the SpaCal energy scale is $\pm 1\%$. In order to estimate the dependence of the measurements on this uncertainty, the energy scale was changed within these limits and the influence on the final measurements was calculated using DJANGOH. This results in an average systematic uncertainty of 0.4%

- The angular resolution of the SpaCal of 1 mrad leading to a systematic uncertainty of about 0.1%.

- The hadronic energy scale uncertainty is known to a precision of 2%. Apart from phase space calculations, which depend on $E - P_z$ of hadronic final state, it affects the boost to HCM frame calculation. This leads to an effect on the measurements of about 0.3%.

- The systematic uncertainty arising from the model dependence of the data correction is obtained as the arithmetic mean value of the correction factors calculated using RAPGAP and DJANGOH:

$$\Delta_{\text{model}} = \frac{1}{2}\left(c^{\text{Rapgap}} - c^{\text{Djangoh}}\right).$$

  The average resulting uncertainty on the measurements is about 1.7% (it varies between 0.01% to 5%).

- The systematic uncertainty associated with the track reconstruction efficiency is estimated to be 1% [131] for the central tracks and 10% for the combined tracks assumed to be constant over the p_T and θ range of the tracks. This results in uncertainties of typically 1.6%.

  As was shown in subsection 8.2.1 the efficiency of the combined tracks was checked using all selected central tracks as well as using pions from K^0_S decay as a function of the transverse momentum and pseudorapidity. Consistent results were obtained from both samples showing agreement of data and MC within 10%.

The total systematic uncertainty is of the order of 2.4%. The resulting average systematic uncertainty for different measured observables is shown in table 9.2.

Source of the errors	$\frac{1}{N}\frac{dn}{dp_T^*}$ cen	$\frac{1}{N}\frac{dn}{dp_T^*}$ fwd	$\frac{1}{N}\frac{dn}{d\eta^*}$ soft	$\frac{1}{N}\frac{dn}{d\eta^*}$ hard
Model dependence	1.2 %	2.3 %	1.1 %	1.9 %
Hadronic energy scale ($\pm$ 2 %)	0.4 %	0.2 %	0.2 %	0.3 %
SPACAL em energy scale ($\pm$ 1 %)	0.5 %	0.2 %	0.3 %	0.4 %
Scat. positron angle ($\pm$ 1 mrad)	0.1 %	0.1 %	0.1 %	0.1 %
Tracking (1 % (cen);10 % (comb))	1.0 %	1.4 %	2.0 %	1.8 %
Total error	1.7 %	2.7 %	2.5 %	2.4 %

Table 9.2: The source of the systematic uncertainties and their impacts on the following measured observables: dp_T^* spectra in $1.5 < \eta^* < 4$ range (labelled in the table as "$\frac{1}{N}\frac{dn}{dp_T^*}$ cen"), dp_T^* spectra in $0 < \eta^* < 1.5$ range (labelled as "$\frac{1}{N}\frac{dn}{dp_T^*}$ fwd"), η^* spectra for the charged particles with $p_T^* < 1$ GeV (labelled as "$\frac{1}{N}\frac{dn}{d\eta^*}$ soft") and η^* spectra for the charged particles with $p_T^* > 1$ GeV (labelled as "$\frac{1}{N}\frac{dn}{d\eta^*}$ hard").

Chapter 10

Results

The measurements of the charged particle transverse momentum and the pseudorapidity distributions, introduced in section 9.1, are presented. The results are shown in figures 10.1 to 10.22.

10.1 Transverse Momentum Distribution of Charged Particles

In figure 10.1 the p_T^* spectra are shown for two different eta ranges. The shape of the measured p_T^* distribution in the two pseudorapidity ranges is very similar. The spectrum falls over more than four orders of magnitude from $p_T^* < 1$ GeV to $p_T^* \simeq 8$ GeV. The statistical and systematic uncertainties are added in quadrature and shown in the figures. Since the uncertainties are small, they are only visible in the ratio plots.

The measurements are compared to various Monte Carlo generators using different approaches to simulate the parton cascade and the hadronisation process. In figure 10.1 the measured p_T^* spectra in the two pseudorapidity intervals are compared to the DGLAP-based model Rapgap, to the CDM model Djangoh and CCFM model Cascade. The DGLAP-based model undershoots the data at high p_T^* and predicts a much softer spectrum compared to the other models. Comparing the predictions in the two pseudorapidity intervals, the strongest deviation of the DGLAP model from the data is observed in the forward region, $0 < \eta^* < 1.5$. Djangoh performs best among the models and provides an acceptable description of the data in both pseudorapidity intervals. In contrast, Cascade is above the data for almost the whole p_T^* range.

In figure 10.2 the measured p_T^* spectra are compared to the Herwig++ and Sherpa predictions. The Herwig++ with POWHEG correction is labelled in all plots as 'Herwig (Powheg)'. The Herwig++ with a matrix element correction based on the approach of [132] is labelled in all plots as 'Herwig'. Sherpa predictions were obtained using both cluster and Lund string model for the hadronisation. At soft p_T^* all models, except the Sherpa (Lund), are above the data and at high p_T^* all models are below the data. This is a case for both forward and central regions. It worth to mention, that Sherpa does not describe the measured F_2 [133], this might affect the description of presented in this thesis data. In addition, both Herwig++

and SHERPA (cluster) do not describe the charged particle multiplicity.

In figures 10.3 and 10.4 the transverse momentum spectra are shown for eight different x and Q^2 bins, in the forward region with a linear and logarithmic scale of the x-axis, respectively. In figure 10.5 the p_T^* spectra are shown for eight different x and Q^2 bins in the central region. The bin sizes are indicated on the plots. For the central region the virtuality Q^2 influences the hardness of the p_T^* spectrum, where it is the relevant scale, while there is little influence in the forward region. For easy comparison the ratios of the MC predictions over the data are shown in figures 10.6 and 10.7. The strongest deviation of the DGLAP model RAPGAP from the data is observed in the forward region and in the lowest x and Q^2 bin. The description becomes better at larger values of x and Q^2. The same trend is observed for the central region, but here the data description is better. The CDM provides a reasonable description of the data over the full kinematic range for both pseudorapidity regions, except in the lowest x and Q^2 bin for the high p_T^* tail, where the prediction is above the data. CASCADE describes the data in the lowest x and Q^2 bin and high p_T^* but has too hard spectrum at high x and Q^2.

In figures 10.8 and 10.9 the measurements are compared to the Herwig++ and SHERPA predictions in the forward and central regions, respectively. The ratio of the Herwig++ and SHERPA predictions over the data are shown in figure 10.10 for the forward and in figure 10.11 for the central region. In the forward region at lowest x and Q^2 bin all models are different from each other and the best description of the data is achieved by SHERPA (cluster), which however does not describe the data. At higher values of x and Q^2 the description of the data is better for all models. In the central region at lowest x and Q^2 bin and high p_T^* all models are below the data. At higher x and Q^2 Herwig++ provides reasonable description of the data. Comparing these results with predictions of earlier discussed RAPGAP, CASCADE and DJANGOH models, one can conclude that for small x and Q^2 and for $p_T^* > 1$ GeV the best description of the data is achieved by DJANGOH and CASCADE, at high x and Q^2 - by DJANGOH, RAPGAP and Herwig++.

At low p_T^* the best description of the data is achieved by CDM, while RAPGAP is slightly above the data, and CASCADE, Herwig++ and SHERPA (cluster) strongly overshoot the data. SHERPA (Lund) is below the data at small x, but provides a reasonable description of the data at high x. Soft p_T^* region is expected to be mainly driven by hadronisation effects and will be discussed below.

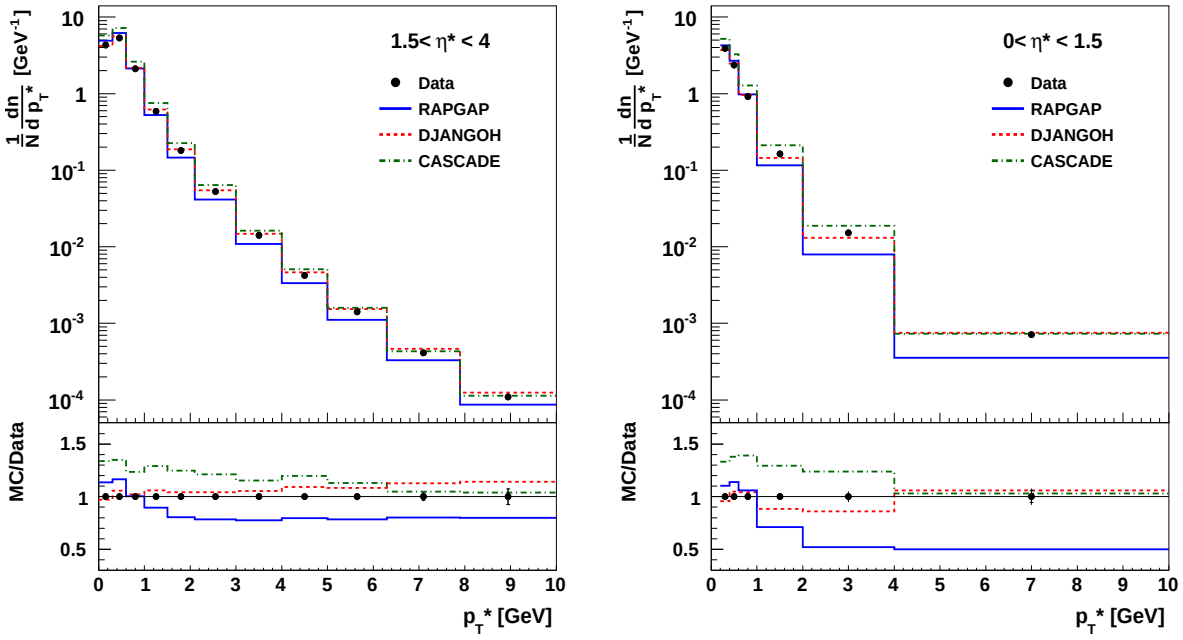

Figure 10.1: Measured p_T^* spectra of charged particles in the hadronic centre of mass system (HCM) in two pseudorapidity intervals, $1.5 < \eta^* < 4$ (left) and $0 < \eta^* < 1.5$ (right), together with RAPGAP, DJANGOH and CASCADE Monte Carlo predictions.

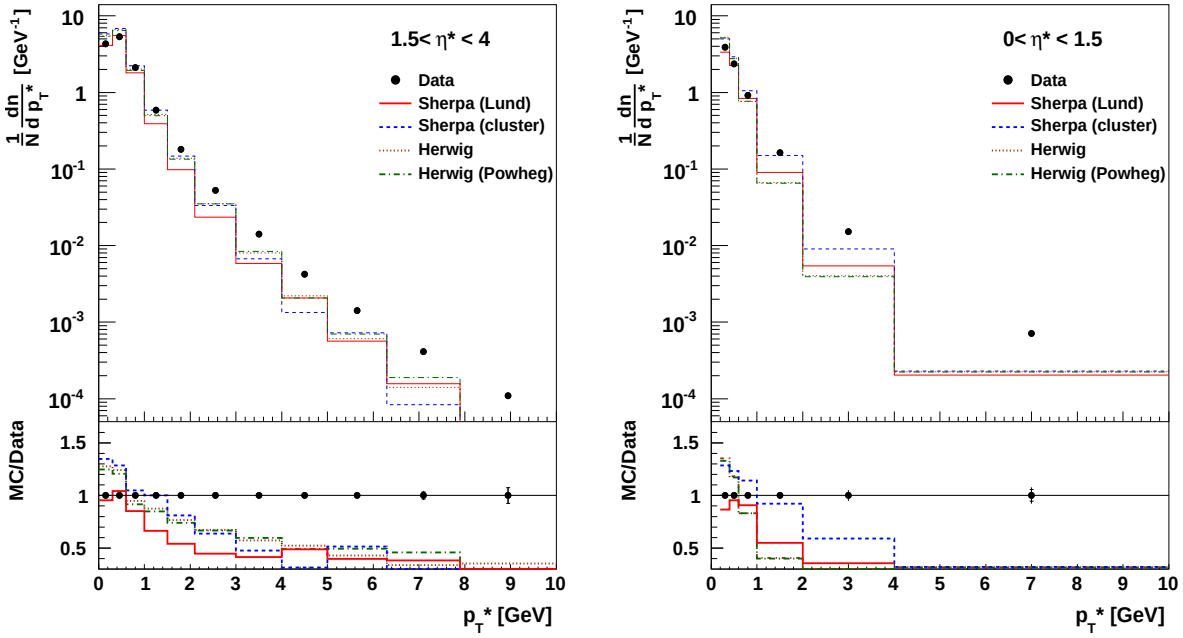

Figure 10.2: Measured p_T^* spectra of charged particles in the hadronic centre of mass system (HCM) in two pseudorapidity intervals, $1.5 < \eta^* < 4$ (left) and $0 < \eta^* < 1.5$ (right) together with Herwig++ and SHERPA Monte Carlo predictions.

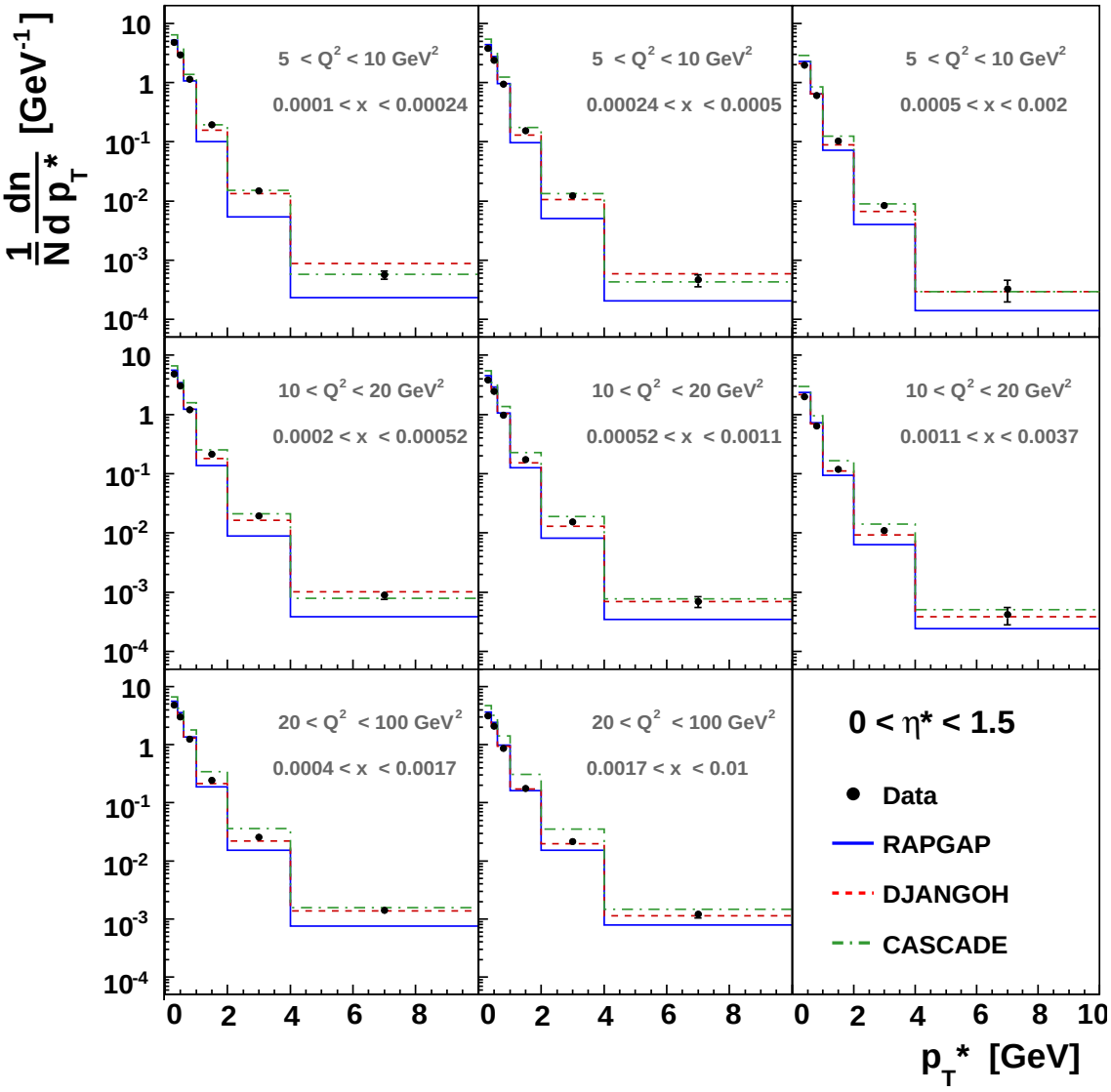

Figure 10.3: Measured p_T^* spectra of charged particles in the hadronic centre of mass system (HCM) in $0 < \eta^* < 1.5$ range for eight intervals of Q^2 and x_{Bj} together with RAPGAP, DJANGOH and CASCADE Monte Carlo predictions.

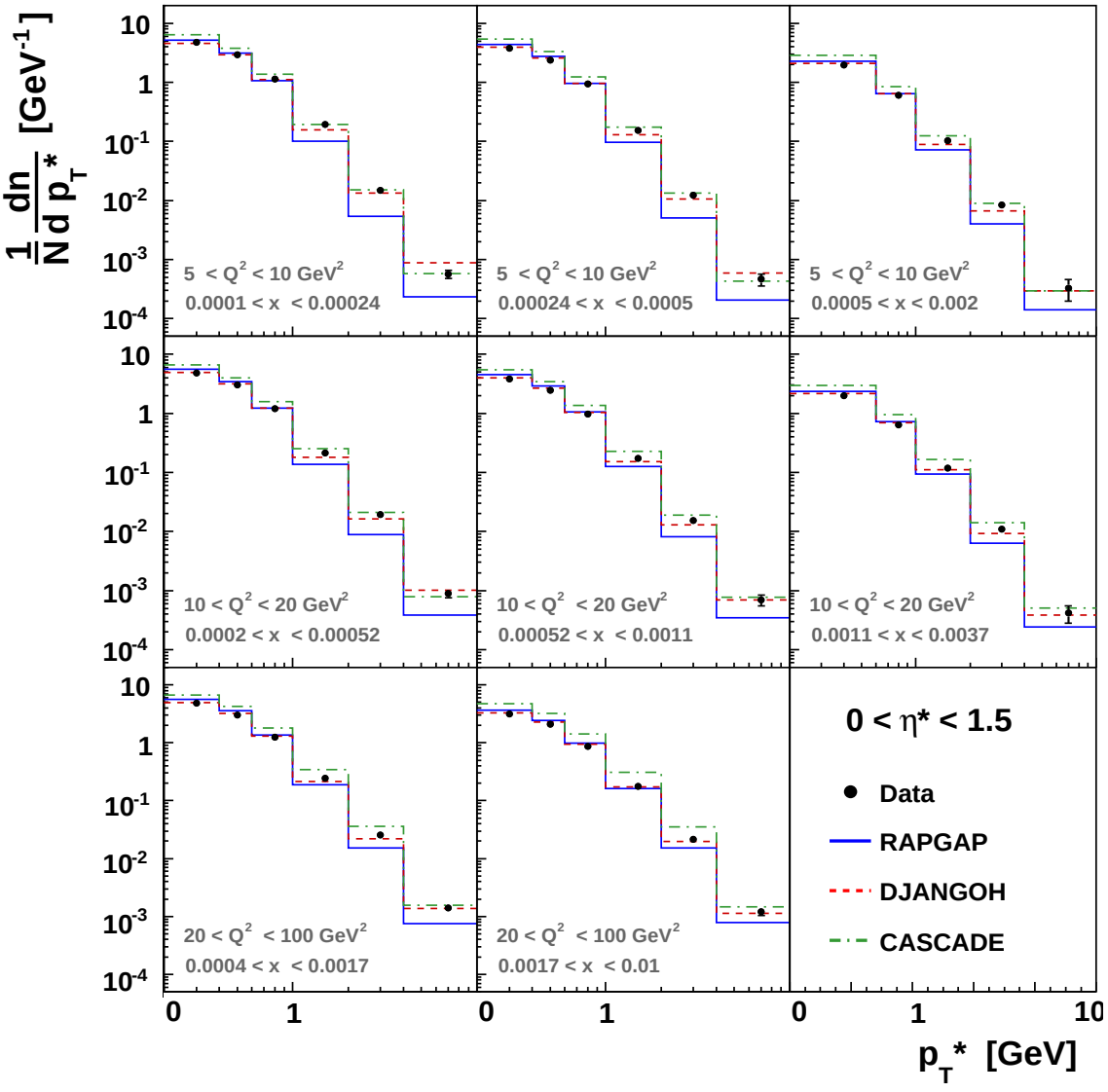

Figure 10.4: Measured p_T^* spectra of charged particles in the hadronic centre of mass system (HCM) in $0 < \eta^* < 1.5$ range for eight intervals of Q^2 and x_{Bj} together with RAPGAP, DJANGOH and CASCADE Monte Carlo predictions.

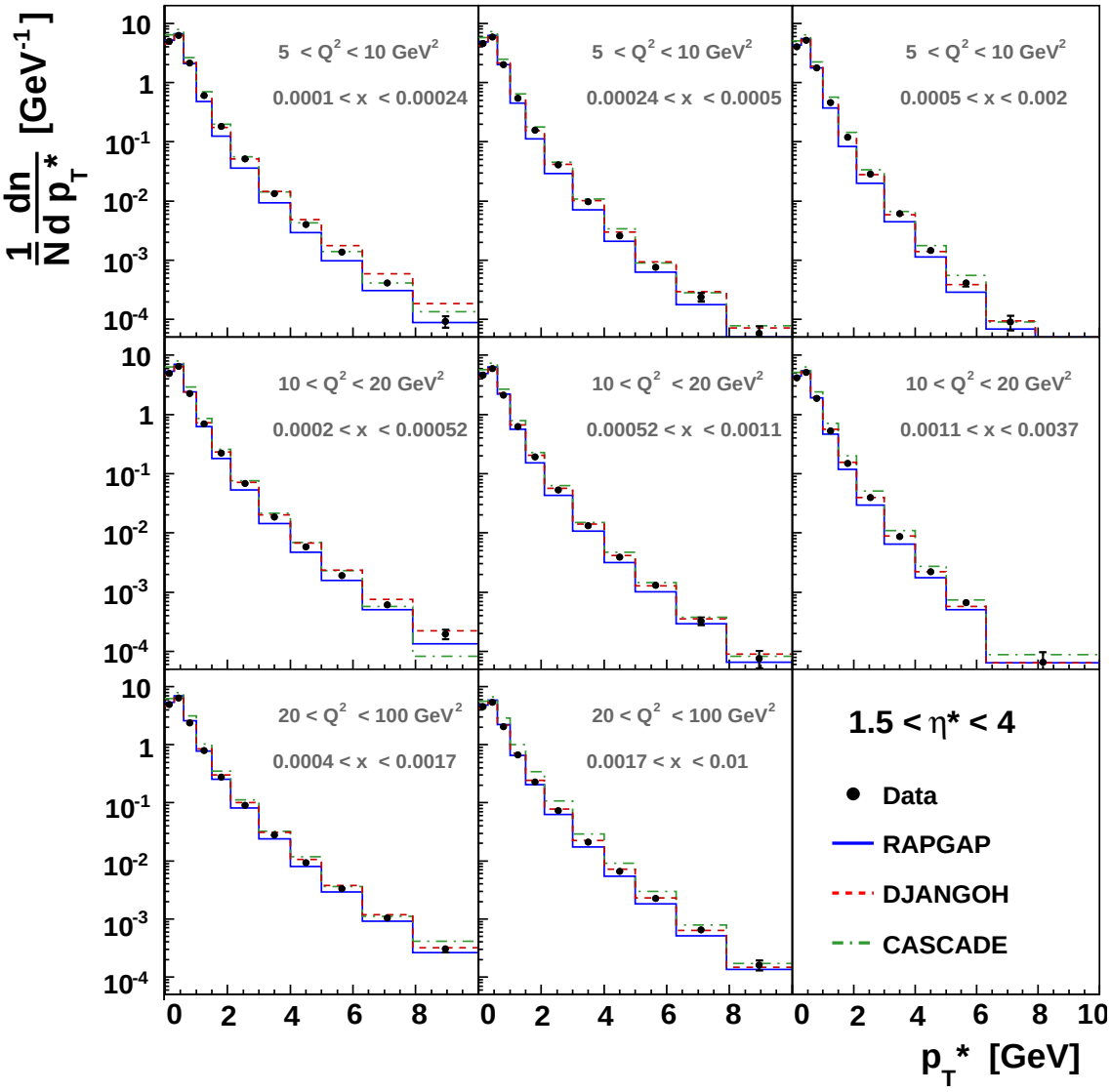

Figure 10.5: Measured p_T^* spectra of charged particles in the hadronic centre of mass system (HCM) in $1.5 < \eta^* < 4$ range for eight intervals of Q^2 and x_{Bj} together with RAPGAP, DJANGOH and CASCADE Monte Carlo predictions.

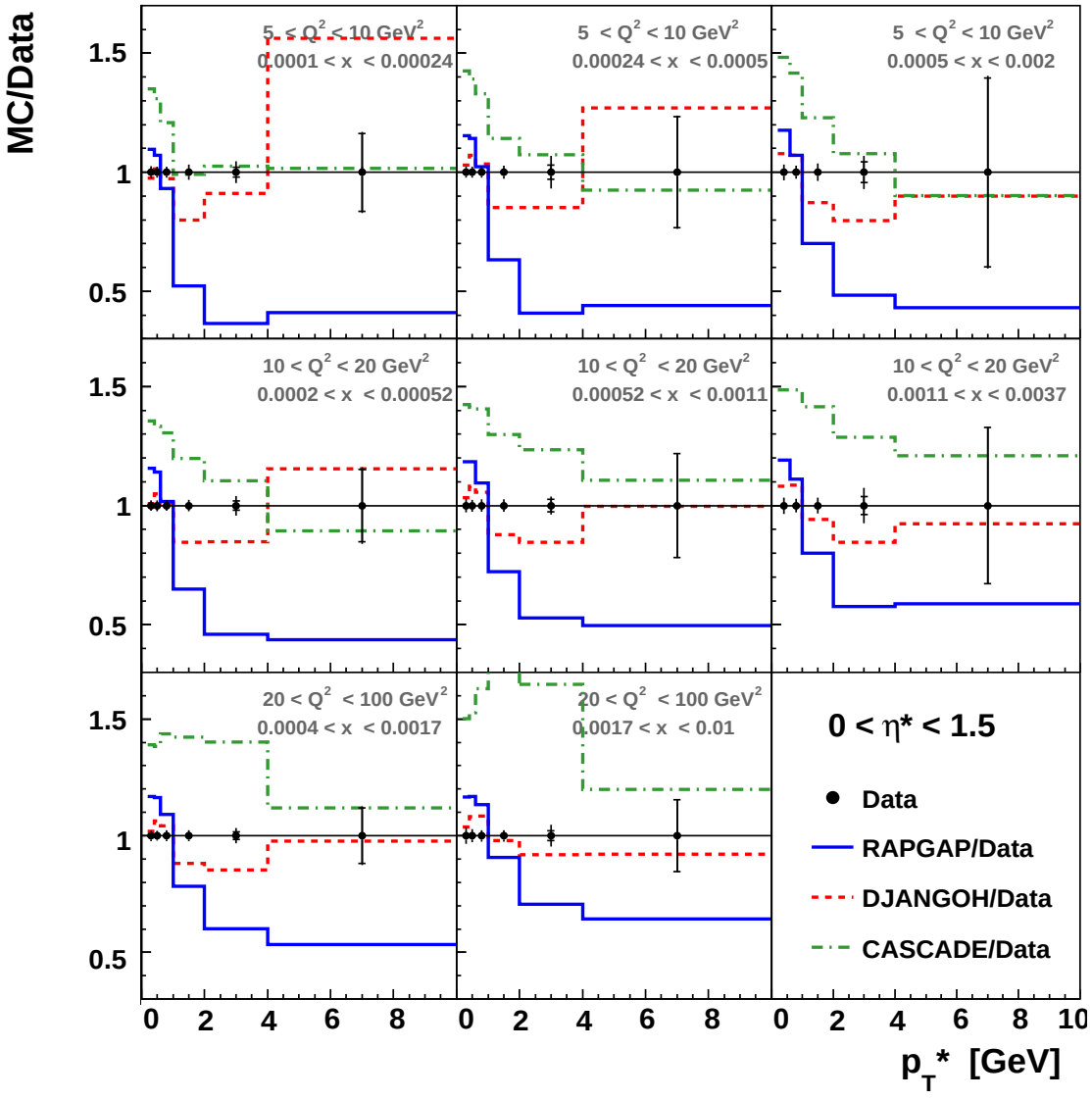

Figure 10.6: The ratios of measured over predicted by Monte Carlo p_T^* spectra of the charged particles in the hadronic centre of mass system (HCM) in $0 < \eta^* < 1.5$ range for eight intervals of Q^2 and x_{Bj}.

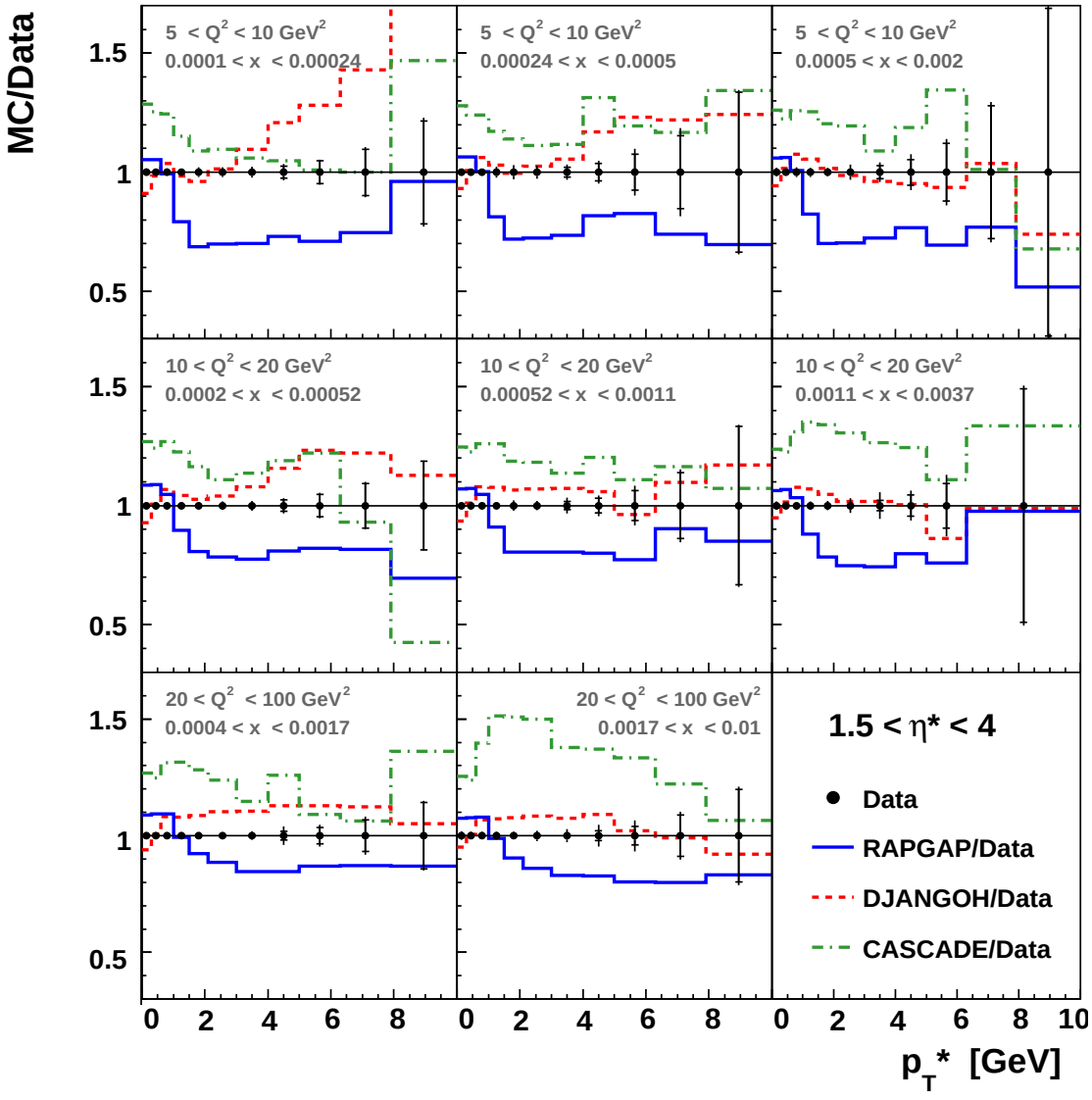

Figure 10.7: The ratios of measured over predicted by Monte Carlo p_T^* spectra of the charged particles in the hadronic centre of mass system (HCM) in $1.5 < \eta^* < 4$ range for eight intervals of Q^2 and x_{Bj}.

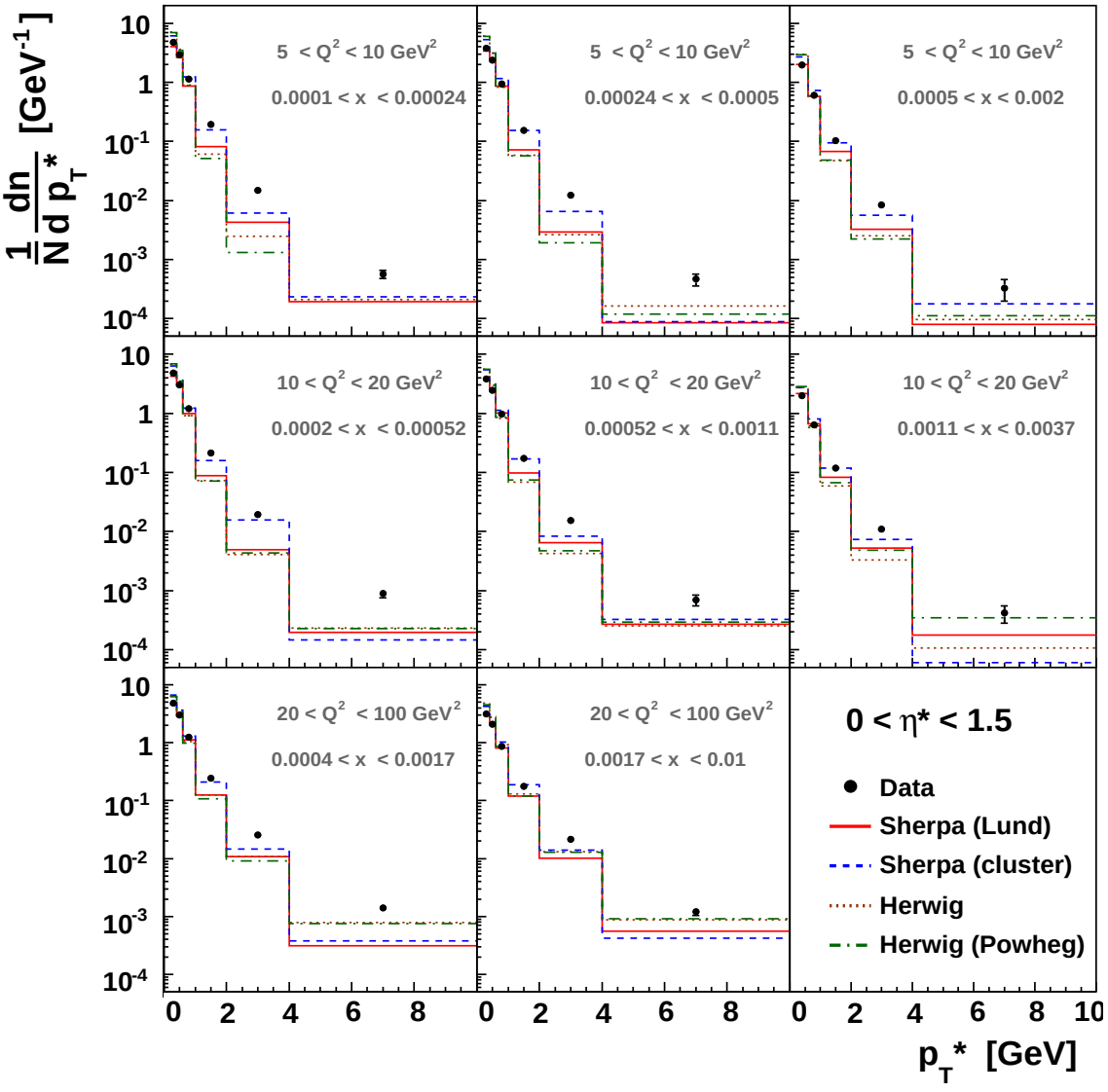

Figure 10.8: Measured p_T^* spectra of charged particles in the hadronic centre of mass system (HCM) in $0 < \eta^* < 1.5$ range for eight intervals of Q^2 and x_{Bj} together with Herwig++ and SHERPA Monte Carlo predictions.

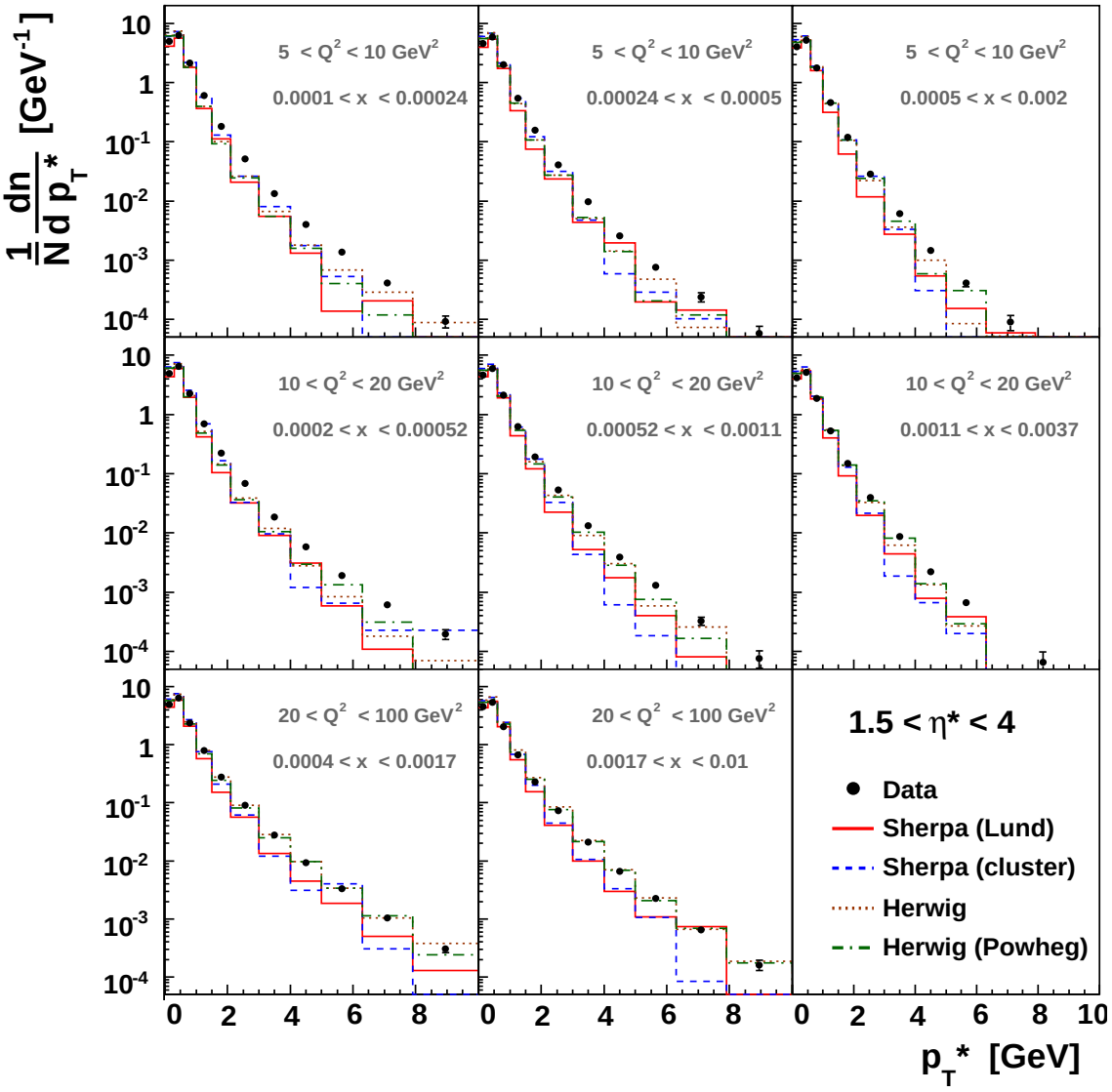

Figure 10.9: Measured p_T^* spectra of charged particles in the hadronic centre of mass system (HCM) in $1.5 < \eta^* < 4$ range for eight intervals of Q^2 and x_{Bj} together with Herwig++ and SHERPA Monte Carlo predictions.

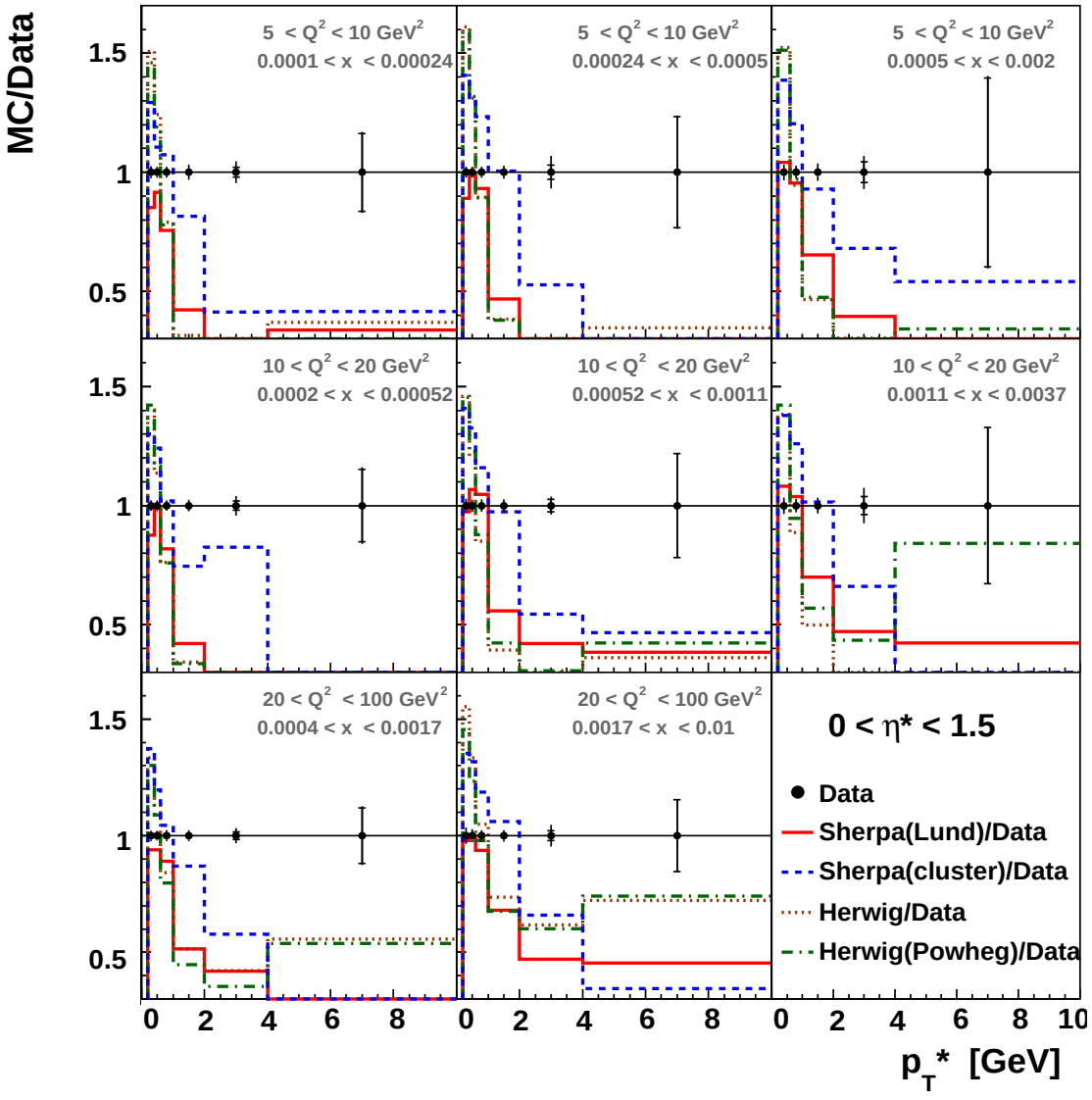

Figure 10.10: The ratios of measured over predicted by Monte Carlo p_T^* spectra of the charged particles in the hadronic centre of mass system (HCM) in $0 < \eta^* < 1.5$ range for eight intervals of Q^2 and x_{Bj}.

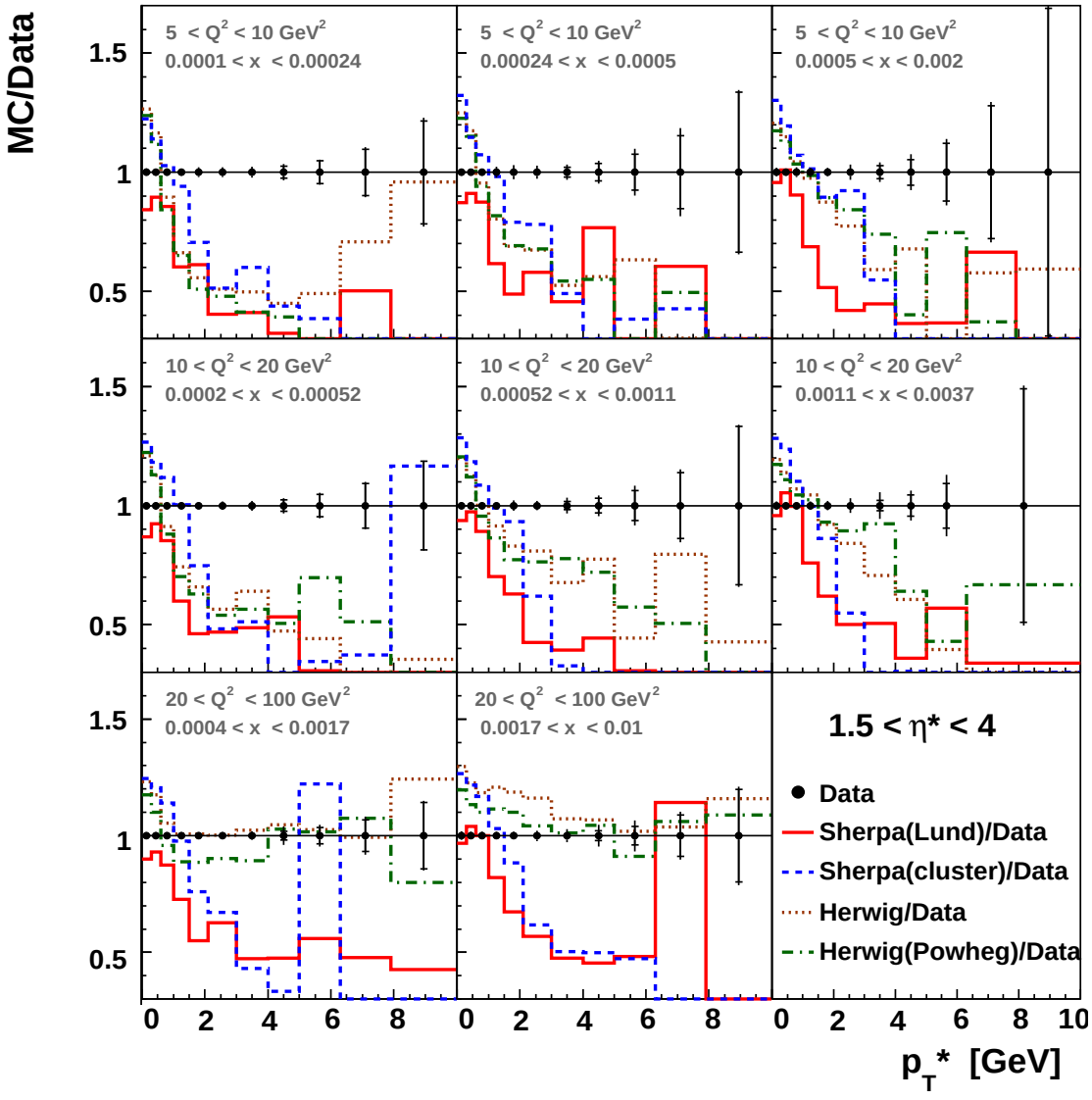

Figure 10.11: The ratios of measured over predicted by Monte Carlo p_T^* spectra of the charged particles in the hadronic centre of mass system (HCM) in $1.5 < \eta^* < 4$ range for eight intervals of Q^2 and x_{Bj}.

10.2 Rapidity Distribution of Charged Particles

As argued in [26], hadronisation effects should be relevant only at small transverse momenta, while hard parton radiation should manifest itself in the tail of the p_T^* distribution. To separate the effects of fragmentation and parton evolution the normalised pseudorapidity distributions were measured for $p_T^* < 1$ GeV and for $p_T^* > 1$ GeV, separately, as shown in figure 10.12. In the soft p_T^* region, the pseudorapidity distribution is plateau-like with about 1.7 charged particle per pseudorapidity unit. In the hard p_T^* region it becomes more peaked in the current region.

To check the sensitivity to hadronisation effects, the RAPGAP prediction with default PYTHIA fragmentation parameters and with parameters tuned by ALEPH [84] are shown in figure 10.12. Significant differences between these two parametrisation are seen in the soft p_T^* region, while for particles with large transverse momenta the discrepancy is much smaller. Predictions from generators with different approaches for QCD radiation are shown in figure 10.13. At both soft and large p_T^* the best description of the data is achieved by DJANGOH.

In figure 10.14 the RAPGAP and CASCADE predictions with PYTHIA fragmentation parameters tuned by ALEPH and by the Professor tuning tool (see section 3.2) are compared. As one can see the predictions obtained with parameters tuned by Professor (see table 10.1) give larger multiplicities at small p_T^* compared to the ALEPH tuning, and provide a worse description of the data. This is mostly due to

MSTJ(11)	5	fragm. function
PARJ(21)	0.325	σ_q
PARJ(41)	0.5	Lund a
PARJ(42)	0.6	Lund b
PARJ(47)	0.67	r_b
PARJ(81)	0.29	Lambda
PARJ(82)	1.65	Parton shower cut-off

Table 10.1: Professor tuned parameters.

the different value of b parameter of the Lund symmetric fragmentation function, to which the predictions are most sensitive. Increasing its value leads to a decreasing multiplicity at soft p_T^*. In the ALEPH tune $b = 0.85$ and in Professor $b = 0.6$.

The prediction of the RAPGAP model presented in figure 10.15 (left) illustrates the sensitivity to the choice of PDF. In the soft p_T^* region all NLO PDFs (HERAPDF1.0 [134], CTEQ6.6 [135], GRV98NLO [136]) show similar results and predict softer spectra compared to calculations using CTEQ6L(LO) [81]. The best description of the data is achieved by the GRV98NLO and GRV98LO PDFs, but they still do not describe the data well. At large p_T^* differences between NLO PDFs are observed and CTEQ6L(LO) is closer to the data than the other PDFs, however prediction with CTEQ6L(LO) is still significantly below the data. The sensitivity to the uPDF in CASCADE is shown in figure 10.15 (right). At large p_T^* the predictions show different shapes of the distribution. Set J2003-set2 [137] including non-singular terms of the gluon splitting function is closer to data than other uPDFs.

In figure 10.16 (left) the measurements are compared to the SHERPA and Herwig++ predictions. In the soft p_T^* region all models, except SHERPA (Lund), are above the data. At large p_T^* the best description of the data is achieved by SHERPA with the cluster model, which is still below the data. Herwig++ strongly undershoots the data towards the proton direction. Almost no difference is seen between the Herwig++ predictions with or without the POWHEG method. Figure 10.16 (right) illustrates the sensitivity to the choice of either LO PDF CTEQ6L or NLO PDF CTEQ6.6 for SHERPA. The results with CTEQ6.6 show a softer multiplicity compared to CTEQ6L(LO). In all further plots the SHERPA predictions are obtained with CTEQ6L(LO).

The charged particle multiplicity as a function of pseudorapidity in eight different x and Q^2 bins is shown in figures 10.17 and 10.18 for $p_T^* < 1$ GeV. The bin sizes are indicated on the plots and in table 9.1. DJANGOH provides a good description of the data in all kinematical ranges, all other models, except the SHERPA (Lund), are above the data independent of x and Q^2. SHERPA (Lund) shows sensitivity to x and Q^2, it undershoots the data at low x and Q^2 bins and provides a satisfactory description of the data in the highest (x,Q^2) bin.

The multiplicity of hard particles with $p_T^* > 1$ GeV is shown in figures 10.19 and 10.20 for the same x and Q^2 bins. A surplus of hard particles in the data over the DGLAP-like model at small x and away from the current region is observed. The best description of the data is achieved by DJANGOH. The plot clearly shows the x, Q^2 dependence of the data description by CASCADE: the best description is achieved at lowest x and Q^2 values and becomes worse at higher values. Herwig++ and SHERPA (Lund) strongly undershoot the data at lowest x and Q^2 values.

10.3 Monte Carlo Studies

The models with different parton radiation scenarios (different parton cascade) need a different tuning of hadronisation and parton cascade parameters. In the previous section it was shown that the η^* distribution for particles with $p_T^* > 1$ GeV is well described by DJANGOH, while RAPGAP slightly overshoots the measured spectra, and CASCADE predicts a much higher multiplicity. To understand the difference between the data and the CASCADE predictions, some additional studies were made. First, the sensitivity of the prediction to the PYTHIA parameters listed in table 3.3 were studied by varying them in the range given in the table, which was used by Professor tool. The new set of parameters used for CASCADE is shown in table 10.2. No special tuning tool was used and parameters were roughly changed such that CASCADE can describe the data at soft transverse momenta. The resulting distributions are shown in figure 10.21 (left). From these five tuned parameters the CASCADE prediction is mostly sensitive to the b parameter of the Lund symmetric fragmentation function. The second largest effect is due to the variation of the parton shower cut-off, Q_0. This parameter is denoted as the minimal invariant mass cut-off of the parton shower, below which partons are not assumed to radiate. The result of a single variation of b and Q_0 is demonstrated in figure 10.21 (right). Here only b (or Q_0) were changed, while all other parameters are from the ALEPH tune. This demonstrates that CASCADE can be tuned to give a reasonable description of

Parameter	ALEPH tune	New tune
σ_q (PARJ(21))	0.382	0.43
Lund a (PARJ(41))	0.437	0.4
Lund b (PARJ(42))	0.85	2.35
Lambda (PARJ(81))	0.23	0.35
Parton shower cut-off (PARJ(82))	1.54	3.0

Table 10.2: Tuned set of parameters used for CASCADE studies.

the data in the soft p_T^* region only by changing the b parameter (within the range given by Professor tool), while other parameters do not influence much. In the hard p_T^* region new predictions show a strong excess of the particles compared to the data.

Apart from CCFM evolution for the parton shower, CASCADE is also interfaced to the leading-log DGLAP parton shower. To check the effect of the different parton shower algorithms another CASCADE prediction was obtained with the DGLAP scenario and compared with RAPGAP. The result is shown in figure 10.22 and illustrates that CASCADE (DGLAP) is similar to the DGLAP-based RAPGAP MC. This demonstrates a strong effect of the CCFM evolution.

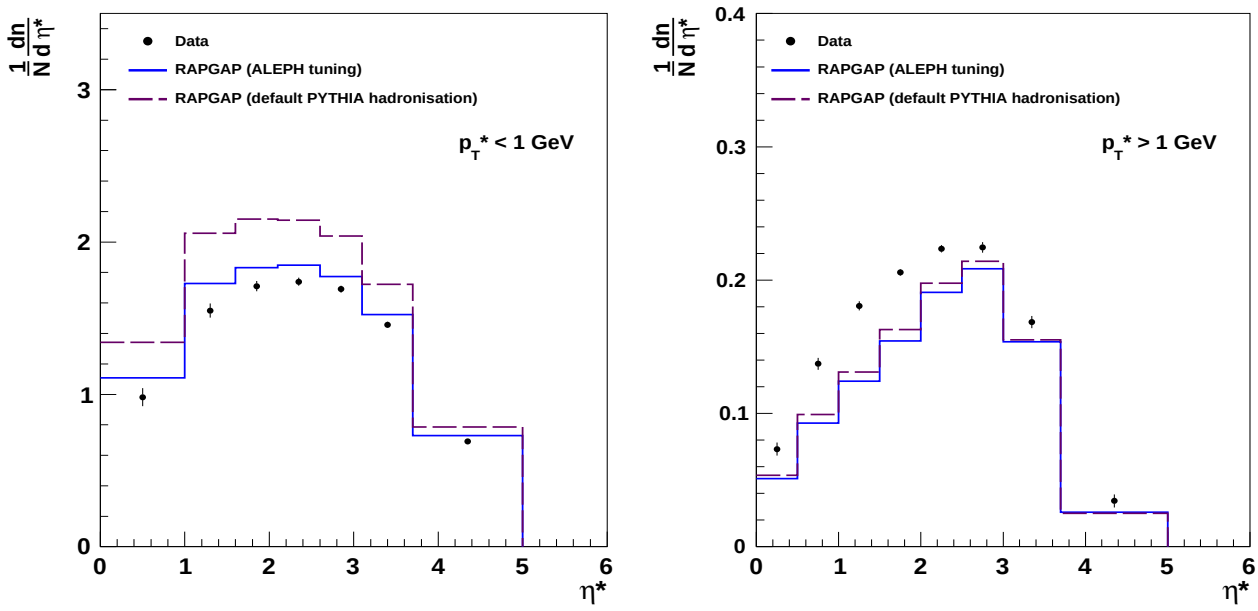

Figure 10.12: Measured η^* spectra in the hadronic centre of mass system (HCM) for the charged particles with $p_T^* < 1$ GeV (left) and with $p_T^* > 1$ GeV (right) together with RAPGAP predictions.

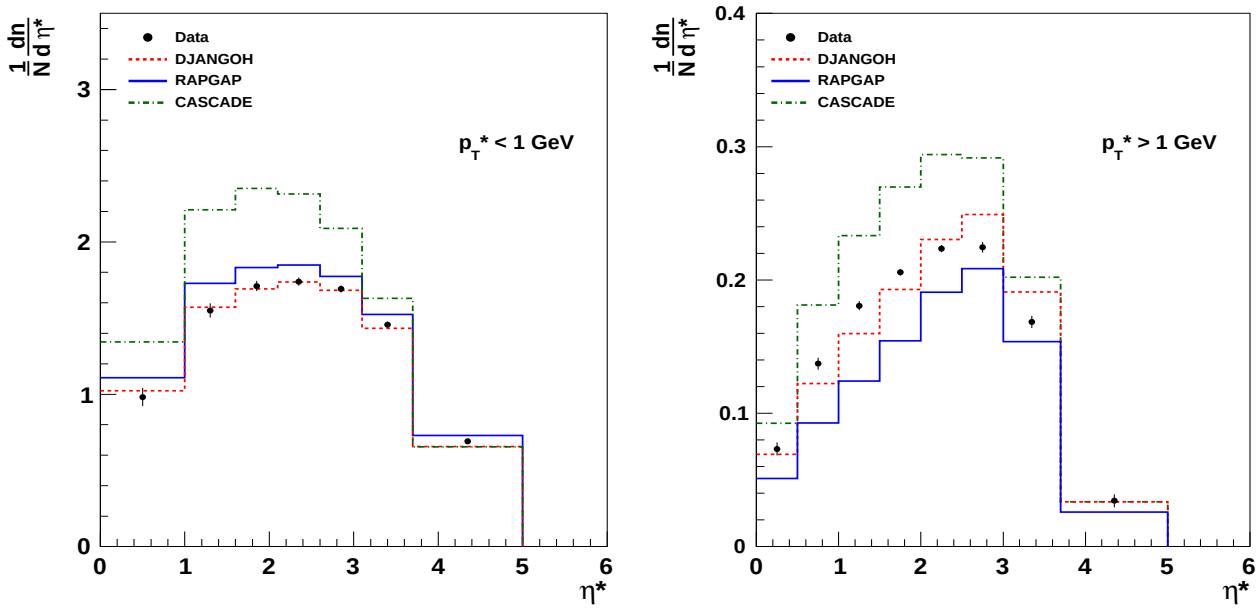

Figure 10.13: Measured η^* spectra in the hadronic centre of mass system (HCM) for the charged particles with $p_T^* < 1$ GeV (left) and with $p_T^* > 1$ GeV (right) together with RAPGAP, DJANGOH and CASCADE Monte Carlo predictions with two different tunings. The proton remnant direction is to the left.

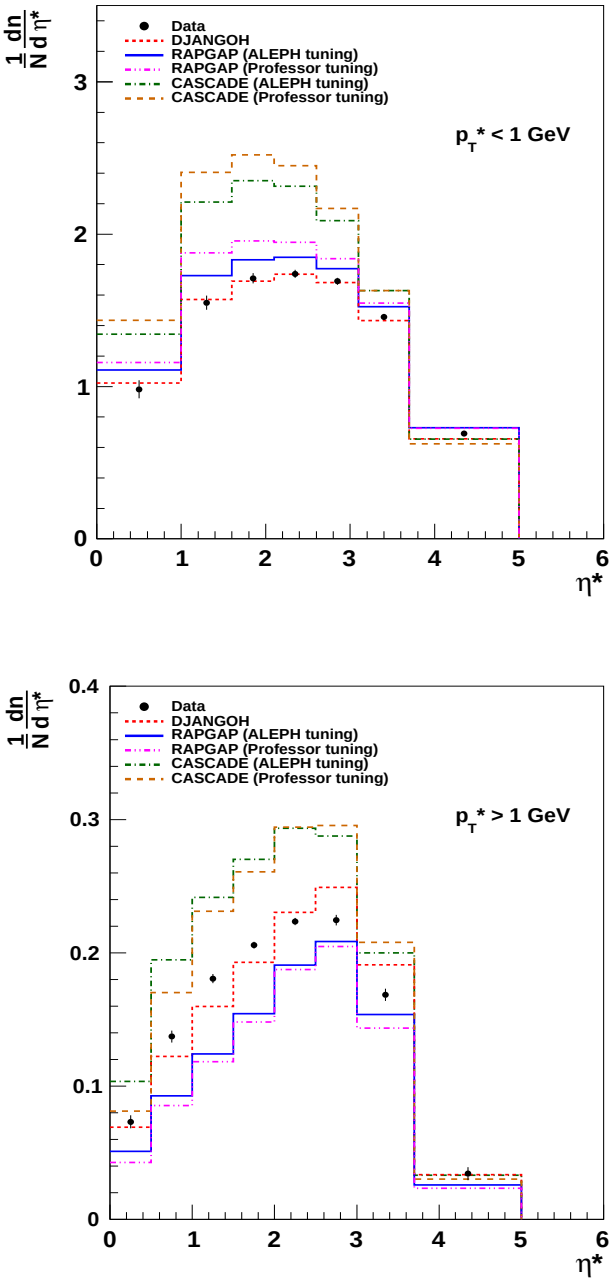

Figure 10.14: Measured η^* spectra in the hadronic centre of mass system (HCM) for the charged particles with $p_T^* < 1$ GeV (top) and with $p_T^* > 1$ GeV (bottom) together with RAPGAP, DJANGOH and CASCADE Monte Carlo predictions with two different tunings. The proton remnant direction is to the left.

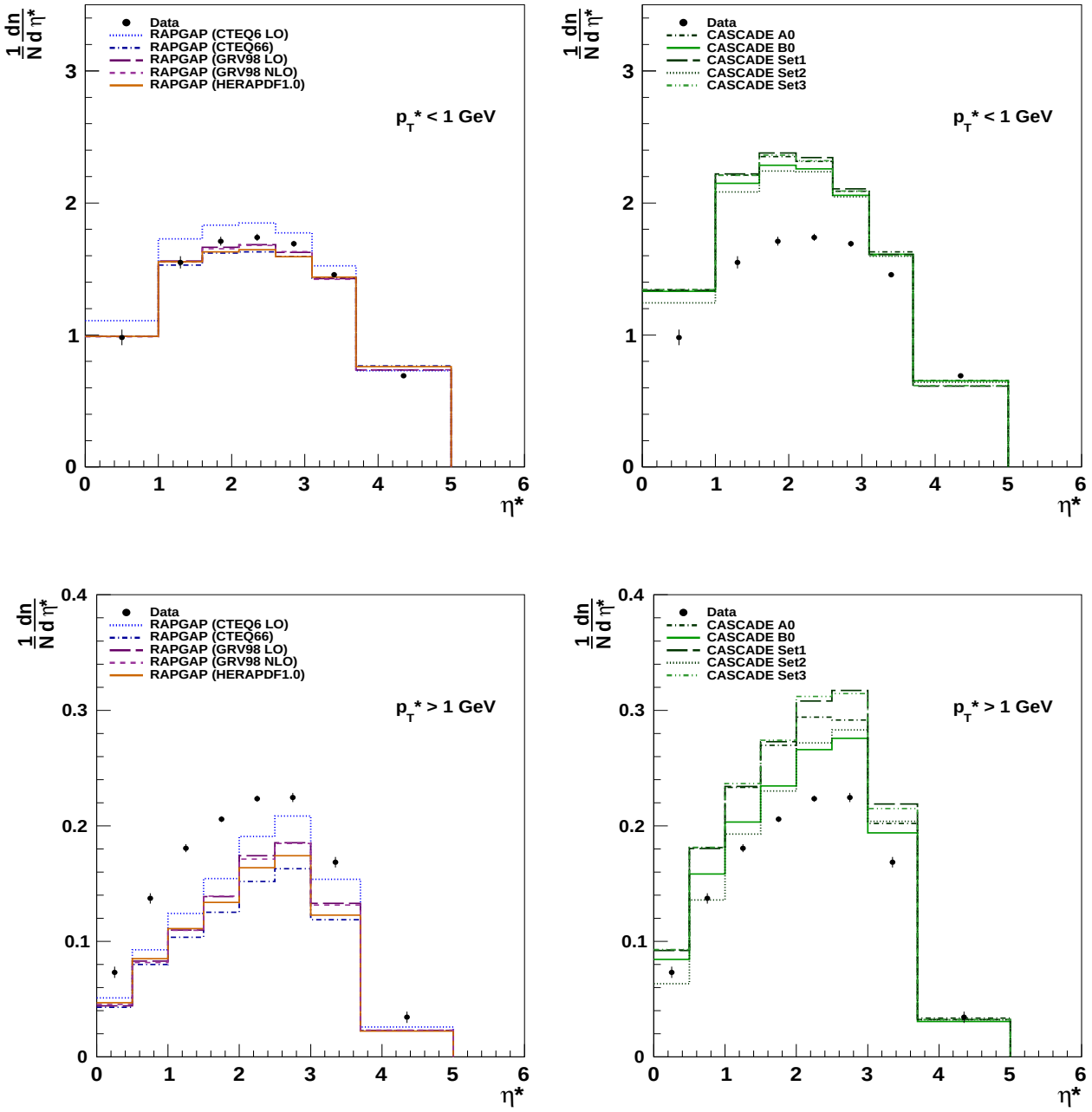

Figure 10.15: Measured η^* spectra in the hadronic centre of mass system (HCM) for the charged particles with $p_T^* < 1$ GeV (top) and with $p_T^* > 1$ GeV (bottom) together with RAPGAP and CASCADE predictions with different PDF and uPDFs, respectively. The proton remnant direction is to the left.

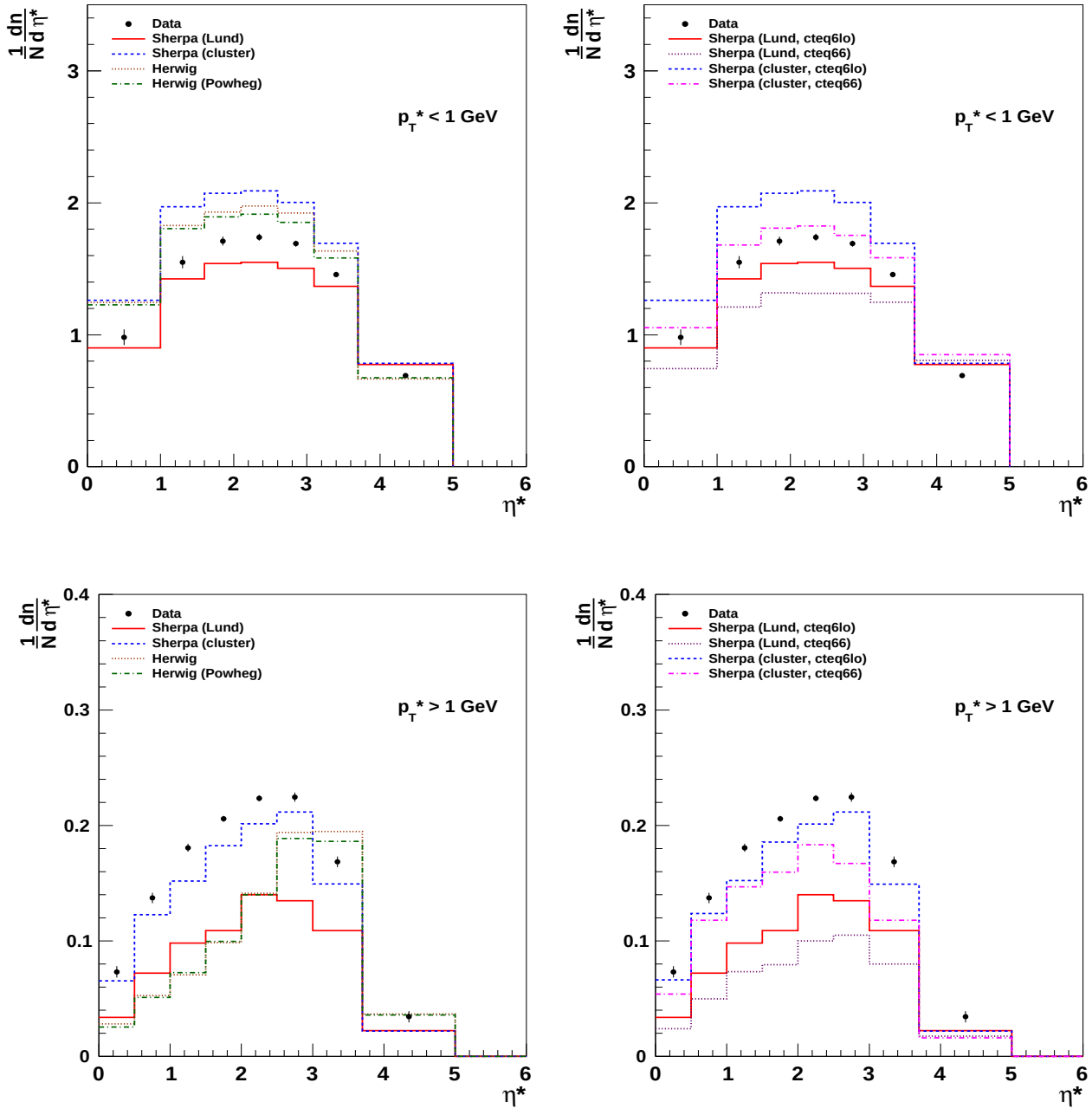

Figure 10.16: Measured η^* spectra in the hadronic centre of mass system (HCM) for the charged particles with $p_T^* < 1$ GeV (top) and with $p_T^* > 1$ GeV (bottom) together with Herwig++ and SHERPA Monte Carlo predictions. The proton remnant direction is to the left.

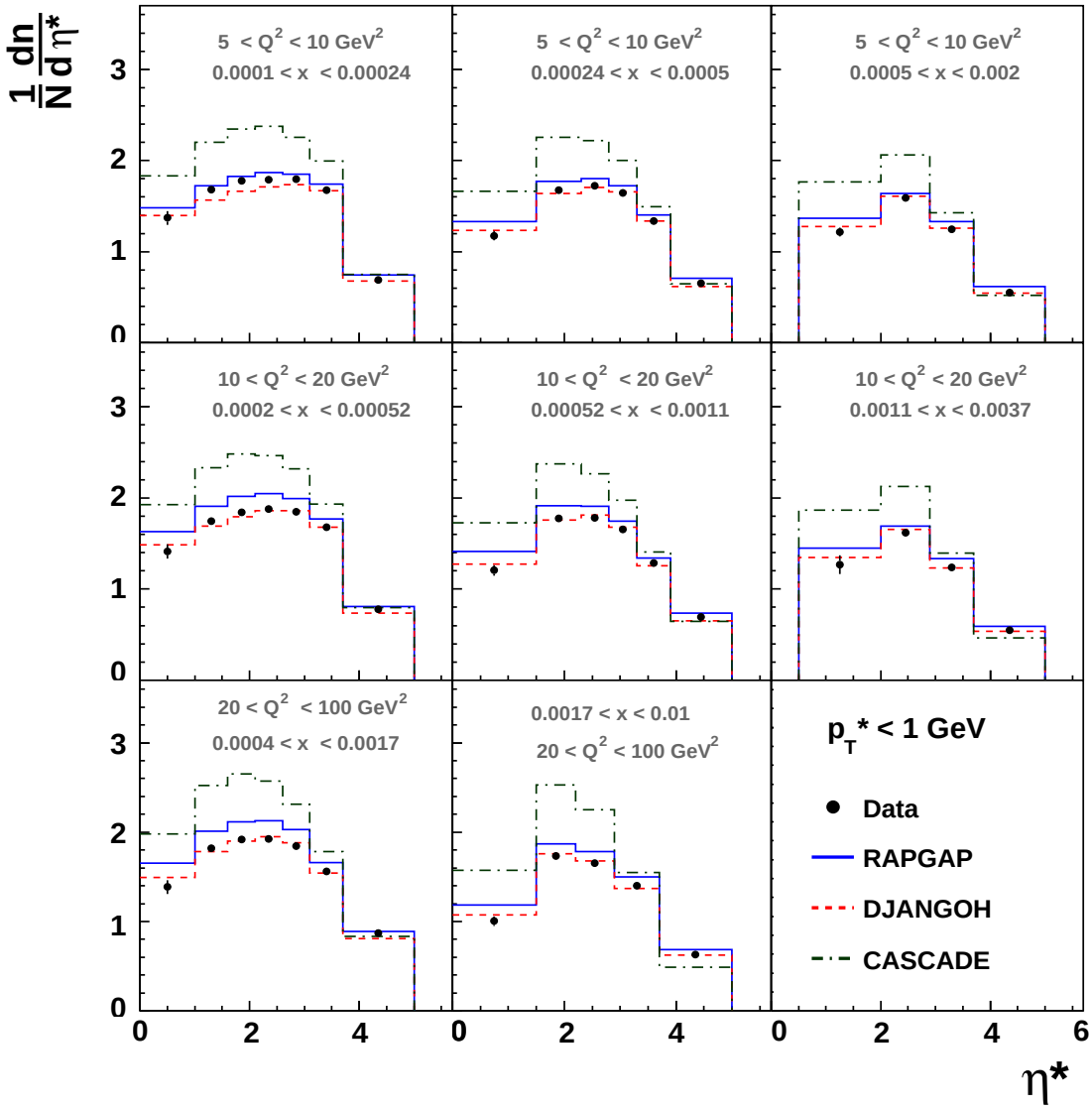

Figure 10.17: Measured η^* spectra in the hadronic centre of mass system (HCM) for the charged particles with $p_T^* < 1$ GeV for eight intervals of Q^2 and x_{Bj} together with RAPGAP, DJANGOH and CASCADE Monte Carlo predictions. The proton remnant direction is to the left.

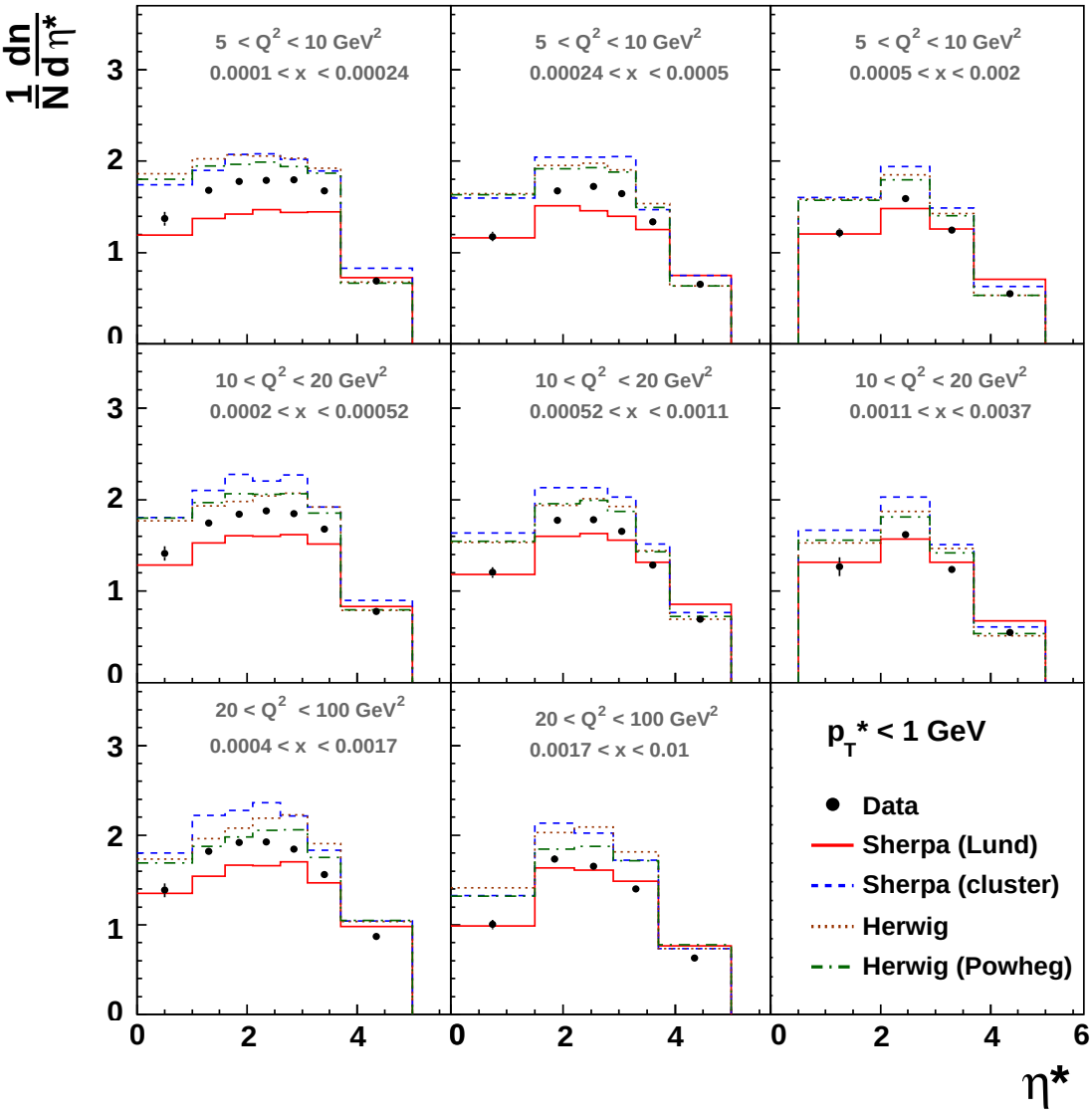

Figure 10.18: Measured η^* spectra in the hadronic centre of mass system (HCM) for the charged particles with $p_T^* < 1$ GeV for eight intervals of Q^2 and x_{Bj} together with Herwig++ and SHERPA Monte Carlo predictions. The proton remnant direction is to the left.

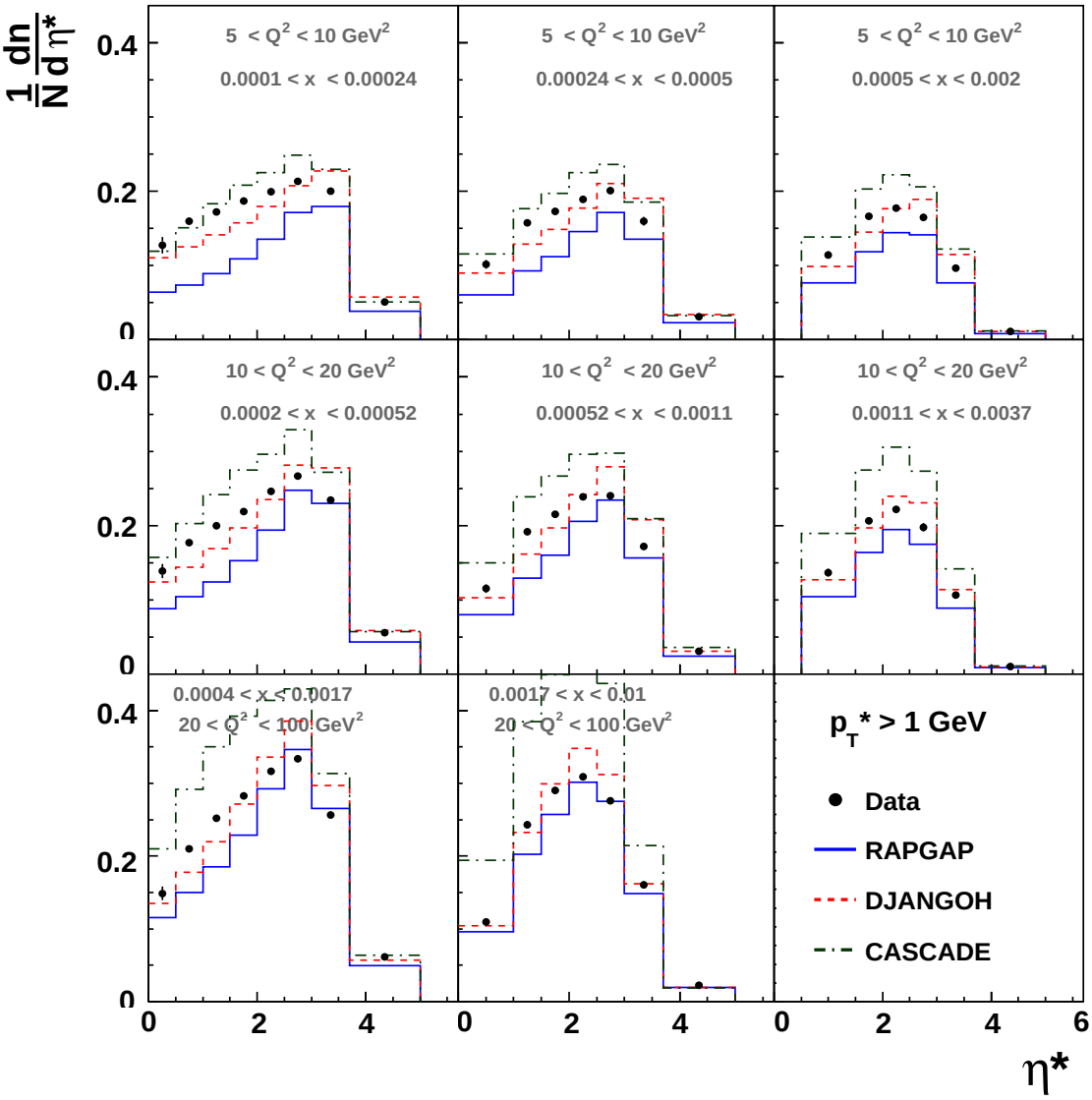

Figure 10.19: Measured η^* spectra in the hadronic centre of mass system (HCM) for the charged particles with $p_T^* > 1$ GeV for eight intervals of Q^2 and x_{Bj} together with RAPGAP, DJANGOH and CASCADE Monte Carlo predictions. The proton remnant direction is to the left.

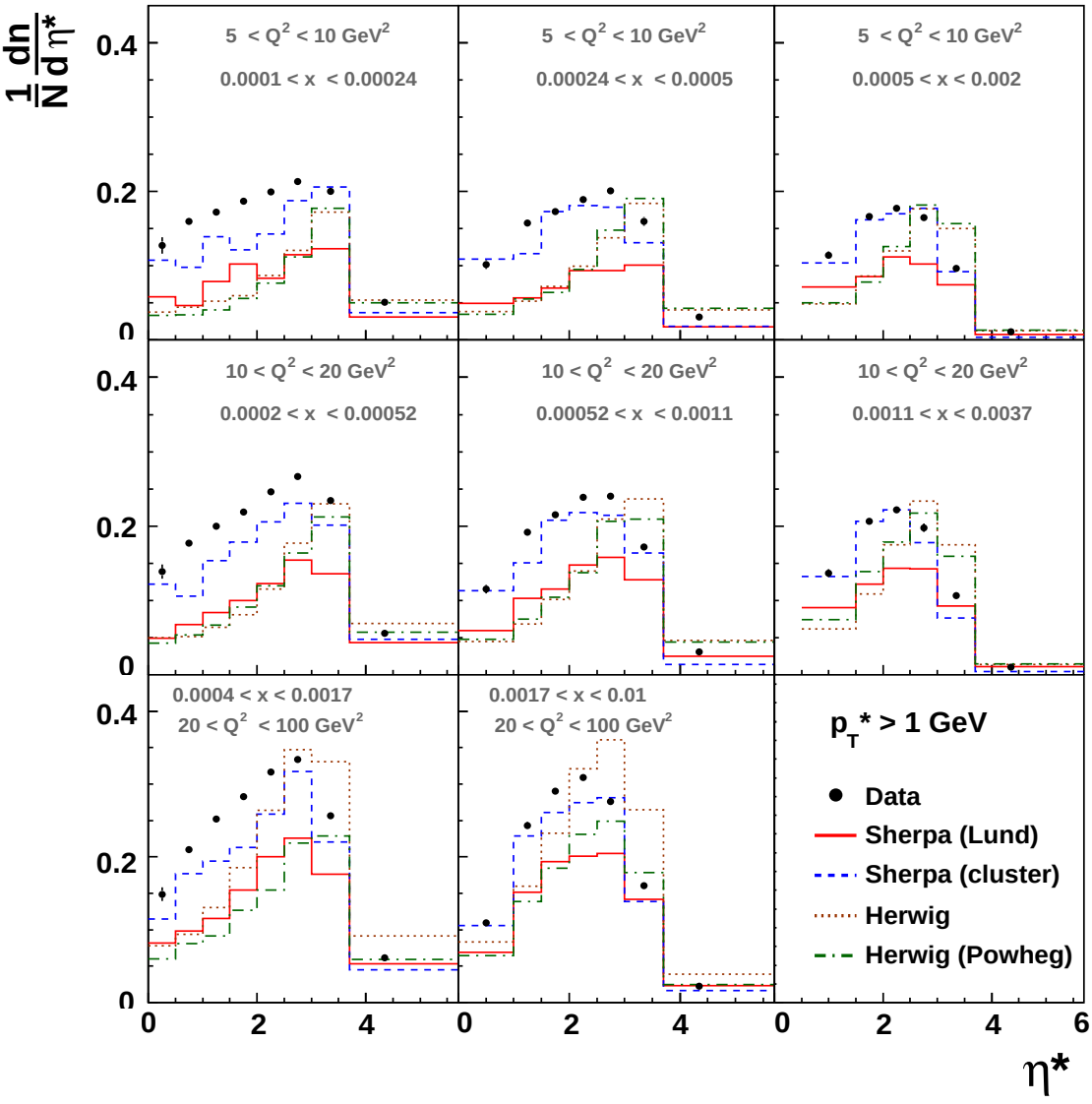

Figure 10.20: Measured η^* spectra in the hadronic centre of mass system (HCM) for the charged particles with $p_T^* > 1$ GeV for eight intervals of Q^2 and x_{Bj} together with Herwig++ and SHERPA Monte Carlo predictions. The proton remnant direction is to the left.

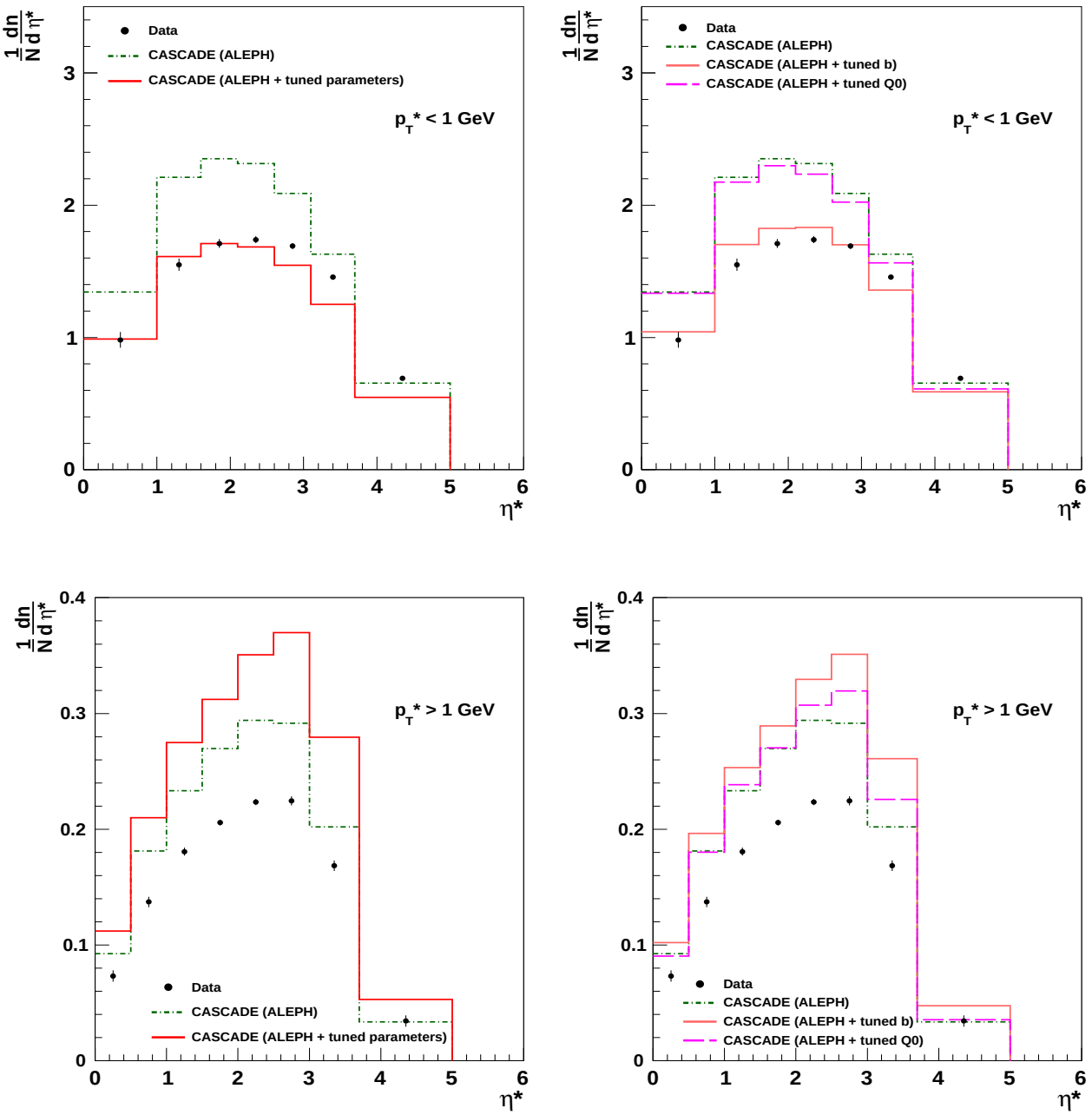

Figure 10.21: Measured η^* spectra in the hadronic centre of mass system (HCM) for the charged particles with $p_T^* < 1$ GeV (top) and with $p_T^* > 1$ GeV (bottom) together with CASCADE prediction. The proton remnant direction is to the left. Left plots show the CASCADE predictions with PYTHIA parameters tuned by ALEPH collaboration and with additionally tuned parameters listed in table 10.2. Right plots show the CASCADE predictions with separately tuned b parameter of the Lund symmetric fragmentation function and the parton shower cut-off, Q_0

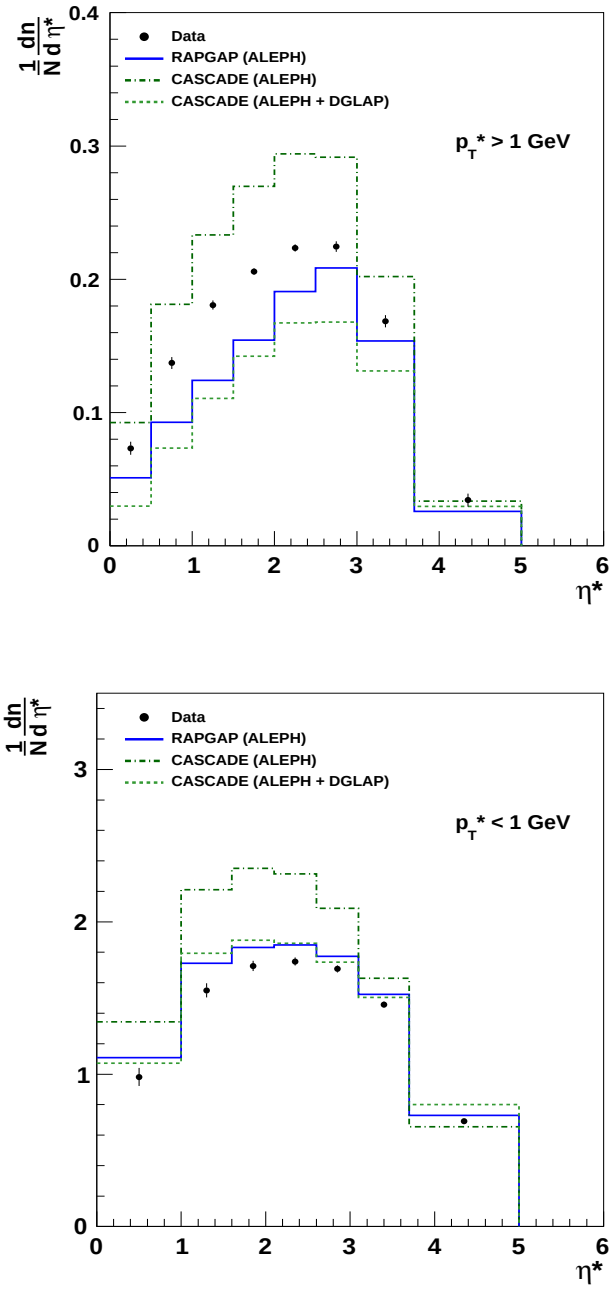

Figure 10.22: Measured η^* spectra in the hadronic centre of mass system (HCM) for the charged particles with $p_T^* < 1$ GeV (top) and with $p_T^* > 1$ GeV (bottom) together with CASCADE and RAPGAP prediction. The proton remnant direction is to the left. The CASCADE predictions are obtained with CCFM and DGLAP parton shower scenarios are labeled on the plots as CASCADE (ALEPH) and CASCADE (ALEPH+DGLAP).

Chapter 11

Conclusion

The normalised charged particle transverse momentum and pseudorapidity distributions have been measured in ep collision in the virtual photon-proton centre of mass frame (hadronic centre of mass frame) with the H1 detector in different regions of x and Q^2. The region of small x is especially of big interest, since the parton (gluon) density becomes very large but the theoretical predictions are inconsistent in this region. The measured transverse momentum distributions offer the possibility for discrimination of the various underlying parton dynamics. For these purposes the measured distributions are compared to the model distributions obtained with the help of different Monte Carlo generators, Rapgap, Djangoh, Cascade, Herwig++ and Sherpa, based on different QCD parton evolution approaches to simulate the parton cascades.

The high statistics of the data taken at HERA II and the substantial improvement of the track reconstruction and calibration by H1 collaboration allowed to measure charged particle distributions with much better precision compared to the measurements performed by H1 collaboration in 1996.

One of the challenging task of this analysis was to reach the forward (towards the proton remnant) direction to the maximum limit allowed by the tracking detector system. This task was motivated by the enhanced sensitivity of the distributions in this region to the various parton dynamics. The inclusion of the tracks reconstructed from the combined hits in central and forward track detectors enlarged the acceptance of the tracking compared to the case of only central track detector data taken into account.

The measurements of the charged particle transverse momentum are performed in two physically different regions: the region of current fragmentation and the region, where the target fragmentation is seen. In the present analysis, it was shown that in the forward pseudorapidity region, i.e. in the region, where the target fragmentation plays a role, the discrepancy between the measured transverse momentum distributions and distributions obtained with the help of Monte Carlo generator Rapgap, based on DGLAP model, is stronger in comparison with the central region, where the current fragmentation dominates. In the range of $2 < p_T^* < 4$ GeV the difference between the data and the DGLAP-based model in the forward region and for the lowest values of x and Q^2 is at the level of 10 standard deviations. On the contrary, the models with parton emissions unordered in transverse momentum, such as CCFM and CDM, provide reasonable description of the data in this region.

With increasing x and Q^2, the predictions of the DGLAP model at high transverse momenta become closer both to the data and to the predictions of the models beyond DGLAP.

The measured transverse momentum distributions are also compared to predictions of the Monte Carlo generators Herwig++ and SHERPA widely used for simulation of events at the LHC. It is demonstrated that none of them describes the data at large transverse momenta and not too large x.

The comparison of the measured pseudorapidity distribution of charged particles with the Monte Carlo generators shows that at small p_T^* the hadronisation effects are dominating, whereas at large p_T^* the details of parton radiation mechanisms play a significant role.

The η^* spectra were also used for studies of different tuning parameters used in the Monte Carlo generators. It is observed that the tuning currently used at H1 and obtained by the ALEPH collaboration in order to properly describe the LEP data, is better for the description of the data, presented in this thesis, than the latest tuning based the LEP data and prepared for the LHC Monte Carlo generators with the tuning tool Professor.

To understand better the observed discrepancy between CCFM-based model CASCADE and the data, some additional studies were performed. They showed that the description of the pseudorapidity distributions of the charged particles with soft p_T^* can be improved, but it makes the Monte Carlo description of the pseudorapidity distributions in the hard p_T^* region worse.

The data presented in this thesis offer the opportunity to test the Monte Carlo generators used at LHC in description of HERA data. It is important not only to observe deviations of the predictions from HERA data, but also to provide detailed simulations.

Detailed study of parton dynamics at HERA, as presented in this thesis, illustrate the importance of understanding the parton cascade, which will also play a crucial role at LHC.

Appendix A

DIS Kinematics in Sudakov and Light-Cone Variables

At very high energies the interacting electron and proton can be considered as massless particles, so that $p^2 = p_e^2 = 0$. It is useful then to work with light-cone variables instead of Cartesian coordinates of four-vectors. The light-cone variables are determined as follows

$$(p_0, p_x, p_y, p_z) \to (p^+, \vec{p}_T, p^-) \ , \qquad p^\pm \equiv \frac{p_0 \pm p_z}{\sqrt{2}} \ , \tag{A.1}$$

$$\vec{p}_T \equiv \{p_x, p_y\} \ ,$$

$$(p_1, p_2) = p_1^+ p_2^- + p_1^- p_2^+ - (\vec{p}_{1T}, \vec{p}_{2T}) \to$$

$$p^2 = 2p^+p^- - p_T^2 \ \to \ p^- = \frac{p^2 + p_T^2}{2p^+} \ . \tag{A.2}$$

By convention, although $\vec{p}_T$ is composed from space-like vectors, it is considered as 2-dimensional euclidean vector and hence p_T^2 is always positive. In what follows instead of $\vec{p}_T$ the simplified notation p_T is used.

The rapidity of a massless particle is defined as

$$\eta = \frac{1}{2} \ln \frac{p_+}{p_-} \ \to \ p_+ = \frac{p_T}{\sqrt{2}} e^\eta \ , \qquad p_- = \frac{p_T}{\sqrt{2}} e^{-\eta} \ . \tag{A.3}$$

Defining the polar angle w.r.t. z axis

$$\tan\theta \equiv \frac{p_T}{p_z} = \frac{1}{\sinh\eta} \ ,$$

one can express the rapidity via this angle

$$\eta = -\ln\tan\frac{\theta}{2} \ . \tag{A.4}$$

Also, the so-called Sudakov parametrisation is used often when there are two fixed noncolinear light-cone momenta in the process, such as p and p_e in our case. Any four-vector can then be decomposed as

$$k = \alpha p + \beta p_e + p_T \ , \tag{A.5}$$

where p_T is perpendicular to the plane spanned between p and p_e . The coefficients α and β in (A.5) are called Sudakov parameters an are equal to

$$\alpha = \frac{(k, p_e)}{(p, p_e)} , \qquad \beta = \frac{(k, p)}{(p, p_e)} . \tag{A.6}$$

Note, that $2(p, p_e) = s$ is squared total invariant mass of the ep system.

The Sudakov parametrisation of the virtual photon momentum is

$$q = -\frac{Q^2}{s} p + y p_e + q_T .$$

Appendix B

Long Range Rapidity Correlations

In September 2010 the CMS collaboration published results on two-particle angular correlations for charged particles emitted in proton-proton collisions at centre-of-mass energies of 7 TeV [138]. Long-range azimuthal correlations for pseudorapidity interval of $2 < \Delta\eta < 4.8$ were studied using two-dimensional $\Delta\eta - \Delta\varphi$ correlation function differentially as a function of charged particle multiplicity and particle transverse momentum. Here $\Delta\eta = |\eta_1 - \eta_2|$ and $\Delta\varphi = |\varphi_1 - \varphi_2|$ are the differences in pseudorapidity and azimuthal angle between the two particles. It was observed that in high multiplicity events ($N_{\text{track}} \geq 110$), a pronounced structure arises in the correlation function at the near side ($\Delta\varphi \sim 0$). The effect is most evident in the intermediate transverse momentum range of $1-3$ GeV. This is the first observation of such a long-range, near-side feature in two-particle correlation functions in hadron-hadron collisions. The physical origin of this observation is not yet understood and all available simulations show absence of the long-range azimuthal correlations, independent of multiplicity and transverse momentum.

This interesting observation encouraged us to look at the similar correlations in ep scattering at HERA, particularly in the phase space presented in this thesis: $5 < Q^2 < 100$ Gev^2, $0.05 < y < 0.6$, $p_{T,\text{track}} > 0.15$ GeV and $-2 < \theta_{\text{track}} < 2.5$.

To have a similarity with proton-proton collision the measurements are performed in the hadronic centre of mass (HCM) system. Transverse momentum and pseudorapidity of charged particles in the HCM frame are labeled as p_T^* and η^*, respectively. The two-dimensional correlation function is calculated as the ratio between the signal and the random background distributions (for the particles in the same events $\Delta\eta^*$ is randomly distributed between its minimal and maximal values and $\Delta\varphi^*$ is randomly distributed between 0 and π). The measurements are performed differentially as a function of charged particle multiplicity and transverse momentum. So high multiplicity events ($N_{\text{track}} \geq 110$) at which CMS has observed the long-range azimuthal correlation are not reachable at HERA, where the correlations were studied for two thresholds: $N \equiv N_{\text{track}} > 15$ and $N > 30$. For higher multiplicity events it is not possible to see any effect due to statistical fluctuations.

In figure B.1 the two-particle angular correlations are shown for the following requirements on the track multiplicity N: (a) - no requirement on N, (b)- events with track multiplicity large that 15 are selected, (c) - events with $N > 30$. Here, no p_T^* requirement is applied. Only positive values of $\Delta\eta^*$ are shown in the distributions, since a reliable η^* region for the central and combined tracks is $0 \lesssim \eta^* \lesssim 5$.

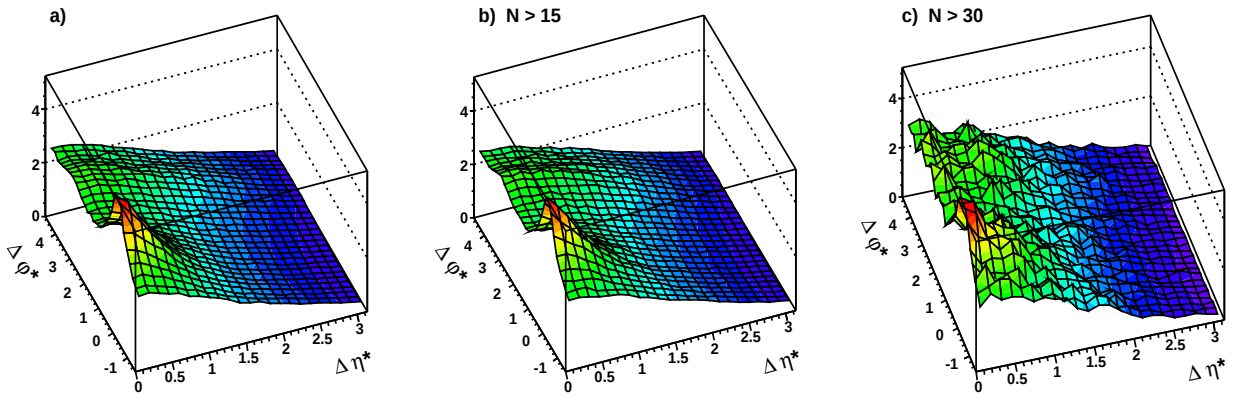

Figure B.1: Measured two-particle correlation in HCM frame for all selected events (a), for events with $N > 15$ (b) and for high multiplicity events with $N > 30$ (c).

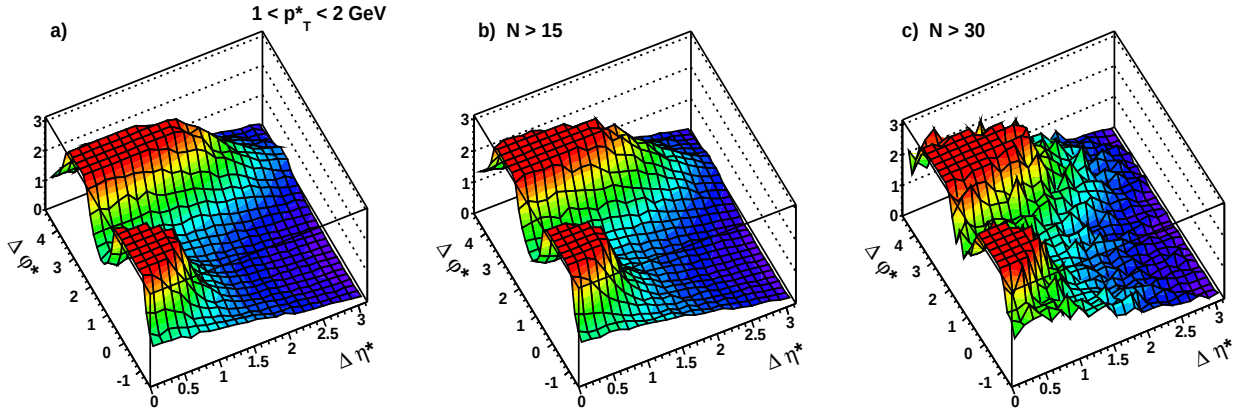

Figure B.2: Measured two-particle correlation in HCM frame with $1 < p_T^* < 2$ GeV for all selected events (a), for events with $N > 15$ (b) and for high multiplicity events with $N > 30$ (c).

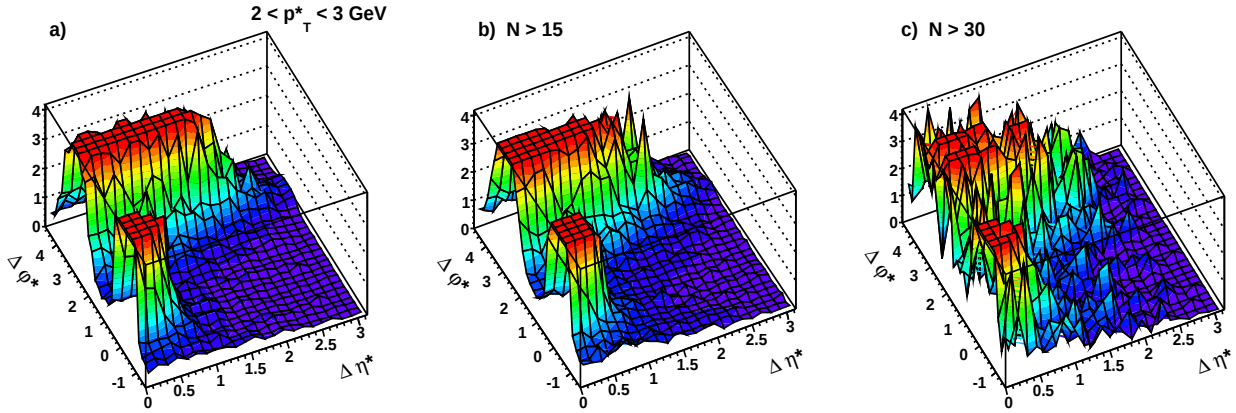

Figure B.3: Measured two-particle correlation in HCM frame with $2 < p_T^* < 3$ GeV for all selected events (a), for events with $N > 15$ (b) and for high multiplicity events with $N > 30$ (c).

In figures B.2 and B.3 the same correlations are shown for particles with $1 < p_T^* < 2$ GeV and $2 < p_T^* < 3$ GeV, respectively.

A peak around $\Delta\eta^* \approx 0$ and $\Delta\varphi^* \approx 0$ indicates that particles close to each other are correlated (particle within a single jet). The second broad elongated peak around $\Delta\varphi^* \approx \pi$ corresponds to correlation of particles between back-to-back jets. This broad ridge is much more pronounced at high p_T^*. The region at $\Delta\eta^* \approx 0$ and intermediate $\Delta\varphi^*$ is dominated by particle emission from clusters with low transverse momentum and thus is more pronounced at low p_T^*. Nothing as long-range at near-side azimuthal correlation is seen in the distributions. The RAPGAP and DJANGOH Monte Carlo generators show distributions similar to what is seen in the measurement: no long range correlations.

Appendix C

List of Used Acronyms

BGF *Boson Gluon Fusion*
BFKL *Balitskii-Fadin-Kuraev-Lipatov*
BPC *Backward Proportional Chamber*
BST *Backward Silicon Tracker*
CC *Charge Current*
CCFM *Catani-Ciafaloni-Fiorani-Marchesini*
CDM *Colour Dipole Model*
CIP *Central Inner Proportional Chamber*
CJC *Central Jet Chamber*
COP *Central Outer Proportional Chamber*
COZ *Central Outer z-Chamber*
CST *Central Silicon Tracker*
CTD *Central Track Detector*
DESY *Deutsches Elektronen-Synchrotron*
DGLAP *Dokshitzer-Gribov-Lipatov-Altarelli-Parisi*
DIS *Deep Inelastic Scattering*
DLL *Double Leading Logarithmic*
DST *Data Summary Tape*
DST *Data Summary Tape*
ET *Electron Tagger*
FMD *Forward Muon Detector*
FST *Forward Silicon Tracker*
FTD *Forward Track Detector*
FTT *Fast Track Trigger*
HAT *H1 Analysis Tag*
HCM *Hadronic Centre-of-mass*
HEP *High Energy Physics*
HERA *Hadron-Elektron-Ring-Anlage*
HFS *Hadronic Final State*
IP *Interaction Point*
LAr *Liquid Argon*
LEP *Large Electron-Positron Collider*
LHC *Large Hadron Collider*
LO *leading order*

MEPS *Matrix element and parton showers*
MODS *Micro Object Data Store*
NC *Neutral Current*
NNLO *Next-to-next-to-leading order*
NLO *Next-to-leading order*
ODS *Object Data Store*
μODS Micro Object Data Store
PETRA *Positron-Elektron-Ring-Anlage*
PDF *Parton Distribution Function*
POT *Production Output Tape*
QED *Quantum Electrodynamics*
QPM *Quark Parton Model*
QCD *Quantum chromodynamics*
QCDC *Quantum Chromodynamic Compton*
SpaCal *Spaghetti Calorimeter*
TC *Tail Catcher*
ToF *Time-of-Flight*
uPDF *Unintegrated Parton Distribution Function*
UV *Ultra-violet*

References

[1] E. Bloom et al., High-energy inelastic ep scattering at 6° and 10°, *Phys. Rev. Lett.*, 23 (1969) 930.

[2] M. Breidenbach et al., Observed behavior of highly inelastic electron-proton scattering, *Phys. Rev. Lett.*, 23 (1969) 935.

[3] J. Friedman and H. Kendall, Deep inelastic electron scattering, *Phys. Rev. Lett.*, 22 (1972) 203.

[4] [CMS Collaboration], Combined results of searches for the standard model Higgs boson in pp collisions at $\sqrt{s} = 7$ TeV, arXiv:1202.1488v1 [hep-ex].

[5] [ATLAS Collaboration], Combined search for the standard model Higgs boson using up to 4.9 fb^{-1} of pp collision at $\sqrt{s} = 7$ TeV with the ATLAS detector at the LHC, arXiv:1202.1408v2 [hep-ex].

[6] V. Gribov and V. Lipatov, Deep inelastic ep scattering in perturbation theory, *Sov. J. Nucl. Phys.*, 15 (1972) 675.

[7] V. Lipatov, The parton model and perturbation theory, *Sov. J. Nucl. Phys.*, 20 (1975) 94.

[8] G. Altarelli and G. Parisi, Asymptotic freedom in parton language, *Nucl. Phys.*, B 126 (1977) 298.

[9] Y. Dokshitzer, Calculation of the structure functions for deep inelastic scattering and e^+e^- annihilation by perturbation theory in Quantum Chromodynamics, *Sov. Phys. JETP*, 46 (1977) 641.

[10] V. Lipatov, E. Kuraev and V. Fadin, Multi-Reggeon processes in the Yang-Mills theory, *Sov. Phys. JETP*, 44 (1976) 443.

[11] V. Lipatov, E. Kuraev and V. Fadin, The Pomeranchuk singularity in nonabelian gauge theories, *Sov. Phys. JETP*, 45 (1977) 199.

[12] Y. Balitsky and V. Lipatov, The Pomeranchuk singularity in Quantum Chromodynamics, *Sov. J. Nucl. Phys.*, 28 (1978) 822.

[13] C. Adloff et al. [H1 Collaboration], Measurement of dijet cross-sections at low Q^2 and the extraction of an effective parton density for the virtual photon, *Eur. Phys. J.*, C 13 (2000) 397, [hep-ex/9812024].

[14] C. Adloff et al. [H1 Collaboration], Di-jet event rates in deep-inelastic scattering at HERA, *Eur. Phys. J.*, C 13 (2000) 415, [hep-ex/9806029].

[15] A. Aktas et al. [H1 Collaboration], Measurement of dijet cross sections in ep interactions with a leading neutron at HERA, *Eur. Phys. J.*, C 41 (2005) 273, [hep-ex/0501074].

[16] S. Chekanov et al. [ZEUS Collaboration], Dijet production in neutral current deep inelastic scattering at HERA, *Eur. Phys. J.*, C 23 (2002) 13, [hep-ex/0109029].

[17] C. Adloff et al. [H1 Collaboration], Low Q^2 jet production at HERA and virtual photon structure, *Phys. Lett.*, B 415 (1997) 418, [hep-ex/9709017].

[18] C. Adloff et al. [H1 Collaboration], Measurement of inclusive jet cross-sections in deep-inelastic *ep*-scattering at HERA, *Phys. Lett.*, B 542 (2002) 193, [hep-ex/0206029].

[19] C. Adloff et al. [H1 Collaboration], Measurements of transverse energy flow in deep-inelastic scattering at HERA, *Eur. Phys. J.*, C 12 (2000) 595, [arXiv:hep-ex/9907027].

[20] S. Aid et al. [H1 Collaboration], Transverse energy and forward jet production in the low x regime at HERA, *Eur. Phys.*, B 356 (1995) 118, [arXiv:hep-ex/9506012].

[21] T. Ahmed et al. [H1 Collaboration], Energy flow and charged particle spectra in deep inelastic scattering at HERA, *Z. Phys.*, C 63 (1994) 377.

[22] S. Aid et al. [H1 Collaboration], Jets and energy flow in photon-proton collisions at HERA, *Z. Phys.*, C 70 (1996) 17, [arXiv:hep-ex/9511012].

[23] M. Derrick et al. [ZEUS Collaboration], Hadronic energy distributions in deep-inelastic scattering, *Z. Phys.*, C 70 (1996) 231.

[24] M. Derrick et al. [ZEUS Collaboration], Comparison of energy flows in deep inelastic scattering with and without a large rapidity gap, *Phys. Lett.*, B 338 (1994) 483.

[25] C. Adloff et al. [H1 Collaboration], Measurement of charged particle transverse momentum spectra in deep inelastic scattering, *Nucl. Phys.*, B 485 (1997) 3, [arXiv:hep-ex/9610006v2].

[26] M. Kuhlen, A new method to probe the low x parton dynamics at HERA, *Phys. Lett.*, B 382 (1996) 441.

[27] R. Feynman, Very high-energy collisions of hadrons, *Phys. Rev. Lett*, 23 (1969) 1415.

[28] R. Brandelik et al. [TASSO collaboration], Evidence for planar events in e^+e^- annihilation at high energies, *Phys. Lett.*, B 86 (1979) 243.

[29] Ta-Pei Cheng and Ling-Fong Li, Gauge Theory of Elementary Particle Physics, Claredon Press, Oxford, 1984.

[30] Michael E. Peskin and Daniel V. Schroeder, An Introduction to Quantum Field Theory, Addison-Wesley Advanced Book Program, 1995.

[31] T. Kinoshita, Mass singularities of Feynman amplitudes, *J. Math. Phys.*, 3 (1962) 650.

[32] T.D. Lee and M. Nauenberg, Degenerate systems and mass singularities, *Phys. Rev.*, 133 (1964) B1549.

[33] W. Furmanski, G. Curci and R. Petronzio, Jet and lepton-pair production in high-energy lepton-hadron and hadron-hadron scattering, *Phys. Rev.*, D 18 (1978) 3252.

[34] R.K. Ellis et al., Perturbation theory and the parton model in QCD, *Nucl. Phys.*, B 152 (1979) 285.

[35] W. Furmanski, G. Curci and R. Petronzio, Evolution of parton densities beyond leading order: the non-singlet case, *Nucl. Phys.*, B 175 (1980) 27.

[36] F. Halzen and A.D. Martin, Quarks and leptons, *John Wiley and Sons, New York*, 1984.

[37] S. Moch, J.A.M. Vermaseren and A. Vogt, The three-loop splitting functions in QCD: The non-singlet case, *Nucl. Phys.*, B 688 (2004) 101.

[38] S. Moch et al. A. Vogt, The three-loop splitting functions in QCD: the singlet case, *Nucl. Phys.*, B 691 (2004) 129.

[39] A. DeRujula et al., Possible non-regge behavior of electroproduction structure functions, *Phys. Rev.*, D 10 (1974) 1649.

[40] A.D. Martin, J. Kwiecinski and P.J. Sutton, Gluon distribution at small x obtained from a unified evolution equation, *Phys. Rev.*, D 52 (1995) 1445.

[41] M. Ciafaloni, Coherence effects in the initial jets at small Q^2, *Nucl. Phys.*, B 296 (1998) 49.

[42] M. Catani, F. Fiorani and G. Marchesini, QCD coherence in initial state radiation, *Phys. Lett.*, B 234 (1990) 339.

[43] M. Catani, F. Fiorani and G. Marchesini, Small x behaviour of initial state radiation in perturbative QCD, *Nucl. Phys.*, B 336 (1990) 18.

[44] M. Ciafaloni, M. Bassetto and G. Marchesini, Jet structure and infrared sensitive quantities in perturbative QCD, *Phys. Rep.*, 100 (1983) 201.

[45] Yu.L. Dokshitzer et al., QCD coherence in high-energy reactions, *Rev. Mod. Phys.*, 60 (1988) 373.

[46] D. Amati et al., A treatment of hard processes sensitive to the infra-red structure of QCD, *Nucl. Phys*, B 173 (1980) 429.

[47] G. Gustafson, B. Andersson and C. Peterson, A semiclassical model for quark jet fragmentation, *Phys. Rep.*, 97 (1983) 31.

[48] B. Andersson et al., Parton fragmentation and string dynamics, *Z. Phys.*, C 1 (1979) 105.

[49] K. Werner, Strings, pomerons and the VENUS model of hadronic interactions at ultrarelativistic energies, *Rhys. Rep.*, 232 (1993) 87.

[50] R.D. Field and R.P. Feynman, A parametrization of the properties of quark jets, *Nucl. Phys*, B 136 (1978) 1.

[51] E. Norrbin and T. Sjöstrand, Production mechanisms of charm hadrons in the string model, *Phys. Lett.*, B 442 (1998) 407,

[52] G. Gustafson, B. Andersson and T. Sjöstrand, A three-dimensional model for quark and gluon jets, *Z. Phys.*, C 6 (1980) 235.

[53] G. Gustafson, B. Andersson and T. Sjöstrand, A model for baryon production in quark and gluon jets, *Nucl. Phys*, B 197 (1982) 45.

[54] G. Ingelman, B. Andersson, G. Gustafson and T. Sjöstrand, Baryon production in lepton-nucleon scattering and diquark fragmentation, *Z. Phys.*, C 13 (1982) 361.

[55] G. Gustafson, B. Andersson and T. Sjöstrand, Baryon production in jet fragmentation and Υ-decay, *Phys. Scripta*, 32 (1985) 574.

[56] B.R. Webber, A QCD model for jet fragmentation including soft gluon interference, *Nucl. Phys.*, B 238 (1984) 492.

[57] H. Jung, QCD and Collider Physics III: Hadronization, Lecture 8 WS 06/07.

[58] G. Gustafson, Dual description of a confined colour field, *Phys. Lett.*, B 175 (1986) 453.

[59] G. Gustafson and U. Pettersson, Dipole formulation of QCD cascades, *Nucl. Phys.*, B 306 (1988) 746.

[60] G. Gustafson, Andersson and L. Lönnblad, Gluon splitting in the colour dipole cascades, *Nucl. Phys.*, B 339 (1990) 393.

[61] G. Gustafson; Parton Cascades, Small x, Multiple Interactions, and Saturation; *Acta Phys. Polon.*, B 42 (2011) 2581.

[62] H. Kharraziha and L. Lönnblad, The linked dipole chain Monte Carlo, *JHEP* 03 (1998) 006, arXiv:hep-ph/9709424v2.

[63] G. Gustafson, B. Andersson and J. Samuelsson; Discrete QCD, a new approximation for QCD cascades; *Lund Preprint*, LU-TP-95-12, 1995.

[64] G. Gustafson, B. Andersson and J. Samuelsson, The linked dipole chain model for DIS, *Lund Preprint*, LU-TP-95-13, 1995.

[65] G. Marchesini and B.R. Webber, Monte Carlo simulation of general hard processes with coherent QCD radiation, *Nucl. Phys.*, B 310 (1988) 461.

[66] S. Gieseke et al., Herwig++ 2.5 release note, arXiv:1102.1672v1 [hep-ph].

[67] H. Jung, RAPGAP 3.1, *Comput. Phys. Commun.*, 86 (1995) 147.

[68] T. Sjöstrand et al., High-energy-physics event generation with PYTHIA 6.1, *Comput. Phys. Commun.*, 135 (2001) 238, arXiv:hep-ph/0010017v1.

[69] H. Spiesberg, A. Kwiatkowski and H.J. Möhring, HERACLES 1.0, *Nucl. Instrum. Meth.*, 69 (1992) 155.

[70] H. Jung, The CCFM Monte Carlo generator CASCADE, *Comput. Phys. Commun.*, 143 (2002) 100.

[71] H. Jung, The CCFM Monte Carlo generator CASCADE 2.2.0, *Eur. Phys. J.*, 70 (2010) 1237.

[72] G.A. Schuler, K. Charchula and H. Spiesberger, DJANGOH 1.4, *Comput. Phys. Commun.*, 81 (1994) 381.

[73] L. Lönnblad, ARIADNE 4.10, *Comput. Phys. Commun.*, 71 (1992) 15.

[74] T. Gleisberg et al., Event generation with SHERPA 1.1, *JHEP*, 0902:007, 2009. arXiv:0811.4622 [hep-ph].

[75] S. Schumann and F. Krauss, A parton shower algorithm based on Catani-Seymour dipole factorisation, *JHEP*, 0803 (2008) 038.

[76] S. Schumann, S. Höche, F. Krauss and F. Siegert, QCD matrix elements and truncated showers, *JHEP*, 0905 (2009) 053, arXiv:0903.1219v2 [hep-ph].

[77] F. Krauss, J. Winter and G. Soff, A modified cluster hadronization model, *Eur. Phys. J.*, C 36 (2004) 381.

[78] G. Marchesin, QCD coherence in the structure function and associated distributions at small x, *Nucl. Phys.*, B 445 (1995) 49, [hep-ph/9412327].

[79] B.R. Webber, S. Catani and G. Marchesini, QCD coherent branching and semi-inclusive processes at large x, *Nucl. Phys.*, B 349 (1991) 635.

[80] Luca D'Errico and Peter Richardson, A positive-weight next-to-leading-order Monte Carlo simulation of deep inelastic scattering and Higgs boson production via vector boson fusion in Herwig++, 2011. arXiv:1106.2983v2 [hep-ph].

[81] J. Pumplin et al., New generation of parton distributions with uncertainties from global QCD analysis, *JHEP*, 0207 (2002) 012, [hep-ph/0201195].

[82] W.J. Stirling, A.D. Martin, R.G. Roberts and R.S. Thorne, NNLO global parton analysis, *Phys. Lett.*, B 531 (2002) 216, [arXiv:hep-ph/0201127].

[83] H. Jung, Unintegrated parton density function in CCFM, *Proceeding of DIS2004*, p.299, [arXiv:hep-ph/0411287].

[84] S. Schael et al. [ALEPH Collaboration], Bose-Einstein correlations in W-pair decays with an event-mixing technique, *Phys. Lett.*, B 606 (2005) 265; G. Rudolph [ALEPH Collaboration], private communication

[85] A. Buckley et al., Systematic event generator tuning for the LHC, *Eur. Phys. J.*, C 65 (2010) 331, arXiv:0907.2973 [hep-ph].

[86] F.D. Aaron et al., Combined measurement and QCD analysis of the inclusive $e^{\pm}p$ scattering cross sections at HERA, *JHEP*, 01 (2010) 109.

[87] R.S. Thorne, A.D. Martin, W.J. Stirling and G. Watt, Parton distributions for the LHC, *Eur. Phys. J.*, C 63 (2009) 189, arXiv:0901.0002v3 [hep-ph].

[88] C.D. White and R.S. Thorne, A global fit to scattering data with NLL BFKL resummations, *Phys. Rev.*, D 75 (2007) 034005, arXiv:hep-ph/0611204.

[89] A.D. Martin, J. Kwiecinski and A.M. Stasto, Unified BFKL and Gribov-Lipatov-Altarelli-Parisi description of F_2 data, *Phys. Rev.*, D 56 (1997) 3991.

[90] A. Aktas et al., Forward jet production in deep inelastic scattering at HERA, *Eur. Phys. J.*, C 46 (2006) 27, arXiv:hep-ex/0508055.

[91] S. Chekanov et al., Forward-jet production in deep inelastic *ep* scattering at HERA, *Eur. Phys. J.*, C 52 (2007) 515, arXiv:hep-ex/0707.3093.

[92] A. Aktas et al. [H1 Collaboration], Forward π^0 production and associated transverse energy flow in deep-inelastic scattering at HERA, *Eur. Phys. J.*, C 36 (2004) 441.

[93] A.H. Mueller, Parton distributions at very small x values, *Nucl. Phys.*, C 18 (1991) 125, arXiv:hep-ex/0707.3093.

[94] F.D. Aaron et al., Measurement of the azimuthal correlation between the most forward jet and the scattered positron in deep-inelastic scattering at HERA, *Submitted to EPJC.*

[95] J. Breitweg et al. [ZEUS collaboration], Measurement of multiplicity and momentum spectra in the current and target regions of the breit frame in deep inelastic scattering at HERA, *Eur. Phys. J.*, C 11 (1999) 251.

[96] J. Derrick et al. [ZEUS collaboration], Charged Particle Distribution in Deep Inelastic Scattering Events at HERA, *Z. Phys.*, C 70 (1996) 1.

[97] http://www-h1.desy.de/h1det/lumi/

[98] I. Abt et al. [H1 collaboration], The H1 detector at HERA, *Nucl. Instrum. Meth.*, A 386 (1997) 310,

[99] I. Abt et al. [H1 collaboration]; The tracking, calorimeter and muon detectors of the H1 experiment at HERA; *Nucl. Instrum. Meth.*, A 386 (1997) 348.

[100] R. Kogler, Measurement of jet production in deep-inelastic *ep* scattering at HERA, *DESY-THESIS-2011-003, MPP-2010-175*, 2010/11.

[101] C. Kleinwort, H1 alignment experience, *CERN-2007-004*, p. 41.

[102] J. Becker et al., A vertex trigger based on cylindrical multiwire proportional chambers, *Nucl. Instrum. Meth.*, A 586 (2008) 190.

[103] S. Eichenberger et al., A fast pipelined trigger for the H1 experiment based on multiwire proportional chamber signals, *Nucl. Instrum. Meth.*, A 323 (1992) 532.

[104] H. Beck, Principles and operation of the z-vertex trigger, *H1-05/96-479*, 1996.

[105] B. List, The H1 silicon tracker, *Nucl. Instrum. Meth.*, A 549 (2005) 33.

[106] M. Nožička, The forward and backward silicon trackers of H1, *Nucl. Instrum. Meth.*, A 501 (2003) 54.

[107] H. Henschel and R. Lahmann, The backward silicon tracker of the H1 experiment at HERA, *Nucl. Instrum. Meth.*, A 453 (2000) 93.

[108] T. Nicholls et al. [H1 SpaCal Group], Performance of an electromagnetic lead/scintillating fibre calorimeter for the H1 detector, *Nucl. Instrum. Meth.*, A 374 (1996) 149.

[109] B. Andrieu et al., The H1 liquid argon calorimeter system, *Nucl. Instrum. Meth.*, A 336 (1993) 460.

[110] B. Andrieu et al. [H1 Calorimeter Group], Results from pion calibration runs for the H1 liquid argon calorimeter and comparison with simulations, *Nucl. Instrum. Meth.*, A 336 (1993) 499.

[111] B. Andrieu et al. [H1 Calorimeter Group]. Beam tests and calibration of the H1 liquid argon calorimeter with electrons, *Nucl. Instrum. Meth.*, A 350 (1994) 57.

[112] R. Brun et al., Geant: Simulation program for particle physics experiments. User guide and reference manual, 1987.

[113] I. Abt et al., The tracking, calorimeter and muon detectors of the H1 experiment at HERA, *Nucl. Instrum. Meth.*, A 386 (1997) 348.

[114] V. Blobel, A new fast track-fit algorithm based on broken lines. *Nucl. Instr. and Meth.*, A 566 (2006) 14,

[115] V. Blobel, Central track reconstruction. March 11, 2004. (available at https://www-h1.desy.de/idet/itracker/TrackingGroup/AgnMin/Meet041103/blobel041103.pdf).

[116] B. Portheault, M. Peez and E. Sauvan, An energy flow algorithm for hadronic reconstruction in 00: Hadroo2, *H1-IN-616*, 2005.

[117] L. West, How to use the heavy flavour working group track, muon and electron selection code, 2000, (available at https://www-h1.desy.de/icas/imanuals/h1phan/track_manual30106.ps).

[118] I. Abt et al. [H1 Collaboration], The H1 detector at HERA, *Nucl. Instrum. Meth.*, A 386 (1997) 310.

[119] J. Engelen, S. Bentvelsen and P. Kooijman, Reconstruction of (x, Q^2) and extraction of the structure functions in neutral current scattering at HERA, 1992.

[120] F.D. Aaron et al. [H1 Collaboration], Measurement of the inclusive ep scattering cross section at low Q^2 and x at HERA, *Eur.Phys. J.*, C 63 (2009) 625, arXiv:0904.0929v2 [hep-ex].

[121] S. Osman and D. Salek, The low pt HFS and jet energy calibration, *H1-IN-631*, 2009.

[122] V.V. Arkadov, Measurement of the deep-inelastic ep scattering cross section using the backward silicon tracker at the H1 detector at HERA, *Humboldt-Univ, Berlin*, 2000.

[123] M. Jacquet et al., Absolute hadronic jet calibration of the H1 liquid argon calorimeter, *H1-04/99-571*, 1999.

[124] U. Bassler and G. Bernardi, On the kinematic reconstruction of deep inelastic scattering at HERA: the σ method, *Nucl. Instrum. Meth.*, A 361 (1995) 197, arXiv:hep-ex/9412004.

[125] M. Wobish, Measurement and QCD analysis of jet cross sections in deep-inelastic positron-proton collisions at $\sqrt{s} = 300$ GeV, *RWTH Aachen, DESY-THESIS-2000-049*, 2000.

[126] V. Lendermann at al., Combining triggers in HEP data analysis, *Nucl. Instrum. Meth.*, A 604 (2009) 707, arXiv:0901.4118v1 [hep-ex].

[127] F.D. Aaron et al. [H1 and ZEUS Collaboration], Measurement of $D^{*\pm}$ meson production and determination of $F_2^{c\bar{c}}$ at low Q^2 in deep-inelastic scattering at HERA, *Eur. Phys. J.*, C 71 (2011) 1769.

[128] K. Daum, Nuclear interactions of kaons and pions. Data vs. MC, 2010, (available at https://www-h1.desy.de/idet/itracker/TrackingGroup/AgnMin/Meet1001/daum.pdf).

[129] *CERN-2007-004*, http://pdg.lbl.gov

[130] S. Schmitt [H1 internal note], Correction of detector effects: bin-by-bin and unfolding, *H1-03/11-633*, 2011.

[131] K. Daum, Nuclear interactions of K and π. Data vs. MC, January 27, 2010, (available at https://www-h1.desy.de/idet/itracker/TrackingGroup/AgnMin/Meet1001/daum.pdf).

[132] M.H. Seymour, Matrix element corrections to parton shower simulation of deep inelastic scattering, *Contributed to 27th International Conference on High Energy Physics (ICHEP)*, Glasgow, Scotland, 20-27 Jul 1994.

[133] Private communication with R. Kogler [H1 Collaboration] and S.Höche.

[134] F.D. Aaron et al. [H1 and ZEUS Collaboration], Combined measurement and QCD analysis of the inclusive $e^{\pm}p$ scattering cross sections at HERA, *JHEP*, 1001 (2010) 109, [arXiv:0911.0884].

[135] P.M. Nadolsky et al., Implications of CTEQ global analysis for collider observables, *Phys. Rev*, D 78 (2008) 013004, [arXiv:0802.0007].

[136] E. Reya, M. Gück and A. Vogt, Dynamical parton distributions revisited, *Eur. Phys. J.*, C 5 (1998) 461, [arXiv:hep-ph/9806404v1].

[137] M. Hansson and H. Jung, Unintegrated parton density function in CCFM, *Proceeding of DIS2003*, p.488, [arXiv:hep-ph/0309009].

[138] [CMS Collaboration], Observation of long-range near-side angular correlations in proton-proton collisions at the LHC, *JHEP09* (2010) 091, arXiv:1009.4122v1[hep-ex].

Acknowledgement

I would like to thank Dr. Carsten Niebuhr and Dr. Hannes Jung for the opportunity to come and work at DESY.

I am very grateful to my supervisor Hannes Jung. Dear Hannes, thank you for perfect supervision, for always having time to help during the work. Even when you are traveling between Hamburg and Geneva, I know that you are ready to help with everything you can. Thank you for organising many inspirational meetings and bringing people together to discuss interesting and challenging issues. This encourage me to work hard and always make me think about physics beyond the analysis. Thank you for growing in us the interest to physics and surrounding world. And of course thank you very much for all the time reading and correcting the thesis, your comments lead to its substantial improvements.

My gratitude to me referees Dr. Thomas Schörner-Sadenius and Prof. Dr. Haller for agreeing to evaluate my work.

I am very thankful to my sister Julia for reading and commenting the thesis.

Many thanks to Mira for helping me to translate the abstract to German.

To people from H1 and especially to the conveners of the HaQ working group, Guenter, Daniel and Krzysztof. Thank you for friendly atmosphere at the meetings, for your help, support and fruitful discussions. All that always encourage me to give talks. To the physics coordinators, Karin and Katja, for the constructive and highly professional comments and remarks.

I want to thank very especially Paul for almost a year of intense work on the analysis extension. Paul, thank you for making me interested in completely new things. Thank you for your patient answers to my multiple questions. Thank you for sharing your energy and interest. Your attitude towards work and people will always be an example for me.

To my lovely office-mate and friend Nelly, who made our office life very cozy and friendly, who always find a word to encourage me and make me believe in myself. Thank you for all our nice conversations and warm atmosphere.

To the "Physics and Cookies" team, which was changing over time, but all of you are in my heart: Mira (my last H1 "Physics and Cookies" survivor friend), Zlatka, Julia, Samanta, Albert, Axel, Lluis, Tobias, Alex, Nil, Michal, Krzysztof, Martin, Panos, Paolo, Pedro, Rico. It was a lot of bright moments and plenty of fruitful discussions with you! Special thanks to Albert, Lluis and Axel for introducing me H1 physics and software in the beginning of my work. It was always a big pleasure

to get some help from our theorists, which explain the trigger efficiency as gluon saturation effect at small x.

To my friends: Aziz, Monica, Roman, Daniel, Pavel, Misha, Vika, Yura, Lena, Olena, Martin, Richard, Dave, Voica, Timon, Igor, Jasna and Anya. You helped me much more than you probably think. Sometimes I just need to talk or to look at you to feel better.

To Lesha and Sasha for always constructive help with SpaCal issues.

To Roman, our H1-wiki, for helping me with SHERPA, with h1oo and with many other things. On behalf of the young generation thanks a lot for your wonderful thesis, which is a source of knowledge.

Whatever I do in future H1 will be always in my heart with warmest memories... Thank you for this!

To my University professors, who made me who I am now and without whom this thesis would never be possible. Especially I would like to thank my former supervisor Grigory Aleksandrovich Feofilov.

Till min älskade Abbe. Tack för din kärlek, din förståelse, ditt stöd och din hjälp.

To my family, my father, my sister, Denis and Svetlana. This thesis is dedicated to you and to the memory of my mother Galina. Thank you for your endless love, for your support. The long path which I went to this point I did together with you and with your help. I love you.